Experimental and analytical investigations of non-skeletal carbonate production

A Thesis Presented to the University of Oxford

in Candidacy for the Degree of Doctor of Philosophy

By

Sascha Roest-Ellis

St. Peter's College
University of Oxford

Advised by Professor Nicholas Tosca

additionally supervised by Professor Stuart Robinson

Trinity 2021

Abstract of the thesis

The overriding aim of this research is concerned with understanding the chemical controls on carbonate sedimentation in naturally occurring highly alkaline systems that produce enigmatic mineral assemblages. The main approach taken here is to characterize the kinetic pathways of Ca-Mg-carbonate precipitation and mineralization in systems lacking a biological carbonate factory and to understand the relationship between fluid chemistry and mineralogy in non-classical nucleation regimes. The first line of research explores the kinetics of Ca-Mg-carbonate nucleation and recrystallization in the presence of phosphate (PO_4) as an inhibitor in high-alkalinity experiments. We identify and constrain new crystallization pathways to Mg-rich carbonates magnesite and disordered dolomite from amorphous precursors that overcome energy barriers under Earth surface conditions. The second line of research explores $CaCO_3$ nucleation under Neoproterozoic seawater conditions. We identify and constrain saturation state thresholds required for nucleation in these settings that are influenced by micromolar concentrations of PO_4. The third line of research explores geological carbonates to test our hypotheses that PO_4 may have influenced the mid-Neoproterozoic $CaCO_3$ factory. We reveal new P records that identify abundant and widespread P distribution at significantly elevated PO_4 concentrations in Neoproterozoic Tonian aged carbonate rocks. Together, this research indicates enhanced P-cycling in the Tonian that influenced the $CaCO_3$ factory and may have resulted in enhanced concentrations of bioavailable P that was crucial for biological evolution.

Long abstract

This research is concerned with understanding alternative carbonate mineral formation pathways to $CaCO_3$ and high-Mg $CaCO_3$ minerals that nucleate in high supersaturation regimes influenced by chemical mediating compounds. To address this problem from a kinetic standpoint, we investigate the impact of inhibition and supersaturation on the styles of Ca-Mg-CO_3 precipitation from synthetic alkaline seawater and lake water solutions. Our approach draws together geochemical constraints for past depositional environments from fluid inclusion data (i.e., Spear et al., 2014) and chemical precipitation boundaries for authigenic minerals calcite microspar, primary dolomite and Mg-silicate (i.e., Tosca et al., 2011; Strauss and Tosca, 2020). We incorporate these into different experimental methods to examine the precipitation of Mg-rich $CaCO_3$ minerals from hyper-alkaline, hyper-saline conditions influenced by millimolar concentrations phosphate (PO_4) concentrations known to inhibit aragonite and calcite (i.e., Burton and Walter, 1990). Our research reveals new, non-classical formation pathways to $CaCO_3$ that likely led to enigmatic calcite microspar cement precipitation that is characteristic of mid-Proterozoic marine carbonates. Environments like these dominated by chemical control can drive kinetic pathways mediated by common compounds available in seawater that inhibit direct aragonite and calcite crystallization and enable mineral pathways to overcome kinetic barriers. Because the stratigraphic abundance of microspar (a direct seawater cement) peaked in the early Neoproterozoic (James al., 1998), this research suggests that $CaCO_3$ nucleation thresholds were repeatedly crossed on a global scale, which may have had drastic influence on biogeochemical cycles and specifically the carbon cycle. Understanding kinetically driven pathways on mineral formation elucidates the chemical controls on global systems that are not buffered by skeletal carbonate productions and are highly sensitive to the surrounding chemical environment.

We have identified that the presence of dissolved PO_4 in water influences enhanced CO_3^{2-}-alkalinity and increases supersaturation relative to carbonate minerals (i.e., $\Omega_{calcite}$ and Ω_{ACMC}). In doing so, we have constrained key chemical nucleation threshold for calcite in mid-Proterozoic

composition seawater that help explain kinetically driven mechanisms of carbonate sedimentation.

Taking these PO_4 derived kinetic constraints further; we address the long-standing problems related to Mg-rich carbonate production – notably of magnesite, high-Mg calcite and dolomite from amorphous precursors that overcome energy barriers under Earth surface conditions. Despite extensive research, lack of conformity to the expected thermodynamic pathways and difficulty in synthetic production experimentally has left significant gaps in our understanding of mineral formation pathways. The problem herein lies in the kinetics of magnesium ions. To address the Mg related problem from a kinetic standpoint, we investigate the impact of inhibition and supersaturation on the styles of Ca-Mg-CO_3 precipitation.

Our approach used two different experimental methods to examine the precipitation of magnesium carbonate minerals from hyper-alkaline, hyper-saline conditions at low diagenetic temperatures (50 ºC) with millimolar concentrations of PO_4. Firstly, from amorphous calcium magnesium carbonate (ACMC) precursors (> 50 mol % Mg) that were added to alkaline-saline solutions and secondly, from homogenous nucleation experiments in alkaline-saline solutions.

We reveal that the ACMC precursor experiments typically resulted in mixtures of very high Mg-calcite (48 mol% Mg), aragonite and dolomite. The homogeneous nucleation experiments promoted the nucleation of Mg-rich (>60 mol% Mg) ACMC spherules, from solutions linked to kinetic inhibition by PO_4 and supersupersaturation caused by enhanced carbonate alkalinity. Crystallization within the evolved solutions led to widespread transformation into hydromagnesite and subsequent recrystallization into magnesite and minor presence of ordered dolomite mineral aggregates with apatite and aragonite. The maintenance of supersaturation and inhibition by PO_4 facilitated magnesium incorporation into crystal structures despite the Mg hydration barrier. Higher PO_4 concentrations (14 m*M*/kg) were conducive to more extensive and faster rates of transformation into magnesite and dolomite.

This study identifies two new formation pathways and mechanisms for magnesite and Mg-Ca-carbonate sediments formation and provides new calculated solubility estimates for amorphous phases > 50 % Mg. This provide insight into reaction pathways and supports our understanding of geochemical carbonate alkalinity and PO_4 cycling processes in natural systems. This is important for characterizing environmental systems that existed in Earth's geological past and may have existed on Mars, where spectroscopic evidence indicates the presence of magnesite and sedimentary PO_4 concentrations higher than those typical on Earth (i.e., Ehlmann et al., 2008).

Although the production of these Mg-rich carbonate minerals can be facilitated by microbial activity, an important finding is that conditions for magnesite and dolomite formation at Earth surface conditions does not require microbial influence. Instead, these pathways emphasize the importance of kinetic inhibitors in mineral formation pathways and signals that alternative calcium carbonate precipitation pathways that may have dominated carbonate sedimentation in paleo-environments and alkaline lake settings through much of Earths history. This provides fundamentally important information in understanding the formation of magnesite that can be met in alkaline lake settings where PO_4 accumulations can reach > 1 m*M* (Toner and Catling, 2020). These conditions enable magnesium hydration barriers to be overcome, which has previously been described as 'virtually impossible' at Earth surface conditions (Xu et al., 2013).

Using the newly constrained geochemical conditions provided by experiments and geochemical modelling, we tested our hypothesis that elevated dissolved PO_4 concentrations in mid-Proterozoic Tonian oceans may be recorded in carbonate sediments. This would and provide insight into the Neoproterozoic geochemical P-cycle; at a key time in Earths history. Because our experimental data show a strong relationship between PO_4, carbonates and apatitic scale microfossils that have been identified in Tonian successions (Cohen et al., 2017) hinting at elevated P concentrations, we examined Tonian aged shallow water carbonates for phosphate to can constrain the relationship further.

Our investigation focused on examining the concentration, speciation, and distribution of phosphorus in non-skeletal shallow water carbonate sediments using a range of microanalytical techniques. In-situ examination of the spatial distribution and molecular configuration of phosphorous in Neoproterozoic carbonate samples was permitted through low-energy synchrotron X-ray absorption spectroscopy (XANES) and micro-XRF mapping. In addition, the molecular environment of phosphorous in carbonate fabrics was constrained using ^{31}P solid-state NMR indicating that phosphorous has been identified bound in the carbonate lattice.

Microcrystalline $CaCO_3$, unambiguously precipitated in place (derived from the water column) is associated with high phosphorous content. This directly supports the hypothesis that dissolved PO_4 was present during nucleation and may have acted as a key inhibitor during mineralization at this time and may have provided bioavailable marine phosphorous that was essential to biological evolution. These datasets have permitted a unique set of constraints on this geochemically important relationship. Additionally, this research indicates that carbonates can host a record of Neoproterozoic dissolved PO_4 availability providing insight into the ancient phosphorous cycle through a key interval of Earth's history.

Furthermore, the Neoproterozoic Era (1000-541 million years ago) saw a major biological evolutionary transition from a prokaryote-dominated biosphere to eukaryote-dominated biosphere. As PO_4 is a key component in all life on Earth, gaining a new perspective on the Proterozoic P-cycle interrelated with the calcium-magnesium-carbonate system is important for identifying potential influences that drove evolutionary shifts. However, the results of this research signal that a revaluation of the role of P this critical time may be required. NMR, show PO_4 is bound principally in carbonate fluorapatite (CFA); deposited as seafloor synsedimentary cements, within Mg-silicate-rich intraclasts, nano-inclusions within microspar cement and talc, and as disseminated detrital particles. Our data show that PO_4 is dominantly carbonate-associated, and only rarely associated with ferric-iron oxide/organic matter in these mid-Neoproterozoic samples; Fe and S-bearing diagenetic minerals, the products of anoxic

respiration, are rare. These data suggest that the enhanced [PO_4] in Neoproterozoic seawater may have permitted non-classical $CaCO_3$ nucleation at high Ω_{Cal}, in turn producing synsedimentary microspar with authigenic Mg-silicates (Strauss and Tosca, 2020), and apatite. Similar regimes may have led to non-classical $MgCO_3$ and Mg-Ca-CO_3 nucleation resulting in widespread primary dolomite and high Mg-calcite sedimentation that dominates through much of the Precambrian.

Overall, our research provides new pathways to enigmatic $CaCO_3$ nucleation and $MgCO_3$ nucleation with corresponding geochemical constraints and explanations for how kinetically driven pathways may have dominated carbonate sedimentation and mineralogy through Earths history. We also reveal new P records that identify abundant and widespread P distribution at significantly elevated PO_4 concentrations in Neoproterozoic Tonian aged carbonate rocks. Together, this research indicates enhanced P-cycling in the Tonian that influenced the $CaCO_3$ factory and may have resulted in enhanced concentrations of bioavailable P that was crucial for biological evolution on the cusp of early eukaryotic diversification.

Disclaimer and Copyright Declaration

I declare that this thesis, which I submit to the University of Oxford for examination in consideration of Doctor of Philosophy in Earth Sciences is entirely my own work except where otherwise indicated. This thesis has not been submitted, either partially or in full, either for this Honour School or qualification or for another Honour School or qualification of this University, or for a qualification at any other institution. I have clearly indicated the presence of all material from other sources, including any diagrams, charts, tables or graphs. I have clearly indicated the presence of all paraphrased material with appropriate references. I have stated below and acknowledged appropriately any assistance I have received in addition to that provided by my adviser. Any publizhed work is clearly indicated and appropriately referenced.

Publication

Chapter 3 is a reproduction of a peer-reviewed publication in *Geology*. The publication copyright is Gold Open Access, © 2021 The Authors. This paper is published under the terms of the CC-BY license. Therefore, reproduction in this thesis is freely permitted.

Citation: Roest-Ellis, S., Strauss, J.V., and Tosca, N.J., 2021, Experimental constraints on nonskeletal $CaCO_3$ precipitation from Proterozoic seawater: Geology, v. 49, p. Geological Society of America, Geology, v. XX (X) p. X, https://doi.org/10.1130/G48044.1

Collection of data

- **XANES and µXRF data collection:** The collection of synchrotron XANES and µXRF spectroscopy was facilitated by Jocelyn Richardson and Sam Webb at Stanford Synchrotron Radiation Lightsource, National Accelerator Laboratory, U.S. Department of Energy, U.S.A.
- **NMR data collection:** The collection of NMR ^{31}P and ^{19}F data was carried out by Brian Phillips, Department of Geosciences, Earth and Space Sciences Building, Stony Brook University, NY, U.S.A.
- **ICP-AES data collection:** Assistance in the collection of ICP-AES data was facilitated by Ian Jarvis at Kingston University, Kingston, UK.
- **ICP-MS data collection:** The collection of ICP-MS data was facilitated by Phil Holdship, Earth Sciences, University of Oxford, UK.
- **XRD data collection:** Assistance in XRD data collection of was facilitated by Kat Clayton and Alice Barrol, Earth Sciences, University of Oxford, UK.
- **SEM data collection:** Assistance in SEM data collection was facilitated by Errin Johnson at the Dunn School of Pathology, University of Oxford, UK, and Jon Wade of the Earth Sciences Department, University of Oxford, UK.
- **Bulk PO_4 data collection:** Assistance in bulk PO_4 data collection was provided by Olivia Gaitonde, Earth Sciences Department, University of Oxford, UK
- **$\delta^{13}C$ and $\delta^{18}O$ isotope data collection:** Assistance in $\delta^{13}C$ and $\delta^{18}O$ data collection was provided by Chris Day.

Acknowledgments

There are several people that I must thank. Firstly, Nick Tosca – my advisor and the most inspirational scientist that I know. You have expanded my passion for geoscience to cover the whole of Earth's history and made me excited about natural systems and geochemical processes on Earth and far beyond. This research would not have been possible without your dynamic vision, guidance and support. The incredible teaching, opportunities and tools that you have provided me with will help me navigate a future career in science.

I must acknowledge the NERC Oil and Gas CDT for funding my research and providing extensive multidisciplinary geoscience training. I am incredibly grateful for the numerous field trips through Europe and the opportunity to be part of a life-long cohort of geoscientists and friends. I would also like to thank ICCR2 for the opportunity to join the carbonate research projects in Brazil.

I would like to thank my examiners Julie Cosmidis and Sam Webb – I thoroughly appreciate the time you have taken to examine my work. I would also like to thank Stuart Robinson for your support in supervision, advice and the opportunity to assist in laboratory practicals.

I am grateful to Justin Strauss – thank you for your collaboration, sample donation, insightful feedback and your ongoing passion. I express deep thanks to Sam Webb and Jocelyn Richardson for guiding analyses at Stanford's Synchrotron SSRL – your insight was invaluable, and the midnight data collection, trips to the Rosewood and mutual appreciation for Burgundy are uniquely memorable.

The collection of numerous datasets that support this thesis would not have been possible without Kat Clayton for assistance with XRD; Errin Johnson and Jon Wade for assistance with electron microscopy; Ian Jarvis and Phil Holdship for assistance with ICP data collection; Brian Phillips for NMR data collection, analysis and collaboration; Chris Day for assistance with isotopic analyses. Jon Wells, James King and Jamie Long for workshop assistance. Pippa Halverson, Marcus Kunzmann, Sarah Wörndle and Phoebe Cohen for providing samples and data.

I am indebted to the entire Tosca Research Group: Clancy Zhijian Jiang, Raphael Pietsch, Rosalie Tostevin, Brooke Johnson, Matt Brady, Ross Anderson, Ricky Sengupta, Ben Tutolo, Lucy Kissik, Kat Clayton and Olivia Gaitonde) for providing encouragement, support and entertainment throughout my time in Oxford. I cannot express enough thanks to Clancy for invaluable advice and support, and Raphael for thought provoking discussions and assistance. I would also like to thank Ian Jarvis for sparking my passion for carbonate sedimentology and geochemistry and the reason I have pursued research.

Personal Acknowledgements

I must recognize the support of my family – my mother, Yvonne for instilling a deep passion of the natural world; my father, Max for continual positivity and encouragement; and my sister, Charlotte and brothers – notably Sebastiaan as well as my in-laws, who have all dedicated their time to me.

Finally, to James, my husband and biggest supporter. You have backed me implicitly over the last 10 years and given me the confidence and encouragement to pursue my passion. Nothing makes me happier than being with you and our two spaniels planning our next expedition. I appreciate the sacrifices you have made and I am sorry that you make a better housewife than I will ever be.

Table of Contents

List of Figures

List of Tables

Chapter 2: A non-classical pathway to Mg-rich calcium carbonates

Supplementary Material

Supplement to Chapter 2:

Supplement to Chapter 3:

List of Abbreviations

ACC ..... Amorphous calcium carbonate
ACMC ..... Amorphous calcium magnesium carbonate
ACP ..... Amorphous calcium Phosphate
AMC ..... Amorphous magnesium carbonate
Arag ..... Aragonite
ASM ..... Apatitic scale microfossils
CAP ..... Carbonate associated phosphate
CCLAP ..... Carbonate-chlorapatite ($Ca_8Na_2([PO_4]_4[CO_3]_2)Cl_2$, often Na-bearing)
C-cycle ..... Carbon cycle
CFA ..... Carbonate fluorapatite
CFAp or CFA ..... Carbonate-fluorapatite ($Ca_{10}([PO_4]_5[CO_3])_3(F,O)$ or $Ca_{10}(PO_4)_5(CO_3F)F_2$)
CLAp ..... Chlorinated apatite ($Ca_{10}(PO_4)_6Cl_2$, often Na-bearing)
CO_3-Ap ..... Carbonate apatite ($Ca_{10}[PO_4])_6[CO_3]H_2O$)
DOL ..... Dolomite
FAp ..... Fluorapatite ($Ca_{10}[PO_4])_6[F]_2$)
FTIR ..... Fourier transform infrared spectroscopy
g ..... Gram
h ..... Hour
HAp or HA ..... Hydroxyapatite ($Ca_{10}[PO_4])_6[OH]_2$)
HMC ..... High-Mg calcite
HMg ..... Hydromagnesite
Mg-C ..... Magnesium calcite
Mg-calcite ..... Magnesium calcite
MHc ..... Monohydrocalcite
Micro-XRF ..... Micro X-ray fluorescence spectroscopy
min ..... Minutes
M ..... Moles/kg
m*M* ..... Millimol/kg
m*M*/L ..... Millimol/litre
µ*M* ..... Micro mol/kg
µm ..... Micrometer
NMR ..... Nuclear magnetic resonance spectroscopy
P ..... Phosphorous

P-cycle ..... Phosphorous cycle

pm ..... Picometre (measurement of ionic radius)

PO_4 ..... Phosphate (PO_4^{3-})

SEM ..... Scanning electron microscope

SEM-EDS ..... Scanning electron microscope energy-dispersive X-ray spectroscopy

SEM-HDBSD ..... Scanning electron microscope high definition backscattered electron detector

TCP ..... Tricalcium phosphate

TEOS ..... Tetraethyl orthosilicate ($Si[OCH_2CH_3]_4$)

v_1 ..... Vibration mode of chemical bonds (FTIR)

VHMC ..... Very high Mg-calcite

XANES ..... X-ray absorption near edge structure

XRD ..... X-ray powder diffraction

Å ..... Angstrom (measurement of ionic radius)

A-type CO_3-Ap ..... CO_3 ion substitution for OH^- ions in apatite

β-type CO_3-Ap ..... CO_3 ion substitution for PO_4^{3-} ions in apatite

Ω (omega) ..... Saturation state

$\%_{mol}$ ..... Mole percent

$\%_{wt}$ – ..... Weight percent

[ ] ..... Ions in square brackets refers to concentration (i.e., calcium concentration [Ca],[Ca^{2+}])

º C ..... Degrees Celsius for temperature

2Θ ..... 2-Theta: x-axis position º 2Θ for XRD peaks

Chapter 1: Introduction

1.1 Summary

This chapter is an introduction to the research on alternative calcium magnesium carbonate formation pathways. Firstly, the chapter lays out the motivation and problems addressed by the research. A full literature review then follows which provides an overview of sedimentary carbonate precipitation styles in the Precambrian and in highly alkaline lacustrine settings and shines a light on several enigmas related to calcium magnesium carbonate precipitation styles and mineralogy. The review then introduces non-classical precipitation pathways via amorphous carbonate precursors and provides explanations for problems related to the incorporation of magnesium into calcium carbonate minerals. The chapter then draws together the problems related to kinetic inhibition of thermodynamically favoured carbonate minerals and explores inhibiting compounds that influence carbonate precipitation with a specific focus on phosphate. From there, the review focusses on the geochemical phosphorous cycle and current constraints on sedimentary phosphorous concentrations.

1.2 Motivation

Calcium carbonate ($CaCO_3$) minerals such as calcite and aragonite and magnesium-rich minerals such as high-Mg calcite, dolomite ($CaMgCO_3$) and magnesite ($MgCO_3$) are observed in modern sediments and geological sedimentary rocks with occurrences spanning throughout Earths history (Morse and Mackenzie, 1990). As a major sedimentary contributor, carbonate minerals play a key role in carbon and calcium biogeochemical cycles (Morse and Mackenzie, 1990). Although $CaCO_3$ is the most abundant biomineral present day (Weiner and Dove, 2003), for much of Earths geological history, skeletal $CaCO_3$ biomineralization was absent and carbonate sediments were controlled by chemical processes. In the absence of a $CaCO_3$ biological buffer through much of the Precambrian, kinetic pathways may have controlled carbonate production and led to high-Mg

$CaCO_3$ mineral production that was widespread during this time. These systems may have been highly sensitive to ocean-atmospheric chemical variations, which would have had a major influence on the global carbon cycle.

In this regard, compounds known to inhibit $CaCO_3$ mineralization pathways are commonly available in seawater; yet elucidating the sedimentological consequences of kinetic inhibition in natural settings remains largely unaccounted for. Furthermore, despite extensive research and the widespread occurrence of primary dolomite, high-Mg calcite and magnesite in the geological record and modern lakes, the inability to reproduce these minerals experimentally has left significant gaps in our understanding of mineral formation pathways (i.e., Mckenzie and Vasconcelos, 2009).

The inability to form both the thermodynamically most stable mineral dolomite and thermodynamically most reactive minerals magnesite and high-Mg calcite experimentally means that our understanding of carbonate deposition over most of Earths history remains largely enigmatic. The lack of conformity to the expected thermodynamic pathway indicates that the formation mechanisms of high-Mg $CaCO_3$ minerals is kinetically controlled (i.e., Lippmann, 1973; Hardie, 1987). However, the hydration of magnesium ions (Mg^{2+}) may be a major energetic barrier that inhibits the formation of these minerals (Bischoff, 1998). Therefore, the identification of energetic barriers and means to overcome them are crucial for understanding carbonate production in natural settings.

The overriding aim of this research is concerned with understanding alternative carbonate mineral formation pathways to high-Mg $CaCO_3$ minerals that result in nucleation in high supersaturation regimes and overcome kinetic barriers. To address this problem from a kinetic standpoint, we investigate the impact of inhibition and supersaturation on the styles of Ca-Mg-CO_3 precipitation. Our approach draws together geochemical constraints for past depositional environments from fluid inclusion data (i.e., Spear et al., 2014) and chemical precipitation boundaries for authigenic minerals calcite microspar, primary dolomite and Mg-silicate (i.e.,

Tosca et al., 2011; Strauss and Tosca, 2020). We incorporate these into different experimental methods to examine the precipitation of Mg-rich $CaCO_3$ minerals from hyper-alkaline, hyper-saline conditions influenced by minor phosphate (PO_4). Together with micro-analyses of geochemical signatures recorded in geological carbonates, we aim to connect kinetically driven geochemical pathways with modern alkaline-saline lakes and marine systems that existed in the Proterozoic Eon (2500-541 million years ago). Because records of this period in Earths history indicate major shifts in atmospheric CO_2, climate, marine redox state and phosphorous cycling, understanding carbonate mineralization pathways as a direct output of these environments will support key questions about past geochemical processes.

Furthermore, the Neoproterozoic Era (1000-541 million years ago) saw a major biological evolutionary transition from a prokaryote-dominated biosphere to a biosphere where eukaryotes became significantly more prevalent. PO_4 is a key component in all life on Earth, gaining a new perspective on the Proterozoic P-cycle interrelated with the calcium-magnesium-carbonate system is important for identifying potential influences that drove evolutionary shifts. However, the results of this research signal that a revaluation of the role of P during this critical time may be required.

1.3 Precambrian carbonates

1.3.1 Precambrian carbonate signatures

Calcium carbonate ($CaCO_3$) minerals such as calcite and aragonite and their magnesium-rich counterparts such as Mg-calcite, dolomite ($CaMg(CO_3)_2$) and magnesite ($MgCO_3$) are observed in modern sediments and sedimentary rocks that span Earth's geological history (Morse and Mackenzie, 1990). These sediments play a key role in Earth's carbon cycle (C-cycle), calcium cycle (Ca-cycles) and influence other major biogeochemical cycles (Zeebe et al., 2008, Zeebe and Wolfe Gladrow, 2001; Holland, 1984; Morse and Mackenzie, 1990) through precipitation, which incorporates ocean-atmospheric CO_2 in the form of bicarbonate ions (HCO_3^-) (Zeebe and Wolfe

Gladrow, 2001; Swart, 2015). Following precipitation, $CaCO_3$ minerals are deposited and stored for millions of years within carbonate sediments and rocks. Despite the apparent chemical simplicity, the formation of carbonate sediments is deceitfully complex owing to the unique reactivity, physical properties and chemical diversity within carbonate minerals, which is further complicated due to their origin from both biogenic and abiogenic sources (Arvidson and Morse, 2014). The precipitation of carbonate sediments occurs typically in marine settings and records chemical signatures of the surrounding environment (Arvidson and Morse, 2014). Therefore, significant information regarding ancient ocean-atmosphere conditions can be captured in geological sediments through the incorporation of trace elements, ions, isotopic ratios and other chemical signatures (i.e., Morse, 1985, Knoll et al., 1986; Swart, 2008; Arvidson and Morse, 2013).

Because carbonate strata have been deposited in oceans on Earth for at least 3 billion years (Ga) (van Kranendok et al.,2003; Allwood et al., 2010; McIntyre and Fralick, 2017) deposition during much Earth's history occurred prior to the evolution of $CaCO_3$ skeletal biomineralization (Grotzinger and James, 2000; Weiner and Dove, 2003; Cantine et al., 2020) when biogenic carbonate production was absent or minor (i.e., dominated by stromatolites, Raaben, 1969; Knoll and Swett, 1990). In fact, the first occurrence of calcareous mineralizing eukaryotes is reported as late as the Neoproterozoic Ediacaran (570–510 million years (Ma); Nama Group of Namibia, Grotzinger et al., 2000) in contrast to the abundance of biomineralogical $CaCO_3$ production that has dominated from the Phanerozoic to the present day (Weiner and Dove, 2003). Therefore, the abiogenic and authigenic nature of Precambrian sediments provides an original and unique chemostratigraphic record from which we can explore mineral formation pathways, sedimentation processes and importantly, the chemical composition of water from the time of precipitation, that together can support reconstructions of ancient depositional environments (Fralick et al., 2017; Grotzinger and James, 2000).

1.3.2 Precambrian precipitation styles

Precambrian carbonate sedimentological records have long indicated distinct shifts in the style of $CaCO_3$ production (i.e., Grotzinger and James, 2000), in response to secular variations in the seawater chemistry (Grotzinger, 1989, Spence et al., 2016). For example, late Archean and early Proterozoic carbonates are characterized by direct seafloor-encrustation of herringbone calcite and aragonite fans (Grotzinger, 1989; Grotzinger and James, 2000; Sumner and Grotzinger, 1996; 2004), whereas their Neoproterozoic counterparts are mostly defined by finely crystalline micrite (carbonate mud) and enigmatic calcite microspar cement (Figure 1. 1) (Knoll and Swett, 1990; Sumner and Grotzinger, 1996; Turner, et al., 1997); a texture that is often attributed to spontaneous/homogeneous precipitation from a supersaturated water body (Grotzinger, 1989; Knoll and Swett, 1990; Hoffman et al., 1998). Calcite microspar most notably fills 'molartooth structures' (MTS)(Figure 1. 1), which are enigmatic structures of variably shaped voids in fine-grained marine carbonates that are synsedimentary (James et al., 1998; Sherman, 2000; Bishop and Sumner, 2006; Hoffman and Macdonald, 2010; Hood et al., 2015). Occurrences of microspar cement filled MTS have been identified in the Precambrian from the Archean to the Ediacaran with a global geographical spread, however, they are almost uniquely confined to the Mesoproterozoic to mid-Neoproterozoic (ca. 1500-720 Ma) and staggeringly account for around 25 % of the precipitated carbonate from this time (James et al., 1998; Shields, 2002; Bishop and Sumner, 2006; Pollock et al., 2006; Hood et al., 2015; Shen et al., 2016; Hodgskiss et al., 2018).

These sediments coincide with drastic perturbations to Earth's C-cycle and major climatic instability in the mid-Neoproterozoic which is archived by distinct carbon isotope excursion events (Knoll et al., 1986; Knoll and Walter, 1992; Des Marais et al., 1992; Halverson et al., 2005, Johnston et al., 2012; Spence et al., 2016) and major changes in ocean-atmospheric geochemical cycling (Holland, 1984; Holland et al., 1986; Halverson et al., 2005, Lenton et al., 2014; Horton, 2015; Reinhard, et al., 2016; Spence et al., 2016; Shields and Mills, 2017; Lenton and Daines, 2018 Wei et al., 2020). In addition, changes in tectonic activity (Harlan et al., 2003; Dallman et

al., 2015) intensity and styles of physical and chemical weathering are recorded during this time (Hoffman et al., 1998; Pierrehumbert, 2011; Och and Shields-Zhou, 2017; Strauss and Tosca, 2020). Furthermore, key biological evolutionary milestones such as the evolution of Eukarya and transition from a prokaryote dominated to a eukaryote dominated biosphere are reflected in the Neoproterozoic (i.e., Canfield et al., 2007; Porter and Knoll, 2000; Porter, 2011; Brocks, 2017) as well as apatite skeletal biomineralization of marine organisms (i.e., Cohen et al., 2017; Cantine et al., 2020). Together, these combined tectonic-climatic-physiochemical conditions influenced biogeochemical cycles and carbonate sedimentological processes in the Proterozoic and resulted in radical changes to Earths evolutionary trajectory. However, the specific chemical factors that control abiogenic $CaCO_3$ production and contribute to the diverse precipitation styles and mineralogy in Precambrian carbonates are poorly constrained.

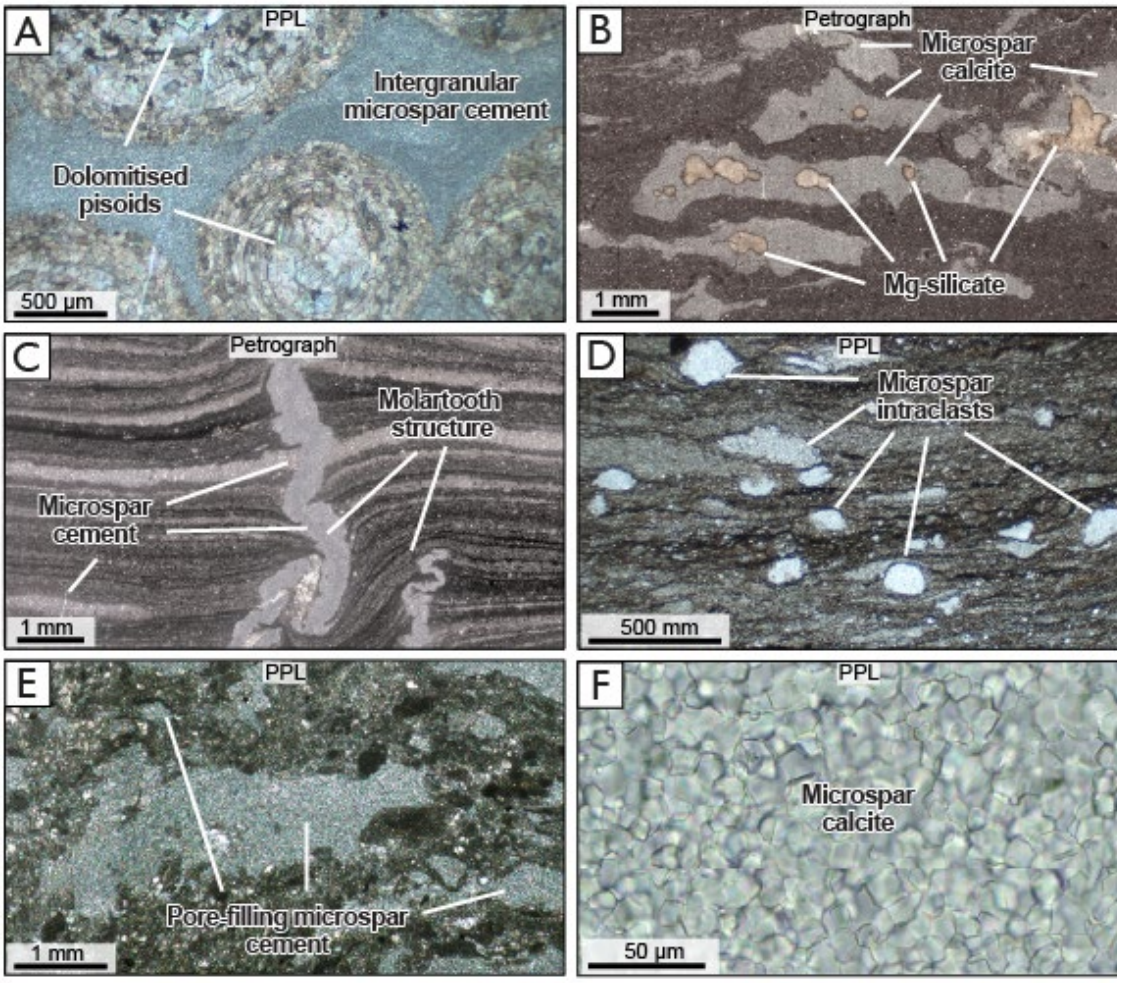

Figure 1. 1 Petrographic and optical images of late Proterozoic sedimentary textures.
A) Intergranular calcite microspar cement matrix supporting dolomitised ooids (Backlundtoppen Formation, Akademikerbreen Group, Svalbard, Norway). B) Mg-silicate (now preserved as talc) nodules within abundant calcite microspar cement within laminated lime mudstone (Svanbergfjellet Formation, Akademikerbreen Group, Svalbard, Norway). C) Molartooth Structure (MTS) filled with calcite microspar cement within laminated micrite that is variably deformed around the MTS indicating syn-sedimentary precipitation in soft-sediment. D) Intraclasts of microspar within organic-rich lime mudstone (Fifteenmile Group, Yukon, Canada). E) Pore-filling calcite microspar cement in an intraclastic wackestone (Svanbergfjellet Formation, Akademikerbreen Group, Svalbard, Norway). F) Characteristically uniform pore-filling microspar cement comprised of euhedral interlocking calcite crystals (Svanbergfjellet Formation, Svalbard, Norway). Optical images are shown in plane-polarised light (PPL).

1.3.3 Precambrian dolomite Mg-Ca-CO_3 problem

In addition to unusual $CaCO_3$ precipitation styles and textural components, Precambrian carbonates are characterized by distinctive mineralogy. Dolomite sediments (commonly termed dolostone) dominate in Precambrian carbonate successions (Grotzinger and James, 2000, Knoll and Swett, 1990; Hood and Wallace, 2018) with common occurrences of high-Mg calcite, yet the occurrence and distribution of dolomite and high-Mg calcite is comparatively minor in Phanerozoic successions and uncommon in recent sediments (i.e., Grotzinger and James, 2000). Precambrian dolomite is typically characterized by dolomicrite mud (Tucker, 1982; Grotzinger, 1989; Grotzinger and Knoll, 1995) that based on isotopic (Shuster et al., 2018), sedimentological and petrographic evidence (Tucker, 1982; Arvidson and McKenzie, 1999; Petrash et al. 2017) is notably of primary to early diagenetic origin, and preserves no evidence of former aragonite (Fairchild and Spiro, 1987). This means that despite common assumptions that dolomite presence was associated with aragonite, primary dolomite appears to form directly from Precambrian seawater that was unlike Phanerozoic and modern seawater in its chemical composition and redox state and may have sustained conditions that promoted more widespread Ca-Mg-CO_3 precipitation than today (Tucker, 1982; Burns et al., 2000; Hood et al., 2011; Hood and Wallace, 2012, 2018; Shuster et al., 2018; Wood et al., 2017). For decades, the formation of dolomite has puzzled geologists owing to the difficulties in producing dolomite experimentally coupled with the shortfalls of predicting and explaining the spatial and temporal geological and geographical distributions of dolomite, which leaves significant gaps in our understanding of dolomite termed 'the dolomite problem' (i.e., Arvidson and Mackenzie, 1999; Fairbridge, 1957; Land, 1998; Warren, 2000; Mckenzie and Vasconcelos, 2009; Gregg et al., 2015). Another problem is that dolomite, and similarly enigmatic Mg-rich carbonates—magnesite and high-Mg calcite—are often notably absent in settings supersaturated with respect to Mg-Ca-CO_3 where the formation of these minerals is thermodynamically favourable. This means that based on thermodynamic theory, the production of dolomite and magnesite should be widespread present day such as in

modern day seawater, yet these minerals are notably absent and instead aragonite and/or calcite predominate (Baker and Kastner, 1981; Hardie, 1987; Wilkinson and Algeo, 1987; Brady et al., 1996). As a consequence, our understanding of the key roles that Ca-Mg-CO_3 sediments play in Earth's C-cycle as a buffer for the ocean-atmospheric CO_2 system (Zeebe et al., 2008, Zeebe and Wolfe Gladrow, 2001; Holland, 1984) and as a product of divergent Precambrian ocean-atmosphere chemistry remain somewhat ambiguous.

1.3.4 Alkaline lakes, magnesite and Mars

Although volumetrically less abundant than dolomite in Precambrian strata, large-scale magnesite ($MgCO_3$) deposits also occur with relatively minor occurrences in the Phanerozoic (White and Young, 1980; Frank and Fielding, 2003) and the modern. Magnesite is typically present in continental high-alkaline evaporitic depositional settings (Müller et al., 1972; Miser et al, 1987; Warren, 1990; Pérez et al., 2002; McKirdy et al., 2010). In addition, evidence for carbonate sediments on Mars suggests that depositional environments interacted with liquid water and may have included lacustrine environments (i.e., Pollack et al., 1987). Based on near-, mid- and far-infrared spectroscopy (Russel et al., 1999; Ehlmann et al., 2008; Palomba et al., 2009; Michalski and Niles, 2010; Bultel et al., 2019) and remote sensing data (Bultel et al., 2019; Horgan et al., 2020), carbonates minerals have been identified on Mars that are composed dominantly of Mg-carbonate minerals magnesite (and possibly huntite; $CaMg_3[CO_3]_4$).

1.3.5 $CaCO_3$ enigmas from the Precambrian

A major problem in understanding Precambrian carbonates relates to the precise saturation state with respect to calcite (Ω_{Cal}, which is expressed by [$\Omega_{Cal} = IAP_{Cal}/K$], where IAP represents ion activity product and K represents the apparent mineral solubility product) associated with non-skeletal $CaCO_3$ precipitation. Although $CaCO_3$ may nucleate inorganically from modern seawater at Ω_{Cal} ~20-25 (He and Morse, 1993), the Ω_{Cal} at which late Proterozoic $CaCO_3$ nucleated is

unquantified. This is critical because Proterozoic carbonate accumulations, particularly fine-grained sediments are thought to reflect pervasive water column nucleation from supersaturated seawater (Grotzinger, 1989; Herrington and Fairchild, 1989; Knoll and Swett, 1990). Recent experimental and theoretical data suggest that the formation of $CaCO_3$ microspar cement during Neoproterozoic times required Ω_{Cal} greatly exceeding that of the modern ocean (Strauss and Tosca, 2020). However, the maintenance of $CaCO_3$ supersaturation through much of the Precambrian, by definition, requires the inhibition and/or modification of $CaCO_3$ precipitation (i.e., Sumner and Grotzinger, 1996). This, in turn, suggests that before skeletons evolved, the rates and pathways of $CaCO_3$ production may have been strongly controlled by kinetic factors. Furthermore, it is generally agreed that the enigmatic precipitation of dolomite, high-Mg calcite and magnesite (i.e,, Chave et al., 1962; Hardie, 1987; Raz et al., 2000; Long et al., 2014) requires a kinetic mediator to overcome energy barriers (Lippmann, 1973; Hardie, 1987; Land, 1998; Arvidson and Mackenzie,1999; Warren, 2000; Petrash et al. 2017; Warren, 2019) that may have later been overcome by biomineralization (Robinson, 2016).

Nevertheless, despite much research to address these problems, the specific chemical control and mechanisms of authigenic shallow water dolomite formation remain poorly understood (Sibley et al., 1987; Gregg et al., 2015; Petrash et al. 2017); and the specific chemical factors and kinetics that control saturation state (Ω_{Cal}) associated with non-skeletal $CaCO_3$ precipitation are poorly constrained. Neoproterozoic seawater chemistry is informed in-part by chemical analysis of primary fluid inclusion studies from halite (Browne Formation, 830 Ma, Officer Basin, Western Australia; Spear et al., 2014); characterized by higher Mg/Ca ratios, lower sulphate content, higher dissolved inorganic carbon (DIC) content, higher total alkalinity (TA) and lower calcium/alkalinity ratios.

Further evidence of kinetic control in Neoproterozoic seawater providing additional chemical constraints is the presence of sedimentary Mg-silicates (now preserved as talc) (i.e., in formations of the ~810-800 Ma Svanbergfjellet Formation, Akademikerbreen Group, Norway and

the ~812 Ma lower Callison Lake Dolostone, Fifteenmile Group, Canada (Macdonald et al., 2009; Tosca et al., 2011; Strauss et al., 2015; Strauss and Tosca, 2020). Based on geochemical experiments, modelling and microanalytical techniques, Mg-silicates provide chemical constraints on Neoproterozoic depositional waters that would have required pH >8.5 and minimum alkalinity:Ca ratios of 2:1 (Strauss and Tosca, 2020). Furthermore, talc provides additional evidence of kinetic control in unusual Neoproterozoic seawaters because, similar to dolomite, talc is thermodynamically favoured yet kinetically inhibited in modern day seawater, indicating that a kinetic barrier was overcome in Neoproterozoic seawater that may have permitted non-classical $CaCO_3$ nucleation at high Ω_{Cal}, in turn producing synsedimentary microspar, authigenic Mg-silicates (Strauss and Tosca, 2020).

Although not common, there are additional sedimentary examples of environments that produce concurrent high-Mg $CaCO_3$-dolomite-Mg-silicate genetic relationships through precipitation by chemically-dominated processes. Experimental studies based on these natural systems can provide important chemical constraints. For example, the Cretaceous Pre-salt lacustrine carbonates of the Santos and Compos basins of Brazil preserve significant volumes of authigenic Mg-silicate minerals that formed closely with dolomite, magnesite and high-Mg calcite minerals from seawater that indicates high Mg/Ca ratios, high pH and high Mg/Si (Wright, 2012; Tosca and Wright, 2018; Tutolo and Tosca, 2018). Based on experimental geochemical studies and modelling of Mg-silicate-carbonate crystallization, Tutolo and Tosca (2018) identified that these systems required high pH > circa 10 and importantly were kinetically controlled. This is because traditional precipitation mechanisms would dominantly produce aragonite due to the high Mg/Ca ratios generated through requirements to sustain both $CaCO_3$ and Mg-silicate growth, however, evidence for aragonite its notably rare/absent in these settings despite elevated Mg^{2+} (Wright and Barnett, 2015; 2020) and pH, and therefore inhibitors to aragonite formation in solution are required to sustain these mineralization pathways (Tutolo and Tosca, 2018) as well

as produce the characteristic spherulitic morphologies that require very high states of supersaturation (Gránásy et al., 2005; Sunagawa, 2007; Shtukenberg et al., 2011).

Similar mineralogical relationships have been recorded in speleothems where authigenic Mg-silicate (kerolite clay) is associated with Ca-Mg carbonate speleothems (containing, dolomite, magnesite, hydromagnesite, monohydrocalcite and gypsum) in basaltic sea caves on the island of Kauai in Hawaii (Léveillé et al., 2002) and speleothems consisting of Ca-dolomite, calcite, gypsum and Mg-silicate are identified in Miocene dolostone caves in Cayman Brac (Jones, 2010).

Chemical and physical conditions of aqueous solutions clearly influence mineralogical pathways and understanding Ca-Mg carbonate pathways compatible with Mg-silicate precipitation is beneficial to elucidate the chemical controls on $CaCO_3$ formation in natural systems where biological calcification is absent.

1.4 Alternative CaCO3 precipitation pathways

1.4.1 Amorphous Ca-Mg-$CaCO_3$

One possibility for explaining the presence of enigmatic Ca-Mg-$CaCO_3$ minerals and variations in precipitation styles is through amorphous precursors controlled by kinetic pathways. Amorphous phases are typically produced in high alkaline settings and may represent alternative energetically favourable pathway for the formation and crystallization of carbonate minerals (Schmidt et al., 2005; Radha et al., 2010; Rodriguez-Blanco et al., 2015; De Yoreo et al., 2015; Purgstaller et al., 2016; Blue et al., 2017; Purgstaller et al., 2019). Amorphous calcium carbonate (ACC; $CaCO_3 \cdot H_2O$) is an unstable, hydrated phase of calcium carbonate that has been produced synthetically from saturated solutions since 1916 (Johnston et al., 1916; Addadi et al., 2003).

However, the role of amorphous phases in producing crystalline carbonate minerals inorganically and in natural sedimentary systems was not appreciated until relatively recently and

amorphous precursors are now widely recognised as an intermediate stage for the biomineralization of high-Mg calcites and biological $CaCO_3$ skeletons (i.e. in marine organisms) (Chave, 1954; Schroeder et al., 1969; Stanley et al., 2002; Gayathri et al., 2007; Ma et al., 2007, 2009; Killian et al., 2009; Politi et al., 2010; Long et al., 2012; Seto et al., 2012; Yang et al., 2016). Amorphous phases have been observed during low temperature inorganic synthesis in natural environments (Böttcher et al., 1997; Fairbridge, 1957) including alkaline lake sediments (Benzerara et al., 2006; Couradeau et a.l., 2012) and speleothems (Demény, et al., 2016) and within microbial communities (Demény, et al., 2016; Tünde Enyedi, 2020). Energetic studies provide evidence for several pathways from reactive amorphous hydrated precursors to more stable, dehydrated $CaCO_3$ phases and crystals upon ageing or heating (Radha, 2010). For example, from ACC to calcite (Radha, 2010; Radha and Navrotsky, 2013; Blue, Rimstidt, and Dove, 2013), from amorphous Ca-Mg-carbonate (ACMC) to high-Mg calcite (i.e. Rahda, 2010; Blue and Dove, 2015; Yang et al., 2016; Purgstaller et al., 2016; 2021) and from amorphous Fe carbonate (AFC) to siderite or chukanovite (Jiang and Tosca, 2019). These investigations leave open the possibility that similar conditions may be reached in natural systems where transient amorphous carbonates may be produced authigenically. However, the metastablility of these phases indicates that amorphous phases may only exist for a matter of hours to days before recrystallizing (i.e., Kelleher and Redfern, 2002), therefore, the mechanisms of formation and subsequent recrystallization in natural environments are rarely recorded and to define these pathways requires further experimental study.

Over recent years, experimental methods for ACC and ACMC nucleation have become refined, and can be precipitated consistently under steady state conditions at ambient temperature with controlled Mg content (i.e., Blue and Dove, 2015; Blue et al., 2017). However, the subsequent transformation to crystalline solid phases with predictable compositions remains a major challenge, particularly linked to Mg-rich carbonates. Recent research by Megelsberg et al., (2020) characterize two amorphous phases with distinct short-range structures and morphological differences based on *in situ* Pair Distribution Function analysis (PDF) and Thermogravimetric

analysis (TGA); these distinct phases are controlled by magnesium and carbonate concentration ([Mg^{2+}] and [CO_3^{2-}]) and are produced from both supersaturated and undersaturated conditions with distinct results. High [CO_3] solutions stabilize Ca-rich ACC, in contrast, low [CO_3] favours ACMC with mixed Ca- and Mg-short range order Megelsberg et al., (2020). The distinctive structures are related to solution CO_3 activity (aCO_3) while solubility is primarily determined by the Mg content of the solid. Based on Cryo-TEM, the structural formation of ACMC has been suggested to form via prenucleation clusters of ACC and AMC that coalesce to form ACMC nuclei with a homogeneous distribution of the Mg^{2+} and Ca^{2+} ions (Yang et al., 2016). In-situ TEM studies by Nielsen et al., (2014), indicate that secondary nucleation of carbonate occurs on the crystal surface of amorphous precursors suggesting that the reactive surface area influences nucleation prior to being consumed, as secondary nucleation progressively decreases the saturation state of the system (Nielsen et al., 2014; Steefel and Van Cappellen, 1990). However, there appear to be several different explanations and pathways for ACMC nucleation.

1.4.2 The role of magnesium

There are major challenges in precipitation of Mg-bearing phases due to the hydration of magnesium. In carbonates, Mg^{2+} is not easily inserted into the lattice of calcite because of the larger hydration radius of Mg^{2+} ion than that of Ca^{2+} ion (Maguire and Cowan, 2002), an effect of the higher free energy of solvation (Pavlov et al., 1998) and the higher dehydration enthalpy (Stephenson et al., 2008) of Mg^{2+} ion than those of Ca^{2+} ion at room temperature (Yang et al., 2016). Increased Mg^{2+} content within calcite also decreases the thermodynamic stability under ambient conditions (Busenberg and Plummer, 1989; B**ö**ttcher et al., 1997; Bischoff, 1998), however, in the case for amorphous phases, Mg^{2+} actually play a key role increasing the stability of the amorphous phase forming ACMC from ACC (Reddy et al., 1976; Raz et al., 2000; Addadi et al., 2003; Tao et al., 2009; Rodriguez-Blanco et al., 2014; Blue and Dove, 2015; Yang et al., 2016; Blue et al., 2017; Jensen et al., 2020) and studies by Blue and Dove, (2015) reveal that the

Mg content of ACMC is regulated by the interplay of three factors at steady state conditions: (1) Mg/Ca ratio; (2) solution [CO_3]; and (3) solution pH.

More recently, research has honed in on additional mechanisms that enhance Mg content of ACMC including increased pH (i.e., Blue et al., 2017), temperature (i.e., Purgstaller et al., 2021) and increased residence times during ACMC nucleation (Megelsberg et al., 2020). Experimental work has shown that Mg^{2+} substitution in amorphous carbonate phases can be extensive, which is a function of ambient pH, Mg/Ca ratio in solution, precipitation rate, and stir rates. For example, Blue et al., (2017) synthesized ACMC inorganically with >50 mol% Mg and based on calorimetric studies, Radha et al., (2012) found that ACMC containing 50 mol% Mg is energetically the most stable composition of ACMC and is metastable with respect to disordered dolomite. The mechanism of enhanced incorporation of Mg^{2+} into Mg-calcite from ACMC is likely enhanced by increased crystal growth rates (Mavromatis et al., 2013; Purgstaller et al., 2021), and leads to structural defects caused by nanometric-sized high-Mg calcite crystals that increase the solubility (Purgstaller et al., 2021). Increased Mg^{2+} incorporation is also enhanced by the promotion of nanocrystal formation and aggregation-based crystal growth (Sánchez-Navas et al., 2013). This may be a result of the reduced solvation energy barrier of aqueous Mg^{2+} and high Mg/Ca ratio of the reactive solutions following initial ACMC precipitation, which can be explained by low solubility of ACMC at elevated temperatures (Purgstaller et al., 2021). Yang et al., (2016) synthesized high-Mg calcite (43 mol% Mg) via polymer stabilized ACMC precursors. Recently, Purgstaller et al., (2021) synthesized very high-Mg calcite with ~50 mol% Mg via ACMC. Recent experimental recrystallization experiments of an ACMC precursor have confirmed that recrystallization of ACMC produces disordered dolomite at elevated temperatures (Rodriquez-Blanco et al., 2015). Sedimentary characteristics of primary dolomite also reflect spherulitic growth processes in some natural settings indicating the involvement of amorphous precursors (Hood et al., 2011; Hood and Wallace 2012; Han et al., 2017).

1.4.3 ACMC transformation

The conditions of the initial solution have an important control on the resultant carbonate polymorph (Riechelmann et al., 2014). New pathways for the precipitation of $CaCO_3$ and Mg-rich $CaCO_3$ or $CaMg(CO_3)_2$ from ions in solution via transformation from amorphous precursors through 'non-classical nucleation' mechanisms may challenge the long-established view on crystallization 'classical nucleation theory' (CNT) (Pokrovsky, 1998), used to understand the nucleation of a thermodynamic phase (liquid or solid) and provide a prediction of the nucleation rate.

In this context, the heightened interest in experimental studies of amorphous precursor phases has begun to unravel some fundamental mechanisms of crystal formation dynamics that were previously overlooked and highlights a potentially energetically favourable pathway towards dolomite formation. However, the identification of amorphous phases has also unleashed a plethora of complexities linked to understanding the physicochemical parameters, such as solubility, structure, cation incorporation, hydration (particularly Mg^{2+}) and the role of inhibiting compounds. Furthermore, the transformation remains a poorly understood pathway that is strongly dependent on both the formation solution and the solution in which it recrystallizes, both of which may be influenced by varying degrees of kinetic control.

1.4.4 Inhibiting compounds

For a crystal to form in a solution, it is typically suggested that a pre-nucleation cluster of molecules must exceed a minimum size to grow into new crystal, otherwise it dissolves (Kittel and Kroemer, 1980; Ohara and Reid, 1973) or that solution saturation states reach a threshold where spontaneous/homogeneous precipitation occurs. However, compounds that inhibit precipitation decrease the nucleation rates of new crystals. The supersaturation of seawater with respect to calcite can be maintained by the presence of inhibitors that reduce carbonate precipitation rates, therefore maintaining high Ca^{2+} and $CO3^{2-}$ ion concentrations in seawater or solution (Sumner and Grotzinger, 1996). Saturation states increase until the effects of the

inhibitors are overcome and the removal of Ca^{2+} and CO_3^{2-}, as calcium carbonate, balances the influx of these ions (Sumner and Grotzinger, 1996). Inhibitors of calcite precipitation have been studied for decades and compounds known to inhibit or modify the precipitation of $CaCO_3$ include Fe^{2+}, Mg^{2+}, Mn^{2+}, SO_4^{2-}, PO_4^{3-} and organic acids (Meyer, 1984, Dromgoole and Walter, 1993; Grotzinger and Kasting, 1993; Sumner and Grotzinger, 1996). Out of these compounds, PO_4^{3-} dramatically influences $CaCO_3$ nucleation and growth kinetics at micromolar concentrations (Simkiss, 1964; Leckie and Stumm, 1970; Pytkowicz, 1973; Reddy, 1977; Walter and Hanor, 1979; Berner et al., 1978; Meyer, 1984; House and Donaldson, 1986; Giannimaras and Koutsoukos, 1987; Burton and Walter, 1990; Dove and Hochella, 1992; Millero et al., 2001; Tadier et al., 2017).

1.4.5 Phosphate as a $CaCO_3$ inhibitor

Dissolved orthophosphate compounds (PO_4^{3-} – here on referred to as PO_4) in seawater and sediment pore-waters may have significant effects on carbonate mineralogy, morphology and growth rates. Laboratory studies indicate that dissolved PO_4 kinetically inhibits aragonite (Leckie and Stumm, 1970; Berner et al., 1978; Burton and Walter, 1990; Dove and Hochella, 1992; Tadier et al., 2017) and to a slightly lesser extent, inhibits calcite (Meyer, 1984; Burton and Walter, 1990). The presence of PO_4 in seawater decreases homogenous precipitation rates (Simkiss, 1964; Pytkowicz, 1973) and heterogeneous precipitation rates (Berner et al., 1978; Mucci, 1986; Burton and Walter, 1990) of calcite and aragonite. Concentrations of total dissolved PO_4 ($[PO_{4Total}]$) in the range of 0.25–8 μM decreases crystal growth rates of aragonite with increasing phosphate concentration (Tadier et al., 2017). $[PO_{4Total}]$ ~2 μM decreases seeded calcite crystallization rates by half (Reddy, 1977) 6 – 10 μM are sufficient to strongly inhibit calcite precipitation rates (Reddy, 1977; Walter and Hanor, 1979; House and Donaldson, 1986; Giannimaras and Koutsoukos, 1987; Walter, 1990; Dove and Hochella, 1992), yet are not high enough to precipitate calcium phosphate (Leckie and Stumm, 1970). Furthermore, the presence of $[PO_{4Total}] > 8$ μM completely inhibits the crystal growth of aragonite (Tadier et al., 2017). Field

studies corroborate laboratory results in which the deposition of carbonate crusts are inhibited by 1 μ*M* of dissolved phosphate (Casanova and Lafont, 1985; Pentecost, 2018).

Phosphate speciation is pH-dependent (Figure 1. 2) (de Kanel and Morse, 1978) and the extent of inhibition, rate of adsorption and amount of PO_4 incorporated into calcite precipitates are all species dependent (Ishikawa and Ishikuni, 1981) and influenced by fluctuations in pH, which is independent of the total phosphate concentration and saturation state (Burton and Walter, 1990). Evidence for pH and species dependence has been refined by experiments in which aragonite growth rates decreased with increasing PO_4 whereas calcite growth rates decrease with increasing concentrations of both PO_4^{3-} and HPO_4^{2-} (Burton and Walter, 1990). This further suggests that pH fluctuations in seawater and sediment pore-waters may control PO_4 speciation and therefore influence $CaCO_3$ precipitation pathways and mineralogy. The uptake of PO_4 is higher in Mg-rich minerals, and decreases by approximately an order of magnitude with crystallization to lower-Mg calcites (Burton and Walter, 1990; Xu et al., 2014). The mechanism by which PO_4 decreases the crystal growth rates of aragonite and calcite are reduced or inhibited by blocking the active growth sites by the adsorption of PO_4 ions (Tadier et al., 2017). The relationship between the crystallization rate constant and the PO_4 ion concentration follows an expression based on the Langmuir-type adsorption model. This relationship suggests that calcite growth inhibition by PO_4 containing anions involves blockage of crystal growth sites on the calcite surface (Reddy, 1977).

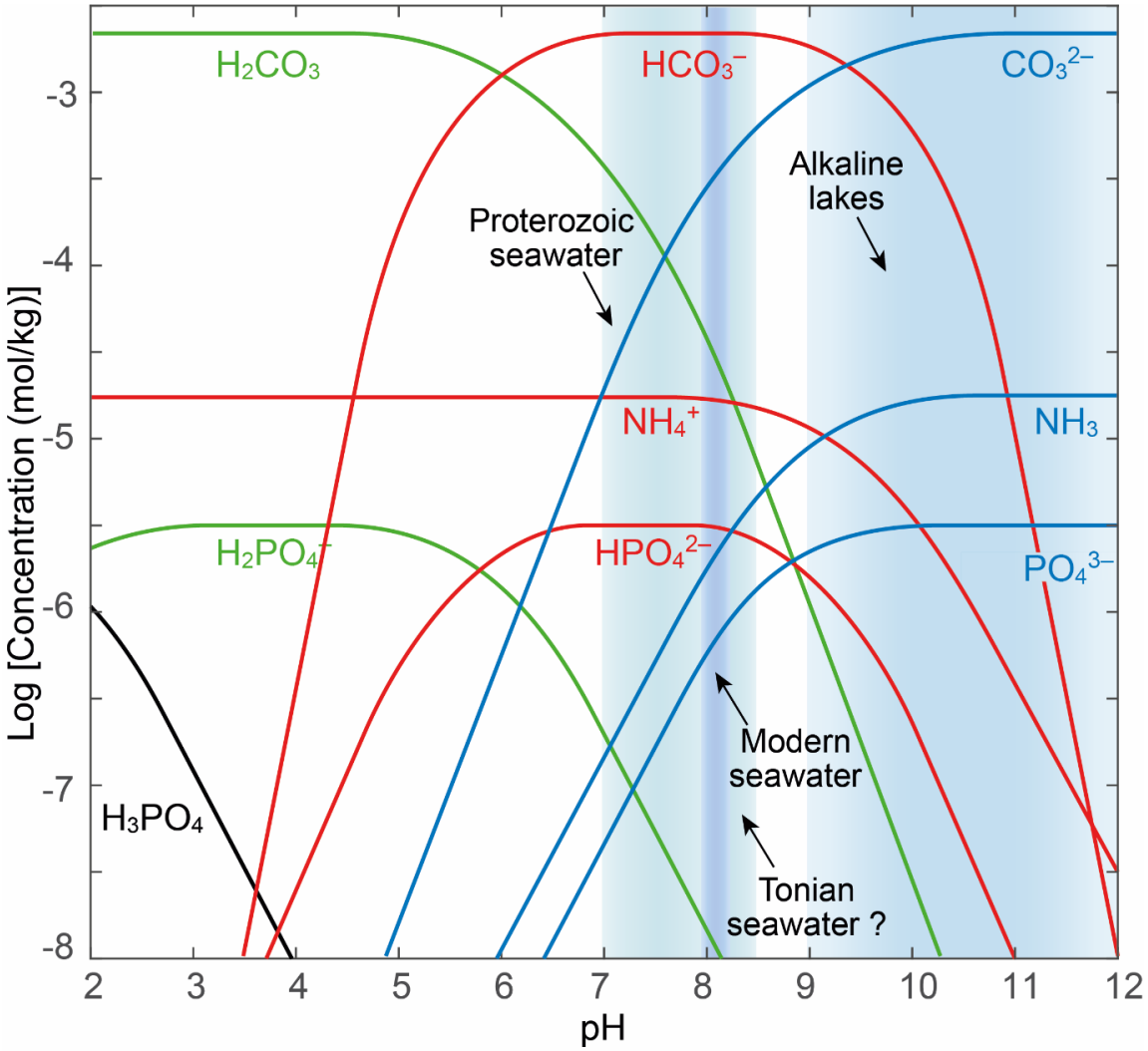

Figure 1. 2 Bjerrum plot of speciation and relative [CO_3],[PO_4] and [NH_4] as a function of pH. Polyprotic acids are capable of losing protons (H^+) in acid-base reactions. When a solution is in equilibrium, it is possible to identify the speciation and relative proportions of these species - aqueous carbonate: [H_2CO_3], [HCO_3^-] and [CO_3^{2-}] from DIC; phosphate: [$H_2PO_4^-$], [HPO_4^{2-}] and [PO_4^{3-}]; ammonium: [NH_4^+] [NH_3], as a function of pH (based on from Zeebe and Wolf-Gladrow, 2001). The green shaded regions with appropriate labels reflect the approximate range of modern surface seawater (Krissansen-Totton et al., 2018) and Proterozoic Tonian seawater (Strauss and Tosca, 2020), modern alkaline lakes and Proterozoic seawater. The colours are to aid visual identification – the red colours indicate the most common species and the blue colours indicate speciation in high-pH alkaline settings.

1.5 Precambrian phosphorous cycle

Observational data and theoretical models indicate that PO_4 was extensively cycled in Precambrian depositional environments (Notholt, and Jarvis, 1984; Cook and Shergold, 1986; Bjerrum et al., 2002; Planavsky, et al., 2010; Horton, 2015; Cohen et al., 2017; Lenton and Daines,

2018; Reinhard et al., 2017; Cantine et al., 2020), and must have been available in concentrations high enough that multiple species used PO_4 (apatite) over $CaCO_3$ to build skeletons (Cohen et al., 2011; 2017; Cantine et al., 2020; Riedman et al., 2018). Despite these observations, and despite the recognition of PO_4 as a known $CaCO_3$ inhibitor, the influence of PO_4 on $CaCO_3$ mineralization in geological systems is not well understood.

Because phosphorous (P) is an essential component in the biomolecular construction and activity of organisms (i.e., Gulick et al, 1955), the availability of P in the bioavailable form of dissolved PO_4 is generally considered the ultimate limiting nutrient in marine primary productivity over geological timescales (>10^5 years; Tyrell, 1999) (Van Cappellen and Ingall, 1996; Laakso and Schrag, 2014; Lenton et al., 2014; Cox et al., 2017; Laakso and Schrag, 2018a, 2018b). In this regard, major changes in ocean-atmosphere chemistry through geological history are related to the evolution of the biosphere (i.e., Holland, 1984; Holland et al., 1986) in which P plays a crucial biogeochemical role (Van Cappellen, 1991) and is associated with key biological milestones such as the evolution of Eukarya (i.e., Brocks, 1999; Canfield et al., 2007; Porter, 2011; Brocks, 2017). Furthermore, the increased availability of dissolved PO_4 likely played an important role in the origin of life on Earth (Gulick et al, 1955; Butusov and Jernelöv, 2013; Fernández-García et al., 2017; Eckford-Soper and Canfield, 2020; Toner and Catling, 2020). This indicates that global biogeochemical perturbations may have been highly sensitive to fluctuations in marine P concentrations (Ingall et al. 1993; Ingall and Jahnke 1994; Van Cappellen and Ingall 1994; Van Cappellen and Ingall 1996; Tyrell, 1999)

Therefore, understanding controls on the availability of PO_4 may be crucial to understanding the evolution of the biosphere through the geological history of Earth (i.e., Fernández-García et al., 2017; Toner and Catling, 2020) both directly by controlling marine productivity, and indirectly by regulating organic carbon burial (i.e., Lenton and Daines, 2018), the C-cycle, partial pressure of oxygen (pO_2) and through feedback mechanisms linked to oxygen,

sulphur, iron, organic matter and P cycling (Van Cappellen and Ingall, 1996; Marz et al., 2008; Mort et al., 2010; Laakso and Schrag, 2014; 2017; 2017; Sperling 2015).

1.5.1 Redox-driven phosphorous processes

Numerous studies and models address P-cycling and P burial in in marine sediments, which influences the longer term availability and concentration of P in the ocean (Notholt, and Jarvis, 1984; Cook et al., 1990; Filippelli and Delaney; 1994; Ruttenberg and Berner, 1993; Glenn et al., 1994; Compton et al., 2000; Bergmann et al., 2004). Much recent research has focused on the Proterozoic because P was essential for the development of metabolic pathways that promoted oxygenic photosynthesis, releasing photosynthetic oxygen as a byproduct and increasing oceanic and atmospheric oxygen (pO_2). This relationship between P and pO_2 is particularly important in the Neoproterozoic with many models of rising O_2 levels or the maintenance of low pO_2 centred around P availability and ocean-redox (Bjerrum and Canfield, 2002, Konhauser et al., 2007; Planavsky et al. 2010; Laakso and Schrag, 2014; Reinhard et al., 2017; Poulton et al., 2017).

For example, it is typically suggested that P scavenging was enhanced under PO_4 limited anoxic-ferruginous ocean conditions because the deposition of organic matter removes bioavailable P from the water column and subsequent anaerobic decomposition results in the reduction of iron (Fe) minerals (ferric oxyhydroxide) in anoxic-ferruginous settings (Froelich, et al., 1979; Ingall, and Jahnke, 1997; Krom, et al., 1991; Slomp, et al., 2004; Poulton and Canfield, 2011; Planavsky et al., 2010; 2011; Derry, 2015; Reinhard et al., 2017). Phosphorous cycling is suggested to be significantly enhanced by redox-cycling in the ocean (Benitez-Nelson, 2015), and microbially driven P-cycling is redox-dependent and exacerbated by anoxic and euxinic bottom waters (Van Cappellen and Ingall, 1996; Poulton, 2017). This is because of the reduction of P-bearing Fe oxyhydroxides by H_2S (Canfield et al., 1992; Dos Santos et al., 1992) and SO_4 reduction (Ingall et al., 1993; Ingall and Jahnke 1994; Van Cappellen and Ingall 1994; Slomp, et al., 2004). Low import fluxes of riverine P (Laakso and Schrag, 2014) can also result in P limited conditions and Fe minerals such as ferrihydrite and green rust (Zegeye et al., 2012; Cosmidis et

al., 2014) and Fe-phosphate minerals such as vivianite (Derry, 2015) provide a 'shuttle' for marine P from the water column to the sediment. Many of these explanations indicate a consequential global decrease in primary production and organic carbon burial subsequently resulting in minimal oxygen production or stable, low-oxygen environments (Poulton and Canfield, 2011; Planavsky et al., 2010; 2011; Reinhard et al., 2016; 2017). Based on these processes, it has also been suggested that P availability was limited in early Neoproterozoic and more broadly in Precambrian oceans (Guilbaud, et al., 2020). Despite numerous different models of P-cycling and pO_2 that have led to a variety of conclusions, there is no consensus on Proterozoic P-cycling or Proterozoic oxygenation of the atmosphere and oceans. Either way, the P-cycle, along with climatic, tectonic and other geochemical cycles appears to have experienced perturbations during the Tonian (800 – 720 Ma) (Lenton et al., 2014; Horton, 2015; Reinhard, et al., 2016; Spence et al., 2016; Lenton and Daines, 2018).

1.5.2 Constraints on aqueous phosphate in the Proterozoic

Despite many efforts to constrain and explain geochemical records of marine P, there are still major gaps in our understanding of PO_4 availability through key intervals such as the Proterozoic. To elucidate questions linked to P availability through geological history, research has looked to geological sediments as chemical archives to help constrain marine P concentration. Our current understanding of P cycling in the late Proterozoic has been dominantly based on bulk black shale-hosted P content (Reinhard et al., 2017) and P/Fe ratios in late Neoproterozoic iron formations of 750 to 635 Ma (Planavsky et al., 2010), which initially indicate that a major change in P burial took place from enriched P concentration in sediments and marine concentrations in the mid to late-Neoproterozoic Tonian-Cryogenian reflecting redox-driven changes in P-cycling and burial from previously P-limited conditions (Bjerrum, and Canfield, 2002 Planavsky et al., 2010; 2011; Reinhard et al., 2016; 2017).

However, new geochemical compilations of bulk shale-hosted P records and geochemical models indicate that shale-hosted geochemical records record no statistically significant perturbations to P fluxes through much of the Precambrian and specifically the Neoproterozoic (Laakso et al., 2020, supplementary material) despite the global phosphogenesis in the Ediacaran (570–510 Ma). However, their research does indicate that pore/bottom water [PO_4] may have been strongly influenced by the degree of internal P recycling suggesting both spatial and temporal variation in Proterozoic P-cycling (i.e., Laakso et al., 2020). At the same time, microfossil data also suggest enhanced availability of marine P during the Tonian based on the presence of Tonian Ca-phosphate biomineralizing organisms known as apatitic scale microfossils (ASM) across numerous basins which were present prior to the evolution of $CaCO_3$ mineralizing organisms (Cohen and Knoll 2012; Cohen et al 2017; Moczydłowska et al., 2018; Cantine et al., 2020; Riedman et al., 2020).

Studies indicate that that shallow marine phosphorous burial was low until the late Tonian when it became abundant – possibly originating from Neoproterozoic rift-basins and P-enriched LIP-emplacement (Horton, 2015). Laakso et al. (2020) showed that large scale changes to the deep-water aqueous phosphate reservoir rather than increased influx may have been driven by Ediacaran increases in marine sulphate concentrations, which in turn facilitated increased organic matter remineralization by sulphate-reducing bacteria. Furthermore, marine [PO_4] could have varied significantly at any one time and appreciable differences in P accumulation rate records relative to continental weathering rates indicates that P influx can become decoupled from other dissolved components, (Filippelli and Delaney, 1992), and P concentration and burial can be decoupled from P input and output (Lenton, 2020).

Either way, whether changes to the P-cycle were related to increased P-flux or changes in the deep water P reservoir, taken together, these observations hint at fundamental shifts in the internal cycling of P that may not be obviously reflected in the bulk P content of siliciclastic rock proxies for changes to P input and output fluxes and would benefit from further research. In this

regard, the nature of P cycling in carbonate depositional environments and the degree to which carbonate sediments archive marine P availability could represent a key archive of P availability that complements siliciclastic records. By understanding the relationship between PO_4, and $CaCO_3$ mineralization pathways, we may be able to shed light on the availability of Precambrian PO_4 and perhaps take a step forward in understanding how major changes in ocean-atmosphere chemistry through geological history were related to the evolution of the biosphere (i.e., Holland, 1984; Holland et al., 1986) in which P plays a crucial role biogeochemically and related to ocean-atmosphere oxygenation (Gulick et al, 1955, Van Cappellen, 1991, Butusov and Jernelöv, 2013; Fernández-García et al., 2017; Eckford-Soper and Canfield, 2020; Toner and Catling, 2020).

1.6 Summary of chapters

1.6.1 Chapter 2: A non-classical pathway to Mg-rich $CaCO_3$

This chapter outlines the experimental method used to synthesize ACMC and lays out a relatively novel experimental method of precipitating enigmatic high-Mg Ca-carbonate and magnesite minerals from ACMC precursors. Two different methods are used to nucleate and subsequently recrystallize ACMC in synthetic highly alkaline, saline lake water solutions at 50 ˚ in the presence of phosphate as a kinetic inhibitor. The data include solid sample analyses using XRD, FTIR, SEM-HDBSD and solution analyses using ICP-AES. The recrystallization experiments produce hydromagnesite, magnesite, very-high-Mg calcite and dolomite minerals through ACMC precursors. Our results indicate that highly alkaline settings containing phosphate enable energetic barriers—likely related to hydrated magnesium ions—to be overcome. Increasing Mg/Ca in these settings results in a direct increase in Mg/Ca of the resultant mineral phases, and increasing phosphate results in enhanced rates of Mg dehydration and magnesite crystallization. Geochemical calculations from the resultant data provide new solubility product estimates values for high–Mg ACMC. The discussion emphasizes on the importance of non-classical mineral formation pathways. The geological implications from the study relate to highly alkaline lake

settings that can accumulate significant phosphate concentrations and sedimentary environments on Mars that preserve Mg-rich carbonates in phosphate influenced depositional settings.

1.6.2 Chapter 3: Non-skeletal $CaCO_3$ precipitation Proterozoic seawater

Having established a better understanding of the constraints of alternative Ca-Mg-carbonate mineral formation pathways through amorphous precursors in Chapter 2, we set out to test the hypothesis that carbonate mineral formation pathways through ACMC precursors may have been involved in producing the high-Mg Ca-carbonate minerals that are widespread in the mid-Proterozoic to the Neoproterozoic, prior to carbonate biomineralization. We investigated $CaCO_3$ precipitation from synthetic Proterozoic seawater using a constant composition experimental design that results in homogeneous ACMC nucleation subsequent crystallization to Mg-calcite and monohydrocalcite.

Primary and early diagenetic fabrics preserved in late Proterozoic marine carbonates have long been interpreted as a reflection of elevated $CaCO_3$ supersaturation (Ω_{Cal}). The maintenance of $CaCO_3$ supersaturation spanning geological timescales requires the inhibition or modification of $CaCO_3$ precipitation rates and pathways. Proterozoic geochemical data, models, and microfossil mineralogy indicate that concentrations of dissolved PO_4, a known inhibitor of $CaCO_3$ precipitation were subject to substantial fluctuations affecting availability, in response to secular changes in the global phosphorous cycle; however, the impact of PO_4 on marine abiotic $CaCO_3$ precipitation is poorly constrained. In an effort to constrain $CaCO_3$ formation pathways influenced by PO_4, this chapter outlines the methodology of a suite of $CaCO_3$ nucleation experiments in synthetic late Proterozoic seawater.

The data produced include solid analyses of samples using FT-IR, in-situ Raman, XRD and SEM-EDS as well as dissolved solid sample and solution ICP-MS analyses. The results indicate that dissolved PO_4 inhibits the nucleation of crystalline aragonite and calcite and permits

the formation of an amorphous Ca-Mg carbonate (ACMC) precursor phase, which rapidly undergoes recrystallization to monohydrocalcite and/or calcite incorporating a range of Mg concentrations. This pathway may be significant in providing an explanation for the sedimentological, petrographic, and geochemical characteristics of the abundant but enigmatic synsedimentary calcite microspar cement that is widely distributed in Precambrian carbonates. Furthermore, this pathway may provide a mechanistic framework for how kinetic inhibitors may have fundamentally altered the dynamics of shallow water $CaCO_3$ precipitation and marine carbonate chemistry throughout the Proterozoic Eon, which in turn may have potentially influenced the long-term carbon cycle.

1.6.3 Chapter 4: Carbonate-hosted PO_4 and the mid-Neoproterozoic P cycle

This chapter outlines our investigation into geological carbonate sediments that aims to investigate whether phosphate is recorded within Neoproterozoic carbonate sediments. This permits a direct test of the hypothesis outlined in Chapter 2 and Chapter 3 where we hypothesize that elevated PO_4 concentrations in Tonian seawater led to kinetically controlled $CaCO_3$ mineral formation pathways linked to PO_4 inhibition. In the absence of skeletal carbonates during this time, kinetic pathways may have controlled the production of high Mg Ca-carbonate minerals that are widespread in mid-Proterozoic to Neoproterozoic carbonates. Chapter 2 and Chapter 3 indicate that this is the case experimentally, therefore, we would expect to see PO_4 recorded in Tonian carbonate sediments if our hypothesis rings true for the carbonate factory during the Neoproterozoic.

The geological carbonate facies investigated are predominantly Proterozoic Tonian aged dolomicrite carbonates containing calcite microspar and phosphorous microfossils from Svalbard, Norway, the Northern Territories, Canada and the Yukon, Canada. A range of microanalytical techniques were used to examine the PO_4 bulk concentration, speciation, and distribution of PO_4

from three different Tonian sedimentary basins. This chapter presents bulk phosphate concentrations of the sediments, SEM-EDS images and chemical data, synchrotron XANES and μXRF to characterize the phosphorous in the carbonates and NMR and identify the identify the P species and spatial-distribution within sediments. The analyses provide evidence for carbonate hosted phosphate enrichment in mid-Tonian carbonates that appear to indicate lattice-bound CO_3-associated PO_4 within carbonate minerals. This may help explain the mechanisms by which phosphate can be recorded within carbonate minerals. This multi-analytical approach has provided a useful tool to inform us of the nature of the Proterozoic phosphorous cycle. Our data suggest that phosphorous was likely not a limiting nutrient during this important geological time.

1.6.4 Chapter 5: Discussion and conclusions

This chapter draws together the experimental research and summarizes how our understanding of Ca-Mg-carbonate mineral formation has developed through investigating kinetic pathways of formation with phosphate as an inhibitor. We tested our hypotheses by conducting experiments in synthetic Proterozoic seawater and highly alkaline lake water and then we tested our hypotheses on geological Proterozoic carbonates. Through investigating multiple avenues, this research strongly emphasizes the importance of kinetic inhibitors in carbonate mineralization. Through identification of alternative mineral formation mechanisms and pathways, we have shed light on new Mg-carbonate and high-Mg $CaCO_3$ pathways that can overcome energetic barriers related to magnesium and inform us of carbonate sedimentological depositional environments and geochemical processes.

Through the application of these mineral formation pathways linked to phosphorous inhibition, we have honed in on a new approach that enables the characterization of phosphorous in authigenic carbonate sediments as apatite and carbonate fluorapatite cements, intraclasts and nanocrystals and in the form of lattice-bound CO_3-assocaited PO_4. This provides a deeper understanding of available P concentrations in marine environments in the Precambrian. Our

research points toward enhanced phosphorous cycling during the Proterozoic. The integration of the results from the different methods used in this research elucidates major controls on the inorganic carbonate factory and the phosphorous cycle that have largely been unaccounted for.

Chapter 2: Non-classical pathways to Mg-rich carbonates

2.1 Abstract

Despite extensive research, the widespread occurrence of primary dolomite and magnesite in the geological record, yet the inability to produce these minerals experimentally has left significant gaps in our understanding of mineral formation pathways. The lack of conformity to the expected thermodynamic pathway means the problem may lie in kinetics. To address this problem from a kinetic standpoint, we investigate the impact of inhibition and supersaturation on the styles of Ca-Mg-CO_3 precipitation.

We use two different experimental methods to examine the precipitation of magnesium carbonate minerals from hyper-alkaline, hyper-saline conditions at low diagenetic temperatures (50 ºC) with millimolar concentrations of PO_4. Firstly, from amorphous calcium magnesium carbonate (ACMC) precursors (50 mol% Mg) that were added to alkaline-saline solutions and secondly, from homogenous nucleation experiments in alkaline-saline solutions. We reveal that the ACMC precursor experiments typically resulted in mixtures of very high Mg-calcite (48 mol% Mg), aragonite and dolomite. The homogeneous nucleation experiments promoted the nucleation of Mg-rich (>60 mol% Mg) ACMC spherules, from solutions linked to kinetic inhibition by PO_4 and supersaturation caused by enhanced carbonate alkalinity. Crystallization within the evolved solutions led to widespread transformation into hydromagnesite and subsequent recrystallization into magnesite and ordered dolomite mineral aggregates with apatite and aragonite. The dominant Mg-Ca carbonates crystalline phase contained up to 54 mol% Mg. The maintenance of supersaturation and inhibition by PO_4 facilitated spherical morphologies composed of crystal aggregates and subsequent growth of the magnesite, dolomite and apatite

crystals. Large crystals with high degrees of twinning protrude from aggregates and appear to produce mineralogical defects related to PO_4 attachment on growth sites. Higher PO_4 concentrations (14 m*M*/kg) were conducive to more extensive and faster rates of transformation into magnesite and dolomite.

These data show that the formation of magnesite and primary dolomite require non-classical nucleation pathways. The pathway can be explained by the nucleation of an amorphous precursor when exposed kinetic inhibitor PO_4 and elevated CO_3 alkalinity under early diagenetic early temperatures. This investigation is of fundamental importance for understanding natural processes that form magnesite and primary dolomite that can be met in highly alkaline-saline lacustrine settings influenced by [PO_4] of 7 m*M*/kg; even in settings with low Mg/Ca of 1 ([Mg^{2+}]/[Ca^{2+}]; 24/28 m*M*/kg).

This study identifies two new formation pathways and mechanisms for magnesite and Mg-Ca-carbonate sediments formation and provides new solubility estimates for amorphous phases > 50 % Mg. This informs us of geochemical carbonate alkalinity and PO_4 cycling processes in natural systems that existed in Earth's geological past and may have existed on Mars, where spectroscopic evidence indicates the presence of magnesite and sedimentary PO_4 concentrations higher than those typical on Earth. Furthermore, the data provide new solubility product data that provide insight into reaction pathways and may inform geochemical models.

2.2 Introduction

For decades, the formation of magnesite ($MgCO_3$) and dolomite ($CaMg[CO_3]_2$) has puzzled geologists. Difficulties in synthesizing primary magnesite and dolomite in low temperature abiogenic settings, coupled with shortfalls in predicting and explaining the spatio-temporal distributions geologically leaves significant gaps in our understanding. In the case for dolomite this enigma is termed 'the dolomite problem' (i.e., Given and Wilkinson, 1987; Land, 1998; Arvidson and Mackenzie, 1999, Gregg et al., 2015).

Distinctive Mg-Ca-carbonate sedimentary successions are abundant in Precambrian and Palaeozoic successions yet their occurrence and distribution is comparatively minor in Phanerozoic successions and modern sediments, which alludes to differences in chemical composition of depositional waters (Tucker, 1982; Grotzinger and James, 2000; Burns et al., 2000; Hood et al., 2011; Hood and Wallace, 2012, 2014, 2015; Wood et al., 2017). Primary dolomite is an authigenic mineral thought to have formed by the process of homogeneous nucleation and in situ stabilization from fluid (Tucker, 1982; Petrash et al. 2017) and is typically characterized by finely crystalline dolomicrite (carbonate mud) (Tucker, 1982; Grotzinger, 1989; Grotzinger and Knoll, 1995). Although volumetrically less abundant than dolomite in Precambrian strata, large-scale magnesite deposits also occur with relatively minor occurrences in the Phanerozoic (White and Young, 1980; Frank and Fielding, 2003) and the modern. $MgCO_3$ deposits are enigmatic because even though sedimentological observations and assumptions from modern sediments might indicate an evaporative depositional setting, magnesite is not associated with $CaSO_4$ minerals in the Precambrian deposits as would be expected from the interaction of excess Ca^{2+} Mg^{2+} and SO_4^{2-} ions relative to HCO_3^- and CO_3^{2-} ions due to evaporative concentration (Frank and Fielding, 2003).

2.2.1 Magnesium carbonates in alkaline lakes

Deposits of Recent primary dolomite are not common but when identified often occur as primary micritic precipitates with hydromagnesite ($Mg5(CO_3)_4(OH)_2{\cdot}_4H_2O$) and occasionally magnesite minerals (Miser et al., 1987). These dolomite-hydromagnesite-magnesite deposits are typically present in marginal continental water-bodies characterized by evaporation, high alkaline pH, high salinity and in some cases temperatures reaching 50 °C such as in sabkha flats, hypersaline lagoons and playa lakes (von der Borch and Lock, 1979; Ohde, 1981; Miser et al, 1987; Tucker and Wright, 1990; Arvidson and McKenzie, 1999; Warren, 1990; Vasconcelos, et al., 2005; McKirdy et al., 2010; Nash et al., 2011; García Del Cura et al., 2014; Petrash et al. 2017; Warren, 2019). For example, these deposits have been identified in the Coorong Lagoon and lakes of South

Australia (Alderman 1959; Walter et al.,1973; Rosen et al., 1989; Warren, 2019) and the coastal lagoon of Lagoa Vermelha, Brazil (Vasconcelos & Mckenzie, 1997; Warthmann et al., 2000). Modern-day primary dolomite is also present in zones of bacterial sulphate reduction or accompanying organic matter degradation processes that may be associated with elevated pore water alkalinity (Baker and Burns, 1985; Middelburg, de Lange, and Kreulen, 1990; Vasconcelos and McKenzie, 1997; Wright and Wacey, 2005). These settings may contain factors that could influence the mechanisms, mineralogy and morphology of carbonate sediment formation during syn-deposition and early diagenesis such as high-alkalinity from elevated concentrations of carbonate ions [CO_3^{2-}], [Mg^{2+}] and [Ca^{2+}] associated with increasing alkalinity and pH, and/or microbial communities (i.e., Vasconcelos, et al., 2005; García Del Cura et al., 2014). However, despite numerous efforts to constrain the formation pathways (outlined in Gregg et al., 2015), the exact chemical control on the mechanisms of dolomite, hydromagnesite and high Mg-carbonate mineral formation remains complex.

Modern magnesite deposits are typically present in continental evaporitic and highly alkaline depositional settings (Müller et al., 1972; Miser et al, 1987; Warren, 1990; Pérez et al., 2002; Power et al., 2009; McKirdy et al., 2010), cave speleothem deposits (i.e., Léveillé et al., 2002) and are commonly associated with biogenic activity within microbial mats (Walter et al.,1973; Last and De Deckker, 1990; Renaut, 1993; Sanz-Montero, 2019) and corals (i.e., Nash et al., 2013). Magnesite deposits are also commonly associated with weathering products of mafic and ultra-mafic minerals, which typically contain high magnesium oxide concentrations (up to 50%$_{wt}$) and are chemically alkaline (i.e., Power et al., 2009). However, magnesite is also associated with siliciclastic minerals (Power et al., 2009; Sanz-Montero and Rodríguez-Aranda, 2012) and sulphate minerals (Thompson and Ferris, 1990; Zhang et al., 2000; Sanz-Montero et al., 2019). In addition, suggestions that carbonate sediments formed on Mars in environments influenced by interaction with liquid water have dated back to the 1980's (i.e., Pollack et al., 1987). Now there is a growing body of evidence that carbonates that outcrop on Mars and are composed dominantly of Mg-carbonate minerals magnesite (and possibly huntite; $CaMg_3[CO_3]_4$)

based on near-, mid- and far-infrared spectroscopy (Russel et al., 1999; Bandfield et al., 2003; Ehlmann et al., 2008; Palomba et al., 2009; Michalski and Niles, 2010; Bultel et al., 2019) and remote sensing data (Bultel et al., 2019; Horgan et al., 2020). Estimations for the quantity of carbonate mineral present on Mars varies, with ranges from 0–3 $\%_{wt}$ carbonate in outcrop rocks (Pollack et al., 1990) to 16–36 $\%_{wt}$ carbonate measured from outcrop rocks (Morris et al., 2010), which are commonly associated with mafic to ultra-mafic mineral assemblages on Mars (Ehlmann et al., 2008).

Magnesite phases are more common in ancient settings as they are a more stable form relative to hydrated counterparts. However, modern settings contain higher abundances of hydrated Mg-carbonate phases (hydromagnesite and nesquehonite [$MgCO_3 \cdot 3H_2O$]), which are often found associated with microbial mats in contemporary saline and alkaline systems (Renaut, 1993; Power et al., 2009; Sanz-Montero et al., 2019). The precipitation of Mg-rich carbonate has been suggested to require pH >8.5 in alkaline aqueous environments with elevated [Mg] and the presence of carboxyl groups (Thompson and Ferris, 1990; Sánchez-Román et al., 2009; García Del Cura et al., 2014; Power et al., 2017; Sanz-Montero et al., 2019).

2.2.2. Kinetic inhibition

One of the main problems is that Mg-rich carbonates and dolomite are often notably absent in settings that are supersaturated with respect to these minerals, settings in which the formation is thermodynamically favourable and should be widespread. In natural settings, such as in modern day seawater, $MgCO_3$ and dolomite are absent and instead aragonite and/or calcite predominate (Baker and Kastner, 1981; Hardie, 1987; Wilkinson and Algeo, 1987; Brady et al., 1996). Thermodynamically, $MgCO_3$ is unstable relative to $CaCO_3$ minerals, yet is more reactive or thermodynamically less stable; indicating that its formation should be common as it is energetically more favourable. However, $MgCO_3$ is not common and recrystallization to $MgCO_3$ may be restricted to geological timescales. The inhibition of magnesite formation synthetically

(i.e., Sayles and Fyfe, 1973) and under Earth's surface conditions represents a distinct but related challenge related to the hydration of Mg ions (Saldi et al., 2009; Kowacz et al. 2007). Alternatively dolomite ($MgCa[CO_3]_2$) is the most thermodynamically stable and least reactive mineral but again it is a challenge to explain. Understanding the enigmatic formation and preservation of these minerals presents two unique but somewhat related challenges.

Because the abiogenic precipitation of magnesite and dolomite at low temperatures is kinetically inhibited, due to the strong hydration of Mg^{2+} ions, it is generally agreed that the precipitation requires a kinetic mediator to overcome kinetic energy barriers (Lippmann, 1973; Vasconcelos et al., 1995; Vasconcelos and McKenzie, 1997; Land, 1998; Sánchez-Román et al., 2009). Research indicates that Mg^{2+} ions stabilize amorphous Ca-carbonate (ACC) phases (Rodriguez-Blanco et al., 2012; Blue and Dove, 2015), therefore, one possibility is that Mg-rich carbonates such as dolomite might recrystallize from amorphous Ca-Mg-carbonate precursors (ACMC) or a series of metastable precursors (Schmidt et al., 2005; Radar et al., 2010; Rodriguez-Blanco et al., 2015; Purgstaller et al., 2016; Kaczmarek and Thornton, 2017; Purgstaller et al., 2020) that provides a more energetically favourable route for the formation of dolomite or magnesite under certain chemical conditions. However, the chemical conditions necessary for hydrous phases such as amorphous Ca-Mg-carbonate (ACMC) to transform into dolomite during formation and growth are poorly understood due to the thermodynamics and kinetics of water content and hydration associated with Mg (Kelleher and Redfern, 2002). Furthermore, how these mineral phases exist in natural environments with respect to the metastablility indicates that amorphous phases may only exist for a matter of days before recrystallizing (i.e., Kelleher and Redfern, 2002). The transformation of ACC and ACMC phases to more stable minerals has been recorded in present day environments such as in biological calcifiers (i.e., Politi et al., 2010), alkaline lake sediments, microbial communities and speleothems (i.e., Demény, et al., 2016).

Although a number of compounds are known to inhibit or modify the precipitation of $CaCO_3$ (including Fe^{2+}, Mg^{2+}, Mn^{2+}, SO_4^{2-}, PO_4^{3-}, organic acids; [Berner, 1975; Meyer, 1984;

Burton and Walter, 1990; Sumner and Grotzinger, 1996] and sulphate-reducing bacteria [i.e., Sánchez-Román et al., 2009), research indicates that PO_4 has a strong influence on the inhibition of nucleation and growth kinetics of aragonite and calcite (i.e., Leckie and Stumm, 1970; Reddy, 1977; Ishikawa and Ishikuni, 1981; Burton and Walter, 1990; Dove and Hochella, 1992). This control is evident at only micromole/kg (μM) concentrations (i.e., Reddy, 1977; Dove and Hochella, 1992; Tadier et al., 2017) and controlled by pH induced PO_4 speciation (Kanel and Morse, 1978; Ishikawa and Ishikuni, 1981).

2.2.3 PO_4 enrichment in alkaline lakes

Settings in which $CaCO_3$ or even Ca-Mg-CO_3 nucleation or precipitation rates are high as a result of high supersaturation states may accumulate higher concentrations of PO_4. Incidentally, the settings that record excessive PO_4 concentrations in modern alkaline lakes often record occurrences of low-temperature, primary dolomite and magnesite within muddy sediments (i.e., Searles Lake Evaporite (Smith and Haines, 1964; Coorong Lakes; Alderman 1959; Stone et al., 2016; Warren, 2019). This is supported by recent research that points to a link between high PO_4 concentrations in settings where primary dolomite is abundant such as in Proterozoic Tonian settings (i.e., Strauss and Tosca, 2020; Roest-Ellis et al., 2020) and Cretaceous Pre-salt carbonate settings that record multiple generations of early diagenetic dolomite with magnesite (Wright and Barnett, 2015; Ceraldi and Green, 2017; Tutolo and Tosca, 2018) alongside high PO_4 concentrations (Pietsch et al., in press). In addition, it is suggested that sediments on Mars contain excessive [PO_4] linked to water-rock interaction, which models indicate could be around 45 times higher than those on Earth (i.e., Adcock et al., 2013), which may coincide with evidence for Mg-Ca-CO_3 deposits on Mars (i.e. Morris et al., 2010). Together, these settings may indicate a link between PO_4 and the styles and mineralogy of CaMg-CO_3, $MgCO_3$ and $CaCO_3$ precipitation.

Geochemical PO_4-enrichment may be explained by recent indications that modern alkaline lakes can accumulate PO_4 to > 1 millimol/kg (mM) concentrations (Toner and Catling, 2020). This can be explained in high-alkalinity conditions where by a relationship with Ca^{2+} ion

removal in the water column through $CaCO_3$ precipitation restricts the precipitation of apatite, because apatite precipitation requires both high PO_4 concentrations and Ca^{2+} ions. The prevention of apatite precipitation subsequently leads to excess PO_4 accumulation in lake waters before hitting apatite saturation thresholds (Gulbrandsen, 1969; Sass, 1981; Toner and Catling, 2020).

Geochemical PO_4 enrichment may also come from the high pH that characterizes modern alkaline lakes, due to the pH-dependent speciation of PO_4 (see Bjerrum plot in Chapter 1, Figure 1.2) (de Kanel and Morse, 1978; Ishikawa and Ishikuni, 1981). This pH dependence is independent of the [PO_{4tot}] and saturation state (Burton and Walter, 1990), which suggests that pH fluctuations in water may influence the [PO_{4tot}] bioavailability. The availability of P as a nutrient is typically regarded as a limiting factor in primary production. However, at high pH, the PO_4 species are shifted to orthophosphate ions (PO_4^{3-}) – the most bioavailable form of P in solution (i.e., Reynolds and Davies, 2001). This raises the problem that if alkaline-saline lakes are enriching bioavailable nutrient [PO_{4tot}], then why are microorganisms not utilizing it? The answer may lie in high-pH induced speciation that controls the deprotonation of aqueous ammonium (NH_4^+), shifting NH_4^+ to NH_3 (ammonia gas) in equilibrium causing nitrogen nutrient loss from the lake waters. Nitrogen limitation in P nutrient-rich environments is typically recorded in soda lakes with high alkaline-saline geochemistry where nutrient loss occurs, for example Mono Lake, California, USA that contains [PO_{4tot}] ~400 µM and ~1.4 *M*/kg salinity (Romero et al., 1993; Jellison and Melack, 2001). High-salinity settings also exacerbate nitrogen limitation by inhibiting nitrogen fixation (Herbst, 1998), and high-salinity contributes to a low species richness (i.e., Chad et al., 2013; Kabede, 1998; Olli et al., 2019; Bernard et al., 2020). Together these factors may decrease the rates of [PO_{4tot}] consumption by microorganisms and lead to a gradual build-up of [PO_{4tot}].

Here, we examine precipitation in highly alkaline, saline conditions at low diagenetic temperatures (50ºC) in solutions that contain millimolar concentrations of PO_4 to investigate the impact of kinetic inhibition on the styles of Ca-Mg-CO_3 precipitation from amorphous calcium

magnesium carbonate (ACMC) precursors that may provide a glimpse into conditions in the geologic past and even conditions on Mars.

2.3 Methods

2.3.1 Experimental setup

To investigate Ca-Mg-CO_3 precipitation from amorphous calcium magnesium carbonate (ACMC) precursors, we performed two sets of experiments with solution chemical conditions (Table 2.1 A) that were based on modern alkaline lake water. The lake conditions simulated were supersaturated with respect to Ca-Mg-CO_3 minerals, produce primary dolomite and can concentrate PO_4 to above 1 m*M* (Toner and Catling, 2020). The solutions contained high Mg/Ca ratios where Ca^{2+} and Mg^{2+} concentrations (hereafter [Ca] and [Mg]) were selected based on concentrations of modern lakes that contained dolomite and magnesite (geochemical review of 21 modern lakes; Chagas et al., 2016). The solutions contained total dissolved PO_4 (hereafter [PO_{4tot}]) that ranged from 7 to 14 m*M*, which is above typical concentrations of modern alkaline lake waters that can reach PO_4 >1 m*M* (Toner and Catling, 2020) and most modern carbonate sediment pore waters that can reach >30 μ*M* (Morse, 1985). For the first set of experiments (Exp. 2), amorphous calcium magnesium carbonate (ACMC) precursor material with controlled content was synthesized *ex situ* at 22±0.5 ˚C, dried in a vacuum desiccator for 24 h and subsequently added to the lake water solutions. The ACMC was left to crystallize in lake water solutions within individual polycarbonate bottles that were submerged in a water bath at 50±1.5 ˚C for 55 days. These experiments investigated changes in dissolved inorganic carbon concentration ([DIC]) that ranged from 4 to 148 m*M*, changes in total alkalinity ([TA]) that ranged from 7 to 251 m*M* and changes in ionic strength that ranged from 0.67 – 1.07 *M* through the addition of nonreactive salt NaCl.

ACMC precursor material was synthesized by homogeneous nucleation from well-characterized solutions that maintain a constant supersaturation and steady state, using the mixed

flow reactor method (Blue, Rimstidt, and Dove, 2013; Blue and Dove, 2015) (Figure 2. 1A). ACMC was produced with a controlled Mg/Ca ratio of 1, by regulating the Mg/Ca ratio of the input solution the carbonate concentration and the pH (Blue and Dove, 2015).

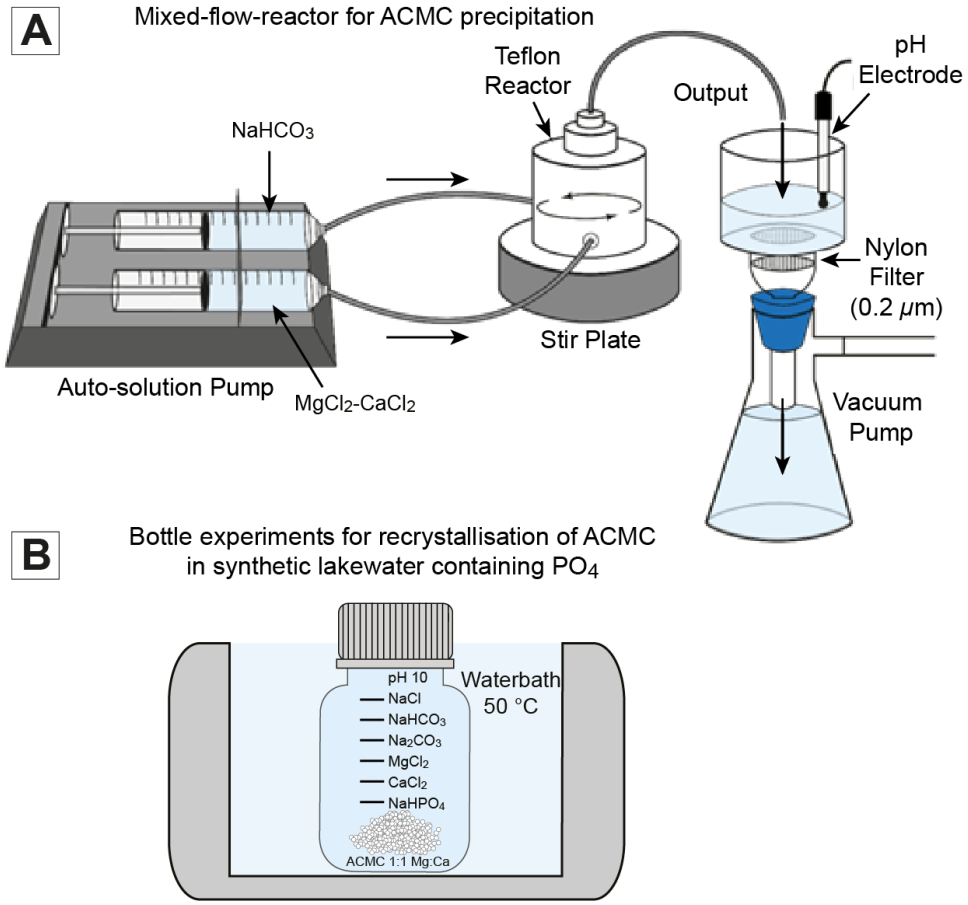

Figure 2. 1 Schematic diagram of the experimental set-up for controlled ACMC precipitation. A: The method uses a steady-state mixed flow reactor to precipitate ACMC with controlled Mg content (after Blue, Rimstidt, and Dove, 2013; Blue and Dove, 2015). Solutions of NaHCO3 and MgCl2-CaCl2 were mixed simultaneously to precipitate ACMC with controlled Mg content. Arrows show direction of flow. B: Schematic diagram of a polycarbonate bottle containing ACMC precursor material or homogeneously nucleated material) in supersaturated solutions for recrystallization experiments. Bottles were placed in a water bath at 50 ºC for 63-64 days.

The second set of experiments – homogenous nucleation experiments (Exp. 7) contained ACMC that was produced *in situ* by homogeneous nucleation from the highly supersaturated lake water solutions at pH ~10 once Ca^{2+} and Mg^{2+} stock solutions were added to the CO_3^{2-} solutions. The solutions contained dissolved $[PO_{4tot}]$ = 7 or 14 m*M*/L that are dominated by PO_4^{3-} species under the high-pH conditions examined here (i.e., Chapter 1, Figure 1.2). The nucleated ACMC were left to crystallize in the reacted lake water solutions within individual polycarbonate bottles

that were submerged in a water bath at 50˚ C for 64 days) (Figure 2. 1B). The experiment sets were divided into three categories: 1) low Mg/Ca; 2) high Mg/Ca and 3) higher PO4 experiments. These are summarized in Table 2.1 A–B. Low Mg/Ca experiments investigated nucleation from solutions with [Mg]/[Ca] = 1–5 and total [Mg^{2+}] = 43 m*M* and [Ca^{2+}] = 8.9 m*M*, and increases in ionic strength from [IS] = 0.40 to 0.82 *M* through the addition of non-reactive salt (NaCl). *High Mg/Ca* experiments investigated increases in [Mg]/[Ca] ratios from 7–17 based on changes in total [Ca^{2+}] and [Mg^{2+}] that ranged from 24–48 and 2.8–28 m*M* respectively. *Higher PO_4* experiments were conducted under the same conditions as the low Mg/Ca experiments apart from increasing dissolved [PO_{4tot}] from 7–14 m*M*/L. One control solution was made that was not warmed in a water bath and upon nucleation was vacuum filtered from the solution and the solid sample was dried and analyzed immediately.

To produce the solutions that were supersaturated with respect to ACMC, magnesite and dolomite, we modelled the theoretical geochemical solutions using Geochemist's Workbench software (GWB) (Bethke and Yeakel, 2015) which utilizes the LLNL thermodynamic dataset and the extended ''B-dot" Debye-Huckel equation for activity coefficients of charged species (Helgeson, 1969; Debye and Hückel 1923). Activity coefficients of unity were assumed for neutral species (Garrels and Christ, 1965). The theoretical geochemical models of synthetic evaporative lake-water solutions that were used indicate that dolomite and magnesite can be produced at low-diagenetic temperatures (50˚ C). Once modelled, the desired synthetic lake water chemistry was produced by adding reagent-grade salts (Sigma-Aldrich) to nanopure (18 Ω) deionized water (Table 2.1 A–B). The solution alkalinity was 'fixed' and the pH was controlled using a bicarbonate buffer system containing $Na_2CO_3^{2-} - NaHCO_3^{2-}$. This is an acid-base homeostatic mechanism that involves the balance of carbonic acid (H_2CO_3), bicarbonate (HCO_3^{3-}), and carbon dioxide (CO_2) in order to maintain pH. The system maintained atmospheric partial pressure of carbon dioxide $\sim 10^{-3.5}$ atm. Estimates of the carbonate chemistry were calculated based on the known quantity of carbonate salt added and the manually adjusted pH. For an extended description of the carbonate chemistry calculations, see the Supplementary

Materials Eq. 1-16. The experiments were conducted in sterile equipment in a closed system with no atmospheric headspace; therefore, gaseous CO_2 had little effect on carbonate speciation throughout the experiments.

ACMC Precursor Experiments												
Exp. 2 No.	ACMC added (g)	Exp. type	Time (Days)	Temp (°C)	Measured pH (initial)	[DIC] m*M*/kg	Ω_{ACMC} (solution)	Ω_{AMC} (solution)	Mg/Ca	CO_3/Ca	[TA] m*M*/kg	Ionic strength *M*/kg
7	0.09		63	50	10.3	148	2888	379	4	9	251	0.81
9	0.07		63	50	10.2	148	2888	379	4	9	251	1.01
11	0.09		63	50	10.1	148	2888	379	4	9	251	1.21
13	0.06	ACMC	55	50	10.3	16	298	39	4	1	27	0.67
15	0.06		55	50	10.1	16	298	39	4	1	27	0.87
17	0.07		55	50	10.0	16	298	39	4	1	27	1.07
19	0.08		53	50	10.4	4	89	12	4	0	7	0.66
21	0.07		53	50	10.2	4	89	12	4	0	7	0.86
23	0.08		53	50	10.1	4	89	12	4	0	7	1.06
Homogeneous Nucleation Experiments												
Exp. 7 No.	ACMC added (g)	Exp. type	Time (Days)	Temp (°C)	Measured pH (initial)	[DIC] m*M*/kg	Ω_{ACMC}	Ω_{AMC}	Mg/Ca	CO_3/Ca	[TA] m*M*/kg	Ionic strength *M*/kg
6.6	0	Contr.	0	22	9.9	148	907	252	5	12	109	0.78
7.0	0		64	51	9.9	148	1512	305	1	4	109	0.70
7.1	0	Low Mg/Ca	64	51	10.0	148	866	248	3	6	109	0.71
7.2	0		64	51	10.1	148	210	102	4	12	109	0.70
7.3	0		64	51	10.0	148	129	77	7	19	109	0.69
7.4	0		64	50	10.4	148	118	76	9	21	109	0.70
7.5	0	High Mg/Ca	64	51	10.0	148	121	77	11	27	109	0.70
7.6	0		64	51	10.0	148	105	71	13	31	109	0.70
7.7	0		64	51	10.0	148	90	65	15	37	109	0.70
7.8	0		64	50	10.0	148	101	72	17	37	109	0.70
7.9	0		64	50	10.0	148	257	120	5	12	109	0.80
8.0	0	Low Mg/Ca	64	48	10.0	148	235	115	5	12	109	0.40
8.1	0		64	51	10.0	148	293	130	5	12	109	0.50
8.2	0		64	48	10.1	148	232	114	5	12	109	0.60
8.3	0		64	50	10.1	148	232	114	5	12	109	0.62
8.4	0		64	51	10.0	148	246	117	5	12	109	0.82
8.5	0	Higher PO_4	64	52	10.1	148	214	108	5	12	109	0.42
8.6	0		64	49	10.1	148	228	110	5	12	109	0.52
8.7	0		64	49	10.3	148	176	96	5	12	109	0.72

Table 2.1 A Initial chemical parameters of the solutions for the ACMC precursor experiments and homogeneous nucleation experiments. Saturation ΩACMC and ΩAMC are calculated for the solutions and do not include the ACMC precursor material. The ΩACMC and ΩAMC values are calculated from values provided by Chang et al., (2021) and Purgstaller et al., (2021) respectively

for the ACMC Precursor Experiments and assume a resultant Mgsolid and Casolid mol% of 50 and the homogeneous nucleation experiment calculations are based on the Mgsolid and Casolid mol% of the resultant solid material (see supplementary material S2 3. for calculations). The homogenous nucleation experiments are categorised into low Mg/Ca, high Mg/Ca and high PO4 indicated in this table by the colours.

ACMC Precursor Experiments										
EXP 2 No.	**Measured pH (initial)**	**[Na] m*M*/kg**	**[Mg] m*M*/kg**	**[Ca] m*M*/kg**	**[Cl] m*M*/kg**	**[PO_4] m*M*/kg**	**[HCO_3] m*M*/kg**	**[CO_3] m*M*/kg**	**[DIC] m*M*/kg**	**[CO_2]$_{aq}$ m*M*/kg**
7	10.3	364.8	47.6	11.1	217.4	7.1	44.5	103.1	147.5	0.0
9	10.2	564.8	47.6	11.1	417.4	7.1	44.5	103.1	147.5	0.0
11	10.1	764.8	47.6	11.1	617.4	7.1	44.5	103.1	147.5	0.0
13	10.3	141.0	47.6	11.1	217.4	7.1	5.5	10.6	16.2	0.0
15	10.1	341.0	47.6	11.1	417.4	7.1	5.5	10.6	16.2	0.0
17	10.0	541.0	47.6	11.1	617.4	7.1	5.5	10.6	16.2	0.0
19	10.4	121.4	47.6	11.1	217.4	7.1	0.9	3.2	4.1	0.0
21	10.2	321.4	47.6	11.1	417.4	7.1	0.9	3.2	4.1	0.0
23	10.1	521.4	47.6	11.1	617.4	7.1	0.9	3.2	4.1	0.0
Homogeneous Nucleation Experiments										
EXP 7 No.	**Measured pH (initial)**	**[Na] m*M*/kg**	**[Mg] m*M*/kg**	**[Ca] m*M*/kg**	**[Cl] m*M*/kg**	**[PO_4] m*M*/kg**	**[HCO_3] m*M*/kg**	**[CO_3] m*M*/kg**	**[DIC] m*M*/kg**	**[CO_2]$_{aq}$ m*M*/kg**
6.6	9.9	675	43	8.9	503	7	44	103	148	0.01
7.0	9.9	765	24	27.7	603	7	44	103	148	0.01
7.1	10.0	765	43	16.6	619	7	44	103	148	0.01
7.2	10.1	765	38	8.9	594	7	44	103	148	0.01
7.3	10.0	765	38	5.5	587	7	44	103	148	0.01
7.4	10.4	765	43	5.0	596	7	44	103	148	0.01
7.5	10.0	765	43	3.9	594	7	44	103	148	0.01
7.6	10.0	765	43	3.3	592	7	44	103	148	0.01
7.7	10.0	765	43	2.8	591	7	44	103	148	0.01
7.8	10.0	765	48	2.8	601	7	44	103	148	0.01
7.9	10.0	865	43	8.9	703	7	44	103	148	0.01
8.0	10.0	465	43	8.9	303	7	44	103	148	0.01
8.1	10.0	565	43	8.9	403	7	44	103	148	0.01
8.2	10.1	665	43	8.9	503	7	44	103	148	0.01
8.3	10.1	679	43	8.9	503	14	44	103	148	0.01
8.4	10.0	879	43	8.9	703	14	44	103	148	0.01
8.5	10.1	479	43	8.9	303	14	44	103	148	0.01
8.6	10.1	579	43	8.9	403	14	44	103	148	0.01
8.7	10.3	779	43	8.9	603	14	44	103	148	0.01

Table 2.1 B Initial chemical composition and ionic concentration of the solutions for the ACMC precursor experiments and homogeneous nucleation experiments. The experimental solutions were prepared from analytical grade standards added to ultrapure deionized water. The compositions presented here do not include the ACMC precursor material. The $[CO_3]^{2-}$, $[HCO_3]^-$ and $[CO_2]$ was calculated based on the known [DIC] and pH according to the cabonate chemistry

system (descrbed in the Supplamentary Material S2 3). The homogenous nucleation experiments are categorised into low Mg/Ca, high Mg/Ca and high PO_4 indicated in this table by the colours.

2.3.2 Experimental setup

1 mL samples were drawn from solution using a needle syringe and filtered through a 0.22 μm Durapore™ PVDF syringe filter. The 1 mL samples were dissolved in 14 mL HNO_3 4 % and analyzed using ICP-AES. Once the experiments were terminated solid precipitates were vacuum-filtered onto 0.22 μm EMD Millipore™ Durapore™ Nylon filters before mineralogical and chemical analyses.

ICP-AES was used to acquire the elemental concentration (Ca, Mg and P) of solution samples and bulk solid samples performed using an Ultima 2C Horiba Jobin Yvon inductively coupled plasma optical emission spectrometer (ICP-AES). Each sample passed through a pneumatic concentric nebulizer and cyclonic quartz spray chamber. The 1 mL samples were dissolved in 4 mL nitric acid. Samples were analyzed with an uptake rate of 2 mL/min. Ca, Mg and P concentrations were determined from calibration curves that were prepared from plasma-grade Sigma-Aldrich element standards. Ca, Mg, and P standards were analyzed in in addition to monitor standards that sandwiched every 5 samples to monitor accuracy and measure long term instrumental drift. Drift was calculated and a correction factor was applied to the data. See supplement S2 3 for full description.

X-ray powder diffraction (XRD) data was acquired using a high-resolution Panalytical Empyrean powder X-ray diffractometer with Co-Kα radiation at the wavelength (λ) of 1.540 Å. X-rays were generated from a Co anode supplied with 40 kV and a current of 20 mA. The scan range was 25–65 º2θ and step size 0.0260 (°2θ) for 96 seconds (s). Fixed anti-scatter and fix-slit were used with a Soller-slit of 0.5° and a beam mask of 10 mm. The instrument subjects samples to X-rays of a fixed wavelength, and the intensity of the reflected radiation was recorded continuously as the sample and detector rotated. Intensity peaks arose when the mineral contained lattice planes with *d*-spacings (Å value) appropriate to diffract X-rays at that reflection value (θ).

To acquire infrared spectra (FTIR) and characterize the style of chemical bonding in compounds in our samples, ~2 mg of the dried samples at room temperature was added to 200 mg K-Br (oven

dried at 150 °C) and milled into a fine-grained homogenous powder, <10 μm. Individual K-Br hydraulically-vacuum pressed plates with the sample incorporated were produced. FTIR spectra were acquired with a Perkin-Elmer Frontier FTIR spectrometer. The data were collected from absorbance or transmittance vs. wavenumber (ν) in the range of 400–4000 cm^{-1}. Spectrum software was used to collect the data. A blank K-Br plate was run as a baseline which was auto-calculated and removed as a background for each sample K-Br plate.

Scanning electron microscope High Definition Electron Backscatter Diffraction (SEM-HDBSD) and Energy-dispersive X-ray spectroscopy (SEM-EDS) data was collected on samples that were powdered, mounted onto carbon tape, and adhered to an SEM stub. The sample stubs were coated with ~12 nm gold (100 seconds) using a Q150R ES sputter coater (Quorum Technologies) at the Dunn School Bio-imaging Facility (University of Oxford). Scanning Electron Microscope (SEM) sample characterization was performed using a FEI Quanta 650 Emission Gun (Thermo Scientific) operated at 8 kV. Sample spectra was acquired for Ca, Mg and O using Energy Dispersive Spectroscopy (EDS) by AZtec (Oxford Instruments) with a 50 mm detector, aperture of 3 and spot size of 4 using an approximate 2nA beam current.

2.4 Results and Discussion

2.4.1 ACMC precursor solid sample characterization

XRD, FTIR and SEM-EDS analyses to examine the solid samples from the ACMC precursor experiments showed that the ACMC precursor material underwent crystallization at temperatures of 50 °C and pH levels of 10. These conditions resulted in solid, Mg-rich $CaCO_3$ mineral phases. Overall, the analyses revealed that the most common mineral phases produced in ACMC precursor experiments were high Mg $CaCO_3$ minerals.

XRD results data from the recrystallized ACMC samples are presented in Figure 2.2. The ACMC recrystallized in solutions that increased in supersaturation (Ω_{ACMC} >89) and are plotted

accordingly from the base to the top of the XRD diagrams. XRD analyses indicate that ACMC recrystallization resulted in hydromagnesite, magnesite, very high Mg-calcite (VHMC), aragonite, dolomite, and brushite/apatite/Ca-Mg-PO_4 minerals. The dominant phase was high-Mg calcite (Figure 2. 2). Estimates of the Mg content of the dominant Mg-Ca-CO_3 phase were determined from *d*-spacing (d_{104} Å) values from the obtained XRD results based on calculations according to Goldsmith et al., (1961) ([Mg] $\%_{XRD}$), which are presented in Table S2.5. In the ACMC precursor experiments, the average content was calculated for the highest d_{104} values, where the mean content of Mg is 42 % and reaches 48 % in experiments where $\Omega_{ACMC} \geq 298$. However, these estimates have a 5 % error (i.e., Bischoff et al., 1983; Zhang et al., 2010). XRD evidence for dolomite is indicated by the presence of d_{104} values = 2.90 Å positioned at 35.95 °2θ, indicating ~50 % Mg and diagnostic ordering peak d_{015} values = 2.54 Å positioned at 41.2 °2θ. The presence of dolomite is observed in samples from solutions with the highest supersaturation ($\Omega_{ACMC} \geq 298$), [DIC] at 16-148 m*M*, [TA] at 27-251 m*M*, Mg/Ca at 4 and [PO_4] at 7 m*M*/L.

The XRD analyses indicate that recrystallization of ~50 Mg % ACMC resulted in high-Mg calcite (Mg 10–30 %) to very high-Mg calcite with (Mg 40–50 %). Increases in Mg % incorporation of the resultant phase (to ~48 Mg %) are indicated by shifts in d_{104} values toward higher position values (°2θ) (Figure 2. 2). Because all of these experiments were conducted in solutions with constant [Mg]/[Ca] = 4, the increased Mg enrichment can be explained by increased CO_3^{2-} alkalinity.

The FTIR analyses (Figure S2. 2) indicate that ACMC recrystallization from the most supersaturated solutions (Ω_{ACMC} >298) contained hydromagnesite and high Mg-calcite, dolomite, aragonite, huntite and brucite $(Mg\text{-}OH)_2$. The presence of brushite (DCDP) is indicated by the band at 800 cm^{-1} indicating libration mode of H_2O from DCPD (Petrov et al., 1967), however, this may also indicate magnesite, nesquehonite or huntite. There are PO_4^{3-} v_4 bands at 600 cm^{-1} of amorphous calcium phosphate (Layrolle and Lebugle, 1994) identified in samples recrystallized in the most supersaturated solutions (Ω_{ACMC} >298). However, 600 cm^{-1} may also be indicative

of hydromagnesite and 595 is indicative of apatitic PO_4. ν_2 PO_4 bands were also identified at 485 cm^{-1}. However, even with bands that characterize PO_4 phases, there was no identification of a band at 3571 cm^{-1} for OH- stretching mode indicative of hydroxyapatite (Bigi et al., 2007). Bands identified at 3700 cm^{-1} in samples from the least supersaturated solutions (Ω_{ACMC} = 98), which are indicative of hydromagnesite, although they may also characterize $Mg(OH)_2$ (brucite) (Choudhari et al., 1973; Frost et al., 1999) or MgO bonds (Selvam et al., 2011). However, this is only observed in samples from ACMC precursor recrystallization experiments conducted in less supersaturated solutions with Ω_{ACMC} = 89. These samples also contain small peaks at 3650 cm^{-1} of hydromagnesite and broad bands around 3400-3500 suggesting possible poorly crystalline hydromagnesite or an amorphous phase. Only experiments 7, 9 and 11 contain clear evidence of hydromagnesite (3516, 3448, 3650 and 744 [and possibly 600] cm^{-1}). Monohydrocalcite is easily identified in one sample and in another sample, a small band at 909 cm^{-1} is indicative of huntite.

The band at 1119 cm^{-1} is observed in FTIR spectra of samples 7, 9, 11 and 13, which may be indicative of hydromagnesite; however, this may also indicate PO_4. The PO_4^{3-} ν_3 band at 1119 cm^{-1} in addition to the CO_3^{2-} ν_1 bands may be indicative of apatite (1111-1112 of poorly crystalline hydroxyapatite or 1120-1150 of HPO_4^{2-} (Gadaleta et al., 1996).

SEM-EDS indicates that the dominant morphology is spheres composed of nanocrystalline dolomite, hydromagnesite and Mg-calcite at various stages of recrystallization. Large euhedral calcite crystals can be identified, poorly crystalline dolomite spheres are present and apatite nanocrystals may also observed. SEM-EDS provides chemical evidence of the mineralogy observed above which provides further evidence of dolomite and hydromagnesite crystals.

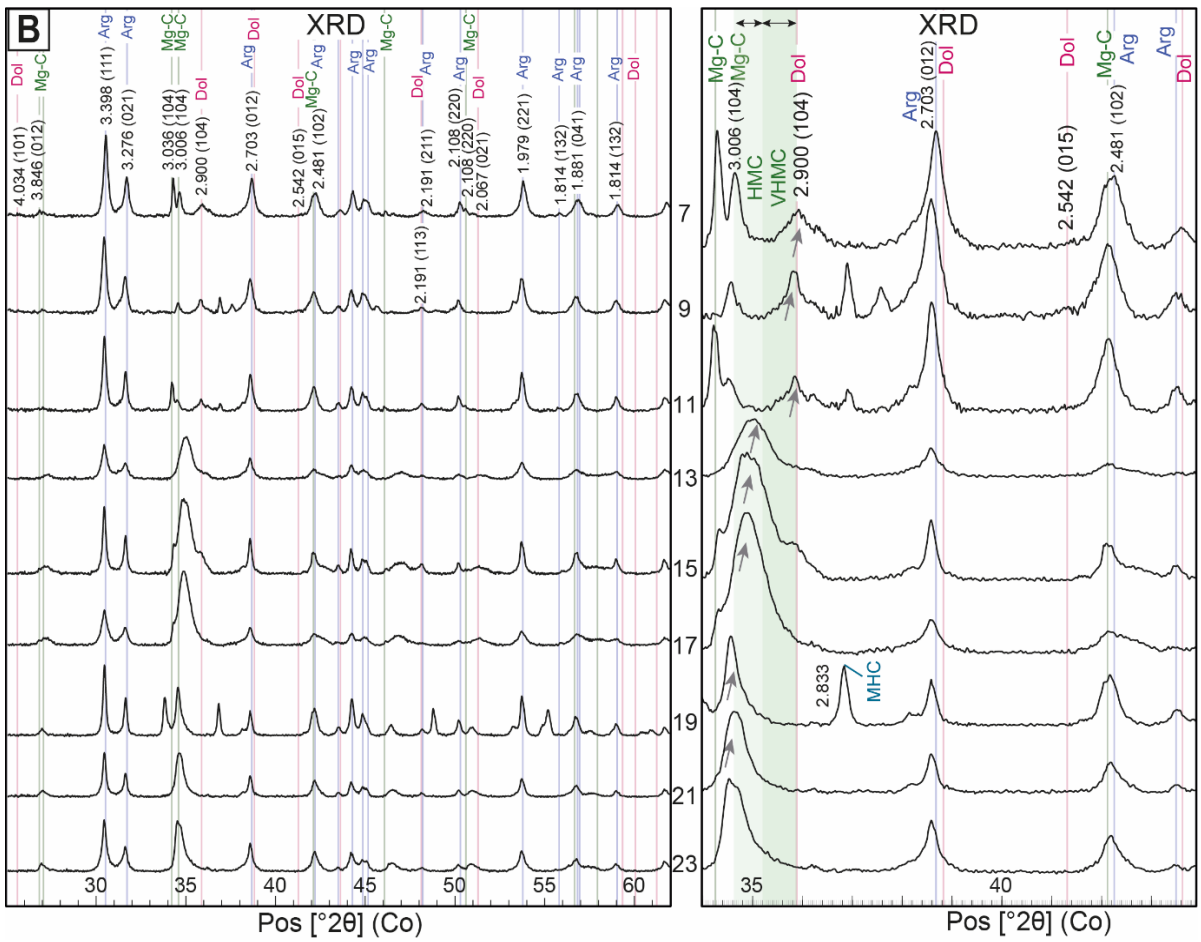

Figure 2. 2 XRD diagrams of the resultant recrystallized solids from ACMC precursor experiments. The XRD analyses indicate that recrystallization of ~50 Mg % ACMC resulted in dominantly high-Mg calcite and aragonite. The green shaded area labelled HMC indicates high-Mg calcite (Mg 10–30 %) and the shaded area labelled VHMC indicates very high-Mg calcite with (Mg 40–50 %). All samples shown were from solutions with [Mg]/[Ca] = 4 and pH = 10. The samples shown are from solutions that increase in CO_3^{2-} alkalinity from the base of the XRD diagram to the top. Corresponding increases in Mg % incorporation are indicated by shifts in d_{104} values toward higher position values (°2θ). This trend is indicated by the grey arrows. *d*-spacing values are labelled and interpreted Bragg ordering (*hkl*) assignments are shown in brackets. The zoomed in section shows XRD evidence for dolomite indicated by the presence of d_{104} values = 2.90 Å positioned at 35.95 °2θ indicating ~50 %Mg and the presence of a small but diagnostic ordering peak d_{015} values = 2.54 Å positioned at 41.2 °2θ. Dol – dolomite; Arg – aragonite; Mg-C – Mg-calcite, MHC – monohydrocalcite.

2.4.2 Homogeneous nucleation solid sample characterization

In the homogenous nucleation experiments, spontaneous nucleation occurred immediately upon mixing of the stock solutions at room temperature (22 °C) producing an amorphous phase. XRD, FTIR and SEM-EDS analyses of the control sample that was not subject to warming in the water

bath (sample 6.6, Table 2.1 A) show that this phase was an Mg-rich ACMC. Based on solid sample ICP-AES, the ACMC contained ~63.9 Mg mol% and based on FTIR ν_1 values of 1081.41 cm^{-1} contained an estimated ~70 Mg mol% (Blue and Dove, 2015) from an initial solution with [Mg]/[Ca] of 5 and [CO_3]/[Ca] of 12 (XRD and FTIR shown in supplementary material Fig. S2.2-2).

Upon nucleation, of the remaining solutions, the amorphous phases subsequently underwent crystallization in 50 °C temperatures at pH 10 resulting in solid precipitates that exhibit a variety of mineralogy and polymorph expression. These experiments were divided into three sets as described in the methods: 1) *low Mg/Ca*, 2) *high Mg/Ca* and 3) *higher PO_4*. A separate figure for the three sets is presented with XRD, FTIR and SEM-HDBSD results (Figure 2. 3; Figure 2. 4; Figure 2. 5). Table S2.1 in the supplementary information provides a semi-quantitative result of the minerals present with the corresponding XRD reference codes as well as the relative proportion of each mineral per sample. The XRD diagrams (Figure 2. 3; Figure 2. 4; Figure 2. 5) reveal that the amorphous phase recrystallizes dominantly into hydromagnesite, which subsequently crystallizes into magnesite, dolomite and brucite (Mg-$OH)_2$ with a number of additional accessory mineral phases including aragonite, calcite, Ca-PO_4, apatite and halite (NaCl).

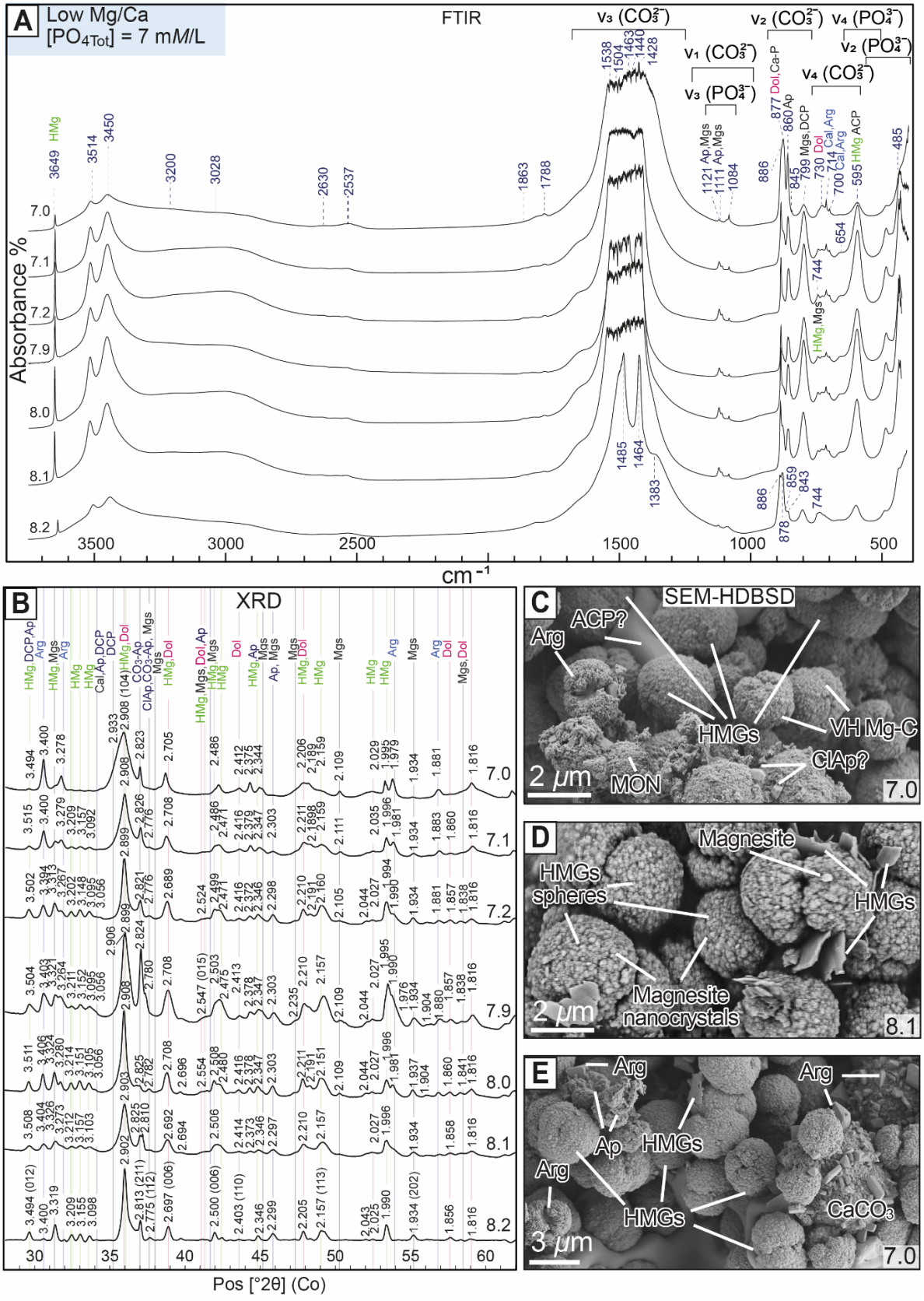

Figure 2. 3 FTIR spectra, XRD diagrams and SEM-HDBSD of *low Mg/Ca* nucleation experiments.

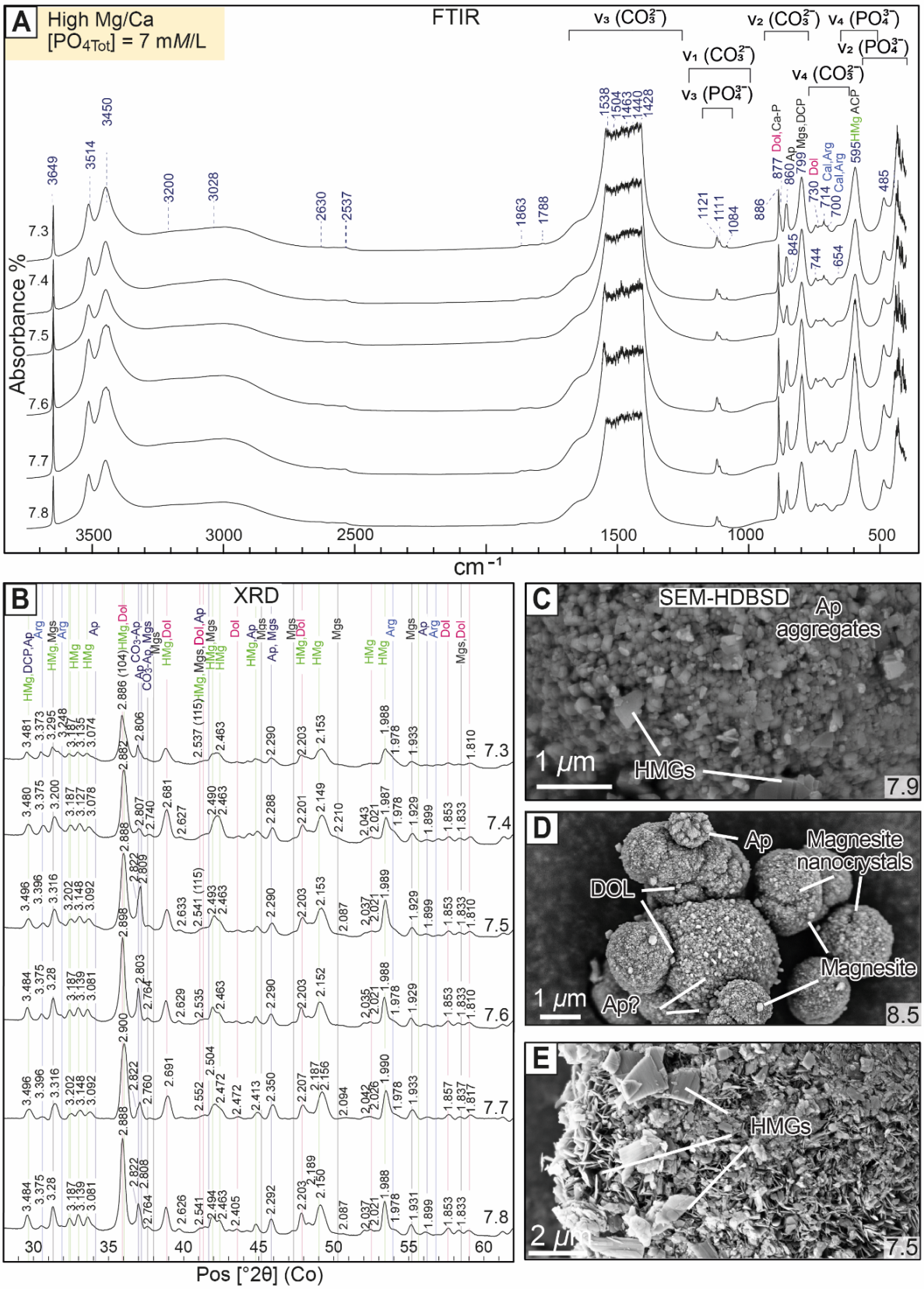

Figure 2. 4 FTIR spectra, XRD diagrams and SEM-HDBSD of *high Mg/Ca* experiments.

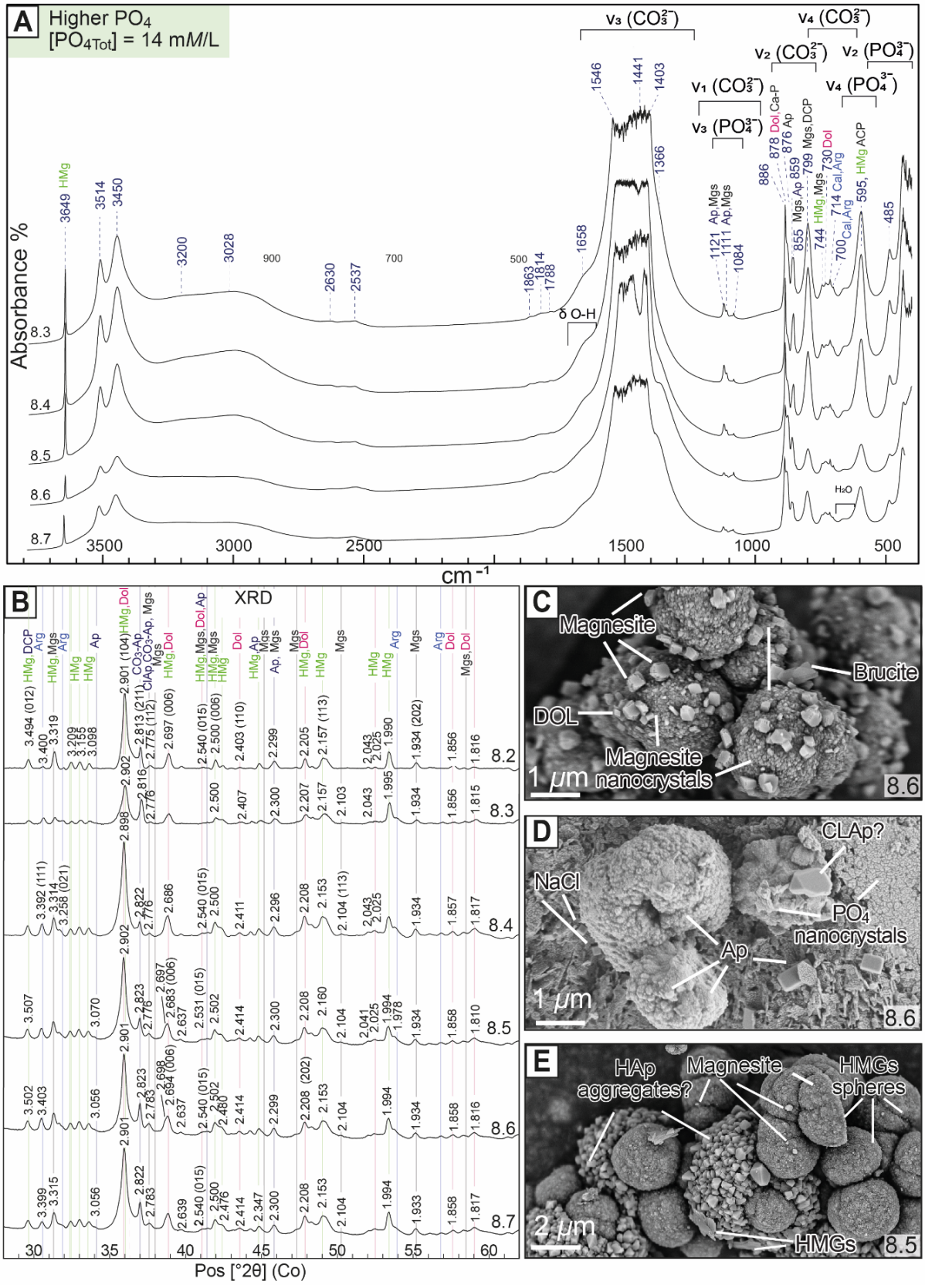

Figure 2. 5 FTIR spectra, XRD diagrams and SEM-HDBSD of *higher PO_4* nucleation experiments.

Figure 2. 3 FTIR spectra, XRD diagrams and SEM-HDBSD of *low Mg/Ca* nucleation experiments. These samples represent the results of the homogenous nucleation experiments from solutions with increasing [Mg]/[Ca] ratio from 1–5 that correspond with increasing sample numbers (7.0–8.2) sample that contained [PO_4] of 7 m*M*/L at pH 10 in 50 ºC temperatures. A: FTIR spectra indicate that hydromagnesite is the most dominant mineral present but magnesite, dolomite and apatite peaks are also observed. Characteristic vibration bands ($\nu_1 - \nu_4$) are labelled. B: Representative XRD diagrams of the samples. The XRD peaks positions (°2θ) and d-spacing (Å) are labelled for the dominant mineral phases hydromagnesite, magnesite, aragonite, dolomite and apatite/PO_4. C-E: Representative SEM-HDBSD images of solid samples from some of the homogenous nucleation experiments. The dominant morphologies are spherulitic aggregates with some coarse euhedral crystals and sheet-like hydromagnesite.

Figure 2. 4 FTIR spectra, XRD diagrams and SEM-HDBSD of *high Mg/Ca* experiments. These samples represent the results of the homogenous nucleation experiments from solutions with increasing [Mg]/[Ca] ratio from 7–17 that correspond with increasing sample numbers (7.3–7.8). The samples nucleated in solutions that contained [PO_4] of 7 m*M*/L at pH 10 in 50 ºC temperatures. A: FTIR spectra indicate that hydromagnesite is the most dominant mineral present but magnesite, dolomite and apatite peaks are also observed. Characteristic vibration bands ($\nu_1 - \nu_4$) are labelled. B: Representative XRD diagrams of the samples. The XRD peaks positions (°2θ) and d-spacing (Å) are labelled for the dominant mineral phases hydromagnesite, magnesite, aragonite, dolomite and apatite/PO_4. C-E: Representative SEM-HDBSD images of solid samples from some of the homogenous nucleation experiments. The dominant morphologies are spherulitic aggregates with some coarse euhedral crystals and sheet-like hydromagnesite.

Figure 2. 5 FTIR spectra, XRD diagrams and SEM-HDBSD of *higher PO_4* nucleation experiments. These samples represent the results of the homogenous nucleation experiments from solutions containing high [PO_{4tot}] at 14 m*M*/L with [Mg]/[Ca] = 5. The only difference between these samples is an increase in salinity that correspond with increasing sample numbers (8.2–8.7). A: FTIR spectra indicate that hydromagnesite is the most dominant mineral present but magnesite, dolomite and apatite peaks are also observed. Apatite is more common in these samples. Characteristic vibration bands ($\nu_1 - \nu_4$) are labelled. B: Representative XRD diagrams of the samples. The XRD peaks positions (°2θ) and d-spacing (Å) are labelled for the dominant mineral phases hydromagnesite, magnesite dolomite and apatite. C-E: Representative SEM-HDBSD images of solid samples from some of the homogenous nucleation experiments. The dominant morphologies are spherulitic aggregates with larger and coarser crystals and sheet-like hydromagnesite is near absent. Apatite is more common in these samples and there is clear evidence of magnesite and dolomite as well as other [PO_4] minerals.

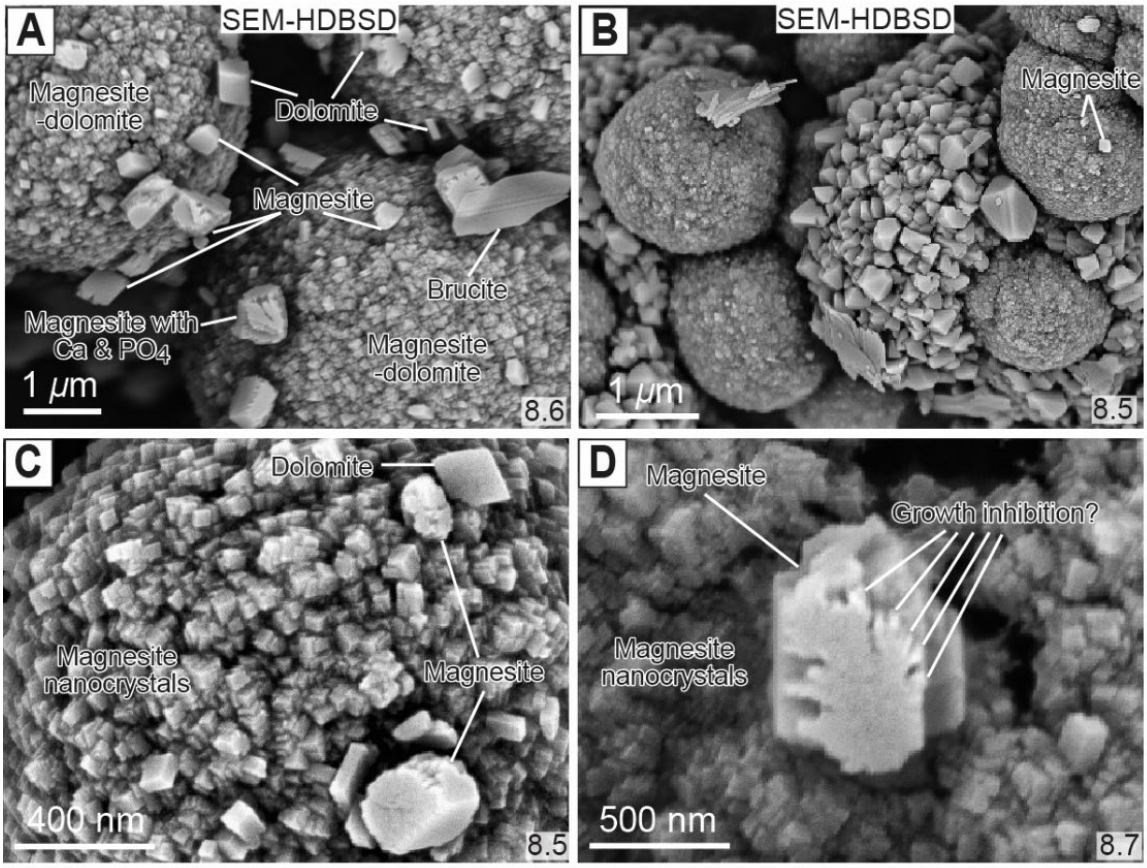

E SEM-EDS

Dolomite				Magnesite				Brucite				Magnesite with Ca and PO_4			
Element	Atomic %	Wt%	Wt% σ (error)	Element	Atomic %	Wt%	Wt% σ (error)	Element	Atomic %	Wt%	Wt% σ (error)	Element	Atomic %	Wt%	Wt% σ (error)
O	44.0	23.9	0.4	O	68.0	51.8	1.2	O	61.1	38.7	0.8	O	60.5	47.2	0.9
Mg	19.2	15.8	0.2	Mg	16.8	19.4	0.5	C	16.4	7.8	1.2	Mg	16.2	19.2	0.4
Ca	19.2	26.0	0.4	C	9.1	5.2	2.1	Mg	15.3	14.7	0.3	C	14.3	12.2	0.3
C	10.7	4.4	1.1	Ca	3.1	5.9	0.2	Au	3.7	29.1	0.9	Ca	6.2	9.4	0.5
Au	3.2	21.5	0.6	Au	1.4	13.0	0.6	Pd	1.9	8.0	0.7	Au	1.0	8.4	1.7
Pd	1.8	6.5	0.3	Pd	0.7	3.5	0.3	N	0.3	0.2	0.1	Na	0.7	1.7	0.3
Na	0.7	0.6	0.0	Na	0.7	0.7	0.1	Ca	0.3	0.4	0.7	Cl	0.3	0.8	0.1
Cl	0.7	0.8	0.1	Cl	0.2	0.3	0.1	Cl	0.2	0.3	0.2	Pd	0.3	0.6	0.1
Si	0.3	0.3	0.1	Si	0.1	0.1	0.1	P	0.2	0.3	0.1	P	0.2	0.2	0.1
K	0.1	0.1	0.1	S	0.1	0.1	0.1	Si	0.2	0.2	0.1	S	0.1	0.2	0.1
P	0.1	0.1	0.1	P	0.0	0.1	0.1	Na	0.2	0.2	0.1	K	0.1	0.1	0.1
S	0.1	0.1	0.1	N	0.0	0.0	0.2	S	0.2	0.2	0.2	Si	0.1	0.1	0.1
Total	100	100	-	Total	100	100	-	Total	100	100	-	Total	100	100	-

Figure 2. 6 SEM-HDBSD images of solid samples from the homogenous nucleation experiments. A: spheres comprised of aggregates of nanocrystalline magnesite and some nanocrystalline dolomite with large (<1 μm) individual magnesite crystals or twinned magnesite crystals are observed as well as large dolomite crystals that protrude out from the surface. B: Hydromagnesite spheres at an earlier stage of recrystallization to magnesite. Aggregates of crystals inferred to be apatite display well developed facets and are observed surrounded by hydromagnesite-magnets spheres. C: High magnification image indicates the well developed nanocrystalline magnesite aggregates that have recrystallized from hydromagnesite spheres. Coarse individual and twinned magnesite are present on the surface. These exhibit growth defects. Coarse dolomite crystals with well developed crystallinity are also observed. D: Coarse magnesite crystal protruding out from the surface of a magnesite sphere. Unusual morphological features are observed on the that exhibit dendritic-like features that appear to be growth inhibition on the growth surface. These areas have a higher P concentration in SEM-EDS spectra which implies that magnesite crystal growth has become inhibited, likely from the attachment of PO_4 to crystal growth sites. E: Representative

SEM-EDS mineral mapping results for the minerals in the corresponding SEM-HDBSD images. The gold (Au), palladium (Pd) and sulphur (S) are derived from the gold coating of the samples.

2.4.3 Low Mg/Ca experiments

XRD analyses of the solid samples recrystallized from the low Mg/Ca homogenous nucleation experiments indicate that the experiments routinely produced hydromagnesite as the dominant mineral with a typical mineral assemblage of hydromagnesite, aragonite, Mg-calcite, dolomite and dicalcium phosphate (DCP; $CaHPO_4$) (Figure 2. 3). The estimated [Mg] $\%_{XRD}$ for the most dominant mineral phase based determined from obtained XRD d_{104} spacing values results provides a mean content of Mg 48 % for the *low Mg/Ca experiments* (Mg/Ca = 1–4) ([Mg] $\%_{XRD}$ presented in Table S2.5) and 74 %mol Mg for the bulk solid based on ICP measurements (Table S2.7).

SEM-EDS indicates that the dominant morphology is spheres composed of nanocrystalline VHMC-dolomite and hydromagnesite at various stages of recrystallization. Large euhedral calcite , aragonite and apatite crystals are also observed along with PO_4 nanocrystals. SEM-EDS provides chemical evidence of the mineralogy observed above which provides further evidence of dolomite and hydromagnesite crystals.

Under the conditions examined here, initial TA and DIC are high but do not vary significantly and do not appear to account for changes in mineralogy between the experiments. On the other hand, the secondary mineralogy and the mineral morphology is strongly influenced by the dissolved [PO_{4tot}], Mg/Ca and CO_3/Ca, ratio.

2.4.4 High Mg/Ca experiments

XRD analyses of the solid samples recrystallized from the *high Mg/Ca experiments* indicate that the experiments routinely produced hydromagnesite as the dominant mineral with a typical mineral assemblage of hydromagnesite, aragonite, dolomite and apatite (dominantly chlorapatite

– Cl-Ap; [$Ca_{9.63}$ $Na_{0.40}$)5Cl(PO_4)$_3$]) (Figure 2. 4). The XRD diagrams (Figure 2. 4) reveal that the amorphous phase recrystallizes dominantly into hydromagnesite, which subsequently crystallizes into magnesite, dolomite and brucite (Mg-OH)$_2$ with a number of additional accessory mineral phases including aragonite, calcite, Ca-PO_4, apatite and halite (NaCl). The estimated [Mg] $\%_{XRD}$ for the most dominant mineral phase determined from obtained XRD d_{104} spacing values Mg content reaches 54 % Mg for the *high Mg/Ca experiments* (Mg/Ca = 9–17) (presented in Table S2.5), and up 95 %mol Mg for the bulk solid. The dominant PO_4 phase identified in the *high Mg/Ca experiments* is a chlorapatite rather than DCP.

2.4.5 Higher PO_4 experiments

XRD analyses of the solid samples recrystallized from the *higher PO_4 experiments* indicate that similar to *high Mg/Ca experiments,* the dominant mineralogy is hydromagnesite a with a typical mineral assemblage of hydromagnesite, aragonite, dolomite and apatite (dominantly chlorapatite – Cl-Ap; [$Ca_{9.63}$ $Na_{0.40}$)5Cl(PO_4)$_3$]) (Figure 2. 5). However the proportion of these minerals present changes with a decrease in aragonite and hydromagnesite and a shift to more crystalline (less hydrated) forms magnesite $MgCO_3$ apatite and dolomite (Table S2.1 semi-quantitative results). The SEM-HDBSD images (Figure 2. 5) and SEM-EDS chemical quantification reveal that the amorphous phase recrystallizes dominantly into hydromagnesite (with Ca and PO_4) which subsequently crystallizes into magnesite and dolomite with brucite (Mg-OH)$_2$ with additional phases of abundant apatite – which may be present in different forms; chlorapatite, hydroxyapatite and carbonate apatite. A number of additional accessory mineral phases including aragonite, calcite and halite (NaCl) are present.

The estimated [Mg] $\%_{XRD}$ for the most dominant mineral phase determined from obtained XRD d_{104} spacing values provide an average Mg = 48 % Mg for the *higher PO_4 experiments* (Mg/Ca = 5; [PO_4] = 14 m*M*) (presented in Table S2.5), and 79 %mol Mg for the bulk solid. This is very similar to the Mg content of the *low Mg/Ca experiments*. The dominant PO_4 phase identified in the *high Mg/Ca experiments* is a chlorapatite rather than DCP.

2.4.6 Solid sample interrogation and challenges

Because there is a polyphase mixture of minerals, disentangling the individual phases and minerals is challenging. Hydromagnesite appears to cover a broad range of chemical composition and morphological variations between the samples. Crystallographic databases would benefit from additional hydromagnesite data that accounts for incorporated C and possibly PO_4. Hydromagnesite peaks are clearly identified and comprise >50 % of most samples, but also strongly overshadow minor dolomite and magnesite peaks which can be identified in many of the spectra. Many of the samples also contain Ca-$Mg(CO_3)_2$ and $MgCO_3$ peaks and all samples contain very high magnesium content ≥) 50 mol% Mg based on *d*-104 spacing value of ≤ 2.90 Å. Furthermore, peaks were observed that did not match any specific mineral references exactly, however, the mineral identification software used indicated that the most similar minerals identified were apatite, monetite, Ca-PO_4 and Mg-PO_4 minerals, chlorapatite and brushite. This suggests that the peaks are linked to the presence of PO_4 minerals and/or possibly PO_4 bound within the carbonate lattice.

The FTIR spectra represent mixed Mg-CO_3 and Ca-Mg-CO_3 mineral phases in all samples (Figure 2. 3). Hydromagnesite and magnesite feature as the dominant mineral present in all of the samples. Hydromagnesite FTIR features are very well defined in all samples with the highest intensity recorded in *high Mg/Ca experiments.* Characteristic bands are displayed at 3649 cm^{-1} resulting from OH stretch that represents the non-hydrogen-bonded water molecule vibration. Broad crystallization water bands are displayed at 3510 and 3450 cm^{-1} with an additional band at 1654 cm^{-1} assigned to the water bending vibration of strongly hydrogen bonded water molecules. Hydromagnesite ν_3 CO_3^{2-} asymmetric stretching bands (1480, 1420, and 1120 cm^{-1}) and ν_2 CO_3^{2-} bending bands (885 and 857 cm^{-1}) are very strong. Small but well pronounced bands at 1110 ad 1120 cm^{-1} characterize hydromagnesite and/or poorly crystalline apatite. The presence of DCDP and/or magnesite is indicated by the band at 800 cm^{-1}. The presence of combination bands at 2535-2538 cm^{-1} results from magnesite and can be identified in all samples

and is strongest in samples *higher PO_4 experiments*. Furthermore, these samples also produce a broad band around 1090-1095cm^{-1} which is indicative of nesquehonite ($MgCO_3 \cdot 3H_2O$) or dolomite (Figure 2. 5).

Hydromagnesite and magnesite are present as sub-spherical 1-5 μm spheres that are prolific throughout the samples (Figure 2. 6). The hydromagnesite spheres are observed at various stages of recrystallization and are comprised of aggregates of nanocrystalline magnesite or hydrated $MgCO_3$ depending on the stage of recrystallization. Some hydromagnesite spheres contain nanocrystalline magnesite and dolomite together. In the well crystallized magnesite aggregates (Figure 2. 6A) and some of the poorly crystalline spheres, large (<1 μm) individual magnesite crystals or twinned magnesite crystals (Figure 2. 6A) are observed as well as large dolomite crystals that protrude out from the surface (Figure 2. 6A,C). Dolomite spheres with 'dumbbell' morphology were identified in many samples are observed at various stages of recrystallization. Surface SEM-EDS spectra of microcrystals within the dolomite dumbbells indicate near equal Mg and Ca $\%_{wt}$ (Figure 2. 6E). In addition, several apatite and PO_4 minerals are observed. These minerals are characterized by a variety of morphologies and are highly crystalline relative to the hydromagnesite phases.

Crystal morphology and structures can be easily altered by the addition of crystal growth inhibitors (Yang et al., 2013). The spherical morphologies, dumbbell morphologies and dendritic morphologies observed are consistent with inhibition mechanisms. For example changes in the crystal morphology can be caused by interaction of inhibitors and the active sites on the surface of the crystals, which changes the stereochemical orientation of $CaCO_3$ growth sites (Reddy and Hoch, 2001; Suharso et al., 2017), and sodium triphosphate inhibitors can produce amorphous spherulites (Yang et al., 2013).

The SEM-EDS corroborates the XRD and FTIR evidence for the presence of dolomite and magnesite. Poorly crystalline hydromagnesite, magnesite, dolomite along with very high Mg-calcite and calcite spheres at early stages of crystallization are also observed in the samples. Many

of these examples at a much earlier stage of crystallization contain higher P concentrations identified by SEM-EDS. A broken sphere composed of partially recrystallized AMC-hydromagnesite-magnesite provides evidence that some of the spheres are hollow.

The large magnesite and dolomite minerals that protrude from the surface of the nanocrystalline spheres exhibit unusual dendritic like features (Figure 2. 3) that appear to be growth inhibition on the crystal surface. These areas have a higher P concentration in SEM-EDS spectra (Figure 2. 6D,E), which may represent crystal growth inhibition from the attachment of PO_4 to crystal growth sites on magnesite and dolomite.

Dolomite FTIR characteristically has a calcite-type structure yet shows a shift of all bands to higher frequencies, and displays characteristic FTIR absorptions at 728-730, 2626 and 3020 cm^{-1} that are identified in all samples. The FTIR bands detected at 3020 cm^{-1} and 2626 cm^{-1} are combination frequencies, and the band at 730 cm^{-1} is assigned to the in-plane bending (ν_4) mode of CO_3^{2-} in the dolomite structure. Dolomite FTIR features at 2626 cm^{-1} and 730 cm^{-1} are present in all samples (Figure 2. 3;Figure 2. 4;Figure 2. 5) with some more prominent than others. The ν_2 CO_3^{2-} bending bands (880 and 850 cm^{-1}) are also present. The 2525 cm^{-1} broad combination frequency band was weak but identifiable in the samples and particularly samples 7.0, 8.2 and 8.6. As is the case with the XRD data, the samples with the strongest dolomite bands were produced from *high Mg/Ca experiments and in PO_4 experiments*. All samples appear to contain some dolomite that is present with varying degrees of crystallinity from a poorly crystalline or 'proto' dolomite to stoichiometric dolomite indicated by the presence of the (015) ordering peak in XRD diagrams.

Calcite displays characteristic FTIR absorptions at 713 cm^{-1} (in-plane bending at 713 cm^{-1}, ν_4 CO_3^{2-}) and ν_2 CO_3^{2-} out-of-plane bending bands (872 and 846 cm^{-1}) indicates Mg-calcite and is weak but present in all samples. Aragonite spectra are distinct from that of calcite as they show a characteristic double peak at 700 and 713 cm^{-1} (in-plane bending, ν_4 CO_3^{2-}) as well as peaks at 843 and 855 cm^{-1} (out-of-plane bending, ν_2 CO_3^{2-}), that can be identified in several samples

(Figure 2. 3;Figure 2. 4;Figure 2. 5). The carbonate symmetric and asymmetric stretching bands of aragonite are located at 1084 and 1484 cm^{-1} respectively. Aragonite double peaks at 713 and 700 cm^{-1} are identified in most samples and are less prominent but still distinguishable in *higher PO_4 experiments*. Bending peaks at 843-844 cm^{-1} and 854-855 $cm^{-1}$are weakly defined in some but not all samples. A broader band at 1440–1570 cm^{-1} may indicate replacement of Ca^{2+} by Mg^{2+} in aragonite structures. Samples from *higher PO_4 experiments and high Mg/Ca experiments* contain only very weak aragonite bands.

Phosphate (PO_4^{3-} group) is identified by the bands at 600 cm^{-1} and 1150 cm^{-1} on the FTIR spectra in all samples. PO_4^{3-} group displays characteristic FTIR bands at 560 and ν_4 600 cm^{-1} (asymmetric bending mode, ν_4 PO_4^{3-}) and 960 (ν_1 symmetric stretching), ν_3 asymmetric stretching at 1000–1160 cm^{-1}. The bands at 1110 and 1120 may indicate HPO_4^{2-} or poorly crystalline apatite but also may indicate CO_3^{2-} asymmetric stretching bands of hydromagnesite. The adsorbed water band is relatively wide, from 3600 to 2600 cm^{-1}, with a peak at 3570 cm^{-1} a weaker peak is formed at 630 cm^{-1}. One of the limitations in mineral identification using FTIR is that several PO_4 and Mg-Ca-carbonate bands in FTIR overlap. For example CO_3^{2-} bands between 1080–1090 cm^{-1} linked to $MgCO_3$ can also be explained as ν_3 PO_4 bands of apatite and CO_3^{2-} bands of 875, 880 linked to $MgCO_3$, $MgCa(CO_3)_2$ and Mg-calcite can also be explained by HPO_4^{2-}.

The solutions with higher phosphate concentration and samples with high CO_3^{2-}/Ca ratios and high Mg/Ca ratios (13-20) appeared to precipitate less aragonite but produce more prominent, poorly crystalline dolomite peaks. Mg/Ca ratio appears to effect the resultant mineralogy, with all samples appearing to produce hydromagnesite, magnesite and minor amounts of aragonite. The lower Mg/Ca ratios have stronger dolomite and aragonite bands. The bump in FTIR at 729/730 cm^{-1} is a unique identifier of dolomite, which is best recorded in *higher PO_4 experiments*. Phosphate concentration influences the resultant polymorph and higher concentrations lead to an increase in apatite minerals.

The SEM-HDBSD photomicrographs (Figure 2. 3Figure 2. 4Figure 2. 5Figure 2. 6) represent the solid precipitates formed from inorganic homogeneous nucleation and recrystallization experiments. Figure 2. 6 portrays some of these microcrystalline textures in higher resolution. The dominant mineral is hydromagnesite followed by apatite, magnesite, dolomite and aragonite. In some samples $CaCO_3$ was observed with varying content of Mg and PO_4 however, it was difficult to identify the exact mineralogy (i.e., calcite, aragonite, Mg-calcite or another $CaCO_3$ mineral) from the SEM-HDBSD images. No observed influence on the resultant mineralogy could be linked to increased ionic strength apart from possibly the presence of the evaporite mineral northupite ($Na_3Mg(CO_3)_2Cl$) that was identified according to XRD analyses and observed by SEM analyses.

Crystals inferred to be apatite (Figure 2. 6B) are present as coarse aggregates that exhibit strong crystallinity. The hydroxyapatite crystals appear to be hexagonal bipyramid shapes that integrate together and are often present with a high proportion of crystal twinning. Minerals resembling the uncommon Mg-PO_4 mineral newberyite and struvite as well as Ca-PO_4 minerals whitlockite, monetite and brushite appear to be present in some samples based on crystal morphology and XRD; however, the mineralogy cannot be confirmed by SEM analysis alone. The SEM-EDS on a selection of the spheres and dumbbells demonstrates hydrous to anhydrous aggregates with ratios of Mg > Ca indicative of $MgCO_3$ or Mg = Ca indicative of dolomite or very high Mg-calcite. Further analyses demonstrate a variety of morphologies including tabular and bladed crystals likely of calcite growing from smaller crystalline aggregates. Bipyramidal calcite is also observed in some samples. There are also some curved shaped Mg-calcite crystals that contain P. Amorphous NaCl minerals are also identified and some contain magnesite crystals embedded on the surface. Halite with a cubic morphology is also identified in some samples. SEM observations indicate that many of the minerals mentioned appear to be near their equilibrium crystalline morphology and there is a surprisingly high proportion of twinned carbonate minerals in these samples.

2.4.7 Aqueous geochemical system

Over the experimental period of 64 days, solution samples were extracted using a needle-syringe through a septum cap and analyzed using ICP-AES measurements (Table S2.2–3, supplementary material). The results indicate that immediately upon nucleation, all [Ca^{2+}] was expended and remained constant at approximately 0 m*M* throughout the experiment. Significant [Mg^{2+}] was also removed from solution immediately but not entirely, as minor concentrations remained in solution. However, it is clearly noticeable that over time, [Mg^{2+}] in solution decreased, indicating slower incorporation of Mg^{2+} ions into the carbonate mineral or recrystallization/ reorganization of the mineral(s). Alternatively, this may indicate the precipitation of Mg-phosphate phases. PO_4 was also removed from the solution immediately upon nucleation by approximately 50%, leaving relatively high [PO_4] in solution. [PO_4] exhibited greater variability throughout the course of the experiment, typically decreasing in solution slightly and then increasing. This may represent adsorption and desorption, or recrystallization of an amorphous phase to a more stable apatite or calcium/magnesium phosphate phase or variable incorporation and release within the carbonate lattice of carbonate minerals such as ACMC and hydromagnesite during recrystallization. However, as P is harder to detect through many analytical techniques including ICP-AES analyses, this may also represent a measurement variability. The pH measurements from the initial pH measurement of 10 were followed by measurements taken throughout the course of the experiment that decreased over time to a pH of around 9.5. This indicates nucleation or crystallization of the nucleated phase within the solutions as CO_3^{2-} ions are removed from the solution.

2.4.8 Bulk solid Mg content

The Mg content ($[Mg]_{ACMC}$) was calculated for the homogenous nucleation experiments according to the equation (S2. Eq.X25) described where [Mg] and $[Ca]_{sol}$ are the measured concentrations of Ca and Mg of the solids from the ICP-AES results. The results and description of the bulk solid

sample characterization are presented in Table. S2.2 and the results for the aqueous solution concentrations are presented in Table S3.3. The [Mg mol%] of the resultant bulk solid ranged from 54.2 – 95.0% (however, this resultant phase is a mixture of phases including crystalline hydromagnesite). The estimated [Mg] $\%_{XRD}$ for the most dominant mineral phase determined from obtained is presented in Table S2.7.

2.4.9 ACMC mineral pathway and solubility product calculations

For the full suite of relevant calculations and descriptions of the carbonate chemical system and ACMC precipitation pathway used in for experiments, please see supplementary material S2 3. Although more common for ACC (Brečević and Nielsen, 1989), thermodynamic datasets for ACMC are not widely available. However, constraints on solubility data of ACMC (Purgstaller et al., 2016, 2019, 2021) and AMC (Chang et al., 2021) have recently been published. The formation reaction for Mg-calcite and ACMC can be used according to Purgstaller et al., (2016) (S2 3.4, Eq. X17). In order to yield thermodynamic data from our experiments and assess the effect of changes to the chemical conditions of the solutions on the solubility (K) of ACMC, we calculated the activities of Ca^{2+}, Mg^{2+} and CO_3^{2-} ions in the initial solution and the bulk ACMC stoichiometry from the resultant solid (Mg and Ca Mol $\%_{ACMC}$), which were used to calculate ion activity product (IAP) and the solubility product (K) values for ACMC (K_{ACMC}; see S2 3).

Based on our nucleation experimental conditions of ~50 °C, we used K values published by Purgstaller et al., (2021) for ACMC nucleation at 60 °C where m = 0.01632 and y0 = -6.910. This yielded Log(K)ACMC values of $Log(K)_{ACMC}$ = -5.36 to -6.05. The less negative solubility product values correspond to higher Mg contents, which were observed in our samples. The ACMC precursor experiments yielded Log(K)ACMC values of $Log(K)_{ACMC}$ = -6.09. Although these values are in accordance with values of ACMC at 60 °C with $Log(K)_{ACMC}$ = -6.13 (Purgstaller et al., 2021), the values are indeed closer to the values for Mg-rich ACMC, where

Mg-rich solubility product Log(K_{ACMC}) = -4.54 and Ca-rich solubility product Log(K_{CMC}) = -6.28 (Purgstaller et al., (2019). These values also correspond closer to AMC values of Log(K) = -5.201 (Chang et al., 2021) than values of ACC at 60 °C of Log$(K)_{ACC}$ = -6.91 (Brečević and Nielsen, 1989) and Log$(K)_{ACC}$ = -7.510 (Gebauer et al., 2008). For reference, the solubility product for calcite in seawater at 25°C is Log$(K)_{calcite}$ = -6.3693 (based on concentration (Mucci, 1983).

Estimations of the apparent ion activity product (IAP) resulted in values obtained for Log(IAP_{AMC}) = -2.72 to -3.39 in homogeneous nucleation experiments and Log(IAP_{AMC}) = -2.63 to -4.15 in ACMC precursor experiment solutions. Using the calculated ion activity product (IAP_{ACMC}: S2 3 Eq. X28) and the apparent mineral solubility product (K_{ACMC}: S2 3 Eq. X26) of the experimental solution we estimated the apparent saturation state (Ω) with respect to ACMC (Ω_{ACMC}) (S2 3 Eq. X29). This yielded Ω_{ACMC} = 176 to 1512 (see Table S2.5) and are shown in Table 2.1 with the chemical conditions of the experiments. The logarithm of the Ω_{ACMC} values provides the Saturation Index (SI), which produced values of 2.0 to 3.18 in homogeneous nucleation experiments and 1.9 to 3.5 in ACMC precursor experiment solutions. In a similar manor, values obtained for Ω_{AMC} = 305 to 65 in homogeneous nucleation experiments and Ω_{AMC} = 379 to 6 in ACMC precursor experiment solutions based on K values obtained from Chang et al., (2021).

2.4.10 Homogenous nucleation influence of PO_4 and Mg/Ca

The estimated [Mg] $\%_{XRD}$ for the most dominant mineral phase determined from obtained XRD d_{104} spacing values indicate that the average Mg/Ca of the resultant solid is directly related to the Mg/Ca of the initial solution under the same pH and CO_3^{2-}–alkalinity regime. Under these highly alkaline conditions, estimated Mg content can be summarized by $[Mg]/[Ca]_{initial} \geq 5$ results in $[Mg]_{solid} \geq 48$ % $[Mg]/[Ca]_{initial} \leq 5$ results in $[Mg]_{solid} \leq 48$ %.

On the other hand, increasing the [PO_4] (*higher PO_4 experiments*) results in higher degree of crystallinity (structural ordering of a solid by regular atomic arrangement) of the minerals;

magnesite, dolomite and apatite. The solid sample characterization analyses show that hydromagnesite and magnesite are the dominant mineral produced across a broad range of conditions around pH 10. Under the conditions examined here, initial TA and DIC are high but do not vary significantly and do not appear to account for changes in mineralogy or the degree of crystallinity between the experiments.

Furthermore, the secondary mineralogy and the mineral morphology is strongly influenced by the dissolved [PO_{4tot}], Mg/Ca and CO_3/Ca, ratio. The solutions that produced the highest proportion of magnesite and dolomite and the greatest degree of crystallinity were the *higher PO_4* experiments that contained [PO_{4tot}] of 14 m*M*/L (Figure 2. 5). These solutions were further characterized by Mg/Ca of 5 and CO_3/Ca of 12 at pH 10 in 50 ºC temperatures. As these experiments were conducted in a 'closed system' the effects of atmospheric ρCO_2 exchange were eliminated and had no impact on the solution chemistry or resultant mineralogy. The experiments also show that dissolved PO_4 strongly controls the resulting Mg-Ca-CO_3 polymorph precipitated from solution. This indicates that presence of PO_4 and highly alkaline conditions that together likely sustain excessive supersaturation and may overcome Mg related barriers.

2.5 Discussion

2.5.1 Homogenous nucleation experiments

Kinetic barriers that inhibit low-temperature magnesite and dolomite precipitation dominantly result from an energy barrier related to Mg^{2+} ions. The hydration of these ions influences the ionic radii; and therefore, the 'hydrated radius'. Smaller ions with a higher charge like Mg tend to be more hydrated and have larger hydrated radii due to a more intense electric field because the ion holds water molecules tightly. [Mg^{2+}] have a radius of 0.65–0.72 Å, which increases to 3.95 Å when hydrated and is the largest hydrated radius of any common cation (Nielsen 1984; Kehres and Maguire, 2002). Furthermore, this increases the hydration-free energy value to -1505 kJ/mol (Kiriukhin, 2002).

These hydration effects play a significant role on Mg-carbonates due to the sluggish reaction kinetics between the hydrated ion and the solution. This inhibits the formation of magnesite (Sayles and Fyfe 1973; Pokrovsky and Schott, 2002; Duckworth and Martin, 2004) and impedes the incorporation of Mg^{2+} into the dolomite crystal lattice (1973 Lippmann; Brady et al., 1996). The dehydration of Mg^{2+} requires a very high activation energy to overcome an activation energy barrier (Lippmann, 1973; Land, 1998; Warren, 2000; Warren, 2019), and despite much research on the topic, to date there has been insufficient evidence to conclusively explain what this kinetic mediator might be. An alternative hypothesis suggests that a fundamental barrier, other than Mg^{2+} hydration exists preventing Mg^{2+} and CO_3^{2-} ions from forming long-range ordered structures (Xu et al., 2013) consisting of regular patterns of arrangement of particles or atoms that repeat periodically. This barrier is proposed to result from the lattice limitation on the spatial configuration of CO_3 groups in magnesite crystals where the CO_3 groups are interlocked between the Mg–O octahedral, which may be rather difficult to produce at ambient conditions unless the Mg-O octahedral are compressed allowing movement of the CO_3 group (Xu et al., 2013). The energy barrier for forming an ordered Mg–CO_3 arrangement may be too high to overcome at low-temperature/pressure conditions because of the entropic loss associated with intensified restrictions on the CO_3 groups in magnesite (Xu et al., 2013). However, we propose that this energy barrier may be overcome due to the inhibition and resulting supersaturation linked to the strong inhibitory effects of PO_4. Although this may not be limited to PO_4, it is clear that PO_4 has strong inhibitory effects relative to other inhibiting compounds at only micromole/kg (μM) concentrations (i.e., Reddy, 1977; Dove and Hochella, 1992; Tadier et al., 2017).

It has been suggested that metastable hydrous magnesium carbonates will likely mature to thermodynamically stable magnesite over time (Zhang et al., 2000). Alternatively, research indicates that the transformation rate of hydromagnesite to magnesite increases with an increase in ionic strength and a decrease in [Mg] (Zhang et al., 2000). Two mechanisms for this transformation have previously been proposed: Firstly from brines with low [Mg], where the dehydration of hydromagnesite and concomitant formation of magnesite and brucite ($Mg[OH]_2$)

minerals are favoured (Zhang et al., 2000) and secondly, in brines with high [Mg], where a hydromagnesite dissolution – magnesite precipitation process is favoured (Zhang et al., 2000). However, in practice and in natural systems, these mechanisms are not well understood.

Our results indicate the formation of magnesite is possible through the influence of high CO_3^{2-} alkalinity conditions and the presence of minor concentrations of PO_4. Our results indicate that this firstly leads to the spontaneous homogenous nucleation of very-high Mg amorphous phases ACMC, AMC and ACP from supersaturated solution. The high pH and [PO_{4tot}] of 7 m*M* act as a kinetic inhibitors to aragonite and calcite. The inhibition may be due to the suppression of aragonite and/or calcite spontaneous nucleation of through early adsorption of PO_4 onto nucleated particles, which blocks active growth sites (i.e., Reddy, 1977; Burton and Walter, 1990; Tadier et al., 2017). The ACMC appears to consistently precipitate as spheres which is consistent with high saturation conditions (i.e., Kelleher and Redfern, 2002). Amorphous phase ACMC is stabilized by [Mg^{2+}] which makes it less reactive (Rodriguez-Blanco et al., 2014; Jensen et al., 2020). Because the initially precipitated ACMC samples in homogenous nucleation experiments contained approximately ≥60 Mg %, and because ACMC is much less reactive than pure ACC, this likely led to the presence of ACMC for prolonged time periods relative to ACC.

The ACMC recrystallized into hydromagnesite and subsequently magnesite and dolomite across a broad range of highly alkaline chemical conditions at high pH and [PO_4] concentrations of 7 m*M*/L and 14 m*M*/L. under the conditions examined here, the formation of high-Mg ACMC and hydromagnesite is not dominantly linked to Mg/Ca or [Mg^{2+}] but linked to high CO_3^{2-} alkalinity conditions and the presence of PO_4.. Together this leads to the nucleation of very high-Mg ACMC and likely sustains excessive supersaturation states (Ω_{ACMC}) and provides a kinetic pathway for the dehydration of Mg and crystallize into magnesite. This is a fundamentally important observation that outlines a pathway to overcome major hydrated Mg^{2+} kinetic barriers or Mg-O CO_3 lattice restriction (Xu et al., 2013).

Our experiments indicate that the crystallization into magnesite was most efficient in *higher PO_4 experiments* indicating the important role that phosphate plays in aqueous carbonate systems.

By outlining the chemical conditions that lead to the formation of primary magnesite and dolomite and provide constraints on the chemistry we can begin to understand how high activation energies are overcome and how the formation conditions may have been met in natural systems. Recent research provides evidence that temperature (Purgstaller et al., 2021) may play a role in the formation of very high magnesium calcite, and based on time-lapse Raman spectroscopic monitoring, a formation pathway for dolomite has been characterized via ACMC>monohydrocalcite>Nesquehonite>dolomite pathway (Montez-Hernandez et al., 2020).

Variations in spherulitic morphologies and growth patterns can be observed by the inclusion of metastable phases with disordered orientation (Gránásy et al., 2005; 2006). This may explain the spherulitic morphologies of amorphous/disordered phases observed in our experiments that mature into hydromagnesite and magnesite, with subsequent surface growth of magnesite and dolomite to larger sized crystals (Gránásy et al., 2005; 2006). We see a wide range of morphologies within Mg-Ca-CO_3 and hydromagnesite-$MgCO_3$ spheres. Some of these spheres are composed of nanocrystalline aggregates and are associated with sheets of hydromagnesite, which may be linked to changes in pH and the degree of crystallization (i.e., Zhang et al., 2010). In addition, high pH conditions can cause an increase in ionic substitutions. Therefore, combining high pH and high salinity conditions together may account for some of the observed variability in the XRD and FTIR spectroscopy.

Changes in solution [Mg^{2+}] and [PO_4^{3-}] observed from ICP-AES throughout the duration of the experiment are likely a result of ACMC/AMC dissolution-precipitation via Ostwald ripening processes at high Ω_{ACMC} values (i.e. Kile and Eberl, 2003). Under the supersaturated experimental conditions, following widespread nucleation, further homogeneous nucleation may have declined and the resulting conditions may have led to the growth of existing crystals. This

may explain SEM observations that show spherical mineral aggregates that contain large crystals protruding out from their surface. Many of the large crystals observed in SEM-HDBSD images appear to be near the crystal equilibrium morphology of the mineral and there is a surprisingly high proportion of twinned carbonate minerals in these samples. Twinning in crystal growth typically occurs as a result of changes in temperature, pressure or stress/strain resulting in growth twins, transformation twins or deformation twins (Nelson, 2019).

2.5.2 ACMC geological implications

The conditions examined here contain high alkalinity and PO_4 conditions that are commonly identified in modern lake environments. The production of uncommon high Mg-minerals (i.e., hydromagnesite, dolomite, magnesite and Mg-PO_4 minerals) at low temperature (50 ºC) demonstrate that at the very least, these minerals can form in environmental settings such as sedimentary pore waters and in highly alkaline lakes where enhanced [PO_4] and salinity contribute to the formation of Mg-rich carbonates and subsequently magnesite and dolomite. These conditions may have been reached temporarily over short time periods or may have prevailed for prolonged periods at specific times in the geological past, possibly present day and may be exacerbated in lacustrine settings that experience cycles of wet and dry conditions.

Recent primary dolomite and hydromagnesite precipitates have been identified in Milne Lake, South East Coorong – near Salt Creek, Australia (Miser et al., 1987) and in North Stromatolite Lake, Pellet Lake, Dolomite Lake and Halite Lake (Warren et al., 2019). This is an important observation for our research findings because Meningie Lake, Lake Coorong South and South Salt Creek and nearby have recorded [PO_{4tot}] up to 7, 8 and 16 m*M* respectively (Stone et al., 2016). Although the dolomite sediments are of Holocene age, and the water samples are taken from modern lake water (and therefore it is possible that [PO_{4tot}] levels may have been influenced by anthropogenic factors) it does suggests that there may have been high [PO_{4tot}] in these lakes when primary dolomite and hydromagnesite were produced. The high [PO_{4tot}] is most likely

present because the lakes drain water from Meso- and Neoproterozoic basins that contain abundant phosphorite deposits linked to the Adelaide geosyncline (Howard et al., 1986). This indicates that in lakes that produce primary dolomite and magnesite, [PO_{4tot}] levels likely reach those examined in our experiments. This provides a compelling geological test for our hypotheses and a possible explanation for the present of these enigmatic mineral assemblages in these settings.

Much research on phosphate mineral precipitation is informed by biochemical and biomaterial fields. However, these studies are still important for understanding the precipitation pathways. Typically, the initial nucleation of amorphous calcium phosphate subsequently transforms to octacalcium phosphate (OCP) and then possibly dicalcium phosphate dehydrate (DCDP) before crystallizing into apatite (Johnsson and Nancollas, 1992). This pathway is observed in natural seawater where apatite forms via OCP precursors (i.e., Baltic Sea – brackish [Gunnars et al., 2004]). However, Mg stabilizes ACP and inhibits the transformation of ACP>HAp or phosphate mineral DCPD (i.e., brushite) and to apatite (i.e., Boskey and Posner, 1974) at ratios as low as [Mg]/[Ca] > 0.2. Although geochemical PO_4-enrichment may be explained in highly-alkaline-saline environments by Ca^{2+} ion removal through $CaCO_3$ precipitation (i.e., Toner and Catling, 2020) and further influenced by decreased biological consumption rates relative to influx rates due to high –pH nitrogen limitation (i.e., Herbst, 1998) and salinity (i.e., Chad et al., 2013), these processes may become complicated in settings influenced by Mg. This is because the precipitation of amorphous $CaCO_3$ phases (ACC) and in the presence of high PO_4 concentrations – amorphous calcium carbonate phosphate (ACP) are promoted in many alkaline lakes due to the high saturation states. Both ACC and ACP phases are stabilized in the presence of Mg^{2+} ions that decreases the solubility (Boskey and Posner, 1974; Blue and Dove, 2017) and inhibits the precipitation of apatite.

This may influence the accessibility of bioavailable PO_4 and may also promote the formation of carbonate associated apatite (CAP) through recrystallization because high pH leads

to an increase in ionic substitutions and may instead lead to the precipitation of Mg-PO_4 minerals such as whitlockite and struvite (i.e., Hilger et al., 2020). However, because Mg stabilizes both ACC (i.e., Blue et al., 2017) and ACP (i.e., Boskey and Posner, 1974; Coombes and Rey, 2010), it decreases the solubility. This inhibits the transformation of ACC to calcite and aragonite, and ACP to HAp. Yet Mg (and CO_3) ionic substitution in apatite actually destabilizes the crystal lattice and decrease the solubility. Therefore, understanding the kinetics of these pathways requires further research to constrain the Mg-Ca-PO_4-CO_3 relationship. The high sensitivity and impact of Mg on these systems appears to influence a number of phases and pathways that may exist for prolonged periods in a metastable phase and may influence geochemical cycles.

Research also indicates that above pH 8.0, Ca-P species ($CaPO_4Ca^0$) form on the surface of calcite, followed by Ca-P phases (ACP, DCP, and HAP) and $MgHPO_4Ca^+$ adsorption complexes form on dolomite surfaces at Mg sites before growing into newberyite ($MgHPO_4$) by incorporating Ca-P and/or Mg-P (Xu et al., 2014). Furthermore, The Mg content in dolomite favours the rapid growth of DCP which indicates that dolomite is a more efficient phosphorus sink than calcite in calcareous environments (Xu et al., 2014) and ACMC is a highly effective adsorbent of phosphate from aqueous solutions as a result of its unique structure and high specific surface area (Xu et al., 2014). Together, these properties may offer an explanation into high [PO_4] observed in high Mg carbonate sediments such as in Precambrian carbonate sediments and modern alkaline lake sediments.

Modern day lacustrine environments can accumulate PO_4 to > 1 m*M* concentrations in alkaline lake settings linked to Ca^{2+} ion removal in the water column through $CaCO_3$ precipitation that restricts the precipitation of apatite and leads to excess PO_4 accumulation (Toner and Catling, 2020). In these settings $CaCO_3$ nucleation or precipitation rates are high as a result of high supersaturation states which leads to further accumulation of PO_4. This can be explained in high-alkalinity conditions where by a relationship with Ca^{2+} ion removal in the water column through $CaCO_3$ precipitation restricts the precipitation of apatite, because apatite precipitation requires

both high PO_4 concentrations and Ca^{2+} ions. The prevention of apatite precipitation subsequently leads to excess PO_4 accumulation in lake waters before hitting apatite saturation thresholds (Gulbrandsen, 1969; Sass, 1981; Toner and Catling, 2020).

In these high alkalinity lake waters, the accumulation of PO_4 and alkalinity leads to $CaCO_3$ (aragonite and calcite) inhibition by PO_4 and a build-up of excessive supersaturation states. This promotes prolific amorphous Ca-Mg-CO_3 nucleation as spherules. This would in turn lead to the maintenance of high supersaturation sustained by PO_4 kinetic inhibition and the prevention of further nucleation leading to a change from nucleation to growth dominated sedimentation processes. Subsequently, the amorphous phases crystallize to more ordered crystal phases dolomite and magnesite via hydromagnesite. Hydromagnesite can contain significant concentrations of calcium that may be micro inclusions resulting from fast nucleation rates and high saturation states, which may crystallize into dolomite. This pathway may explain occurrences of low-temperature, primary dolomite within muddy sediments in modern alkaline lakes that record excessive PO_4 concentrations such as Searles Lake, California (Smith and Haines, 1964) and the Coorong Lakes of Australia (Alderman 1959; Warren, 2019).

Furthermore, these conditions may shed light on early aqueous environments that existed on Mars where magnesite ($MgCO_3$), huntite ($CaMg_3(CO_3)_4$) and hydromagnesite minerals are identified in sedimentary environments based on spectroscopy (i.e., Palomba et al., 2009; Horgan et al., 2020) and remote sensing data (i.e., Bultel et al., 2019). Mars is also suggested to contain excessive [PO_4] linked to water-rock interaction, which models indicate could be between 10–45 times higher than those on Earth (i.e., Dreibus and Wänke,1985; Adcock et al., 2013).

2.5.3 ACMC precursor experiments

The ACMC precursor experiments indicate that the formation VHMC with minor dolomite is possible in highly alkaline conditions influenced by PO_4. This suggests that similar

conditions may lead to primary dolomite formation, which may subsequently undergo increased structural ordering over time or under slightly different chemical conditions.

This formation pathway may also begin to explain the presence of distinctive Mg-carbonate and Mg-Ca-carbonate sedimentary successions dominant in Precambrian and Palaeozoic rocks. For example, the primary dolomite Neoproterozoic successions in which sediments are characterized by finely crystalline dolomicrite (carbonate mud) (Tucker, 1982; Grotzinger, 1989; Grotzinger and Knoll, 1995; Burns et al., 2000; Hood et al., 2011; Hood and Wallace, 2012). Recent research indicates that these sediments may also contain evidence for enhanced P cycling in the water column due to minimal organic matter burial and remineralization processes (i.e., Lenton and Daines). Enhanced PO_4 coupled with high carbonate alkalinity provides an interesting set of chemical parameters that together overcome the hydration barrier of Mg in Mg-Ca-carbonate precipitation that has previously remained enigmatic.

2.6 Conclusions

Although dolomite is thermodynamically the most stable form of Mg-Ca-carbonate, the formation of dolomite at Earth surface temperatures is enigmatic. Alternatively, magnesite and Mg-bearing carbonates are highly reactive compared to Ca- and Ca-Mg-carbonate minerals, and are therefore relatively unstable. This indicates that Mg-bearing carbonates should form readily, yet their formation is inhibited by sluggish kinetics due to the hydration barrier of Mg. These two pathways present two unique but somewhat related challenges for understanding the formation and preservation of these minerals over geological timescales.

The results produced in this experimental study reveal insight into the formation of very high-Mg calcite, magnesite, dolomite, and PO_4 minerals under early-diagenetic conditions at 50˚ C with pH = 10. We reveal that the recrystallization of ACMC from precursors under these conditions typically resulted in mixtures of very high Mg-calcite (48 mol% Mg) with minor aragonite and dolomite.

The presence of kinetic inhibitor PO_4 and high CO_3-alkalinity in homogenous nucleation solutions led to the precipitation of AMC and ACMC as well as likely amorphous calcium phosphate phases. This crystallizes into hydromagnesite as the abundant and dominant phase, which subsequently crystallizes into magnesite and dolomite minerals that remain stable. This offers a non-classical explanation for the presence of enigmatic, high-Mg carbonate minerals heavily influenced by the initial solution composition. These chemical conditions can be met in highly alkaline, supersaturated waters that are influenced by PO_4 and Mg.

This may be explained by high pH settings that lead to speciation of dissolved inorganic carbon (DIC) in solution shifting the dominant species from HCO_3- to CO_3^- (Figure 1.2). In addition, supersaturation is enhanced by high CO_3-alkalinity in the presence of kinetic inhibitor PO_4 that prevents the production of calcite and aragonite minerals by increasing nucleation thresholds. Together, these processes lead to the production of ACMC with very-high Mg content ≥ 50 % and leads to relatively fast recrystallization into crystalline phases. The rate of crystallization is increased with increased [PO_4].

Our results indicate that under high carbonate alkalinity conditions, with pH 10 and PO_4 = 7 m*M,* increased Mg/Ca ratios result in increased Mg/Ca of the resultant mineral phase (*low and high Mg/Ca experiments*). Increasing the [PO_4] (*higher PO_4 experiments*) results in higher degree of crystallinity of the mineral – notably magnesite, but also minor ordered dolomite minerals and apatite. Increased salinity and [PO_4] appears to result in chlorapatite rather than DCP minerals.

This investigation outlines two important pathways that form in high carbonate alkalinity and pH conditions under Earth surface conditions, with supersaturation enhanced by PO_4 inhibition of calcite and aragonite minerals:

1) A pathway to magnesite crystallization prompted by the production of *very* high-Mg ACMC and AMC. These conditions overcome crystallization inhibition related to Mg^{2+} hydration barriers.

2) A pathway to very high-Mg calcite-dolomite crystallization prompted by the production and subsequent recrystallization of high-Mg ACMC.

Furthermore, the thermodynamic data collected and calculated from the experimental datasets provide solubility product estimates for high Mg-ACMC and very high Mg-ACMC that can be used to inform future research. This provides fundamentally important information in understanding the formation of magnesite that can be met in alkaline lake settings where PO_4 accumulations can become significantly enriched. This pathway may offer insight into ancient carbonate factory and its links to major geochemical cycles. Furthermore, these conditions may shed light on early aqueous environments that existed on Mars where magnesite dominates carbonate deposits and excessive PO_4 concentrations are linked to mafic water-rock interaction (i.e., Adcock et al., 2013).

Supplementary material

Supplementary material is located at the end of the document in the Supplementary Materials – S2.

Chapter 3: Non-skeletal $CaCO_3$ precipitation from Proterozoic seawater

3.1 Linking Chapter 2 and Chapter 3

Having established a better understanding of the constraints of alternative Ca-Mg-carbonate mineral formation pathways through amorphous precursors in Chapter 2, we set out to test the hypothesis that carbonate mineral formation pathways through ACMC precursors may have been involved in producing the high Mg Ca-carbonate minerals that are widespread in the mid-Proterozoic to the Neoproterozoic, prior to carbonate biomineralization. We investigated $CaCO_3$

precipitation from synthetic Proterozoic seawater using a constant composition experimental design that results in homogeneous ACMC nucleation subsequent crystallization to Mg-calcite and monohydrocalcite.

3.2 Summary

Primary and early diagenetic fabrics preserved in late Proterozoic marine carbonates have long been interpreted as a reflection of elevated $CaCO_3$ supersaturation (Ω_{Cal}). The maintenance of $CaCO_3$ supersaturation spanning geological timescales requires the inhibition or modification of $CaCO_3$ precipitation rates and pathways. Proterozoic geochemical data, models, and microfossil mineralogy indicate that concentrations of dissolved PO_4, a known inhibitor of $CaCO_3$ precipitation, were subject to substantial fluctuations affecting availability, in response to secular changes in the global phosphorous cycle; however, the impact of PO_4 on marine abiotic $CaCO_3$ precipitation is poorly constrained. In an effort to constrain $CaCO_3$ formation pathways influenced by PO_4, this chapter outlines the methodology of a suite of $CaCO_3$ nucleation experiments in synthetic late Proterozoic seawater. The data produced include solid analyses of samples using FT-IR, in-situ Raman, XRD and SEM-EDS as well as dissolved solid sample and solution ICP-MS analyses. The results indicate that dissolved PO_4 inhibits the nucleation of crystalline aragonite and calcite and permits the formation of an amorphous Ca-Mg carbonate (ACMC) precursor phase, which rapidly undergoes recrystallization to monohydrocalcite and/or calcite incorporating a range of Mg concentrations. This pathway may be significant in providing an explanation for the sedimentological, petrographic, and geochemical characteristics of the abundant but enigmatic synsedimentary calcite microspar cement that is widely distributed in Precambrian carbonates. Furthermore, this pathway may provide a mechanistic framework for how kinetic inhibitors may have fundamentally altered the dynamics of shallow water $CaCO_3$ precipitation and marine carbonate chemistry throughout the Proterozoic Eon, which in turn may have potentially influenced the long-term carbon cycle.

Experimental constraints on nonskeletal $CaCO_3$ precipitation from Proterozoic seawater

Sascha Roest-Ellis[1], Justin V. Strauss[2] and Nicholas J. Tosca[1*]

[1] Department of Earth Sciences, University of Oxford, South Parks Road, Oxford OX1 3AN, UK

[2] Department of Earth Sciences, Dartmouth College, Hanover, New Hampshire 03755, USA

*Current address: Department of Earth Sciences, University of Cambridge, Downing Street, Cambridge CB2 3EQ, UK.

[1]Supplemental Material. Experimental method with figures, solution compositions, and solid sample characterization. Please visit https://doi .org/10.1130/ GEOL.S.13377239 to access the supplemental material, and contact editing@geosociety.org with any questions. Manuscript received 18 June 2020 Revised manuscript received 8 October 2020 Manuscript accepted 15 November 2020.

CITATION: Roest-Ellis, S., Strauss, J.V., and Tosca, N.J., 2021, Experimental constraints on nonskeletal CaCO3 precipitation from Proterozoic seawater: Geology, v. 49, p. Geological Society of America | GEOLOGY | Volume XX | Number XX | www.gsapubs.org 1
https://doi.org/10.1130/G48044.1

3.3 Abstract

Precambrian carbonates record secular variations in the style of $CaCO_3$ nucleation and growth, yet the geochemical conditions recorded by some enigmatic textures remain poorly quantified. Here, we performed $CaCO_3$ nucleation experiments in synthetic seawater in order to constrain the mineralization pathways of synsedimentary calcite microspar cement, a prolific component of Proterozoic carbonates. We found that dissolved PO_4 above ~12 μmol/L (μ*M*) inhibits the nucleation of aragonite and calcite and permits the formation of an amorphous Ca-Mg carbonate (ACMC) precursor once $CaCO_3$ supersaturation (Ω_{Cal}) is ≥ 45. Depending on seawater Mg/Ca, ACMC then rapidly recrystallizes to monohydrocalcite and/or calcite. This precipitation mechanism is consistent with sedimentological, petrographic, and geochemical characteristics of

Proterozoic synsedimentary calcite microspar cement, and it suggests that kinetic interactions among common seawater ions may open non-traditional $CaCO_3$ mineralization pathways and sustain high $CaCO_3$ supersaturation.

3.4 Introduction

Before the advent of skeletal biomineralization, $CaCO_3$ production is thought to have been strongly influenced by inorganic processes. For example, distinctive sedimentary and early diagenetic fabrics documented in Precambrian rocks record secular variations in marine carbonate chemistry (Grotzinger and James, 2000); however, the specific chemical controls on abiotic $CaCO_3$ production are poorly constrained.

A particularly enigmatic product in this regard is synsedimentary calcite microspar cement, a widespread and abundant primary pore-filling component of Mesoproterozoic to Neoproterozoic (Tonian) carbonates (Figure 3. 1; James et al., 1998). This cement comprises mosaics of equant 5–15 μm calcite crystals that share identical cathodoluminescence characteristics and preserve evidence for initial spheroidal particle precipitation with polygonal overgrowths (Fairchild and Spiro, 1987; Pollock et al., 2006). Sedimentological evidence indicates that these cements crystallized rapidly relative to surrounding sediment (e.g., James et al., 1998), while geochemical data and mass balance constraints indicate an origin from fluids dominated by contemporaneous seawater (Frank and Lyons, 1998; Bishop and Sumner, 2006). Unlike other late Proterozoic carbonate components that clearly preserve evidence of former aragonite (consistent with relatively high Mg/Ca in Tonian seawater; Spear et al., 2014), the primary mineralogy of microspar is unconstrained.

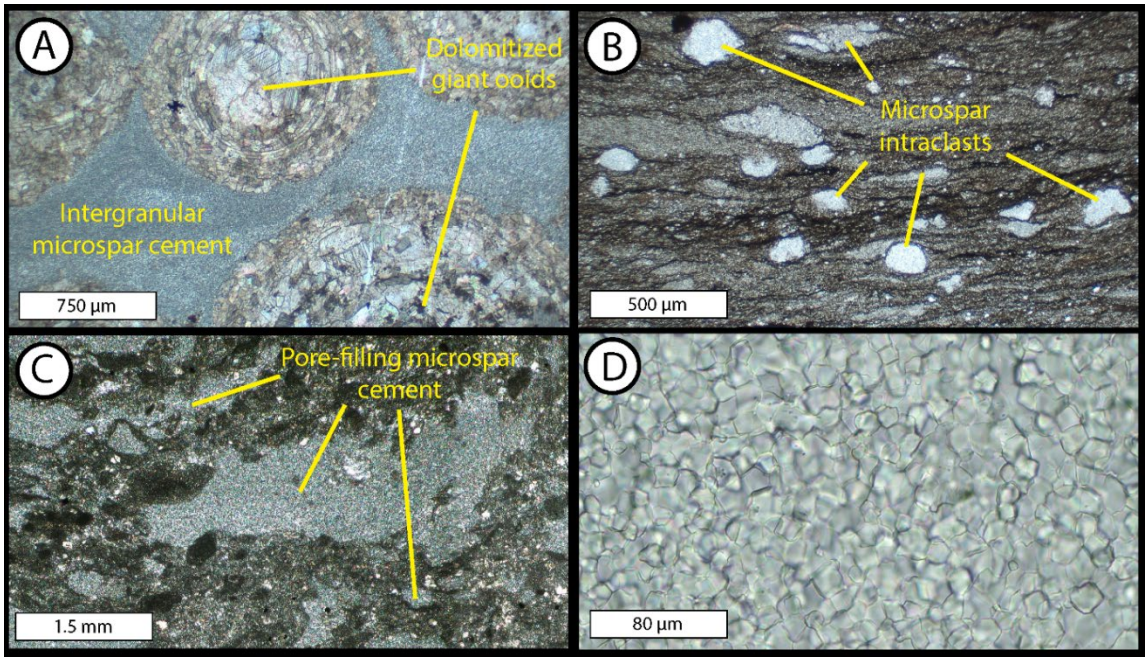

Figure 3. 1 Examples of late Proterozoic synsedimentary calcite microspar cement. (A) Intergranular calcite microspar cement (Backlundtoppen Formation, Svalbard, Norway). (B) Calcite microspar cement intraclasts in organic-rich lime mudstone (Fifteenmile Group, Yukon, Canada). (C) Pore-filling calcite microspar cement in intraclast wackestone (Svanbergfjellet Formation, Svalbard, Norway). (D) Euhedral interlocking calcite crystals of pore-filling microspar cement (Svanbergfjellet Formation, Svalbard, Norway). All images in plane-polarized light.

The formation of calcite microspar cement has recently been suggested to have required $CaCO_3$ supersaturation (Ω_{Cal}) greatly exceeding that of the modern ocean (Strauss and Tosca, 2020). The maintenance of $CaCO_3$ supersaturation through much of the Precambrian, by definition, would have required the inhibition and/or modification of $CaCO_3$ precipitation (i.e., Sumner and Grotzinger, 1996). This, in turn, suggests that before skeletons evolved, the rates and pathways of $CaCO_3$ production may have had a strong kinetic control.

Although several compounds are known to inhibit or modify the precipitation of $CaCO_3$ (including Fe^{2+}, Mg^{2+}, Mn^{2+}, SO_4^{2-}, PO_4^{3-}, and organic acids; Burton and Walter, 1990; Sumner and Grotzinger, 1996), relatively few studies have elucidated the sedimentologic consequences of kinetic inhibition. For example, PO_4 dramatically influences nucleation and growth kinetics at µmol/L (µ*M*) concentrations (i.e., Burton and Walter, 1990), and although observational data and theoretical models indicate both spatial and temporal variations in Precambrian PO_4 cycling (e.g.,

Laakso et al., 2020), the consequences for nonskeletal $CaCO_3$ production are virtually unknown. Here, we examined the influence of common seawater ions on the dynamics of $CaCO_3$ precipitation from Precambrian seawater, with a specific focus on dissolved PO_4.

3.4 Methods

We examined $CaCO_3$ nucleation in the presence of PO_4 with two types of experiments conducted in synthetic Tonian seawater at 22 ± 1.5 °C and stirred at 250 rpm: (1) degassing experiments, and (2) constant composition experiments (Fig. S3.1 in the Supplemental Material). Synthetic Tonian seawater (based on fluid inclusion constraints; Spear et al., 2014) was prepared from reagent-grade salts, stock solutions, and deionized water (see Table S3.1). Total dissolved PO_4 (hereafter $[PO_{4tot}]$) ranged from 0 to 100 μ*M*, the higher values of which exceed most modern carbonate sediment pore waters (which can reach >30 μ*M*; Morse, 1985). In degassing experiments, nucleation thresholds were approached by saturating the solution with 10% CO_2 gas and fixing total alkalinity (TA). CO_2 was then degassed by N_2 purging, which increased Ω_{cal} until nucleation occurred. Continuous monitoring of pH, with known $[Ca^{2+}]$ and TA, constrained the carbonate chemistry at the point of nucleation. In constant composition experiments, the desired Ω_{cal}, dissolved inorganic carbon (DIC), ionic strength, and TA were kept constant via autotitration of $CaCl_2$ and Na_2CO_3- $NaHCO_3$-NaOH titrants until $CaCO_3$ nucleation occurred (Fig. S3.1). Continuous monitoring of pH and $[Ca^{2+}]$, with ion-selective and AgCl reference electrodes, constrained carbonate chemistry at the point of nucleation. Reactor headspace was effectively eliminated in order to minimize CO_2 exchange between the solutions and atmosphere.

During both types of experiments, solution samples were extracted, syringe-filtered, and acidified to measure Ca, Mg, P, and Si concentrations via a PerkinElmer NexION 350D inductively coupled plasma–mass spectrometer (ICP-MS). $[PO_{4tot}]$ was determined using the ascorbic acid method (see the Supplemental Material). Immediately upon nucleation, solids were vacuum-filtered, rinsed with isopropanol, and dried in a vacuum-desiccator at 25 °C for 24 h.

Solids were analyzed with a PANalytical Empyrean X-ray diffractometer (XRD) with a Co-Kα source (40 kV and 40 mA). The Mg content of the solids was estimated by Rietveld refinement (Tables S3.2 A and S3.2 B).

Solids were also analyzed using a Perkin-Elmer Frontier Fourier transform infrared (FT-IR) spectrometer. KBr powder was milled with vacuum-dried samples (~3 mg) and pressed into optically transparent discs. Scanning electron microscope (SEM) and energy dispersive X-ray spectroscopic (EDS) analyses on Au-coated solids were performed using an FEI Quanta 650 field emission gun operated at 3.5–5 kV under high vacuum. *In situ* Raman spectra were collected using a Tornado HyperFlux PRO Plus Raman spectrometer in constant composition experiments with 12 scans averaged over 120 s intervals.

3.5 Results

Degassing and constant composition experiments showed that the Ω_{Cal} threshold at which $CaCO_3$ nucleation occurs is strongly influenced by dissolved PO_4 (Figure 3. 2; Tables S3.1 C and S3.1 D). Below 6 μ*M* PO_{4tot}, spontaneous $CaCO_3$ nucleation occurred at Ω_{Cal} between 20 and 30 (Figure 3. 2); under the conditions examined here, this range was largely independent of DIC and TA. In contrast, at [PO_{4tot}] greater than ~12 μ*M*, $CaCO_3$ nucleation was strongly inhibited, and the minimum threshold for $CaCO_3$ nucleation corresponded to Ω_{Cal} of ~45 (Figure 3. 2;Figure 3. 3). No detectable $CaCO_3$ nucleation occurred below this threshold, even over extended experiment durations (19 d). For experiments where precipitation was observed, $CaCO_3$ nucleation induction time (or the time elapsed between the establishment of supersaturation and nucleation) increased strongly with increased [PO_{4tot}] from 25 to 100 μ*M* (Figure 3. 3). The experiments also showed that dissolved PO_4 strongly controlled the resulting $CaCO_3$ polymorph precipitated from seawater solutions (Figure 3. 2). Specifically, below 6 μ*M* [PO_{4tot}], aragonite was consistently produced. Above 6 μ*M* PO_{4tot}, no aragonite was observed, and precipitates were dominated by monohydrocalcite and/or Mg-calcite. Our data show that in the presence of PO_4, monohydrocalcite is

produced across a broad range of Mg/Ca and CO_3/Ca ratios; however, lower Mg/Ca and CO_3/Ca ratios promote Mg-calcite formation over monohydrocalcite (Figure 3. 2). XRD, *in situ* Raman spectroscopy, and *ex-situ* FT-IR analyses showed that in the presence of PO4, amorphous Ca-Mg-carbonate (ACMC) initially nucleated from solution and recrystallized to either mono-hydrocalcite and/or Mg-calcite (Figs. S3.2–S3.3) in minutes to hours (Figure 3. 4). Amorphous calcium phosphate (ACP) nucleated in experiments where PO_{4tot} approached 100 μ*M* (along with ACMC), which recrystallized to octacalcium phosphate over 48 h (Fig. S3.3).

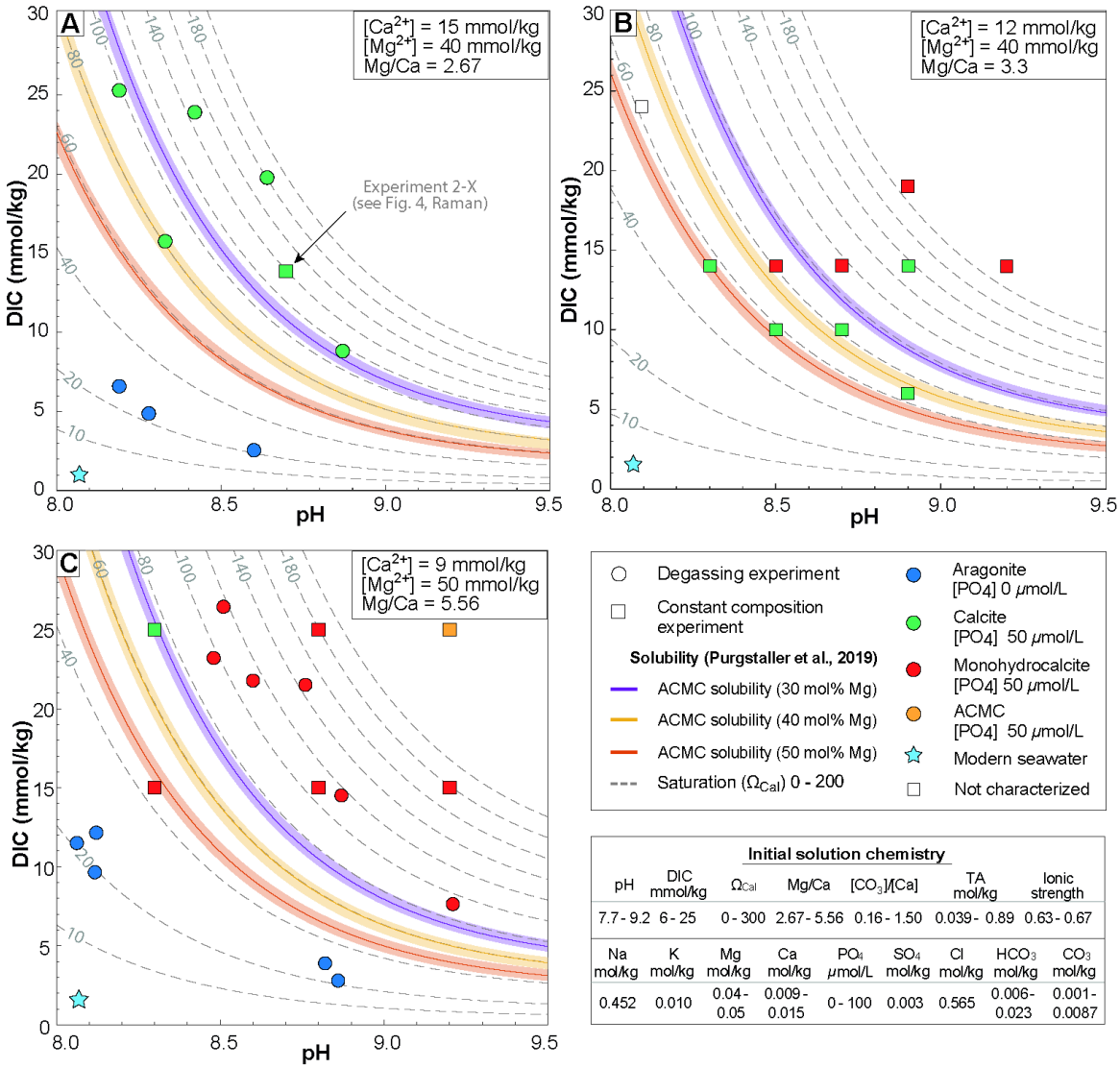

Initial solution chemistry

pH	DIC mmol/kg	Ω_{Cal}	Mg/Ca	$[CO_3]/[Ca]$	TA mol/kg	Ionic strength
7.7 - 9.2	6 - 25	0 - 300	2.67 - 5.56	0.16 - 1.50	0.039 - 0.89	0.63 - 0.67

Na mol/kg	K mol/kg	Mg mol/kg	Ca mol/kg	PO_4 µmol/L	SO_4 mol/kg	Cl mol/kg	HCO_3 mol/kg	CO_3 mol/kg
0.452	0.010	0.04 - 0.05	0.009 - 0.015	0 - 100	0.003	0.565	0.006 - 0.023	0.001 - 0.0087

Figure 3. 2 Results of $CaCO_3$ nucleation experiments in synthetic late Proterozoic seawater at 22 ± 1.5 °C with different Mg/Ca ratios. (A) Mg/Ca = 2.67, (B) Mg/Ca = 3.3, and (C) Mg/Ca = 5.56. Dashed gray contours represent $CaCO_3$ supersaturation (Ω_{ca}) determined using apparent solubility product (K_{sp}*) of calcite ($10^{-6.37}$ at 25 °C) in seawater based on concentrations (Mucci, 1983). Colored contours represent solubility product estimates of amorphous Ca-Mg carbonate (ACMC), where $\log K_{spACMC} = 0.018 \times (\text{mol\% Mg}) - 6.28$ at 25 °C, at 30, 40, and 50 mol% Mg^{2+} (Purgstaller et al., 2019). DIC—dissolved inorganic carbon; TA—total alkalinity. Data points represent crystalline polymorphs precipitated at corresponding solution compositions.

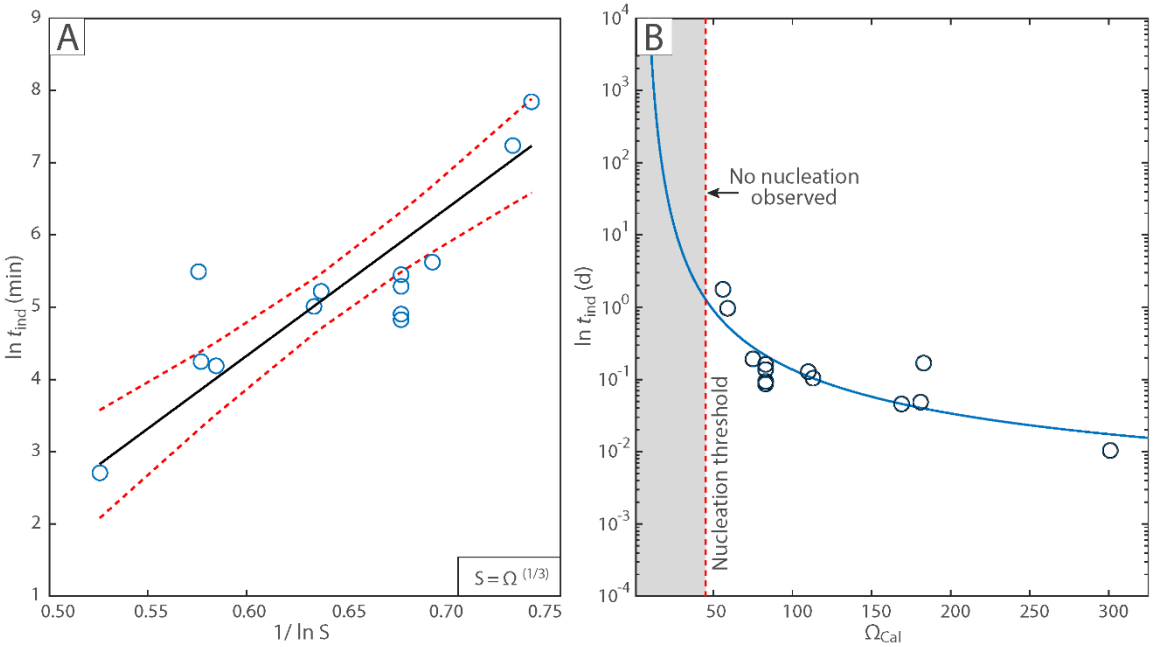

Figure 3. 3 (A) Relationship between natural logarithm of measured $CaCO_3$ nucleation induction time (t_{ind}) and calculated saturation ratio, $S = \Omega_{(1/N)}$, where N = number of ions in ACMC = 3(Ca^{2+}, Mg^{2+}, and CO_3^{2-}). (B) Relationship between calculated induction time and Ω_{Cal}. Gray shaded area indicates minimum nucleation threshold of Ω_{Cal} = 45 in seawater with elevated [PO_{4tot}].

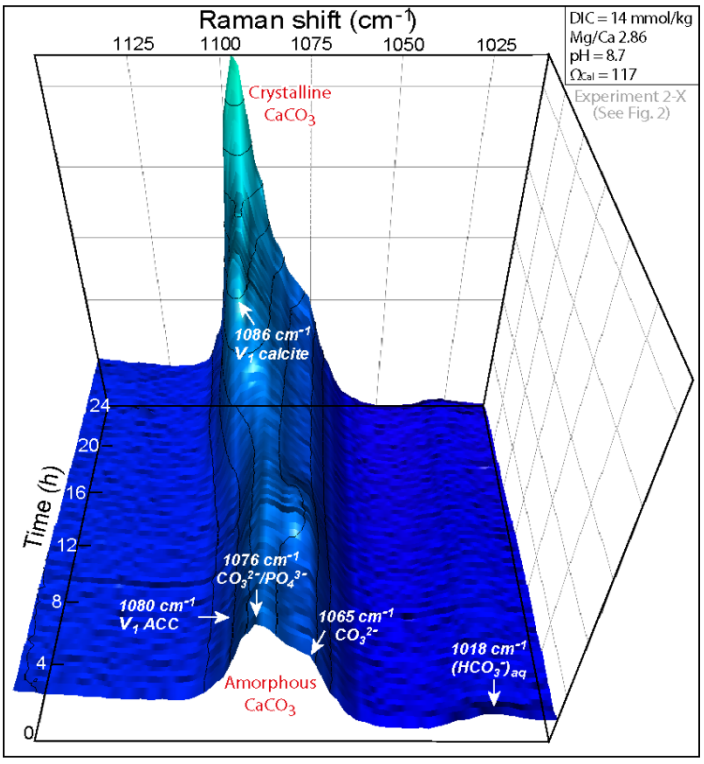

Figure 3. 4 *In situ* Raman spectroscopic results obtained from constant composition experiments conducted in Tonian seawater with 50 µmol [PO_{4tot}]. Raman spectra indicate amorphous Ca-Mg carbonate (ACMC) (~30–50 mol% Mg) precipitation and recrystallization to calcite within 24 h,

which are represented by shifts in absorption wavenumber and transition to higher intensity values. ACC—amorphous calcium carbonate; DIC—dissolved inorganic carbon.

The experiments also showed that dissolved PO_4 strongly controlled the resulting $CaCO_3$ polymorph precipitated from seawater solutions (Figure 3. 2). Specifically, below 6 μ*M* [PO_{4tot}], aragonite was consistently produced. Above 6 μ*M* PO_{4tot}, no aragonite was observed, and precipitates were dominated by monohydrocalcite and/or Mg-calcite. Our data show that in the presence of PO_4, monohydrocalcite is produced across a broad range of Mg/Ca and CO_3/Ca ratios; however, lower Mg/Ca and CO_3/Ca ratios promote Mg-calcite formation over monohydrocalcite (Figure 3. 2). XRD, *in situ* Raman spectroscopy, and *ex-situ* FT-IR analyses showed that in the presence of PO4, amorphous Ca-Mg-carbonate (ACMC) initially nucleated from solution and recrystallized to either monohydrocalcite and/or Mg-calcite (Figs. S3.2–S3.3) in minutes to hours (Figure 3. 4). Amorphous calcium phosphate (ACP) nucleated in experiments where PO_{4tot} approached 100 μ*M* (along with ACMC), which recrystallized to octacalcium phosphate over 48 h (Fig. S3.3).

3.6 Discussion

Our results indicate that [PO_{4tot}] above ~12 μ*M* suppresses the spontaneous nucleation of aragonite and/or calcite in synthetic Tonian seawater, most likely through adsorption onto nascent particle nuclei and subsequent inactivation of growth sites (Burton and Walter, 1990). This permits the formation of ACMC under suitably saturated conditions, which explains several experimental observations. First, the minimum Ω_{cal} nucleation thresholds observed in our experiments correspond closely with ACMC solubility estimates (Figure 3. 2; Purgstaller et al., 2019). ACMC solubility is a function of its Mg content, which is influenced by solution Mg/Ca, [$CO_3$2–], and pH (Blue and Dove, 2015). Vibrational spectroscopy (Raman *v*1 values) indicates that the ACMC formed in our experiments varied between 30 and 50 mol% Mg (i.e., Purgstaller et al., 2019; see Figure 3. 4).

The initial nucleation of ACMC in Tonian seawater (when $[PO_{4tot}] > 12$ μ*M*) also reconciles experimental observations of $CaCO_3$ polymorph selection. ACMC is metastable and rapidly transforms to Mg-bearing calcite or monohydrocalcite (Blue et al., 2017). The resulting crystalline phase is dependent on the Mg content of ACMC, solution Mg/Ca, CO_3/Ca, pH, and stirring rate (Blue et al., 2017; Purgstaller et al., 2019). Consistent with this, our observations indicate that lower Mg/Ca ratios promote calcite (Figure 3. 2), whereas higher Mg/Ca ratios promote monohydrocalcite. Although monohydrocalcite may also recrystallize to Mg-calcite (Fukushi and Matsumiya, 2018; Purgstaller et al., 2019), this pathway was not observed under the conditions examined here.

ACMC nucleation provides a simple explanation for an apparent $CaCO_3$ nucleation threshold in seawater when $[PO_{4tot}] > 12$ μ*M*. Spontaneous $CaCO_3$ nucleation induction time has been shown to continuously increase with decreasing Ω_{Cal} in modern seawater, as predicted by classical nucleation theory (CNT; Pokrovsky, 1998). Conversely, our experiments show that in seawater with elevated $[PO_{4tot}]$, no nucleation occurs below an Ω_{Cal} threshold of 45 (Figure 3. 3), even over time scales where nucleation should have occurred according to CNT. This result is consistent with molecular dynamic calculations of supersaturated $CaCO_3$ solutions (Wallace et al., 2013), which show that once a key Ω_{cal} threshold is crossed, amorphous $CaCO_3$ can form through the rapid production of dense liquid droplets. This liquid-liquid separation process occurs in a compositional regime that may only be accessed if the precipitation of crystalline polymorphs is suppressed.

ACMC-mediated precipitation pathways may, in turn, strongly influence the loci of $CaCO_3$ nucleation in marine systems where elevated PO_4 is present. In the modern ocean, inorganic $CaCO_3$ nucleation is often linked to the presence of microbial substrates (Robbins and Blackwelder, 1992). This is because nucleating calcite on a microbial substrate requires less energy than the direct nucleation of calcite from aqueous solution (e.g., Obst et al., 2009). However, in the presence of PO_4 (or other compounds that inhibit crystalline CaCO3 nucleation), the energy barrier to ACMC nucleation is lower than the barrier to CaCO3 nucleation on a foreign

substrate (Wallace et al., 2013; De Yoreo et al., 2015). This in turn implies that foreign surfaces are unlikely to influence $CaCO_3$ nucleation thresholds in supersaturated systems where calcite and aragonite nucleation is inhibited, consistent with experimental and natural systems (Reddy and Hoch, 2012; Fukushi and Matsumiya, 2018); thus, ACMC would be expected to nucleate where variations in temperature, pressure, and/or fluid composition exceed its solubility in natural systems.

Our experimental observations provide new insight into Precambrian nonskeletal carbonate sedimentation. Specifically, these experimental data begin to constrain the origin of fabrics associated with rapid $CaCO_3$ nucleation, such as synsedimentary calcite microspar cement (James et al., 1998). We hypothesize that the lack of petrographic evidence for former aragonite in late Proterozoic microspar (Fairchild and Spiro, 1987) is most consistent with ACMC nucleation and subsequent transformation to calcite (Bishop and Sumner, 2006). Spheroidal cores and crystal size distributions observed in microspar cement are also consistent with Ostwald ripening of an ACMC precursor formed at high Ω_{Cal} values (greater than 69–100; Kile and Eberl, 2003), as is enhanced Sr incorporation into the resulting calcite because ACMC favors trace-element uptake (Littlewood et al., 2017). Together, these observations support the hypothesis that microspar cement reflects precipitation pathways enabled only under high Ω_{Cal} (Strauss and Tosca, 2020).

Crucially, it is the suppression of aragonite and calcite in marine systems that enables ACMC formation, which in turn opens subsequent recrystallization pathways to $CaCO_3$. Although Fe^{2+}, Mg^{2+}, Mn^{2+}, SO_4^{2-}, or organic acids may modify $CaCO_3$ growth rates, they are not known to suppress aragonite nucleation at high Mg/Ca (Bots et al., 2011). Thus, among known inhibitors, PO_4 is likely to have influenced shallow-water $CaCO_3$ production through much of the Proterozoic. In fact, elevated $[PO_{4tot}]$ has been shown to maintain high Ω_{Cal} and lead to the production of metastable precursors in several synthetic and natural systems (Gallagher et al., 2013; Lin et al., 2018), including many alkaline lakes (Bischoff et al., 1993; Fukushi and Matsumiya, 2018). These observations, in combination with our experimental data, suggest that

the stratigraphic distribution of depositional fabrics reflecting high Ω_{Cal} such as microspar, and possibly cap carbonates and giant ooids (Grotzinger and James, 2000; Trower, 2020), could together reflect kinetic controls on $CaCO_3$ precipitation through the effects of elevated pore and/or bottom water [PO_4]. Although shale-hosted geochemical records indicate relatively minor perturbations to net P flux through much of the Precambrian (including intervals of global phosphogenesis; Laakso et al., 2020), pore/bottom water [PO_{4tot}] may have been most strongly influenced by the degree of internal PO_4 recycling (Ingall et al., 1993) and/or the apatite burial efficiency controlled by seawater [Ca^{2+}] (e.g., Zhao et al., 2020). Although the details of PO_4 cycling and burial in Precambrian $CaCO_3$ depositional environments are poorly constrained, Tonian Ca-phosphate biomineralizing organisms (Cohen et al., 2017) record enhanced P availability in the water column at a time when synsedimentary microspar peaked in its stratigraphic distribution (James et al., 1998).

3.7 Conclusions

Our data show that kinetic interactions among common seawater ions may generate nontraditional mineralization pathways that offer new explanations for enigmatic Precambrian carbonate fabrics such as synsedimentary calcite microspar cement; thus, future interpretations of isotopic and trace-elemental variations in Precambrian carbonates should take explicit account of these $CaCO_3$ mineralization pathways and their associated expressions. More broadly, our data show that because [PO_{4tot}] strongly increases nucleation thresholds, while effectively arresting the growth rates of preexisting $CaCO_3$ (Mucci, 1986), periods of enhanced PO_4 recycling, whether driven by ecological factors (Lenton and Daines, 2018) or ocean-atmosphere redox (Laakso et al., 2020), may have fundamentally altered the dynamics of $CaCO_3$ precipitation throughout much of the Proterozoic Eon.

3.8 Acknowledgments

We thank the University of Oxford, the Natural Environment Research Council (NERC) Centre for Doctoral Training (CDT) in Oil and Gas, and the donors of the American Chemical Society Petroleum Research Fund (grant 58780-DNI8 awarded to Strauss) for support of this research, and Kat Clayton and Phil Holdship for assistance in sample analysis. We thank Peir Pufahl, Patricia Dove, Malcolm Wallace, and editor William Clyde for valuable input and feedback that significantly improved this manuscript.

Supplementary material

Published Supplementary Material and additional material is located at the end of the document in the Supplementary Materials – S3.

Chapter 4: Carbonate-hosted phosphate and mid-Neoproterozoic P cycling

Sascha Roest-Ellis, Justin Strauss, Brian Phillips, Galen Halverson, Jocelyn Richardson, Samuel Webb, Olivia Gaitonde and Nicholas Tosca.

4.1 Linking Chapter 3 and Chapter 4

This chapter outlines our investigation into geological carbonate sediments that aims to answer whether phosphate is recorded within Neoproterozoic carbonate sediments and if so, how it is recorded. This permits a direct test of the hypothesis outlined in Chapter 2 and Chapter 3 where we hypothesize that elevated PO_4 concentrations in Tonian seawater led to kinetically controlled $CaCO_3$ mineral formation pathways linked to PO_4 inhibition. In the absence of skeletal carbonates during this time, kinetic pathways may have controlled the production of high-Mg $CaCO_3$ minerals that are widespread in mid-Proterozoic to Neoproterozoic carbonates. Chapter 2 and Chapter 3 indicate that this is the case experimentally. Therefore, we would expect to see PO_4 recorded in Tonian carbonate sediments if our hypothesis rings true for the carbonate factory during the Neoproterozoic. This chapter uses a range of microanalytical techniques to examine the PO_4 bulk concentration, speciation, and distribution of PO_4 from three different Tonian sedimentary basins.

4.2 Summary

With a view to test the hypothesis that elevated dissolved phosphorus concentrations in Tonian oceans may be recorded in carbonate sediments and to provide insight into the Neoproterozoic geochemical P-cycle; we examine phosphorus in Tonian aged shallow water carbonates. Our experimental data show a strong relationship between phosphate, carbonates and apatitic scale microfossils that have been identified in Tonian successions (Cohen et al., 2017) hinting at elevated P concentrations, but by analysing geological carbonates for phosphate we can constrain the relationship further.

Our investigation focuses on examining the concentration, speciation, and distribution of phosphorus in non-skeletal shallow water carbonate sediments using a range of microanalytical techniques. In-situ examination of the spatial distribution and molecular configuration of phosphorous in Neoproterozoic carbonate samples was permitted through low-energy synchrotron X-ray absorption spectroscopy (XANES) and micro-XRF mapping. In addition, the molecular environment of phosphorous in carbonate fabrics was constrained using ^{31}P solid-state NMR indicating that phosphorous has been identified bound in the carbonate lattice.

Microcrystalline $CaCO_3$, unambiguously precipitated in place (derived from the water column) is associated with high phosphorous content. This directly supports the hypothesis that dissolved PO_4 was present during nucleation and may have acted as a key inhibitor during mineralization at this time and may have provided bioavailable marine phosphorous that was essential to biological evolution. These datasets have permitted a unique set of constraints on this geochemically important relationship. Additionally, this research indicates that carbonates can host a record of Neoproterozoic dissolved PO_4 availability providing insight into the ancient phosphorous cycle through a key interval of Earth's history.

4.3 Introduction

As a critical nutrient and basic component of all life on Earth, phosphorus plays a central role in structuring terrestrial and marine ecosystems (Gulick et al, 1955; Van Cappellen, 1991, Butusov and Jernelöv, 2013; Fernández-García et al., 2017), and in regulating long-term changes in ocean-atmosphere redox. Because phosphorous (P) availability is thought to limit marine primary productivity over geological timescales (>10^5 years) (Tyrell, 1999), perturbations to net P inputs or outputs, or to the degree of biological recycling (Ingall et al. 1993) are considered to drive fluctuations in primary production, net organic carbon burial, and ultimately atmospheric pO2. At the same time, because P burial in marine sediments is redox-dependent, the global biogeochemical cycle of phosphorus is intimately connected to those of oxygen, carbon, sulfur, and iron through important feedback mechanisms (Van Cappellen and Ingall 1994; 1996, Marz et al., 2008) (Figure 4.1).

Although geochemical data and biogeochemical models have examined the causes and consequences of shifts in P-cycling through much of Earth's history (Filippelli, and Delaney, 1992; 1994; Glenn et al., 1994; Compton et al., 2000; Bergmann et al., 2004), the nature of the Precambrian phosphorus cycle, and its role in the long term oxygenation of the atmosphere and oceans, remains open to debate (Bjerrum and Canfield 2002, Konhauser 2007; Planavsky et al. 2010; Reinhard et al., 2017; Poulton 2017; Laakso et al. 2020). In particular, because the Neoproterozoic Era (1000-541 Ma) witnessed significant shifts in the intensity of physical and chemical weathering (Tosca et al., 2010; Bahlburg and Dobrzinski, 2011; Mills, Lenton, Watson, 2014; Cox et al., 2016), atmospheric pCO_2 and climate (Hoffman et al., 1998; Pierrehumbert, 2011; Och and Shields-Zhou, 2017; Strauss and Tosca, 2020), and the redox state of marine systems (Van Cappellen and Ingall, 1996; Marz et al., 2008; Mort et al., 2010; Laakso and Schrag, 2014; 2017; 2017; Sperling 2015), much intellectual focus has centered on how changes in P-cycling may have contributed to a shift in the prokaryote-dominated biosphere and low pO_2

atmosphere that characterized much of the early-mid Proterozoic, eventually facilitating a rise in eukaryotes within the late Neoproterozoic biosphere.

Available constraints on the Neoproterozoic P-cycle have been almost exclusively derived from the bulk P concentration in sedimentary rocks. Several recent studies have proposed that secular variations in bulk sedimentary P reflects corresponding perturbations to the size of the marine bioavailable P reservoir (Bjerrum and Canfield, 2002, Konhauser et al., 2007; Planavsky et al. 2010; Laakso and Schrag, 2014; Reinhard et al., 2017; Poulton et al., 2017). For example, in a study of more than 8,000 shale samples, Reinhard et al. (2017) argued, on the basis of biogeochemical modelling, that an apparent Tonian-Cryogenian increase in sedimentary P reflected redox-driven changes in P cycling and burial that ultimately established a larger bioavailable P pool. At the same time, because sedimentary biomarker data indicate an apparent shift to eukaryote-dominated primary production in Cryogenian rocks, Brocks et al. (2017) hypothesized that this major ecological milestone was facilitated by Tonian-Cryogenian changes in P availability as hypothesized by Reinhard et al. (2017).

However, because bioavailable phosphorus concentrations in the water column are controlled by the recycling of P released from sediments in addition to input and burial fluxes (i.e., Figure 4.1) (Ingall et al., 1993; Ingall and Jahnke 1994; Van Cappellen and Ingall 1994; Slomp, et al., 2004), the degree to which shale-hosted P might reflect the evolution of the marine P-cycle remains unclear. For example, Laakso et al. (2020) showed that large scale changes to the deep-water aqueous phosphate reservoir may have been driven by Ediacaran increases in marine sulfate concentrations, which in turn facilitated increased organic matter remineralization by sulfate-reducing bacteria. This conclusion implies that changes in P-cycling may be triggered by internal biological recycling mechanisms rather than by large scale shifts in erosional P fluxes. Consistent with this suggestion, a new compilation of shale-hosted P reported by Laakso et al. (2020) shows no statistically resolvable variation across the Neoproterozoic despite the onset of global phosphogenesis in the Ediacaran.

Although large-scale perturbations to P cycling in marine systems may not be reflected in average bulk shale-hosted P concentration (Laakso et al., 2020,), these studies and others (Planavsky et al., 2010 Lenton et al., 2014; Horton, 2015; Reinhard, et al., 2016; Spence et al., 2016; Lenton and Daines, 2018) make it clear that further constraining Neoproterozoic P cycling requires observational constraints on the size of the aqueous P reservoir and on the mechanisms by which sediments record bioavailable P. Unfortunately, direct constraints on sediment pore/bottom water P concentrations have proven elusive. Unambiguous evidence for synsedimentary P precipitation in siliciclastic lithologies is difficult to obtain, and where such evidence is available, the presence of P-bearing minerals alone is insufficient to constrain aqueous P concentrations in the absence of independent chemical constraints. Nevertheless, early-mid Neoproterozoic carbonate rocks (ca. 811 Ma) do host the earliest reported evidence for biologically-controlled mineralization in the form of Ca-phosphate (apatite) (Cohen and Knoll 2012; Cohen et al 2017; Moczydłowska et al., 2018; Cantine et al., 2020; Riedman et al., 2020). These microfossils, which record complex, template-controlled crystallization of apatite preserved at the nanometer scale (Cohen et al 2017) provide independent evidence that aqueous phosphate reached water column concentrations high enough to offer a potential ecological opportunity to ancient eukaryotic organisms (Riedman et al., 2020). Even so, this observation has remained enigmatic in the context of Neoproterozoic P-cycling.

Here, in an effort to provide observational constraints on the nature of P-cycling through the Neoproterozoic, we examine the concentration, speciation, and distribution of phosphorus in non-skeletal carbonate sediments. We focus here on carbonate rocks deposited during the Tonian period in order to test the hypothesis that elevated aqueous P concentrations, qualitatively inferred from apatitic scale microfossils (Cohen et al., 2017) may in fact be reflected in Tonian carbonate sedimentary rocks more broadly. In what follows, we present a variety of microanalytical data that specifically target the speciation and distribution of carbonate-associated P. We then place these data in an aqueous geochemical framework to unravel the behaviour of aqueous phosphate during the formation and diagenesis of mid-Neoproterozoic carbonate rocks. Finally, and more

broadly, we evaluate the degree to which non-skeletal carbonates may shed important light on P-cycling in shallow carbonate platform settings both through the Neoproterozoic and perhaps through earlier stratigraphic intervals.

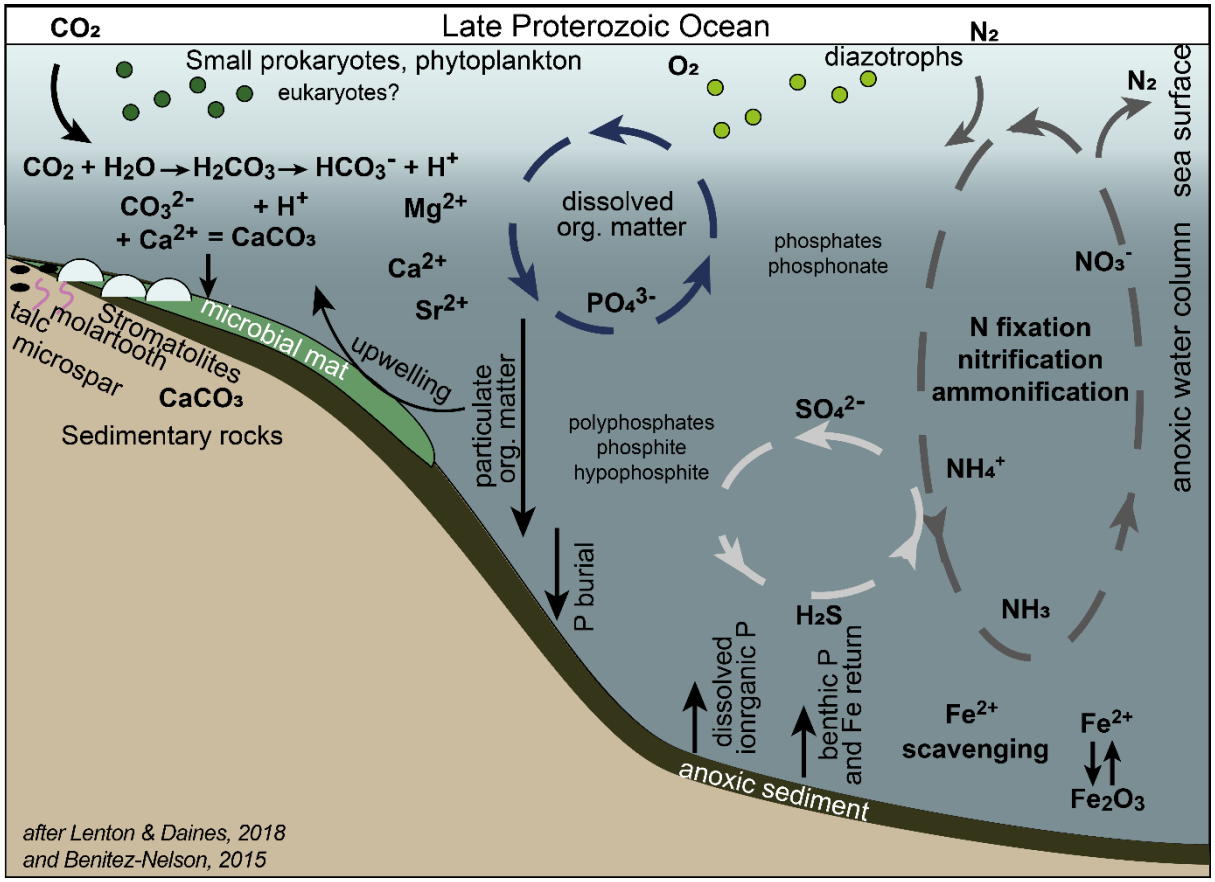

Figure 4. 1 Schematic diagram of key late Proterozoic ocean cycles (this is not exhaustive and is for illustration purposes only), highlighting key geochemical and biogeochemical cycles and P species. Key late Proterozoic carbonate sedimentary features are also indicated. Modified after Lenton and Daines, 2018 and Benitez-Nelson, 2015.

4.4 Geological setting

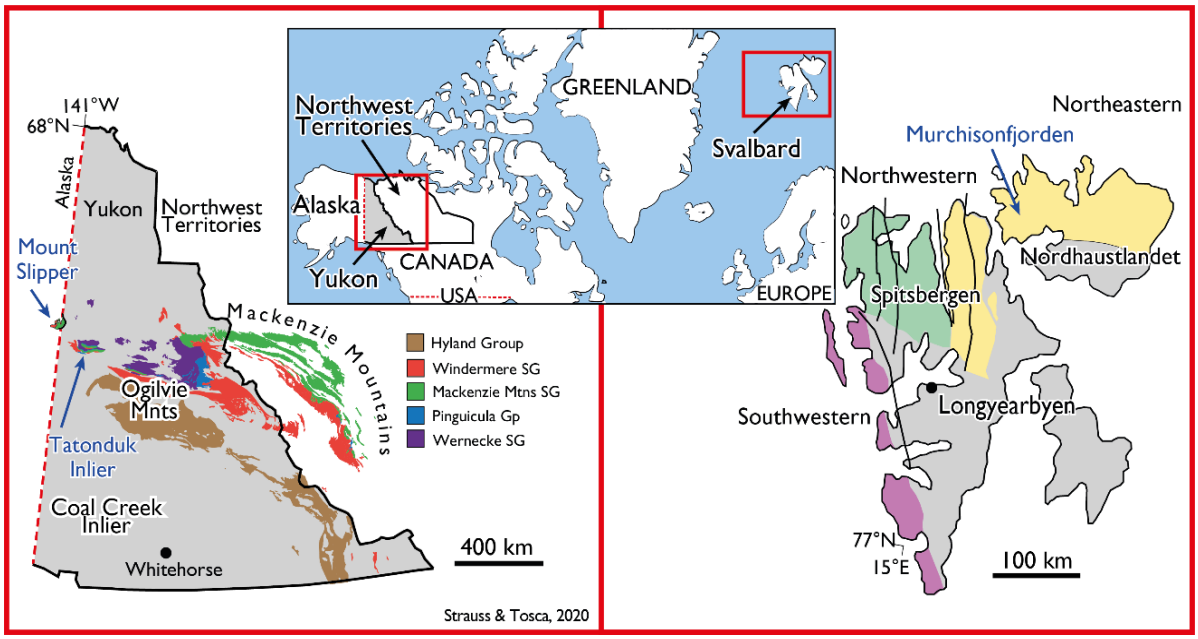

Figure 4. 2 Map indicating the geographical locations of the Neoproterozoic successions analyzed, the arrows point to the geographical locations (after Strauss and Tosca, 2020). A: Fifteenmile Group, Mount Slipper, Tatonduk Inlier, Ogilvie Mountains, Yukon, Canada, and the Little Dal Group, Stone Knife River, Mackenzie Mountains, Northwest Territories, Canada. B: Akademikerbreen Group, Svalbard, Norway.

The results of the analyses are presented for three successions: (1) R1, Akademikerbreen Group, Svalbard, Norway; (2) P1401, Fifteenmile Group, Mount Slipper, Tatonduk Inlier and Coal Creek Inlier, Ogilvie Mountains, Yukon, Canada; (3) M304, Little Dal Group, Ram Head and Snail Spring, Stone Knife River, Mackenzie Mountains, Canada. Figure 4. 2 gives the current geographical location of these successions.

4.4.1 Akademikerbreen Group, Norway

Analyses were conducted on samples of mid-Neoproterozoic Akademikerbreen Group from outcrops in Roaldtoppen, Murchisonfjorden in northeastern Svalbard, Norway (Figure 4. 2). The Akademikerbreen Group consists of well preserved mid-Neoproterozoic sediments of the upper Hecla Hoek Series of the Northeastern basement province. These successions are exposed within the north-south trending fold and thrust belt (Figure 4. 2) (Harland and Wilson, 1956; Sandford, 1956; Wilson, 1961) and were deposited around the time that supercontinent Rodinia was fragmenting (Harlan et al., 2003; Dallman et al., 2015; Halverson et al., 2018). The Akademikerbreen Group is a ca. 1350–2500 thick almost exclusively carbonate sequence that was deposited at tropical latitudes (Maloof et al., 2006) within stable thermally subsiding metamorphic basin complex (Halverson et al., 2018; Maloof et al., 2006)

The mid–upper Tonian Akademikerbreen group (equivalent to the Hunnberg and Ryssø formations [Flood et al., 1969]) is subdivided into the Grusdievbreen, Svanbergfjellet, Draken and Backlundtoppen formations (Wilson, 1961; Knoll and Swett, 1990; Halverson et al., 2007; 2018). These formations record the complete Bitter Springs carbon isotope excursion anomaly (BSA) (ca. 810–800 Ma) (Halverson et al., 2005, 2007, 2018; Maloof et al., 2006; Macdonald et al., 2010, 2018; Swanson-Hysell et al., 2015; Cohen et al., 2017) within the upper Grusdievbreen through the lower Svanbergfjellet Fm. (Figure 4. 3). The Svanbergfjellet Fm. is further subdivided into units that progressing up section are described as the Lower Dolomite, Lower Limestone, Algal Dolomite and Upper Limestone (Knoll and Swett, 1990; Halverson et al., 2007; Maloof et al., 2006). The BSA spans from the contact between the upper and lower members of the Grusdievbreen Fm. to the contact between the Lower Dolomite and the Lower Limestone members of the Svanbergfjellet Fm. (Figure 4. 3). Both contacts are subaerial exposure surface contact disconformities that correspond with negative carbon isotope shifts of ca. 8‰ that define the BSA (Wörndle et al., 2019).

The ~250 m thick upper Grusdievbreen Formation consist of dominantly limestone calcilutite to grainstone and wackestone with recrystallized limestone and dolostone conglomerates (Halverson et al., 2007; 2018; Wörndle et al., 2019). Sedimentary structures include minor crossbedding, minor microbial laminations (Halverson et al., 2007; 2018) and authigenic talc (Mg-silicate) is present (Halverson et al., 2007; Tosca et al., 2011). The overlying ca. 600 m Svanbergfjellet Fm. (805–788 Ma; Halverson et al., 2018) consists dominantly of dolomite sediments and hosts abundant molar tooth structures, stromatolitic laminae and voids that are filled with calcite microspar cement and associated with authigenic Mg-silicate nodules. Mg-silicate becomes more abundant in the Svanbergfjellet Fm. relative to the Grusdievbreen Fm. as nodules and significant cm- to m-scale talc rich mudstone deposits (Tosca et al., 2011; Strauss and Tosca, 2020). The Svanbergfjellet Fm. represents overall shallowing up carbonate cycles deposited in subtidal to peritidal settings on a tropical carbonate ramp progressing to a rimmed platform (Knoll and Swett, 1990; Maloof et al., 2006; Worndle et al 2019). The Lower Dolomite member comprises dolomite sequences that contain stromatolitic boundstone, intraclast packstone to wackestone and dolograinstone as well as dolomitic and siliciclastic mudstone (Knoll and Swett, 1990; Maloof et al., 2006; Halverson et al., 2007). Mudcracks and tepees indicate exposure surfaces and stromatolites, cross-bedded oolitic grainstones, and finely laminated carbonate and siliciclastic mudstones characterize subtidal environments (Knoll and Swett, 1990; Maloof et al., 2006; Halverson et al., 2007; Strauss and Tosca, 2020). Talc nodules and aggregates are present in the Lower Dolomite member and are associated with calcite microspar cement and talc-rich black mudstone (Tosca et al., 2011; Strauss and Tosca, 2020). The overlying Lower Limestone member is limestone dominated and contains red, green, grey, and black shales, stromatolites and dark grey to black finely laminated to wavy carbonate and siliciclastic mudstones with abundant molar tooth structures and stromatolites, which indicate a shallow subtidal depositional environment (Knoll and Swett, 1990). The overlying Algal Dolomite member contains series of shale to stromatolite cycles of bedded limestone that contains molar tooth structures and stromatolites. (Knoll and Swett, 1990; Maloof et al., 2006; Halverson et al., 2007). Talc nodules

and aggregates are also present and are associated with calcite microspar cement and talc-rich black mudstone deposits reach up to a meter in thickness (Tosca et al., 2011; Strauss and Tosca, 2020). The Algal Dolomite member is capped by a distinctive biostrome (Knoll and Swett, 1990; Maloof et al., 2006; Halverson et al., 2007). The overlying Upper Limestone member consists of thickly laminated, parallel to irregular and wavy bedded, muddy calcimicrite to lutite finely bedded carbonate, with interbedded wackestones and rudstones (Halverson et al., 2007; 18) that also contains talc nodules (Tosca et al., 2011; Strauss and Tosca, 2020).

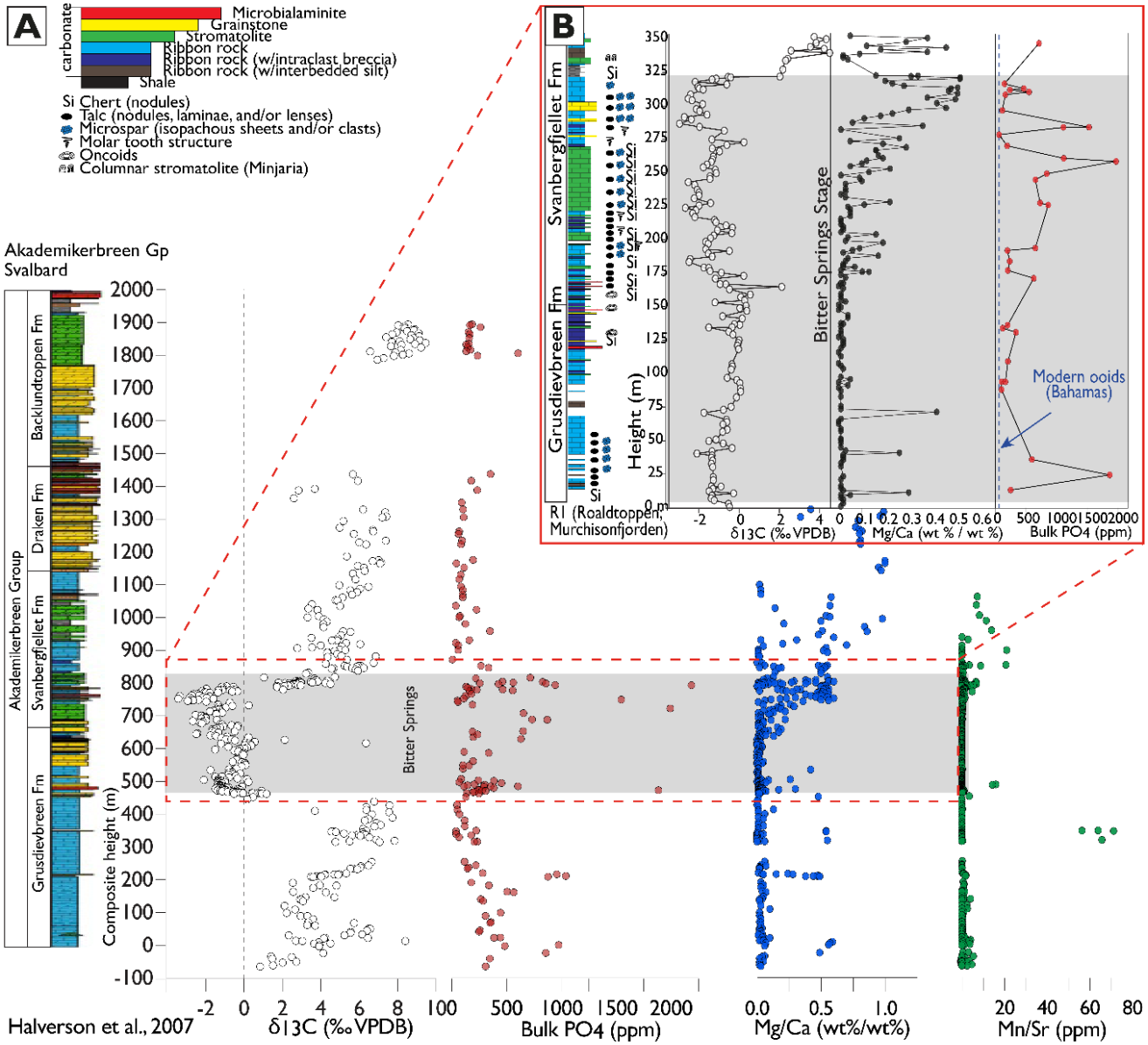

Figure 4. 3 A: Bulk PO_4 concentrations of carbonates from the Akademikerbreen Group, Svalbard, Norway, presented against δ13C isotopic signatures (Halverson et al., 2007), lithological stratigraphy with chemostratigraphic [Mg]/[Ca] and [Mn]/[Sr] ratios (Halverson et al., 2007). The Bitter Springs Stage (carbon isotope anomaly) is indicated by the grey shaded area. B: Zoomed in area presents a higher resolution sample set, but note that the stratigraphic height in meters between A and B do not correspond. Modern ooid [PO_4] are represented by the grey dashed line for comparison.

4.4.2 Fifteenmile Group, Canada

Analyses were conducted on samples from the Fifteenmile Group outcrop that is exposed in the Tatonduk Inlier faulted anticline (Young, 1982; Macdonald et al., 2012) and the Coal Creek Inlier of Mount Slipper (Macdonald et al., 2012). Both inliers are located in the western Ogilvie Mountains which spans the Yukon (Canada)–Alaska (USA) border (Figure 4. 4). (Macdonald and Cohen, 2011;Macdonald et al., 2011; Macdonald et al., 2013b, 2018). The Fifteenmile Group (Macdonald et al., 2015) was previously named the Upper Tindir Group (Macdonald et al., 2010). The Fifteenmile Group was deposited on the margin of Laurentia (Cohen and Knoll, 2012) that formed part of the supercontinent Rodinia. The Fifteenmile Group was deposited in an intracratonic basin that was subject to thermal subsidence in (Halverson et al., 2018). An age of 810.7 ± 5.8 Ma was reported from Re-Os geochronology from black, organic-rich shale from the Fifteenmile Group, Mount Slipper, Ogilvie Mountains, Yukon (Cohen et al., 2017) an age of 811.5 ± 0.25 Ma (zircon U/Pb ID-TIMS) was reported from a tuff from the Fifteenmile Group in the Ogilvie Mountains (Macdonald and Roots 2010; Macdonald et al. 2010) that is stratigraphically ca. 50 m below where $\delta 13C_{carb}$ values begin to decrease in the Fifteenmile Group as part of the BSA ((Macdonald et al., 2010, 2012). A minimum age for the Fifteenmile Group based on U/Pb ID-TIMS of volcanic rhyolite flows is 717.43 ± 0.14 Ma (Macdonald et al. 2010).

The Fifteenmile Group exposed at the Tatonduk Inlier of Mount Slipper presents exposures that consist of >350 m stromatolitic dolostone and an additional ca. 500 m of black shale interbedded with quartz sandstone and minor carbonate that are assigned to the Reefal assemblage (Figure 4. 4). The samples analyzed here correspond with the fossiliferous zones in the upper strata of the Reefal assemblage as described by Cohen et al., (2017) in Fifteenmile Group assemblages that predate the onset of the Bitter Springs Anomaly. The sediments consist of ca. 60 m of interbedded planar-laminated lime mudstone, calcareous black and gray shale, and sparse tabularclast conglomerate and calcisiltite interbedded with discontinuous matrix-supported

rudstone and chert nodules that contain apatitic-scale fossils (ASMs) (as well as in the carbonate matrix) (Macdonald et al., 2010; Cohen and Knoll, 2012; Cohen et al., 2017).

The Fifteenmile Group of the Coal Creek Inlier has recently been subdivided into the Gibben and Chandindu formations and the overlying Reefal assemblage. (Halverson et al., 2012; Macdonald et al., 2011; 2012). Following a disconformable contact, this is overlain by the Callison Lake Formation dolostone (Macdonald and Roots, 2010; Strauss et al., 2015; Halverson et al., 2018). The Reefal assemblage exposed in the Coal Creek Inlier contains platform and distal foreslope facies with stromatolite reef facies, intertidal to supratidal carbonate facies, which includes dark grey limestone microbialaminites indicative of lagoonal depositional settings, dolomitic microbialaminites indicative of supratidal settings and abundant grainstone indicative of supratidal and proximal reef settings (Macdonald et al., 2012). Carbonate mudstone that contain abundant molar tooth structures are also present within facies dominated by talus reef breccias that are indicative of upper foreslope settings (Macdonald et al., 2012).

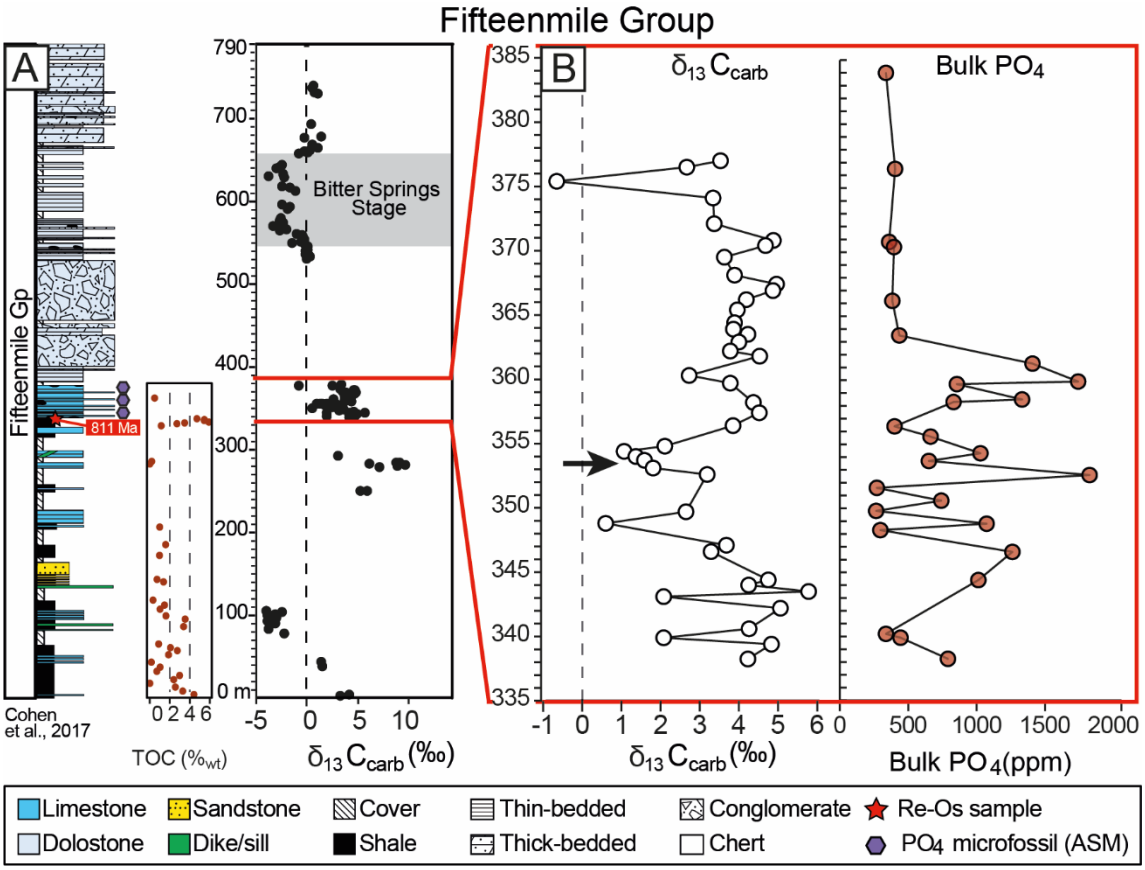

Figure 4. 4 Lithological stratigraphy and $\delta^{13}C$ isotopic signatures from carbonates of the Fifteenmile Group from Mount Slipper, Yukon (Macdonald et al., 2010, 2011). The Bitter Springs Stage (carbon isotope anomaly) is indicated by the grey shaded area. B: Bulk PO_4 concentrations of carbonates are presented against a zoomed in section of the $\delta^{13}C$ stratigraphy. Note that the Fifteenmile group samples analyzed in this investigation are pre-Bitter Springs Event. The black arrow indicates the location of the samples shown in Figure 4. 8 with µXRF, XANES and SEM data. The purple symbols indicate the location of the apatitic ASMs (Cohen et al., 2017).

4.4.3 Little Dal Group, Canada

Analyses were conducted on samples from the mid-Neoproterozoic stratigraphy of the Little Dal Group, which is part of the Mackenzie Mountains Supergroup exposed at Ram Head and Snail Spring, of the Stone Knife River in the Mackenzie Mountains, Northwest Territories, Canada Aitken 1981; Halverson 2006; Worndle, et al., 2019) (Figure 4. 5). The Little Dal Group is part of the ca. 500 km long Mackenzie Mountains Supergroup deposited in an intracratonic basin. The basin was subject to thermal subsidence (Halverson et al., 2018) and associated with Neoproterozoic tectonic activity from the breakup of the supercontinent Rodinia (~825-580 Ma)

characterized by distinct magmatic events indicating upwelling mantle plumes (Li et al., 2008, Ernst and Bleeker, 2010). Based on abrupt changes in the formation thickness and stratigraphic relationships, it is suggested that synsedimentary sub-basins underwent irregular subsidence caused by excessive episodic subsidence along growth faults that may have developed during the extension of a basin into a lower plate segment of an evolving passive margin border (Turner and long, 2008).

Age constraints for the Little Dal Group place deposition between 775 – 1005 Ma, based on corresponding U-Pb detrital zircons from the underlying Katherine Group (Leslie, 2009) and diabase U-Pb zircons within unconformably overlying Little Dal Basalts of the Ram Head Fm. (Aitken, 1982; Milton et al., 2017). These have been correlated with the Gunbarrel igneous event mafic intrusions assigned an age of ca. 775-780 Ma (Dudás and Lustwerk 1997; Harlan et al., 2003; Halverson et al., 2006). The BSA is archived in the upper Snail Spring Formation through to the lower Ram Head Formation (Halverson, G. P., 2006; Wörndle, et al., 2019). Carbon isotope chemostratigraphy enables correlation of sequences between the Fifteenmile Group, Little Dal Group, and Shaler Supergroup (Macdonald et al. 2010; 2011; Turner, 2011) as well as the Akademikerbreen Group, Svalbard (Wörndle, et al., 2019).

The Little Dal Group is a mixed carbonate-siliciclastic succession that consists of shale, limestone, dolostone, evaporates and sandstone with major reef complexes (Figure 4. 5). Reef complexes up to 300 m in height and 8 km in diameter contain major microbial build-ups surrounded by nodular limestone and carbonate interbedded with shale (Aitken, 1981; Turner et al., 1992). The Snail Spring Formation consists of mudstone with interbedded siltstone and quartz arenite overlain by laminated and reefal carbonates that were deposited in a shallow marine environment (Aitken, 1981; Worndle, et al., 2019). The overlying Ram Head Fm. consists of stromatolites and ooid grainstones that were deposited on a high energy carbonate platform (Aitken, 1981; Turner et al., 1993, 1997; Turner and Long, 2008, 2012; Worndle, et al., 2019).

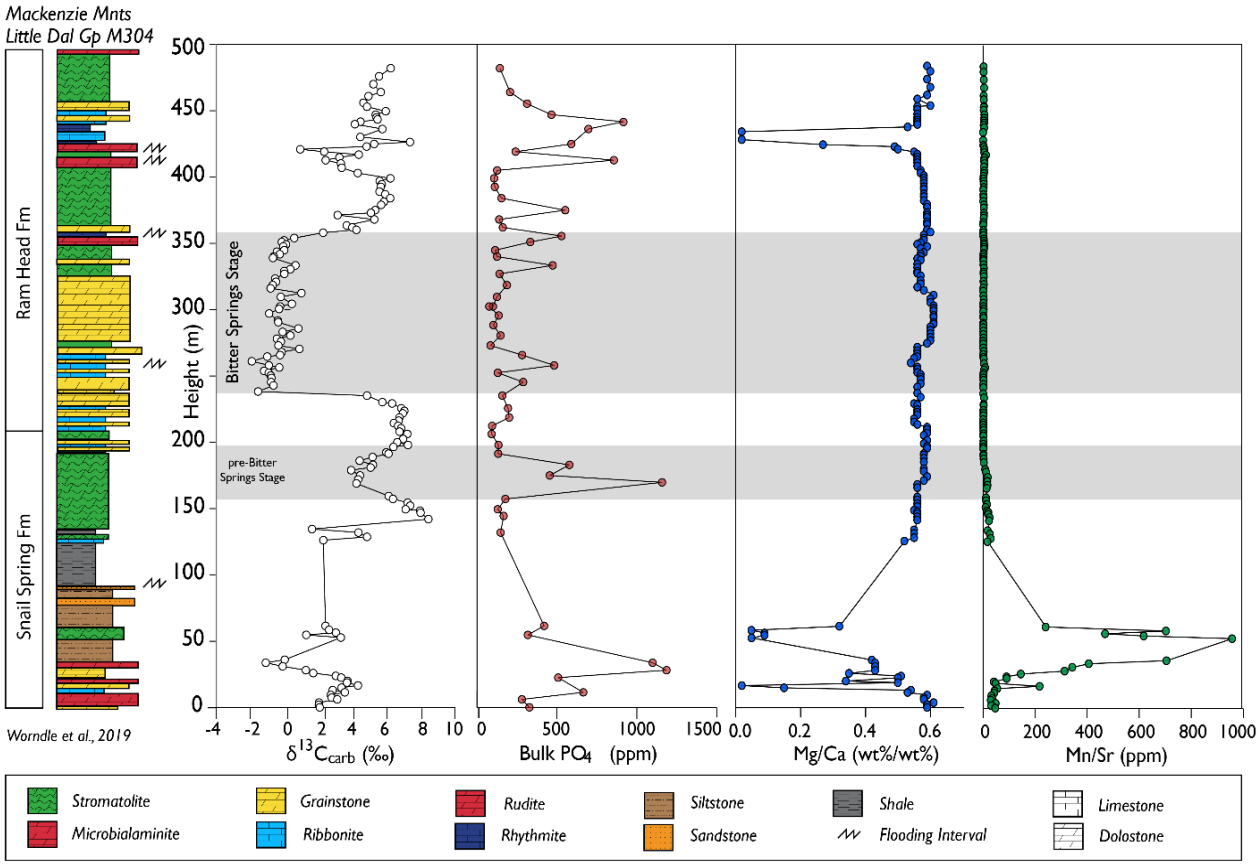

Figure 4. 5 Bulk PO_4 concentrations of carbonates from the Little Dal Group presented against δ13C isotopic signatures, lithological stratigraphy with chemostratigraphic [Mg]/[Ca] and [Mn]/[Sr] ratios (Aitken, 1981; Halverson 2006; Turner and Long, 2008; Wörndle, et al., 2019). The Bitter Springs Stage (carbon isotope anomaly) is indicated by the grey shaded area.

4.5 Methods

4.5.1 Sample selection

A total of 275 samples from 4 stratigraphic sections were analyzed during this study. For bulk carbonate-associated P and solid-state NMR analyses (discussed below), powders were micro-drilled from lithologies that either clearly represented syn-depositional or early diagenetic fabrics (i.e., calcite microspar cement) or were unaffected by later diagenetic veining. Corresponding thin sections were made, cut to 30 microns thickness, doubly polished to facilitate a variety of

microanalyses, characterized by optical microscopy, and imaged correspondingly to link microanalyses to petrographic characteristics.

4.5.2 Bulk PO_4

In order to determine bulk PO_4 concentrations of micro-drilled powders, powdered carbonate rock samples were digested in 10 mL of 1 mol HCl for 24 hours. To fix pH to the desired rage, 2.425 mL aliquots of this solution were added to 2.575 mL of 1 mol NaOH before diluting with deionized milliQ water when necessary. Total dissolved PO_4 analyses of the resulting solutions was spectrophotometrically using the ascorbic acid method, whereby orthophosphate present in the solution is reacted with molybdate in an acid medium to produce a mixed phosphate/molybdate complex. The complex then becomes reduced by ascorbic acid, yielding an intense molybdenum blue color that was measured at 880 nm using a HACH DR2800 spectrophotometer (Baird et al., 2017).

4.5.3 ^{31}P and ^{19}F solid state NMR

In order to constrain the nuclear environment and therefore dominant host phases of P and F present in micro-drilled samples, solid state phosphorous-31 nuclear magnetic resonance (^{31}P NMR) and fluorine-19 nuclear magnetic resonance ($^{1}9F$ NMR) experiments were conducted at Stony Brook University .

4.5.4 Synchrotron µXRF and XANES

Synchrotron X-ray Absorption Near Edge Structure (XANES) and microscopic X-ray fluorescence (µ-XRF and XANES) analyses of carbonate thin sections were performed at the P K-edge (2153 eV) at beamline 14-3 and Fe K-edge (7200 eV) and Sr and Mn K-edge (16200 eV) at beamline 2-3 at the Stanford Synchrotron Radiation Lightsource (SSRL), SLAC National

Accelerator Laboratory. The experiments were performed with the Stanford Positron Electron Accelerating Ring (SPEAR) storage ring containing 500 mA at 3.0 GeV in top-off mode.

The incident energy at both BL 14-3 and BL 2-3 is obtained using a Si(111) double crystal monochromator. The energy at BL 14-3 was calibrated using fluorapatite mineral powder at the P K-edge at 2153 eV. The energy at BL 2-3 was calibrated so that the first derivative maximum inflection of an Fe metal foil was defined to be 7112 eV.

The beamline utilizes a Kirkpatrick-Baez mirror system to micro-focus the beam to achieve a 5x5 micron spot at BL 14-3, and a 2x2 micron spot at BL 2-3. Samples were mounted at 45° to the incident x-ray beam and were spatially rastered in continuous scan mode in front of the incident beam using Newport VP-XL-25 stages. Several thin sections could be mounted simultaneously on a motorized multi-sample holder in the sample chamber.

The incident and transmitted x-ray intensities were measured with helium (BL14-3) or nitrogen (BL2-3) filled ion chambers. The fluorescence lines of the elements of interest were monitored using a silicon drift Vortex detector, using Xpress3 pulse processing electronics. This detector configuration enabled the collection of high-energy resolution fluorescence data at high count rates with minor loss in energy resolution or peak shifts, and an overall reduction in noise (Barkan et al., 2003).

Elemental maps were taken at a resolution of 10-15 micron step size with a dwell time of 250 milliseconds. Data was processed using standard methods using the MicroAnalysis Toolkit (Webb et al., 2011) and SIXPACK software (Webb et al., 2005).

4.5.5 SEM-EDS backscatter

Scanning Electron Microscope (SEM) analyses of highly polished, carbon coated thin sections were performed using a FEI Quanta 650 Emission Gun operated at an accelerating voltage of 15 kV under high vacuum with a dwell time of 10 μs. The SEM is also equipped with an Energy

Dispersive X-Ray detector to facilitate semi-quantitative chemical analysis via Energy Dispersive Spectroscopy (EDS) by AZtec (Oxford Instruments) with a 50 mm detector, aperture of 3 and spot size of 4 using an approximate 2nA beam current.

4.6 Results

4.6.1 PO_4 record within Neoproterozoic carbonates

For each sedimentary succession examined in this study, we present datasets principally to address the following questions: (1) at what concentrations is P present in micro-drilled components?; (2) what minerals host P identified in the samples?; (3) how is P spatially distributed and in which sedimentary/diagenetic components? To address these questions, for each succession we present the results of bulk P analyses and solid-state NMR data of micro-drilled components followed by synchrotron μ-XRF and XANES as well as SEM-EDS data from carbonate hosted phosphate thin-section samples.

4.6.2 Akademikerbreen Group

4.6.2.1 Bulk PO_4

The bulk PO_4 concentration ([PO_4]) of powdered carbonates from the Akademikerbreen Group are presented in Figure 4. 3 along with corresponding $\delta^{13}C_{carb}$ (Halverson et al., 2004, 2005, 2007, 2018; Wörndle, et al., 2019) and [Mn]/[Sr] and [Mg]/[Ca] ratios, which provide a proxy for diagenetic alteration (i.e. Derry et al., 1992; Brand and Veizer, 1980) and a crude geochemical metric for dolomitization, respectively (Figure 4. 3). The overall [PO_4] of the Akademikerbreen Group carbonates exceeds that of modern ooids. Overall, the Akademikerbreen Group is characterized by high [PO_4] throughout, at concentrations that exceed those of modern Bahamian aragonitic ooids (that have concentrations of around 77 ppm [PO_4]; Figure 4. 3, though an increase in [PO_4] values is observed through the Bitter Springs C-isotopic Stage. The Akademikerbreen

Group carbonates exhibit some degree of stratigraphic variability in [PO_4], with elevated concentrations typically corresponding with the more negative $\delta^{13}C$ isotopic values. Bulk [PO_4] generally increases as the succession shallows upward, through the upper interval of the Svanbergfjellet Formation, reaching maximum values in an interval associated with stromatolitic bioherms and dolomitic mudstones and very fine grainstones. Although no correlation between the PO_4 concentrations and [Mn]/[Sr] ratio is evident in these data, high PO_4 concentrations often, though not exclusively, occur with elevated [Mg]/[Ca] ratios in the Grundiesvebreen Fm. and the Svanbergfjellet Fm. However, this relationship is not apparent in the Draken Fm., which generally records syn-depositional and early diagenetic dolomitization and variable silicification (Figure 4. 3), and synchrotron-hosted μ-XRF, XANES, and SEM-EDS.

4.6.2.2 Solid state NMR

Solid state ^{31}P and ^{19}F NMR data were acquired from a subset of micro-drilled powders in order to characterize the mineralogical hosts and local bonding environment of P within the carbonates. Solid state ^{31}P NMR spectra indicate that the mineral phase that hosts PO_4 in the Akademikerbreen Group carbonates is almost entirely apatite, with a chemical shift of ca. 2.5-2.8 ppm. ^{19}F data further show that the dominant host of F is consistent with a trioctahedral silicate (likely talc given petrographic and XRD analyses. In addition, a chemical shift of -102 ppm highlights the presence of fluorapatite, while the presence of a weak band at -88 ppm further corresponds to a "francolite-type defect" arising from F-bonding environments sensitive to the substitution of carbonate for phosphate in francolite (Yi et al. 2013) (Figure 4. 6 and supplementary material, Figure S4 6). Together, these data indicate that much of the P hosted within Akademikerbreen Group carbonates is carbonate fluorapatite (CFA) and P is dominantly carbonate associated PO_4 within CFA. In addition, incorporation of PO_4 into the calcite lattice may be observed by minor changes in the ^{31}P NMR chemical shift of orthophosphate (PO_4) group identified by a broad peak with a chemical shift ca. 3.5 ppm with narrow resonance at 2.9 ppm (Figure 4. 7) (Mason et al., 2007; Philips et al., 2016).

4.6.2.3 μ-XRF and XANES, SEM-EDS

The location and distribution of PO_4 within the Akademikerbreen Group carbonates were both characterized by synchrotron based μ-X-ray Fluorescence imaging (μ-XRF) and XANES analyses, in addition to petrographic and SEM-EDS analyses on thin section samples. μ-XRF mapping reveals that P is widespread and abundant throughout the carbonates and is particularly concentrated within talc cement. XANES spectra taken at the K-edge indicate that P is locked in the mineral apatite (Figure 4. 6). However, μ-XRF and XANES also provide evidence for CO_3-associated, lattice-bound PO_4 that is disseminated within $CaCO_3$ calcite microspar cement and micrite (Figure 4. 7). This carbonate associated PO_4 appears to be characterized by a featureless peak with no post-edge shoulder (as is present in apatite) and a shift to higher energy values (ca. 0.2–0.3 eV) (Figure 4. 7). The spatial distribution of P also indicates that in addition to lattice-bound P and small micron-scale disseminated particles, high concentrations of P are associated with PO_4-rich intraclasts (Figure 4. 6).

SEM-EDS analyses reveal that large P-rich regions are composed of a mixture of talc and apatite where individual crystals of apatite hundreds of nanometers in size are embedded within a talc matrix. This intimate mixture of apatite and talc is often observed as a pore filling cement (Figure 4. 7) or may constitute intraclasts that appear to have precipitated during sediment deposition and early diagenesis, and were subsequently re-worked into surrounding sediments. CFA crystals are engulfed by calcite microspar crystals (Figure 4. 6). SEM-EDS analyses also revealed that individual apatite crystals have been engulfed by coarser calcite and dolomite crystals (Figure 4. 7) and CFA masses define zones concentrated along the edges of coarser calcite and dolomite crystals with euhedral faces. Together these relationships indicate that overgrowths of micrite and/or microspar crystals and diagenetic recrystallization of calcite and dolomite remobilized lattice-bound PO_4 and pre-existing apatite crystals, suggesting that PO_4 concentration within carbonates largely predated early diagenesis. Our analyses also show that apatite-rich cements and intraclasts are associated with thin intraclast conglomerate horizons, suggesting that

apatite filled sedimentary pores at the seafloor which was then physically re-worked (Figure 4. 6). μ-XRF and XANES spectroscopy also identified abundant apatite crystals and intraclasts that were trapped and concentrated along stromatolitic laminae (Figure 4. 7). The relationships of these particles with surrounding calcite and dolomite crystals and the textural features indicative of trapping and binding rather than precipitation processes (Knoll, 2015) strongly indicate a detrital origin. For example by the observed upward accretion of the finely laminated structure (Bosak et al, 2013) and the observed particles suggests that CFA intraclasts and particles were continuously provided from the water column or surrounding sediments during the time that stromatolites were trapping and binding sediment on the seafloor. This may have been facilitated by hypothetical exopolymeric substances (EPS) that traps nanoscale detrital particles and nutrients (Papineau et al 2015), which is hypothesized to be the principal accretion mechanism of stromatolites in Proterozoic oceans (Knoll, 2015).

μ-XRF analyses also reveal that Akademikerbreen Group carbonates are characterized by elevated Sr in calcite microspar and high background Sr in the carbonate matrix as well as low Mn/Sr and slightly contrasting distributions of Sr and Mn within thin beds (not shown). The low Mn/Sr indicates that the carbonates are well preserved (i.e., Derry et al., 1992), and have not undergone significant diagenesis that would have expelled Sr and incorporated Mn (i.e., Brand and Veizer, 1980). Ca and Sr are closely associated with a positive correlation. Fe is very minor within the samples and XANES spectra show that Fe appears to be bound in detrital chlorite rather than in minerals such as pyrite or iron oxide minerals.

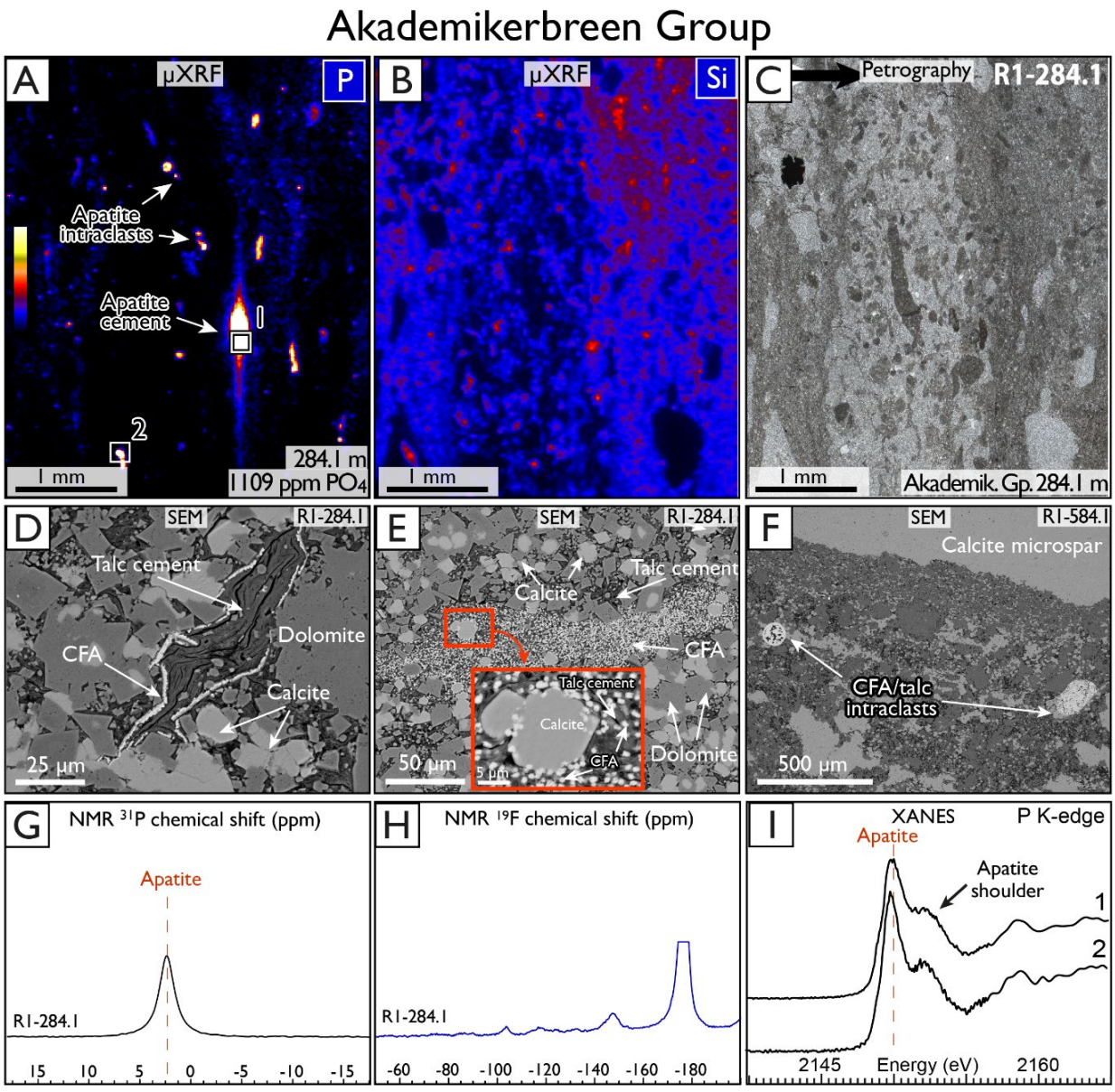

Figure 4. 6 Synchrotron based µ-XRF and XANES analyses of Akademikerbreen Group carbonate sample from the Svanbergfjellet Formation, Svalbard. A: P µXRF map indicates the distribution of P. B: µXRF map indicates the corresponding distribution of Si. High µXRF elemental abundance is indicated by lighter colours (white–red) and low abundance is indicated by cooler colours (black–blue). P mapping reveals P cement, P intraclasts and abundant disseminated P within calcite microspar and micrite. C: Petrographic image of the corresponding mapped area in plane polarized light indicate an intraclast-rich microspar horizon. D: SEM-EDS analyses of the P-rich bright spots reveals that P is hosted by CFA associated with talc cement, as intraclasts and bound within calcite. I: XANES spectra provide evidence that the P is present as apatite, identified by the characteristic 'apatite shoulder'. The XANES spectra are numbered with locations labelled on the P µXRF map (A).

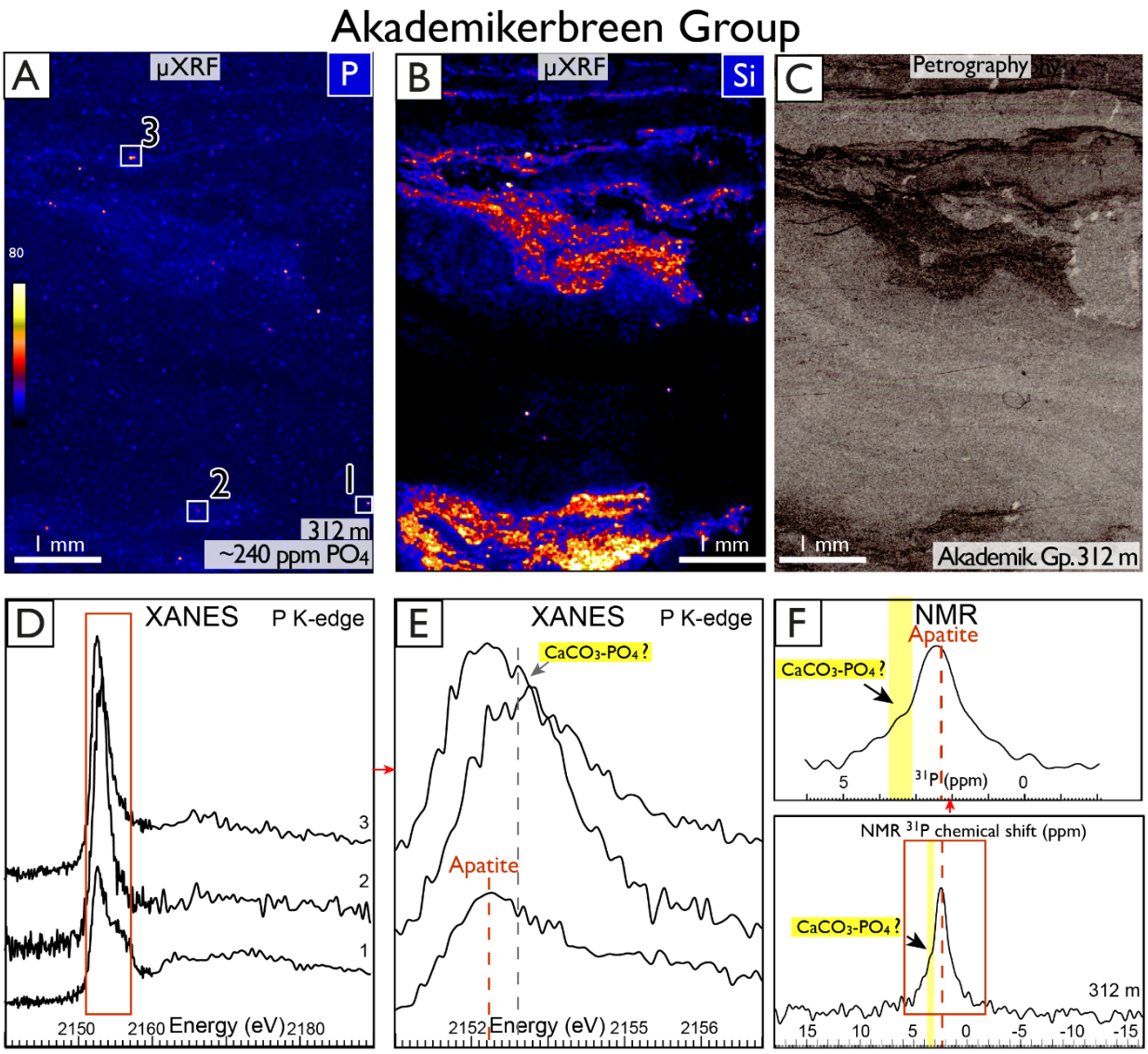

Figure 4. 7 Synchrotron based µ-XRF and XANES analyses of Akademikerbreen Group carbonate sample from the Svanbergfjellet Formation, Svalbard. A: P µXRF map indicates the distribution of P which is present as CO_3-associated PO_4 that is disseminated within $CaCO_3$ calcite microspar cement and micrite. The spatial distribution of P also indicates that in addition to lattice-bound P, high concentrations of P are associated with PO_4-rich intraclasts and micron-scale disseminated particles. B: µXRF map indicates the corresponding distribution of Si. C: Petrographic image of the corresponding mapped area in plane polarized light. D: XANES spectra of the carbonate associated PO_4 are characterized by a featureless peak (spectra 2 and 3) with no post-edge shoulder (as is present in apatite – spectra 1) and a shift to higher energy values (ca. 0.2–.3 eV). E: Zoomed in area emphasizing the shift in energy values characteristic of the CO_3-associated PO_4. XANES spot spectral analyses locations are labelled on the P µXRF map (A). F: Bulk ^{31}P NMR analyses with a zoomed in section over the dominant P bearing phase is apatite. Additional incorporation of PO_4 into the calcite lattice may be observed by the small shoulder observed at ca. 3.4 consistent with minor changes in the ^{31}P NMR chemical shift of orthophosphate (PO_4) group within the calcite lattice (Mason et al., 2007; Philips et al., 2016).

4.6.3 Fifteenmile Group

4.6.3.1 Bulk PO_4

Overall, bulk PO_4 concentrations through the Fifteenmile Group within the Tatonduk Inlier (Cohen et al., 2017) increase upward through the stratigraphic section with concentrations well over 1000's ppm. Trace element data determined by ICP-MS on bulk digested sample powders (i.e., from Cohen et al., 2017) show that P concentrations generally increase with $CaCO_3$ content (Figure 4. 4). The Fifteenmile Group has both higher average and individual [PO_4] relative to the Akademikerbreen Group. Although there is minor presence of TOC in the section, there is no apparent relationship corresponding with high [PO_4]. The Fifteenmile Group carbonates appear to exhibit some stratigraphic variability in PO_4, with lower [PO_4] corresponding with the dolostone lithology and a slightly more positive $\delta^{13}C$ isotopic signature, which corresponds with the post Bitter Springs Stage of the Akademikerbreen Group carbonates. This signal may be a result of early marine diagenesis.

4.6.3.2 µ-XRF and XANES, SEM-EDS

µ-XRF and XANES spectroscopy indicate that P is dominantly located in authigenic apatite intraclasts and finely disseminated apatite crystals that are abundant in the largely micritic carbonate matrix; these components are particularly concentrated along bedding laminations (Figure 4. 8). SEM-EDS and µ-XRF spectroscopy were also used to identify examples of P in pore-filling authigenic apatite cement. Together, the presence of several different types of PO_4 within the Fifteenmile Group carbonates suggests that PO_4 was available at the time of sedimentation as detrital sediment and as a dissolved species in seawater or pore water.

The Sr µ-XRF distribution maps (Figure 4. 8) also reveal that Fifteenmile Group samples are characterized by elevated Sr in the carbonate matrix and particularly concentrated in calcite microspar intraclasts and cement. Low total Mn and low Mn/Sr are also observed, which indicates

that the carbonates are well preserved (i.e., Derry et al., 1992), and have undergone minimal recrystallization (i.e., Brand and Veizer, 1980).

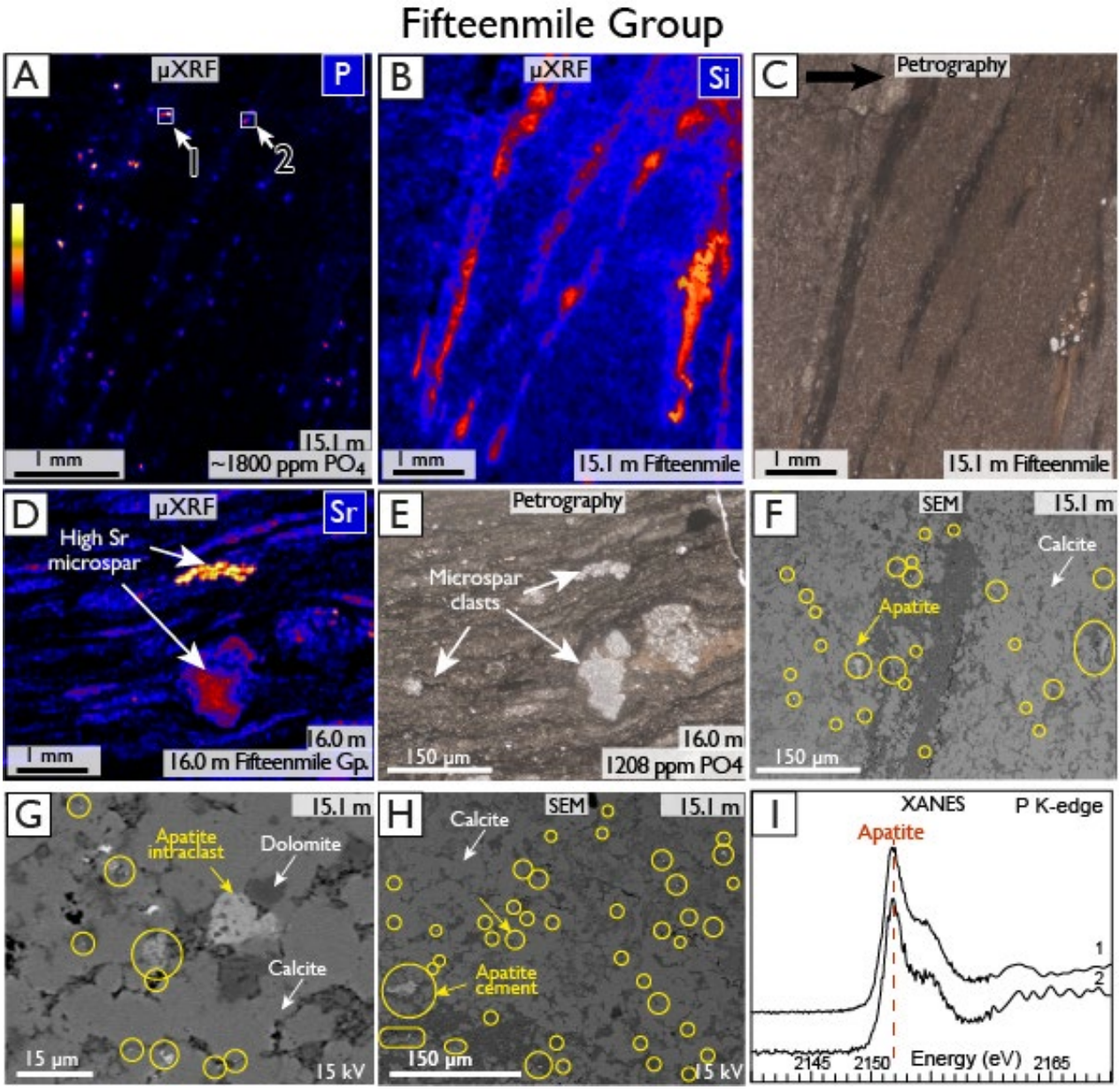

Figure 4. 8 Synchrotron based µ-XRF and XANES analyses of Fifteenmile Group carbonate sample from the Tatonduk Inlier Reefal assemblage. A: P µXRF map indicates the distribution of P, which is present as authigenic intraclasts, disseminated within $CaCO_3$ calcite microspar cement and throughout the micrite. The spatial distribution of P also indicates that in addition to lattice-bound P, high concentrations of P are associated with PO_4-rich intraclasts, pore-filling cement. B: Si µXRF map indicates corresponding concentrated Si along bedding planes. C: Petrographic image of the mapped area in plane polarized light corresponding with images A and B. Arrow indicates way up. D: Sr µ-XRF map acquired at the Fe K-edge (7200 eV) indicates elevated Sr concentrated in calcite microspar intraclasts and cement. E: Petrographic image corresponding with the Sr mapped area in plane polarized. F–H: SEM-EDS analyses of apatite cement, CO_3-associated PO_4 cement circled in yellow and apatite intraclasts. I: XANES spectra of apatite cement and intraclasts. XANES spot spectral analyses locations are labelled on the P µXRF map (A).

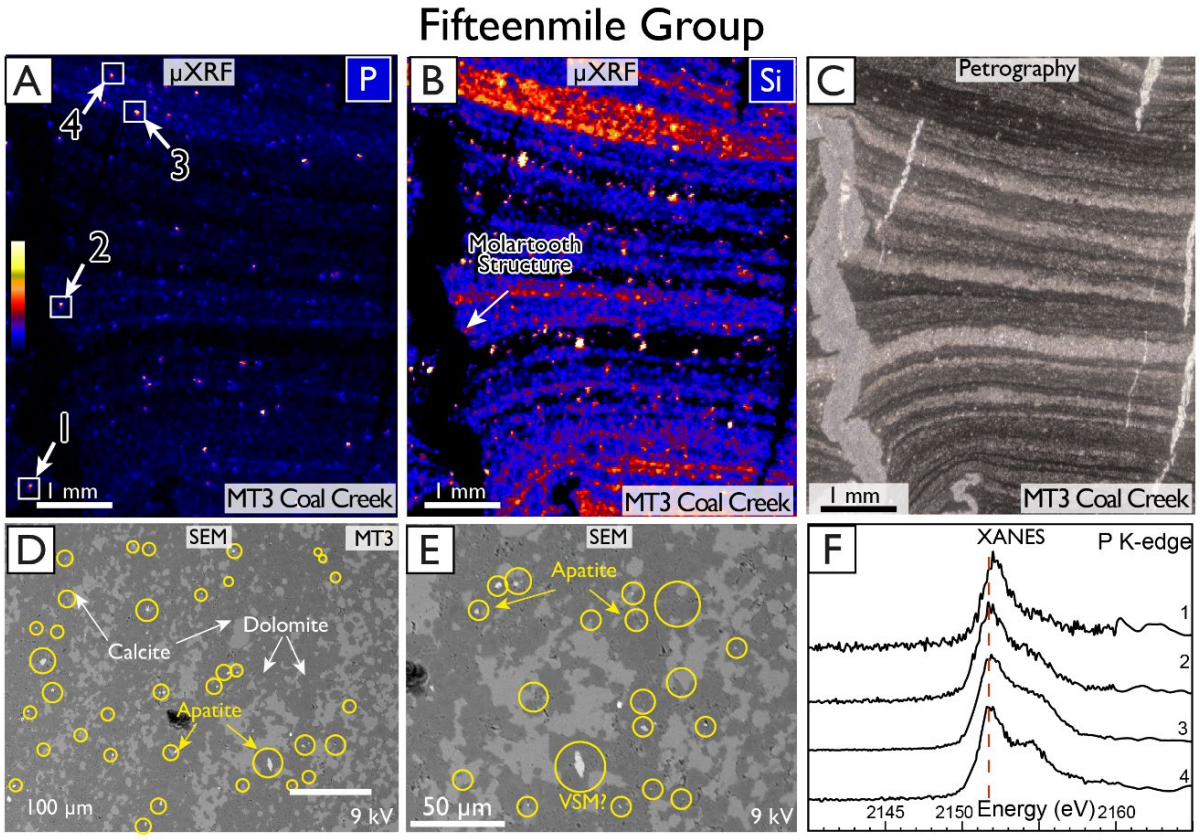

Figure 4. 9 Synchrotron based µ-XRF and XANES analyses of Fifteenmile Group molar tooth structure filled with calcite microspar within laminated microspar-dolomicrite from the Coal Creek Inlier, Canada. A: P µXRF map indicates the distribution of P, which is present as is disseminated within $CaCO_3$ calcite microspar cement and micrite. The spatial distribution of P also indicates high concentrations of P in PO_4-rich intraclasts and micron-scale disseminated particles throughout the laminar horizons. B: µXRF map indicates the corresponding distribution of Si. C: Petrographic image of the corresponding mapped area in plane polarized light indicating syn-depositional molar tooth structures. D–E: SEM-EDS analyses indicates that disseminated apatite crystals are abundant in the largely micritic carbonate matrix and are identified within calcite and dolomite crystals and in between crystal boundaries. F: XANES spectra contain a characteristic shoulder indicative of apatite with two possible variations. XANES spot spectral analyses locations are labelled on the P µXRF map (A).

4.6.4 Little Dal Group

Bulk [PO_4] within the Little Dal Group is characterized by minimum values of ca. 77 ppm increasing to maximum values ca. 1185 ppm with a mean of ca. 326 ppm (Figure 4. 5). The base of the section is characterized by high [PO_4], which then rapidly decreases. This trend repeats and is followed by an overall increasing trend higher up in the stratigraphic section. The Little Dal

Group carbonates do exhibit some stratigraphic variability in which high [PO_4] corresponds strongly with more negative $\delta^{13}C$ isotopic signatures (Figure 4. 5), broadly consistent with both the Akademikerbreen Group and the Fifteenmile Group. The Little Dal Group exhibits some lithological variability with significantly high [PO_4] of around 1185 ppm characterizing stromatolitic horizons and the highest bulk [PO_4] generally corresponding with microbialaminite, stromatolites and ribbonites.

4.6.4.2 Solid state NMR

^{31}P NMR spectra from a subset of micro-drilled samples indicate that the mineral phase that hosts PO_4 in the Little Dal Group carbonates is predominantly apatite with resonance peak identifiable on the NMR spectra (Figure 4. 10). The ^{31}P NMR phosphorous speciation data generally yields an apatite-like ^{31}P signal ca. 2.8 ppm (Figure 4. 10). ^{19}F data indicate a fluorapatite F peak, and some but not all of the Little Dal Group spectra contained a carbonate defect determined by a resonance peak shift in the NMR spectra that indicates carbonate substitution for PO_4, known as β-type carbonate substitution (supplementary material Figure S4 6). However, the ^{19}F "francolite-type defect" is difficult to discern in these spectra due to the typically low fraction of F, which is sensitive to CO_3 substitution. The ^{19}F peak near -150 ppm likely arises from dioctahedral phyllosilicates Sample 28.2 yielded very broad ^{31}P and ^{19}F peaks this may result from high-Fe content as suggested by the broad peaks and wide spinning sideband pattern in the ^{19}F spectrum (supplementary material Figure S4 6). In addition, incorporation of PO_4 into the calcite lattice may be observed by minor changes in the ^{31}P NMR chemical shift of orthophosphate (PO_4) group within the calcite lattice identified by a broad peak with a chemical shift near ca. 3.5 ppm with narrow resonance at 2.9 ppm (Figure 4. 7) (Mason et al., 2007; Philips et al., 2016).

4.5.4.3 µ-XRF and XANES, SEM-EDS and petrography

µ-XRF and XANES spectroscopy show that P is present as apatite, which is widely distributed and prolific within the micrite matrix. Most significantly, however, these microanalyses indicate

that the apatite is in the form of a cement that may be a product of diagenetic remobilization (Figure 4. 10). SEM-EDS shows large, up to 50 μm, euhedral apatite minerals that are abundant and exhibit hexagonal morphology. These occur extensively within dolomite minerals and K-Al-Si-rich clays (Figure 4. 10). Smaller euhedral apatite crystals are also abundant and occur within clay and dolomite and throughout micritic sediment within the formation. Apatite is clearly abundant in the Little Dal Group and is most notably present as large intraclasts within dolomite crystals, surrounding mineral crystal boundaries, within clays and within pore space (Figure 4. 10). SEM-EDS analyses identified the presence of another style of morphologically distinctive elongate lath-like apatite minerals that are common in some samples and are concentrated in dolomite minerals or pore spaces within some of the Little Dal samples (Figure 4. 10).

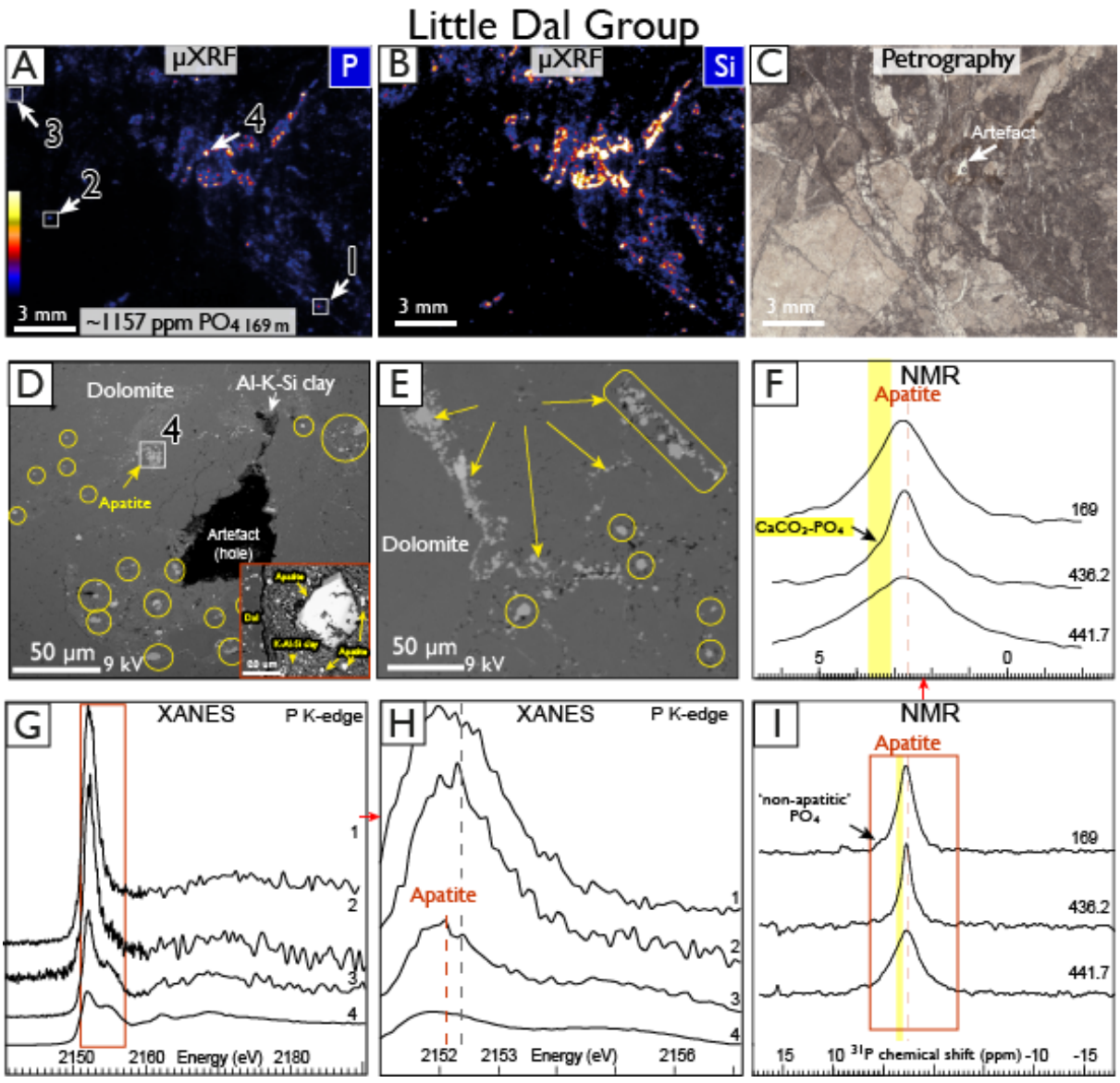

Figure 4. 10 Synchrotron based µ-XRF and XANES analyses of Little Dal Group carbonate sample from the Snail Spring Formation, Canada. A: P µXRF map indicates the distribution of P, which is widely distributed and prolific within the micrite matrix. Significant apatite is present in the form of a cement that may be a product of diagenetic remobilization or syn-diagenetic fluid interaction. D: SEM-EDS show extensive widespread concentrations of apatite including large, up to 50 µm, euhedral PO_4 minerals with hexagonal morphology within dolomite minerals and K-Al-Si-rich clay. E: Large, up to 30 µm apatite concentrated within and between boundaries of dolomite crystal. Smaller euhedral apatite crystals are also abundant and occur throughout micritic sediment, clay and dolomite. Additional varieties of PO_4 are also present including CO_3-associated PO_4. F: ^{31}P NMR speciation data generally yields an apatite-like ^{31}P signal (ca. 2.8 ppm) but is broad and shifted to slightly higher values ca. 3.0 ppm. Shoulder and low-intensity broad peaks characterize the presence of additional species and CO_3-associated PO_4 is indicated by a small hump ca. 3.4 ppm. G: XANES spectra indicate apatite with two possible variations (spectra 3–4). Possible CO_3-associated PO_4 are characterized by a featureless peak (spectra 1–2) with no post-edge shoulder and a shift to higher energies (ca. 0.2–0.3 eV). In addition, self-absorption effects are evident in the XANES spectra. H: Zoomed in area emphasizes the energy shift characteristic of CO_3-associated PO_4 (XANES locations are labelled on the P µXRF map (A). I: Zoomed out area of ^{31}P NMR speciation data (image F above) indicating variations between samples.

4.7 Discussion

4.7.1 $CaCO_3$-associated P in Tonian carbonate rocks

Together, our data show that Tonian carbonate successions are generally associated with high concentrations of PO_4 compared to modern carbonate sediments. The carbonate-associated phosphate can be categorised into (1) individual PO_4 ions incorporated within the calcite and/or dolomite lattice (or "lattice-bound" phosphate), (2) individual micron to sub-micron-sized crystals of CFA of largely intraformational origin, (3) authigenic apatite-talc precipitates that fill pores and occasionally re-distributed as intraclasts, and (4) diagenetically remobilized P. The presence and distribution of these phosphatic components provides strong evidence that several Tonian carbonate depositional environments were characterized by elevated aqueous concentrations of PO_4. For instance, laboratory studies have shown that P may be incorporated into the calcite lattice if the crystal grows in an aqueous environment containing sufficient aqueous PO_4 (Mason et al, 2007; Phillips et al., 2016). This lattice-bound P occurs dominantly within calcite microspar cement, which is a ubiquitous and distinctive component of Tonian carbonate rocks (James et al., 1998; Sherman, 2000; Bishop and Sumner, 2006). Geochemistry, sedimentology and petrography have shown that calcite microspar cement is largely syn-depositional in origin (James et al., 1998; Sherman, 2000; Bishop and Sumner, 2006) derived from fluids dominated by contemporaneous seawater and reflects unusually high $CaCO_3$ supersaturation (Strauss and Tosca, 2020). Thus, our documentation of lattice-bound PO_4 within this component indicates that PO_4 was available in the water column as microspar nucleated from pore/bottom waters that were highly supersaturated with respect to $CaCO_3$.

In addition, the widespread production of CFA crystals and their continuous sedimentation in carbonate mudstones, grainstones and stromatolites indicates that CFA was produced authigenically at or near the seafloor. First, authigenic apatite of marine origin typically produces sub-micron scale CFA crystallites (Lucas and Prevot-Lucas, 1997) which we have

documented are ubiquitous in Tonian carbonate successions. In contrast, detrital igneous apatite typically occurs as macroscopic, euhedral crystals (Paquet and Clauer, 1997) composed of fluorapatite rich in trace and rare-earth elements (Nash, 1984). All three sedimentary successions analyzed in this investigation preserve remarkable evidence or microscopic CFA though, the Little Dal Group provides evidence of euhedral fluorapatite of potential detrital/igneous origin, consistent with higher concentrations of dioctahedral silicates. Finally, in addition to sub-micron scale authigenic CFA crystals, CFA co-precipitation with talc as cements and intraclasts further indicates that the two minerals were occasionally generated from the same fluid and that relatively alkaline conditions were sometimes associated with appreciable concentrations of aqueous phosphate.

4.7.2 Controls on P availability during $CaCO_3$ sedimentation

What processes may have increased the concentration of aqueous phosphate in Tonian carbonate depositional environments? Phosphorus can be concentrated in modern sediments deposited in coastal upwelling environments through the microbial degradation of organic matter within sediments, which can be further aided by the release of polyphosphate. Alternatively, P can be concentrated in modern non-upwelling oxic sediments through the remineralization of organic matter and the reductive dissolution of Fe-oxides; this liberates previously adsorbed phosphate to sediment pore waters and produces early diagenetic apatite. Sediments deposited under euxinic conditions typically release PO_4 liberated from organic matter back to the water column (i.e., Lenton and Daines, 2018).

However, our data are inconsistent with redox-dependent remineralization of organic matter as the principal source of phosphate to Tonian carbonate successions. First, the samples investigated here are all exceptionally lean in organic matter (i.e., Cohen et al., 2017) which is consistent with low TOC values recovered in siliciclastic equivalents of the stratigraphy investigated here (Kunzmann et al., 2015). Although very low organic matter concentrations

could be interpreted to indicate efficient remineralization under, for example, oxic conditions, the geochemical consequences of aerobic remineralization are at odds with geochemistry required for the generation and preservation of calcite microspar, a ubiquitous component of these successions (James et al., 2000). This is because aerobic remineralization produces DIC with no overall change in total alkalinity which serves to decrease $CaCO_3$ supersaturation (Soetaert et al., 2007). In other words, if this process were dominant in providing PO_4 to pore and bottom waters, $CaCO_3$ would eventually become undersaturated and promote $CaCO_3$ dissolution, as it does in modern temperate carbonate depositional environments (James et al., 2005). In addition, our observations are also inconsistent with anaerobic remineralization of organic matter. For example, although microbial iron reduction is an efficient alkalinity pump (Soetaert et al., 2007) mass balance considerations demand that significant quantities of Fe^{2+} be released to accompany this metabolic process. Specifically, laboratory constraints show at the $CaCO_3$ supersaturation (and associated DIC and alkalinity) required to promote microspar and talc precipitation, even minimal amounts of Fe^{2+} would be immediately precipitated as siderite (Roest-Ellis et al., 2020; Jiang C. Z. and Tosca, 2019). Indeed, extensive characterization of the concentration and distribution of Fe through micro-XRF, XANES, and SEM-EDS shows that it is largely present at minor to trace concentrations and bound almost exclusively in detrital silicate minerals such as chlorite and illite (supplementary material Figure S4 1 and S4 2 in appendix). Although ocean-atmosphere redox pumping leads to enhanced PO_4 accumulations (Laakso et al., 2020), we see no significant evidence for Fe minerals, indicating that Fe redox pumping is likely not a major contributor to the enhanced PO_4 accumulations in the depositional environments investigated here. Similarly, these data show that pyrite is relatively rare within the intervals investigated here; indicating that microbial SO_4 reduction of organic matter played a minimal role in providing aqueous PO_4 to the depositional system.

In addition to chemical release of phosphate from polyphosphate (reductive dissolution), microbes can influence PO_4 accumulations. For example, increased phosphate concentrations recorded in some anoxic sediments may result from the active microbial release of phosphate

from polyphosphate (Brock, 2011). These microbes may have also played a role in fixing phosphate in marine sediments in the Proterozoic and Archean following the Great Oxidation event (ca. 2.4 Ga) when nearshore environments became sufficiently enriched in photosynthetic oxygen to facilitate Fe-redox pumping of pore water phosphate by coupled microbial and redox concentration of bioavailable phosphorus in coastal settings (Brock, 2011). However, there is little observed evidence (or at least little preserved evidence) of Fe-redox mechanisms.

Minimal concentrations of organic matter, a lack of metabolic products recording the influence of anaerobic remineralization, and geochemical constraints on Tonian $CaCO_3$ production all indicate that diagenetic production of phosphate played a negligible role in providing it to Tonian carbonate depositional systems. This indicates that significant background concentrations of aqueous phosphate may have instead been supplied directly by seawater. A variety of petrographic observations support the conclusion that the $CaCO_3$, talc and apatite components we observe formed syn-depositionally and from solutions dominated by contemporaneous seawater.

First, a variety of data shows that $CaCO_3$ microspar precipitation, the dominant component of successions examined here, took place (1) before appreciable compaction of the sediment, and (2) while the sediment itself was susceptible to physical re-working. For example, differential compaction features of sediment around microspar cements commonly represent more than 10x collapse of the initial sediment thickness at the time microspar crystallized (Westphal et al., 2000), indicating a highly porous substrate containing more water than sediment. In addition, microspar clasts and microspar grainstone lags are widely common in a number of late Mesoproterozoic and Tonian carbonate successions, which reflects the erodibility of the sediment shortly after microspar precipitated (Figure 4. 7). In fact, the fine-grained lime mudstones of the Fifteenmile Group in the Tatonduk inlier (Figure 4. 7) are largely composed of re-worked and eroded $CaCO_3$ microspar and include microclasts of apatite.

In addition, the presence of talc and microspar within Tonian successions further attests to a syn-depositional origin from fluids dominated by seawater. Although Tosca et al. (2011) initially interpreted the Mg-silicate nodules within the Svanbergfjellet Formation as a wholly diagenetic phenomenon, this explanation is at odds with mass balance constraints as well as geochemical and sedimentological data. The presence of pore-filling microspar and talc requires the delivery of significant amounts of seawater through the uppermost portion of the sediment (Bishop & Sumner, 2006). If we assume that seawater [Ca] was equivalent to 10 mmol/kg (i.e., Spear et al., 2014), and assume that only 50% of the microspar volume was originally precipitated (and the remaining 50% precipitated as a later overgrowth), a microspar-rich ribbon 7 x 5 x 1 cm in size requires more than 47 liters of seawater to form. This strongly supports the inference that synsedimentary microspar cement, like any other syn-depositional $CaCO_3$ cement, reflects seawater more than diagenetic fluids (a conclusion reached by many previous authors, including Bishop and Sumner, 2006 and James et al., 1998). In fact, Bishop and Sumner (2006) proposed that such large amounts of seawater could be injected into underlying permeable and porous sediments through the combination of hydrostatic responses to wave oscillation (i.e., storms or fair-weather waves).

In light of geochemical and petrographic evidence that $CaCO_3$ microspar and talc represent authigenic precipitates derived from contemporaneous seawater, it follows that lattice-bound PO_4 within microspar, commonly identified in XANES spectra (and NMR) reflects the presence of background concentrations of PO_4. Similarly, the co-precipitation of talc and apatite in the form of pore-filling cements and intraclasts allows us to place strong constraints on the concentration of total inorganic phosphorus in contemporaneous seawater. A number of experimental studies have shown that the homogeneous precipitation of apatite from seawater instead begins with the nucleation of a precursor phase, which arises from the strong inhibitory effect of Mg^{2+} on apatite growth (Golubev et al., 1999; Johnsson and Nancollas, 1992; Gunnars et al., 2004). These studies have shown that the precursor phase is commonly octacalcium phosphate (OCP), which then recrystallizes to hydroxyapatite or carbonate fluorapatite (CFA)

(i.e., Oxmann and Schwendenmann, 2014). If we accept that OCP nucleation represents a key threshold that seawater must have exceeded in order to trigger apatite precipitation, then we can examine the controls on this threshold in light of our observation that apatite co-precipitated with talc. Accepting that talc precipitation from seawater requires a minimum pH of 8.5 (Tosca et al., 2011; Strauss and Tosca, 2020) the total inorganic phosphorus required to nucleate OCP can then be evaluated as a function of Ca^{2+} concentration (Figure 4. 11). Available constraints on marine Ca^{2+} concentration for Tonian successions can be derived from fluid inclusions from the Browne Formation (Spear et al., 2014) and the presence of gypsum-before-halite evaporites deposited intermittently through Tonian global stratigraphy. This implies that seawater Ca^{2+} likely resided within the range of 6-12 mmol/kg (Spear et al., 2014). These constraints in turn imply that in order to generate talc-apatite co-precipitates total inorganic phosphorus concentrations likely fell within the range of 30-80 μmol/kg P, over an order of magnitude higher than modern global marine phosphorus concentrations.

This relationship also implies that changes in Ca^{2+} are likely exert a strong control on the degree of PO_4 accumulation in seawater and sediments. For instance, if marine Ca^{2+} decreases, then marine phosphate concentrations in turn increase, which may increase sedimentary concentrations of P accordingly. This may provide a simple explanation for stratigraphic variability in total P we observe within the Akademikerbreen and Fifteenmile Groups, which show variability in P that corresponds with petrographic indications of high alkalinity (i.e., microspar and talc; Figure 4. 11) which may have led to transiently low Ca concentrations.

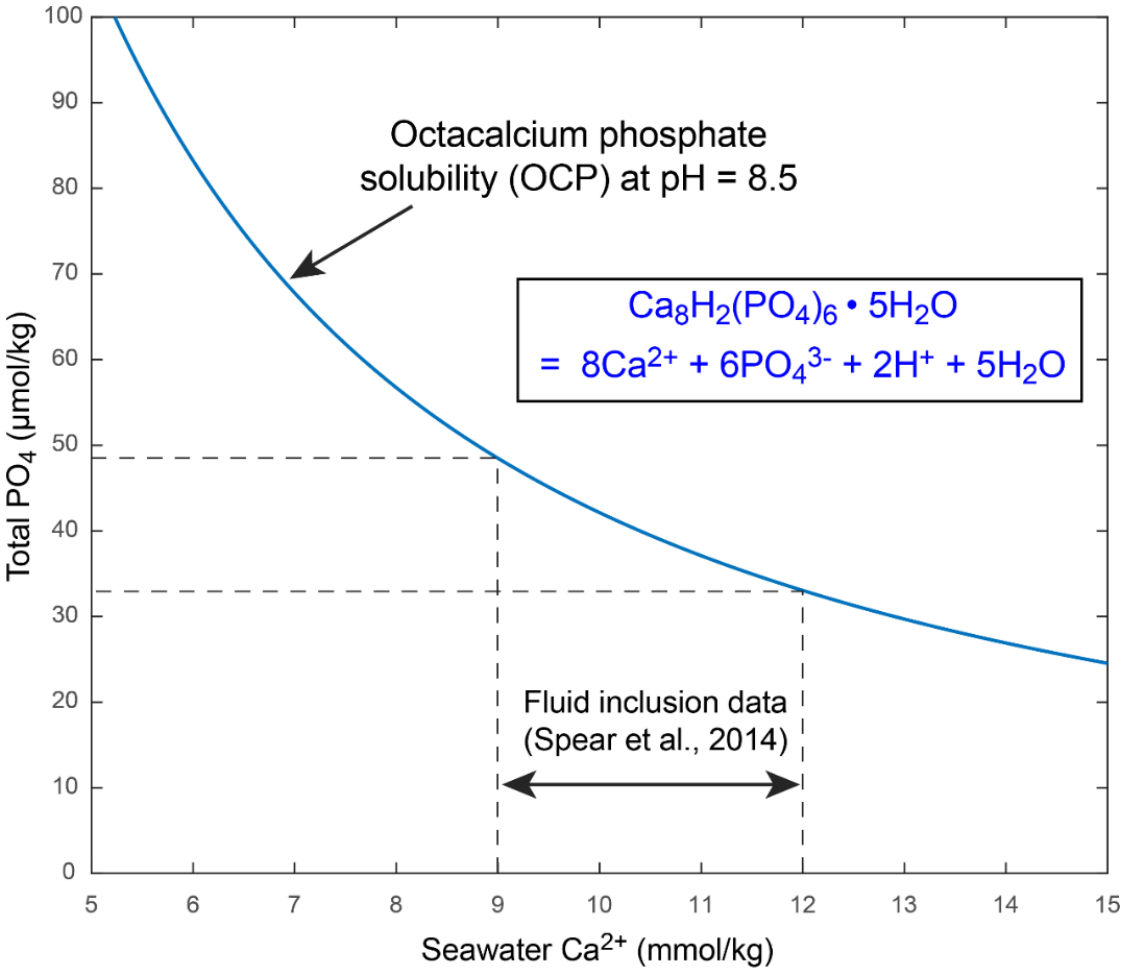

Figure 4. 11 Solubility of OCP precursor phase to hydroxyapatite and carbonate CFA in seawater. Accepting that talc precipitation from seawater requires a minimum pH of 8.5 (Tosca et al., 2011; Strauss and Tosca, 2020) the total inorganic phosphorus required to nucleate OCP can then be evaluated as a function of Ca^{2+} concentration. For Tonian successions Ca^{2+} concentration can be derived from fluid inclusions from the Browne Formation (Spear et al., 2014). These constraint indicate that in turn imply that in order to generate talc-apatite co-precipitates, total inorganic phosphorus concentrations likely fell within the range of 30-80 µmol/kg P, over an order of magnitude higher than modern global marine phosphorus concentrations.

4.8.3 Implications for the late Proterozoic P cycle

Our observations expand upon increasing evidence that aqueous PO_4 was abundant and bioavailable in Tonian basins across the world, and provide geochemical and petrographic constraints that illuminate the state of the Tonian P cycle. For example apatite scale microfossils (ASMs) have been identified within the Tonian Fifteenmile Group within the Tatonduk Inlier (Cohen and Knoll 2012; Cohen et al 2017) and in the Vsingso Group, Sweden (Moczydłowska et al., 2018), as well as phosphatic scales in vase shaped microfossils across four sedimentary basins (Riedman et al., 2020). These observations all indicate that phosphate was available at non-limiting concentrations in order to support independent acquisition of apatite biomineralization (Cohen et al 2017). Our data confirm this conclusion, and provide observational evidence that the standing pool of total dissolved phosphate was significantly higher through much of the Tonian than in the modern ocean.

The burial efficiency of seawater P in marine sediments has been suggested to influence the cycling and concentration of P in the ocean (Filippelli and Delaney, 1992; Ruttenberg and Berner, 1993) yet appreciable differences in P accumulation rate records relative to continental weathering rates indicates that P influx can become decoupled from other dissolved components (Filippelli and Delaney, 1994). Although P appears to have been cycled intensely during the late Proterozoic, and the following Ediacaran period is characterized by periods of phosphogenesis, recent compilations of sedimentary P content from shales coupled with mass balance constraints show that phosphorite deposits only account for a minor proportion of the total P influx to the ocean (Laakso, et al., 2020). It is important to note that these compilations do not provide a statistically significant difference in sedimentary P content throughout much of the Neoproterozoic (Laakso et al., 2020). Therefore, the style of P cycling during the late Proterozoic may be more suitably explained by major water column remineralization and internal P cycling models of P accumulation and burial outlined by Lenton and Daines (2018) and Ingall et al., (1993) that likely influenced total aqueous PO_4 concentrations rather than changes to overall

oceanic P fluxes (Laakso et al., 2020). This is supported by the low export flux of organic-C that is well documented from Precambrian sediments (Schrag et al., 2013; Kunzmann et al., 2015; Laakso and Schrag, 2018; Sperling and Stockey, 2018) and corroborated by our observations from this investigation that indicate a lack of organic-C and a lack of minerals linked to anoxic respiration. Following this, toward the end of the Neoproterozoic and early Paleozoic, a 'biological pump' would have become increasingly efficient in the Paleozoic as eukaryotes evolved and enhanced P and organic-C burial and facilitated oxygen sensitive bioturbation that expanded the oxygenated zone and helped to regulate early oxygen and P cycles (i.e., Boyle et al., 2014; Lenton and Daines, 2018).

4.8.4 Implications for $CaCO_3$ precipitation

Tonian aged carbonates often record high Sr concentrations and increasing $^{87}Sr/^{86}Sr$ values which indicates a time of high hydrothermal and river water flux, likely related to the breakup of the supercontinent Rodinia (i.e., Derry et al., 1989; Asermon et al., 1991; Halverson, et al., 2007). In addition, high Sr concentrations are often recorded in carbonate sediments of Neoproterozoic age which is often used to infer that the primary mineralogy is aragonite or was former aragonite that may have recrystallized to the energetically more stable calcite or dolomite. Yet although we observe high Sr concentrations in these carbonates, we observe no petrographic evidence for aragonite in any of these samples. This observation was also noted by Fairchild and Spiro, (1987) who identified no preserved evidence of former aragonite based on petrographic examination of late Proterozoic microspar cement. The carbonates from the three successions investigated in this study are also dominated by microspar, an enigmatic carbonate cement that has an unconfirmed primary mineralogy (i.e., James et al., 1998), but is characterized by high Sr. Recent research hypothesizes that the lack of an aragonite precursor to Proterozoic calcite microspar cement can be explained by non-traditional $CaCO_3$ mineralization pathways under high $CaCO_3$ saturation seawater (Strauss and Tosca, 2020) in the presence of high atmospheric pCO_2 that sustained excessive marine $CaCO_3$ supersaturation (Tosca et al., 2011). This pathway is made possible by

the presence of dissolved inhibiting compounds that would have subsequently influenced rates and styles of $CaCO_3$ sedimentation (Strauss and Tosca, 2020). This formation pathway for late Proterozoic calcite microspar cement may be explained by the precipitation of an amorphous $CaCO_3$ (ACC) precursor and subsequent recrystallization to calcite (Bishop and Sumner, 2006; Pollock et al., 2006) in the presence of minor concentrations of dissolved PO_4 in late Proterozoic Tonian composition seawater (Roest-Ellis, et al., 2020). This is further supported by experimental evidence and μXRF analyses showing that synthetic PO_4-doped calcite produces PO_4 species very similar to those recorded in Proterozoic carbonates (supplementary material, Figure S4. 5).

The observed high Sr in Proterozoic calcite microspar is also supported by the formation of calcite via an amorphous precursor to calcite. This is because ACC is relatively indiscriminate to trace element uptake and therefore captures unusually high concentrations of Sr (Littlewood et al., 2017). Together, the conditions resulting in elevated marine PO_4 may have played a significant role in the mineralogy and style of Precambrian carbonate deposition. This would explain the presence of high [PO_4] within these carbonates alongside calcite microspar cement that records high Sr concentrations. High PO_4 concentrations in Proterozoic seawater may also be linked to kinetic controls that influenced secular variation in Proterozoic carbonate precipitation (i.e., James et al., 1990).

4.9 Conclusions

Recent geochemical compilations of Proterozoic shale P have indicated that P burial did not vary significantly in the Proterozoic (Laakso et al., 2020). By incorporating several analytical techniques to understand and constrain Proterozoic P in carbonate sediments, we reveal new P records that identify abundant and widespread P distribution at significantly elevated [PO_4] concentrations in Neoproterozoic Tonian aged carbonate rocks. P is located in several distinctive types of CO_3-associated P and carbonate fluorapatite in Tonian aged carbonate rocks. The authigenic nature of much of this P and the incorporation into precipitating calcite minerals

provides contextual evidence for seafloor precipitation associated with elevated P concentrations. The evidence weighs in favour of an enhanced P-cycle with water column remineralization heightened by the absence of major organic matter burial (i.e., Lenton and Daines). Thus, this dataset provides an opportunity to further understand Proterozoic marine P availability and burial. Because Ca^{2+} ions can influence modern alkaline settings, enabling concentrations of PO_4 to reach > 1 mol, it is possible that similar processes may have influenced late Proterozoic marine conditions as a result of high alkalinity and high supersaturation with respect to $CaCO_3$. By extension, our data suggest that Proterozoic marine basins contained enhanced P-cycling on a global scale, which may have lasted for prolonged periods of time and may have had significant implications for Proterozoic carbonate deposition styles and may have provided bioavailable marine [PO_4] that was essential to biological evolution.

4.10 Acknowledgements

We thank Jocelyn Richardson and Sam Webb for assisting in XANES and μXRF data collection and processing at Beamline 14-3 and 2-3, Stanford Synchrotron Radiation Lightsource, National Accelerator Laboratory, U.S. Department of Energy, U.S.A. We thank Brian Phillips for the collection of NMR ^{31}P and ^{19}F data, Department of Geosciences, Earth and Space Sciences Building, Stony Brook University, NY, U.S.A. Samples and chemostratigraphic data were provided by Justin Strauss, Phoebe Cohen, Galen Halverson, Marcus Kunzmann and Sarah Wörndle. Assistance in bulk PO_4 data collection was provided by Olivia Gaitonde, Earth Sciences Department, University of Oxford, UK

Supplementary material

Supplementary material is located at the end of the document in the Supplementary Materials – S4.

Chapter 5: Discussion and conclusions

5.1 Overview of research aims

For much of Earths geological history, skeletal $CaCO_3$ biomineralization was absent and carbonate sediments were controlled by chemical processes. In the absence of a $CaCO_3$ biological buffer through much of the Precambrian, kinetic pathways dominated carbonate production and led to widespread high-Mg $CaCO_3$ mineral production. However, these systems may have been highly sensitive to ocean-atmospheric chemical variations, which would have had a major influence on key geochemical cycles.

Elucidating the sedimentological consequences of kinetic inhibition in natural settings through experimental and geological analyses is important for understanding geochemical cycles and processes that lead to enigmatic high-Mg $CaCO_3$ and $MgCO_3$ precipitation. By identifying $CaCO_3$–$MgCO_3$, pathways linked to kinetic mediation by common ions in seawater and lake systems, we aim to shed light on mechanisms that underpin enigmatic high-Mg carbonate mineral formation. In doing so, we set out to geochemically constrain carbonate precipitation processes and gain a new perspective on phosphorous availability during key periods in Earths history.

5.2 Chapter 2 conclusions summary

Magnesite and Mg-rich carbonates are highly reactive compared to Ca- and Ca-Mg-carbonate minerals (calcite and dolomite). This indicates that Mg-bearing carbonates should form readily, yet their formation is inhibited at Earths surface conditions. Alternatively, dolomite is thermodynamically the most stable form of Mg-Ca-carbonate, yet the formation of primary dolomite at Earth surface conditions remains largely unexplained. Challenges for understanding

the formation and preservation of these minerals over geological timescales have remained enigmatic but appear to be related to kinetics and the major influence of an enlarged hydration radius of Mg ions resulting in sluggish kinetics. Our experimental results reveal insight into very high-Mg calcite, magnesite and dolomite mineralization pathways under Earth surface conditions. Two important pathways are characterized:

3) A pathway to very high-Mg calcite-dolomite crystallization from ACMC precursors in highly alkaline settings where supersaturation is influenced by $[PO_4]$ = 7 m*M*/kg. This pathway is prompted by the recrystallization of high-Mg ACMC that typically resulted in mixtures of very high Mg-calcite (ca. 48 mol% Mg) with minor aragonite and dolomite.
4) A pathway to magnesite crystallization via hydromagnesite. This pathway is prompted by the homogenous nucleation of very high-Mg ACMC and/or AMC in high alkalinity settings where supersaturation is influenced by $[PO_4] \geq 7$ m*M*/kg.

These results indicate that (A) under high carbonate alkalinity conditions influenced by $[PO_4]$ = 7 mM, increased Mg/Ca ratios resulted in increased Mg/Ca of the final mineral where Mg ≥ 50 %. (B) Increasing the $[PO_4]$ led to an increase in the extent and rate of crystallization, notably of magnesite, but also minor dolomite minerals and apatite. (3) Increased salinity and $[PO_4]$ resulted in the formation of chlorapatite rather than monetite that was associated with lower salinity and $[PO_4]$ settings. (4) Morphological changes are characterized by the presence of spherules that are composed of microcrystalline aggregated of either hydromagnesite or magnesite depending on the extent of crystallization or very-high Mg-calcite in precursor experiments. (5) These conditions led to an unusually high abundance of crystal twinning.

These results shed light on long-standing enigmas related to magnesite and dolomite formation and expand our current understanding of possible geochemical environments that can lead to Mg–Ca–CO_3 mineral production. This provides important insight into kinetically driven processes that may have influenced carbonate sedimentation and related geochemical cycles in

geological history and helps identify possible formation mechanisms that result in magnesite mineral production in Martian environments.

5.3 Chapter 3 conclusions summary

Our data show that kinetic interactions among common seawater ions may generate non-traditional mineralization pathways that offer new explanations for enigmatic Precambrian carbonate fabrics such as synsedimentary calcite microspar cement; thus, future interpretations of isotopic and trace-elemental variations in Precambrian carbonates should take explicit account of these $CaCO_3$ mineralization pathways and their associated expressions. More broadly, our data show that because [PO_{4tot}] strongly increases nucleation thresholds, while effectively arresting the growth rates of pre-existing $CaCO_3$ (Mucci, 1986), periods of enhanced PO_4 recycling, whether driven by ecological factors (Lenton and Daines, 2018) or ocean-atmosphere redox (Laakso et al., 2020), may have fundamentally altered the dynamics of $CaCO_3$ precipitation throughout much of the Proterozoic Eon. This may indicate that secular variations observed in carbonate successions in the Precambrian relate to secular variations in the concentration or relative proportion of kinetic mediating compounds such as PO_4.

5.4 Chapter 4 conclusions summary

Our observations expand upon increasing evidence that aqueous PO_4 was abundant and bioavailable in Tonian basins on a global scale, and provide geochemical and petrographic constraints that illuminate the state of the Tonian P-cycle. By incorporating several analytical techniques to constrain Proterozoic P in carbonate sediments, we reveal new P records that identify abundant and widespread P distribution at significantly elevated [PO_4] concentrations in Neoproterozoic Tonian aged carbonate rocks. P is located in several distinctive types of CO_3-associated P and carbonate fluorapatite in Tonian sediments. The authigenic nature of much of this P and the incorporation into precipitating calcite minerals provides contextual evidence for authigenic seafloor precipitation associated with P enrichment.

The evidence weighs in favour of an enhanced P-cycle with water column remineralization heightened by the absence of major organic matter burial (i.e., Lenton and Daines). Thus, this dataset provides an opportunity to further understand Proterozoic marine P availability and burial. Because Ca^{2+} ions can influence modern alkaline settings concentrating PO_4 to > 1 mol, it is possible that similar processes influenced late Proterozoic alkaline and supersaturated marine conditions. By extension, our data suggest that Proterozoic marine basins contained enhanced P-cycling on a global scale, which may have lasted for prolonged periods of time and may have had significant implications for Proterozoic carbonate deposition styles and may have provided bioavailable marine [PO_4] that was essential to biological evolution. However, if evidence that points toward PO_4 enrichment during this time coincides with no corresponding increase in primary production and organic matter burial as these sediments indicate, this may signal that biological P limitation was usurped by possible nitrogen limitation. This could be explained by elevated pH induced that results in a shift from aqueous ammonium (NH_4^+) to ammonia gas (NH_3) that removes nitrogen from water. This would support observations of a build-up of PO_{4tot} without an increase in organic-C burial.

5.5 Geological $CaCO_3$ production discussion

These data suggest that the enhanced [PO_4] in Neoproterozoic seawater may have permitted non-classical $CaCO_3$ nucleation at high Ω_{Cal}, in turn producing synsedimentary microspar with authigenic Mg-silicates (Strauss and Tosca, 2020), and apatite. Similar regimes may have led to non-classical $MgCO_3$ and Mg-Ca-CO_3 nucleation resulting in widespread primary dolomite and high Mg-calcite sedimentation that dominates through much of the Precambrian.

In fact, the stratigraphic abundance of microspar peaked in the early Neoproterozoic (James al., 1998), indicating that nucleation threshold were repeatedly crossed across multiple basins. An addition, evidence that highly alkaline settings influenced by PO_4 leads to non-classical $MgCO_3$ and Mg-Ca-CO_3 nucleation (Mg > 50 %) indicates that similar kinetically controlled environments may have existed through much of the Precambrian and contributed to the

production of widespread primary dolomite and high Mg-calcite sedimentation that dominates through much of the Precambrian.

Together, these chemical constraints and newly identified kinetic thresholds uncover mechanisms that control the shallow water Precambrian $CaCO_3$ factory that underwent significant variations in response to biogeochemical changes throughout Earth's history.

5.6 Proterozoic P-cycle discussion

By understanding the relationship between PO_4, and $CaCO_3$ mineralization pathways, we can shed light on the availability of Precambrian PO_4 and perhaps take a step forward in understanding how major changes in ocean-atmosphere chemistry through geological history were related to the evolution of the biosphere in which P plays a crucial role biogeochemically (Gulick et al, 1955, Holland, 1984; Holland et al., 1986; Van Cappellen, 1991, Eckford-Soper and Canfield, 2020).

The results from multiple lines of research conducted in this thesis overwhelming point toward an enhanced PO_4 cycle in the Tonian, with high PO_4 turnover and significant PO_4 concentrations within the mid-Neoproterozoic ocean system compared to the modern ocean and times preceding and following the mid-Neoproterozoic. Our observations, based on bulk carbonate PO_4 analyses to identify PO_4 concentrations, ^{31}P NMR and XANES analyses to identify the P speciation and μXRF, SEM-EDS and petrography to characterize the spatial distribution and mineralogical context of PO_4 expand upon increasing evidence that aqueous PO_4 was abundant and bioavailable in Tonian basins on a global scale.

We provide geochemical and petrographic constraints that illuminate the state of the Tonian P-cycle and support observations that phosphate PO_4 was non-limiting through much of the Tonian at concentrations conducive to apatite biomineralization (i.e., Cohen et al 2017).

The availability of P as a nutrient is typically regarded as a limiting factor in primary production. However, at high pH, the PO_4 species are shifted to orthophosphate ions (PO_4^{3-}) – the

most bioavailable form of P in solution (i.e., Reynolds and Davies, 2001). Therefore, two key questions remain: what caused mid-Tonian PO_4 enrichment and if alkaline-saline lakes are enriching bioavailable nutrient [PO_{4tot}], then why are microorganisms not utilizing it?

The burial efficiency of seawater P in marine sediments has been suggested to influence the cycling and concentration of P in the ocean (Filippelli and Delaney, 1992; Ruttenberg and Berner, 1993) yet appreciable differences in P accumulation rate records relative to continental weathering rates indicates that P influx can become decoupled from other dissolved components (Filippelli and Delaney, 1994). Although P appears to have been cycled intensely during the late Proterozoic, and the following Ediacaran period is characterized by periods of phosphogenesis, recent compilations of sedimentary P content from shales coupled with mass balance constraints show that phosphorite deposits only account for a minor proportion of the total P influx to the ocean (Laakso, et al., 2020).

Therefore, the style of P cycling during the late Proterozoic may be more suitably explained by major water column remineralization and internal P cycling models of P accumulation and burial outlined by Lenton and Daines (2018) and Ingall et al., (1993) that likely influenced total aqueous PO_4 concentrations rather than changes to overall oceanic P fluxes (Laakso et al., 2020). This is supported by the low export flux of organic-C that is well documented from Precambrian sediments (Schrag et al., 2013; Kunzmann et al., 2015; Laakso and Schrag, 2018; Sperling and Stockey, 2018) and corroborated by our observations from this investigation that indicate a lack of organic-C and a lack of minerals linked to anoxic respiration. Following this, toward the end of the Neoproterozoic and early Paleozoic, a 'biological pump' would have become increasingly efficient in the Paleozoic as eukaryotes evolved and enhanced P and organic-C burial and facilitated oxygen sensitive bioturbation that expanded the oxygenated zone and helped to regulate early oxygen and P-cycles (i.e., Boyle et al., 2014; Lenton and Daines, 2018).

Furthermore, [PO_4]-enrichment may be explained by recent indications that modern alkaline lakes can accumulate PO_4 to > 1 m*M* concentrations (Toner and Catling, 2020). This can be explained in high-alkalinity conditions where by a relationship with Ca^{2+} ion removal in the water column through $CaCO_3$ precipitation restricts the precipitation of apatite and leads to excess PO_4 accumulation in lake waters (Gulbrandsen, 1969; Sass, 1981; Toner and Catling, 2020).

Geochemical PO_4 enrichment may also come from the high pH that characterizes modern alkaline lakes, due to the pH-dependent speciation of PO_4 (de Kanel and Morse, 1978; Ishikawa and Ishikuni, 1981). The availability of P as a nutrient is typically regarded as a limiting factor in primary production. However, at high pH, the PO_4 species are shifted to orthophosphate ions (PO_4^{3-}) – the most bioavailable form of P. However, pH > 8 and high alkalinity also shifts aqueous ammonium NH_4^+ to NH_3 (ammonia gas) in equilibrium causing nitrogen nutrient loss from the water through degassing. Furthermore, ammonia can be highly toxic to biological organism and inhibits photosynthesis by binding to the oxygen-evolving complex (Abeliovich and Azov, 1976; Wang et al., 2019). Together, these factors may decrease the rates of [PO_{4tot}] consumption by microorganisms and lead to a gradual build-up of [PO_{4tot}] but have potentially damaging consequences on productivity and perhaps maintaining low levels of atmospheric oxygen (i.e., Planavsky et al., 2018).

Although our data and published models point toward an enhanced PO_4 cycle, we cannot rule out the possibility of an increase in P influx (i.e., Horton, 2015, Cox et al., 2016) – even if it is a local one. In the case of the Little Dal Group, it is not inconceivable that an additional presence of PO_4 was derived from of either a) a serpentonite derived source of elevated PO_4, b) a magmatic derived source of apatite or c) reworking of apatite sediments. Geochemical investigations into possible influence of serpentonite derived or igneous derived P-enrichment in mid-Tonain basins are required to better understand the mineralogy and source of PO_4 cycling and possible sources.

a) Mantle serpentinization may have acted as a route to liberating P during alteration from olivine to serpentonite in ultramafic rocks leading to orthophosphate and pyrophosphate (Pasek et al., 2020).

b) Alternatively, although the Laurentian plate records no apparent volcanism ca. 830-817 Ma (Harlan et al., 2003; Thompson et al., 2014), Rodinia passing over a mantle plume prior to basin subsidence may have resulted in crustal fluid interaction. This coincides with the Guibei (China) and Gairdner (Australia) large igneous provinces and the Olympic Dam dolerite (Park et al., 1995; Macdonald et al. 2012; Apukhtina et al., 2016). These events are dated at 817 ± 11 Ma based on titanite grains (Apukhtina et al., 2016), which marginally precedes the Bitter Springs Stage ~811 Ma, and these events culminated in the Laurentian Gunbarrel event ~780 Ma (Macdonald et al., 2012). All of these igneous events are associated with significant igneous P enrichment with apatite assemblages and concentrations up to P_2O_5 = 8200 ppm (i.e., Apukhtina et al., 2016). Interaction with igneous derived minerals may account for some anomalies identified in the P-enriched Little Dal Group carbonates, notably the multiple sources of apatite, presence of TiO_2 minerals and Sr-rich microspar cement that records up to 700 ppm in these carbonates (Halverson et al., 2007).

Either way, whether changes to the P-cycle were related to increased P-flux or changes in the deep water P reservoir, taken together, these observations hint at fundamental shifts in the internal cycling of P that may not be obviously reflected in the bulk P content of siliciclastic rock proxies for changes to P input and output fluxes and would benefit from further research. In this regard, the nature of P cycling in carbonate depositional environments and the degree to which carbonate sediments archive marine P availability could represent a key archive of P availability that complements siliciclastic records. By understanding the relationship between PO_4, and $CaCO_3$ mineralization pathways, we may be able to shed light on the availability of Precambrian PO_4 and perhaps take a step forward in understanding how major changes in ocean-atmosphere chemistry through geological history were related to the evolution of the biosphere (i.e., Holland, 1984;

Holland et al., 1986) in which P plays a crucial role biogeochemically and related to ocean-atmosphere oxygenation (Gulick et al, 1955, Van Cappellen, 1991, Butusov and Jernelöv, 2013; Fernández-García et al., 2017; Eckford-Soper and Canfield, 2020; Toner and Catling, 2020).

5.7 Concluding remarks

Our research reveals new, non-classical formation pathways that lead to high-Mg calcite, magnesite, dolomite and apatite minerals at Earth surface temperatures in hyper-alkaline, hyper-saline environments. These environments drive kinetic pathways mediated by common compounds that inhibit direct aragonite and calcite crystallization.

The presence of dissolved PO_4 in water influences enhanced CO_3-alkalinity and increases supersaturation relative to carbonate minerals (i.e., $\Omega_{calcite}$ and Ω_{ACMC}). These pathways can help explain kinetically driven mechanisms that exist present day on Earth and likely existed in the geologic past. Our approach draws together geochemical constraints for past depositional environments from fluid inclusion data (i.e., Spear et al., 2014) and chemical precipitation boundaries for authigenic minerals calcite microspar, primary dolomite and Mg-silicate (i.e., Tosca et al., 2011; Strauss and Tosca, 2020). We incorporate these into different experimental methods to examine the precipitation of Mg-rich $CaCO_3$ minerals from hyper-alkaline, hyper-saline conditions influenced by millimolar concentrations phosphate (PO_4) concentrations known to inhibit aragonite and calcite (i.e., Burton and Walter, 1990).

We have identified that the presence of dissolved PO_4 in water influences enhanced CO_3^2-alkalinity and increases supersaturation relative to carbonate minerals (i.e., $\Omega_{calcite}$ and Ω_{ACMC}). This opens up non-classical formation pathways to $CaCO_3$ that likely led to the enigmatic calcite microspar cement precipitation that is characteristic of mid-Proterozoic marine carbonates. In doing so, we have constrained key chemical nucleation thresholds for carbonate nucleation in mid-Proterozoic composition seawater that helps explain kinetically driven mechanisms of carbonate sedimentation. This research suggests that $CaCO_3$ nucleation thresholds were

repeatedly crossed on a global scale in the Neoproterozoic, which may have had drastic influence on biogeochemical cycles and specifically the carbon cycle. Understanding kinetically driven pathways on mineral formation elucidates the chemical controls on global systems that are not buffered by skeletal carbonate productions and are highly sensitive to the surrounding chemical environment. This indicates that the Precambrian shallow water $CaCO_3$ factory may have been subject to major fluctuations through most of Earth's history.

Through identification of alternative mineral formation mechanisms and pathways, we have shed light on new Mg-carbonate and high-Mg $CaCO_3$ pathways that can overcome energetic barriers related to magnesium hydration and inform us of carbonate sedimentological depositional environments and geochemical processes. Although the production of these Mg-rich carbonate minerals can be facilitated by microbial activity, an important finding is that conditions for magnesite and dolomite formation at Earth surface conditions do not require microbial influence. Instead, these pathways emphasize the importance of kinetic inhibitors in mineral formation pathways and signals that alternative calcium carbonate precipitation pathways that may have dominated carbonate sedimentation in paleo-environments and alkaline lake settings for ca. 3 billion years. This provides fundamentally important information in understanding the formation of magnesite that can be met in alkaline lake settings where PO_4 accumulations can reach > 1 m*M* (Toner and Catling, 2020). The integration of the results from the different methods used in this research elucidates major controls on the inorganic carbonate factory and the phosphorous cycle that have largely been unaccounted for. These conditions are very relevant for understanding early aqueous environments that existed on Mars leading the deposits of magnesite that dominate carbonate sediments (i.e., Ehlmann, 2008. These environments happen to contain $MgCO_3$ as well as excessive PO_4 concentrations linked to mafic water-rock interaction (i.e., Adcock et al., 2013).

In characterizing the nature of P within geological carbonates, NMR show that PO_4 is bound principally in carbonate fluorapatite (CFA); deposited as seafloor synsedimentary cements, within Mg-silicate-rich intraclasts, nano-inclusions within microspar cement and talc, and as

disseminated detrital particles. Our data show that PO_4 is dominantly carbonate-associated, and only rarely associated with ferric-iron oxide/organic matter in these mid-Neoproterozoic samples; Fe and S-bearing diagenetic minerals, the products of anoxic respiration, and organic matter are rare. These data suggest that the enhanced [PO_4] in Neoproterozoic seawater may have permitted non-classical $CaCO_3$ nucleation at high Ω_{Cal}, in turn producing synsedimentary microspar with authigenic Mg-silicates (Strauss and Tosca, 2020), and apatite. Similar regimes may have led to non-classical $MgCO_3$ and Mg-Ca-CO_3 nucleation resulting in widespread primary dolomite and high Mg-calcite sedimentation that dominates through much of the Precambrian.

Through the application of these mineral formation pathways linked to phosphorous inhibition and geochemical interrogation of Proterozoic carbonates, we have honed in on a new approach that enables the characterization of P concentration, speciation and distribution in authigenic carbonate sediments as apatite and carbonate fluorapatite cements, intraclasts and nanocrystals and in the form of lattice-bound CO_3-assocaited PO_4. This provides a deeper understanding of available P concentrations in marine environments in the Precambrian. Our research points toward enhanced phosphorous cycling during the Proterozoic and reveals that mid-Neoproterozoic seawater featured enhanced bioavailable marine PO_4. This carries a number of significant implications for the global P-cycle, on the cusp of early eukaryotic diversification.

5.7.1 Future research

This research has resulted in a significant platform from which future experimental investigations can be leveraged. Needless to say, further investigation into the newly identified pathways would be highly beneficial. The pathway to high-Mg calcite and dolomite would benefit from further investigation by broadening the experimental conditions with a specific focus on characterizing the conditions and mechanisms of formation in Precambrian environments and modern lacustrine environments (i.e., Coorong Lagoon and Searles Lake).

The pathway to magnesite crystallization from hydromagnesite would benefit from characterization from experiments that focus on depositional environments with a specific focus

on mafic mineral and PO_4 interactions, for example drawing on chemical conditions of modern natural deposits and deposits that may be present on Mars. Supporting in situ analyses to characterize the mechanisms by which hydration barriers related to Mg ions may be overcome would be of key importance.

Emphasis on understanding lattice bound CO_3-associated PO_4 is an exciting area of research that will benefit from further experimental geochemical investigations and kinetic constraints, supported by microanalytical characterization (i.e., XANES and μXRF – Richardson and Webb, SSRL; and ^{31}P NMR, Phillips, Stonybrook).

Furthermore, the inhibitory effect of Mg^{2+} on octacalcium phosphate transformation to apatite in seawater would support geochemical models. But perhaps more importantly, because PO_4 is a key component in all life on Earth, investigating the calcium-magnesium-carbonate-phosphate system in highly alkaline settings may be of fundamental importance in probing geochemical environments related to biological evolution and for understanding the geochemical conditions that may have led to the precursors of biomolecular building blocks that eventually ended up as RNA that marks the origin of life on Earth.

Further geological analyses to identify PO_4 in additional successions and time periods will only strengthen our understanding of the Proterozoic P-cycle.

Geochemical investigations into the causes of enhanced PO_4 in sedimentary basins would be of great importance to the geological and biological community. Possible lines of research relate to possible influence of serpentonite derived P-enrichment or igneous derived P-enrichment in mid-Tonain basins specifically related to the Little Dal Group. Furthermore, investigations into why PO_4 is not being utilized by organisms in the mid-Tonian could start with a focus on investigating whether high pH caused deprotonation and a resultant nitrogen nutrient crash.

End

Bibliography

Abeliovich, A and Azov, Y., 1976, Toxicity of ammonia to algae in sewage oxidation ponds, Applied Environmental Microbiology, v. 31(6), p. 801–806,

Addadi L., Raz. S. and Weiner, S., 2003, Taking advantage of disorder: amorphous calcium carbonate and its roles in biomineralisation, Advanced Materials, v. 15(12) p. 959-970, https://doi.org/10.1002/adma.200300381

Aitken, J.D., 1981. Stratigraphy and sedimentology of the Upper Proterozoic Little Dal Group, Mackenzie Mountains, Northwest Territories. Proterozoic Basins of Canada: Geological Survey of Canada Paper 81 (10), 47–71.

Allwood, A.C., Kamber, B.S., Walter, M.R., Burch, I.W and Isik Kanik, 2010, Trace elements record depositional history of an Early Archean stromatolitic carbonate platform, Chemical Geology, v. 270(1–4), p. 148-163, https://doi.org/10.1016/j.chemgeo.2009.11.013

Apukhtina, O.B., Kamenetsky, V.S., Ehrig, K. *et al.* Postmagmatic magnetite–apatite assemblage in mafic intrusions: a case study of dolerite at Olympic Dam, South Australia. Contrib Mineral Petrol 171, 2 (2016). https://doi.org/10.1007/s00410-015-1215-7

Arvidson, R.S. and Morse, J.W., 2014, Formation and Diagenesis of Carbonate Sediments, 9.3, Editor(s): Heinrich D. Holland, Karl K. Turekian, Treatise on Geochemistry (Second Edition), Elsevier, 2014, p. 61-101, ISBN 9780080983004, https://doi.org/10.1016/B978-0-08-095975-7.00703-8

Arvidson, R.S., Mackenzie, F.T., 1999, The dolomite problem: control of precipitation kinetics by temperature and saturation state. American Journal of Science, v. 299, p. 257-288, https://doi.org/10.2475/ajs.299.4.257

Asmerom, A., Jacobsen, S.B., Knoll, A.H., Butterfield, N.J., Swett, K., 1991, Strontium isotopic variations of Neoproterozoic seawater: Implications for crustal evolution, Geochimica et Cosmochimica Acta, vol. 55(10), pp. 2883-2894, https://doi.org/10.1016/0016-7037(91)90453-C

Baird, R., A. D., Eaton, D., Andrew, E. W., Rice and L., Bridgewater, L. 2017, Standard methods for the examination of water and wastewater, American Public Health Association. v. 23, p. 4500-P PHOSPHORUS, https://doi.org/10.2105/SMWW.2882.093

Baird, R., Eaton, A.D., Andrew, D., Rice, E.W. and Bridgewater, L., 2017, Standard methods for the examination of water and wastewater: American Public Health Association. v. 23, p. 4500, https://doi.org/10.2105/SMWW.2882.093

Balan, E., Delattre, S., Roche, D., Segalen, L., Morin, G., Guillaumet, M., Blanchard, M., Lazzeri, M., Brouder, C. and Salje, E.K.H., 2010, Line-broadening effects in the powder infrared spectrum of apatite. Physics and Chemistry of Minerals, v. 38(2), p. 111-122, https://doi.org/10.1007/s00269-010-0388-x

Baldermann, A., Mittermayr, F., Bernasconi, S.M. et al. Fracture dolomite as an archive of continental palaeo-environmental conditions. Communications Earth and Environment, v. 1, p. 35, 2020, https://doi.org/10.1038/s43247-020-00040-3

Bandfield, J.L., Glotch, T.D., Christensen, P.R., 2003, Spectroscopic Identification of Carbonate Minerals in the Martian Dust, Science, v. 301(5636), p. 1084–1087, https://doi.org/10.1126/science.1088054

Benitez-Nelson, C., 2015, The Missing Link in Oceanic Phosphorus Cycling?" Science American Association for the Advancement of Science, 348.6236, 2015: 759-60, https://doi.org/10.1126/science.aab2801

Beck, R., Seiersten, M., and Andreassen, J.P., 2013, The constant composition method for crystallization of calcium carbonate at constant supersaturation: Journal of Crystal Growth, v. 380, p. 187–196, https://doi.org/10.1016/j.jcrysgro.2013.05.038.

Benzerara, K., Menguy, N., López-García, P., Yoon, T.-H., Kazmierczak, J.. Tyliszczak, T., Guyot F. and Brown, G.E., 2006, Nanoscale Detection of Organic Signatures in Carbonate Microbialites, Proceedings of the National Academy of Sciences of the U.S.A., v. 103(25), p. 9440–9445, https://doi.org/10.1073/pnas.0603255103

Berg. C., 2017, Thesis: Influence of Magnesium in the Formation of Phosphate Spheres A simple method for the fabrication of spherical particles of calcium and magnesium phosphate, Teknisk-naturvetenskaplig fakultet UTH-enheten, http://www.diva-portal.org/smash/get/diva2:1119449/FULLTEXT02.pdf

Bergman, N.M., Lenton, T.M. and Watson, A.J., 2004, COPSE: A new model of biogeochemical cycling over Phanerozoic time, American Journal of Science, v. 304(5), p. 397-437; https://doi.org/10.2475/ajs.304.5.397

Bernard, C., Escalas, A., Villeriot, N. et al., 2019, Very Low Phytoplankton Diversity in a Tropical Saline-Alkaline Lake, with Co-dominance of Arthrospira fusiformis

(Cyanobacteria) and Picocystis salinarum (Chlorophyta), Microbial Ecology, v. 78, p. 603–617, https://doi.org/10.1007/s00248-019-01332-8

Berner, R.A., Westrich, J.T. Graber, R. Smith J. and Martens C., 1978, Inhibition of aragonite precipitation from supersaturated seawater; a laboratory and field study, American Journal of Science June 1978v. 278(6), p. 816-837, https://doi.org/10.2475/ajs.278.6.816

Bethke, C.M., Yeakel, S., 2015The Geochemist's Workbench Release 10.0 GWB Essentials Guide. Aqueous Solutions, LLC, Champaign, Illinois.

Bischoff, J.L., Stine, S., Rosenbauer, R.J., Fitzpatrick, J.A., and Stafford, T.W., 1993, Ikaite precipitation by mixing of shoreline springs and lake water, Mono Lake, California, USA: Geochimica et Cosmochimica Acta, v. 57, p. 3855–3865, https://doi.org/10.1016/0016-7037(93)90339-X.

Bischoff, W.D. Bishop, F.C. Mackenzie, F.T., 1983, Biogenically produced magnesian calcite: In homogeneities in chemical and physical properties; comparison with synthetic phases. American Mineralogist, v. 68, p. 1183–1188.

Bishop, J.W., and Sumner, D.Y., 2006, Molar tooth structures of the Neoarchean Monteville Forma-tion, Transvaal Supergroup, South Africa. I: Con-straints on microcrystalline CaCO3 precipitation: Sedimentology, v. 53, p. 1049–1068, https://doi.org/10.1111/j.1365-3091.2006.00801.x.

Bjerrum, C. J. and Canfield, D. E, 2002,Ocean productivity before about 1.9 Gyr ago limited by phosphorus adsorption onto iron oxides. Nature, v. 417, p. 159

Blue, C.R., and Dove, P.M., 2015, Chemical controls on the magnesium content of amorphous cal-cium carbonate: Geochimica et Cosmochimica Acta, v. 148, p. 23–33, https://doi.org/10.1016/j.gca.2014.08.003.

Blue, C.R., Giuffre, A., Mergelsberg, S., Han, N., De Yoreo, J., and Dove, P., 2017, Chemical and physical controls on the transformation of amor-phous calcium carbonate into crystalline CaCO3 polymorphs: Geochimica et Cosmochimica Acta, v. 196, p. 179–196, https://doi.org/10.1016/j.gca.2016.09.004.

Bosak T, Knoll AH, Petroff AP. 2013. The meaning of stromatolites. Annu Rev Earth Planet Sci 41: 21–44, https://doi.org/10.1146/annurev-earth-042711-105327

Boskey, A.L. and Posner, A.S., 1974, Magnesium stabilization of amorphous calcium phosphate: A kinetic study, Materials Research Bulletin, v. 9(7), p. 907-916, https://doi.org/10.1016/0025-5408(74)90169-X

Boskey, A.L. and Posner, A.S., 1974, Magnesium stabilization of amorphous calcium phosphate: A kinetic study, Materials Research Bulletin, v. 9(7), p. 907-916, https://doi.org/10.1016/0025-5408(74)90169-X.

Bots, P., Benning, L., Rickaby, R., and Shaw, S., 2011, The role of SO4 in the switch from calcite to ara-gonite seas: Geology, v. 39, p. 331–334, https://doi.org/10.1130/G31619.1.

Brand, U. and Veizer, J., 1980. Chemical diagenesis of a multicomponent carbonate system–1: trace elements, J. Sediment. Res., vol. 50(4), pp. 1219–1236. https://doi.org/10.1306/212F7BB7-2B24-11D7-8648000102C1865D

Brečević, L. and Nielsen , A. E., 1989, Solubility of Amorphous Calcium Carbonate, Journal of Crystal Growth, v. 9, p. 504 -510, https://doi.org/10.1016/0022-0248(89)90168-1

Broecker, W. S. Peng, T.-H. Beng, Z., 1982. Tracers in the Sea (Lamont-Doherty Geological Observatory, Columbia University,). vol. 2.

Bruce., Wilkinson, 1989, Sedimentary carbonate record of calcium-magnesium cycling. American Journal of Science., v. 289, p. 1158-1194, https://doi.org/10.2475/ajs.289.10.1158

Burton, E.A., and Walter, L.M., 1990, The role of pH in phosphate inhibition of calcite and aragonite precipitation rates in seawater: Geochimica et Cosmochimica Acta, v. 54(3), p. 797–808, https://doi.org/10.1016/0016-7037(90)90374-T.

Canfield, D.E., Raiswell, R. and Bottrell, S.H., 1992, The reactivity of sedimentary iron minerals toward sulphide, American Journal of Science, v. 292(9), p. 659-683 https://doi.org/10.2475/ajs.292.9.659

Carino, A., Testino, A., Andalib,i M.R., Pilger, F., Bowen, P. and Ludwig, C, 2017, Thermodynamic-Kinetic Precipitation Modeling. A Case Study: The Amorphous Calcium Carbonate (ACC) Precipitation Pathway Unravelled. Crystal Growth and Design, v. 17, p. 2006–2015, https://doi.org/10.1021/acs.cgd.7b00006

Chad A. Larson, Gary E. Belovsky, Salinity and nutrients influence species richness and evenness of phytoplankton communities in microcosm experiments from Great Salt Lake, Utah, USA, Journal of Plankton Research, Volume 35, Issue 5, September/October 2013, Pages 1154–1166, https://doi.org/10.1093/plankt/fbt053

Chang, C-Y., Yang, S-Y. and Chan, J.C.C., 2021, Solubility product of amorphous magnesium carbonate. Journal of the Chinese Chemical Society, v. 68, p. 476– 481. https://doi.org/10.1002/jccs.202000527

Chang, B., Li, C., Liu, D. et al., 2020, Massive formation of early diagenetic dolomite in the Ediacaran ocean: Constraints on the “dolomite problem”, Proceedings of the National Academy of Sciences, v. 117(25), p. 14005-14014, https://doi.org/10.1073/pnas.1916673117

Chave, K.E., Smith, S.V., Roy, K.J., 1972, Carbonate production by coral reefs, Marine Geology, v. 12(2), p. 123-140, https://doi.org/10.1016/0025-3227(72)90024-2

Cheng, Z. Y., Fernández-Remolar, D. C., Izawa, M. R. M., Applin, D. M., Chong Díaz, M., Fernandez-Sampedro, M. T., García-Villadangos, M., Huang, T., Xiao, L., and Parro, V., 2016, Oxalate formation under the hyperarid conditions of the Atacama desert as a mineral marker to provide clues to the source of organic carbon on Mars, Journal of Geophysical Research Biogeosciences, v. 121, p. 1593–1604, https://doi.org/10.1002/2016JG003439

Chopin, C., Ferraris, G., Prencipe, M., Brunet, F. and Medenbach, O., 2001, Raadeite, Mg7(PO4)2(OH)8: A new dense-packed phosphate from Modum (Norway). European Journal of Mineralogy, v. 13, p. 319-327. https://doi.org/10.1127/0935-1221/01/0013-0319

Cohen, P.A. and Knoll, A.H., 2012, Scale Microfossils from the Mid-Neoproterozoic Fifteenmile Group, Yukon Territory, Journal of Paleontology, v. 86(5), p. 775–800, https://doi.org/10.1666/11-138.1

Cohen, P.A., Strauss, J.V., Rooney, A.D., Sharma, M., and Tosca, N.J., 2017, Controlled hydroxyapatite biomineralization in an ∼810 million-year-old unicellular eukaryote: Science Advances, v. 3,(6), p. e1700095, https://doi.org/10.1126/sciadv.1700095.

Combes, C. and Rey, C., 2010, Amorphous calcium phosphates: synthesis, properties and uses in biomaterials. Acta Biomaterialia, v. 6(9), p. 3362-3378. https://doi.org/10.1016/j.actbio.2010.02.017

Compton, J., Mallinson, D., Glenn, C.R., Filippelli, G., Foellmi, K., Shields, G. and Zanin, Y., 2000, Variations in the global phosphorus cycle. Special Publication, Society for Sedimentary Geology, v. 66, p. 21–33, http://dx.doi.org/10.2110/pec.00.66.0021

Cook, P.J., Shergold, J.H., Burnett W.C. and Riggs, S.R., 1990, Phosphorite research: a historical overview Geological Society, London, Special Publications, v. 52, p. 1-22, https://doi.org/10.1144/GSL.SP.1990.052.01.02

Cosmidis, J., Benzerara, K., Morin, G., Busigny, G., Lebeau, O., Jézéquel, D., Noël, V., Dublet, G. and Othmane, G., 2014, Biomineralization of iron-phosphates in the water column of Lake Pavin (Massif Central, France), Geochimica et Cosmochimica Acta, v. 126, 2014, Pages 78-96, https://doi.org/10.1016/j.gca.2013.10.037

Cosmidis, J., Benzerara, K., Nassif, N., Tyliszczak, T. and Bourdelle. F., 2015, Characterization of Ca-phosphate biological materials by scanning transmission x-ray microscopy (STXM) at the Ca L 2,3 -, P L 2,3 -and C K- edges. Acta Biomaterialia, Elsevier, v. 12, p. 206-269, https://doi.org/10.1016/j.actbio.2014.10.003

Couradeau, E., Benzerara, K., Gerard, E., Moreira, D., Bernard, S., Brown, G.E. and Lopez-Garcia, P., 2012, An Early-Branching Microbialite Cyanobacterium Forms Intracellular Carbonates, Science, v. 336(6080), p. 459–462, https://doi.org/10.1126/science.1216171

Cox, G.M., Halverson, G.P., Stevenson, R.K., Vokaty, M., Poirier, A., Kunzmann, M., Li, Z.-X., Denyszyn, S.W., Strauss, J. V., and Macdonald, F.A., 2016, Continental flood basalt weathering as a trigger for Neoproterozoic Snowball Earth: Earth and Planetary Science Letters, vol. 446, pp. 89–99, doi: 10.1016/j.epsl.2016.04.016.

Dar Shamim, A., Khan, K.F. and Birch, W.D, 2017, Sedimentary: Phosphates, Reference Module in Earth Systems and Environmental Sciences, Elsevier, p. 10.1016/B978-0-12-409548-9.10509-3

de Kanel, J.W. Morse, 1978, The chemistry of orthophosphate uptake from seawater onto calcite and aragonite, Geochimica Cosmochim. Acta, v. 42 p. 1335-1340, https://doi.org/10.1016/0016-7037(78)90038-8

De Yoreo, J.J., Gilbert, P.U.P.A., Sommerdijk, N.A.J.M., Penn, R.L., Whitelam, S., Joester, D. Zhang, H.Z. Rimer, J.D. Navrotsky, A. Banfield, J.F. Wallace, A.F. Michel, F.M. Meldrum, F.C. Cölfen, H. and Dove, P.M., 2015, Crystallization by Particle Attachment in Synthetic, Biogenic, and Geologic Environments, Science, v. 349, p. 6760, https://doi.org/0.1126/science.aaa6760

Debye, P and Hückel, E., 1923. Zur Theorie der Elektrolyte. I. Gefrierpunktserniedrigung und verwandte Erscheinungen" [The theory of electrolytes in Lowering of freezing point and related phenomena]. Physikalische Zeitschrift, v, 24, p. 185–206

Delaney, M.L., 1994, The oceanic phosphorus cycle and continental weathering during the Neogene, Paleoceanography, https://doi.org/10.1029/94PA01453.

Derry L. A., Keto L. S., Jacobsen S. B., Knoll A. H. and Swett K., 1989, Sr isotopic variations in upper Proterozoic carbonates from Svalbard and East Greenland. Geochim. Cosmochim. Acta vol. 53, pp. 2331-2339.

Derry, L., 2015, Causes and Consequences of mid-Proterozoic Anoxia. Geophysical Research Letters, v.42, p. 8538– 8546 https://doi.org/10.1002/2015GL065333

Derry, L.A., Kaufman, A.J. and Jacobsen S.B., 1992, Sedimentary cycling and environmental change in the Late Proterozoic: evidence from stable and radiogenic isotopes, Geochem. Cosmochim. Acta, vol. 56, pp. 1317-1329. https://doi.org/10.1016/0016-7037(92)90064-P

Dickson, A. G., 1981, An exact definition of total alkalinity and a procedure for the estimation of alkalinity and total inorganic carbon from titration data. Deep-Sea Research Part a-Oceanographic Research Papers, v. 28, p. 609-623, https://doi.org/10.1016/0198-0149(81)90121-7

Ding, H., Pan, H., Xu, X. and Tang, R., 2014, Toward a Detailed Understanding of Magnesium Ions on Hydroxyapatite Crystallization Inhibition, Crystal Growth and Design v. 14(2), p. 763-769, https://doi.org/10.1021/cg401619s

Donnelley T.H., Shergold, J.H., Southgate, P.N., and Barnes, C.J., 1990, Events leading to global phosphogenesis around the Proterozoic/ Cambrian boundary. *From* Notholt, A.J.G. and Jarvis, I., 1990, Phosphorite Research and Development Geological Society Special Publication vol. 52, pp. 273-287.

Dorozhkin,, S., 2011, Calcium orthophosphates, Occurrence, properties, biomineralization, pathological calcification and biomimetic applications, Biomatterials, v. 1(2), p. 121–164, https://doi.org/10.4161/biom.18790

dos Santos, A.M. and Stumm, W. 1992, Reductive dissolution of iron(III) (hydr)oxides by hydrogen sulfide. Langmuir v. 8, p. 1671–1675, https://doi.org/10.1021/la00042a030

dos Santos, H.N., Neumann, R. Ávila, C.A., 2017, Mineral Quantification with Simultaneous Refinement of Ca-Mg Carbonates Non-Stoichiometry by X-ray Diffraction, Rietveld Method, Minerals, v. 7, p. 164, https://doi.org/10.3390/min7090164

Dove, P.M., Hochella, M.F., Calcite precipitation mechanisms and inhibition by orthophosphate: In situ observations by Scanning Force Microscopy, Geochimica et Cosmochimica Acta, v. 57(3), v. 1993, p. 705-714, https://doi.org/10.1016/0016-7037(93)90381-6

Dreibus, G. and Wänke, H., 1985, Mars, a volatile-rich planet. Meteoritics, v. 20, p. 267-381, http://adsabs.harvard.edu/full/1985Metic..20..367D

Dromgoole, E.L. and Walter, L.M., 1990, Inhibition of calcite growth rates by Mn2+ in CaCl2 solutions at 10, 25, and 50°C, Geochimica et Cosmochimica Acta, v. 54(11), 1990, p. 2991-3000, https://doi.org/10.1016/0016-7037(90)90116-3

Ehlmann, B.L., Mustard, J.F., Murchie, S.L., Poulet, F., Bishop, J.L., Brown, A.J., Calvin, W.M., Clark, R.N.,. Des Marais, D.J., Milliken, R.E., Roach, L.H., Roush, T.L., Swayze, G.A. and Wray, J., 2008, Orbital Identification Of Carbonate-Bearing Rocks On Mars, Science, v. 322(5909), p. 1828-1832, https://doi.org/10.1126/science.1164759

Elizabeth C. Turner and Darrel GF Long , 2008, Basin architecture and syndepositional fault activity during deposition of the Neoproterozoic Mackenzie Mountains supergroup, Northwest Territories, Canada, Canadian Journal of Earth Sciences, v. 45(10), https://doi.org/10.1139/E08-062

Enyedi, N.T., Makk, J., Kótai, L., Berényi, B., Klébert, S., Sebestyén, Molnár, Z., Borsodi, A.K., Leél-Őssy, S., Demény A. and 0-0 Németh, P., 2020, Cave bacteria-induced amorphous calcium carbonate formation. Scientific Reports, v. 10, p. 8696, https://doi.org/10.1038/s41598-020-65667-w

Ernst, R. Bleeker W., 2010, Large igneous provinces (LIPs), giant dyke swarms, and mantle plumes: significance for breakup events within Canada and adjacent regions from 2.5 Ga to the Present Can. J. Earth Sci., v. 47, p. 695-739

Macdonald, F. A. Smith, E. F. Strauss, J. V. Cox, G. M. Halverson, G. P. Roots, C. F., 2010, Neoproterozoic and early Paleozoic correlations in the western Ogilvie Mountains, Yukon. Yukon Explor. Geol. 2010, 161–182

Macdonald, F. A. Cohen, P. A. Dudás, F. Schrag, D. P., 2010, Early Neoproterozoic scale microfossils in the Lower Tindir Group of Alaska and the Yukon Territory. Geophys. J. R. Astron. Soc. 38, 143–146

Macdonald, F. A. Cohen, P. A., 2011, The Tatonduk inlier, Alaska–Yukon border. Geol. Soc. London Memoirs 36, 389–396

Fairchild, I.J., and Spiro, B., 1987, Petrological and isotopic implications of some contrasting late Precambrian carbonates, NE Spitsbergen: Sedi-mentology, v. 34, no. 6, p. 973–989, https://doi.org/10.1111/j.1365-3091.1987.tb00587.x.

Filippelli, G.M. and Delaney, M.L., 1994, The oceanic phosphorus cycle and continental weathering during the Neogene, Paleoceanography, https://doi.org/10.1029/94PA01453

Fralick, P., Planavsky, N., Burton, J., Jarvis, I., Addison, A.D., Barrett, A.D., Brumpton, G.R., 2017, Geochemistry of Paleoproterozoic Gunflint Formation carbonate: Implications for hydrosphere-atmosphere evolution, Precambrian Research, v. 290, p. 126-146, https://doi.org/10.1016/j.precamres.2016.12.014

Frank, T.D., and Lyons, T.W., 1998, "Molar- tooth" struc-tures: A geochemical perspective on a Proterozoic enigma: Geology, v. 26, p. 683–686, https://doi.org/10.1130/0091-7613(1998)026<0683:MTSAGP>2.3.CO;2.

Froelich, P. N. et al., 1979, Early oxidation of organic matter in pelagic sediments of the eastern equatorial Atlantic: suboxic diagenesis. Geochim. Cosmochim. Acta v. 43, p. 1075–1090, https://doi.org/10.1016/0016-7037(79)90095-4

Froelich, P.N. Klinkhammer, G.P. Bender, M.L. Luedtke, N.A. Heath, G.R. Cullen, D., Dauphin, P., Hammond, D., Hartman, B. and Maynard, V., 1979, Early oxidation of organic matter in pelagic sediments of the eastern equatorial Atlantic: suboxic diagenesis, Geochimica et Cosmochimica Acta, v. 43(7), p. 1075-1090, https://doi.org/10.1016/0016-7037(79)90095-4.

Fukushi, K. and Matsumiya, H., 2018, ACS Earth Space Chemistry, Control of Water Chemistry in Alkaline Lakes: Solubility of Monohydrocalcite and Amorphous Magnesium Carbonate in CaCl2 MgCl2−Na2CO3 Solutions, v. 2, p. 735−744, https://doi.org/10.1021/acsearthspacechem.8b00046

Fukushi, K., and Matsumiya, H., 2018, Control of water chemistry in alkaline lakes: Solubility of mono-hydrocalcite and amorphous magnesium carbon-ate in CaCl2-MgCl2-Na2CO3 solutions: ACS Earth and Space Chemistry, v. 2, p. 735–744, https://doi.org/10.1021/acsearthspacechem.8b00046

Fukushi, K., Suzuki, Y., Kawano, J., Ohno, T., Ogawa, M., Yaji, T. and Takahashi, Y. Speciation of Magnesium in Monohydrocalcite: XANES, Ab Initio and Geochemical Modelling. Geochimica Cosmochimica Acta, 2017, v. 213, p. 457−474, https://doi.org/10.1016/j.gca.2017.06.040

Gallagher, K.L., Braissant, O., Kading, T.J., Dupraz, C., and Visscher, P.T., 2013, Phosphate-related artifacts in carbonate mineralization experiments: Journal of Sedimentary Research, v. 83, p. 37–49, https://doi.org/10.2110/jsr.2013.9

García Del Cura, M. Á, Sanz-Montero, M. E., De Los Rios, M. A., and Ascaso, C., 2014, Microbial dolomite in fresh water carbonate deposits. Sedimentology, v. 61, p. 41–55, https://doi.org/10.1111/sed.12047

Gelli, R., Ridi, F. and Baglioni, P., 2019, The importance of being amorphous: calcium and magnesium phosphates in the human body. Adv Colloid Interface Science, https://doi/10.1016/j.cis.2019.04.011

Giannimaras, E.K. and Koutsoukos, P.G., 1987, The crystallization of calcite in the presence of orthophosphate. Journal of Colloid and Interface Science p. 116(2), v. 423-430, https://doi.org/10.1016/0021-9797(87)90138-X

Glenn CR, Föllmi KB, Riggs SR, Baturin GN, Grimm KA, Trappe J, Abed AM, Galliolivier C, Garrison RE, Ilyin AV, Jehl C, Rohrlich V, Sadaqah RMY, Schidlowski M, Sheldon RE, Siegmund H, 1994, Phosphorus and phosphorites: sedimentology and environments of formation. Eclogae Geol Helv v. 87, p. 747–788, https://doi.org/10.1111/j.1365-3091.1994.tb01397.x

Goldsmith, J.R., Graf, D.L., Heard, H.C., 1961, Lattice constants of the calcium magnesium carbonates, American Mineralogist, 1961, v. 46 (3-4 Part 1), p. 453–459. https://pubs.geoscienceworld.org/msa/ammin/article-abstract/46/3-4_Part_1/453/541758

Golubev, S. V., Pokrovsky, O. S., and Savenko, V. S.: Unseeded precipitation of calcium and magnesium phosphates from modified seawater solutions, J. Cryst. Growth, 205, 354–360, 1999.

Graham, R.J. and Pierrehumbert. R., 2020, Thermodynamic and Energetic Limits on Continental Silicate Weathering Strongly Impact the Climate and Habitability of Wet, Rocky World, Astrophysical Journal, American Astronomical Society., v. 896(2), p. 115, https://doi.org/10.3847/1538-4357/ab9362

Gregg, J.M. Bish, D.L.,. Kaczmarek, S.E. and Machel, H.G., 2015, Mineralogy, nucleation and growth of dolomite in the laboratory and sedimentary environment: A review, Sedimentology v. 62, p. 1749–1769, https://doi.org/10.1111/sed.12202

Grotzinger, J.P., and James, N.P., 2000, Precam-brian carbonates: Evolution of understanding, in Grotzinger, J.P., and James, N.P., eds., Carbon-ate Sedimentation and Diagenesis in the Evolv-ing Precambrian World: Society for Sedimentary Geology (SEPM) Special Publication 67, p. 3–20, https://doi.org/10.2110/pec.00.67.0003

Guerrero, J., Unabia, R., Vequizo, R., Gambe, J., Odarve-Vequizo, M.K. and Sambo, B., 2014, Effects of 42khz Ultrasonic Treatment to the Crystallite Size and Morphology of Chemically-Prepared Carbonated-Hydroxyapatite.

Gulick, A., 1955. Phosphorus as a factor in the origin of life. Am. Sci. vol. 43, pp. 479–489.

Gulick, A., 2006, Phosphorus and the origin of life. Annals of the New York Academy of Sciences, v. 69, p. 309 - 313. https://doi.org/10.1111/j.1749-6632.1957.tb49666.x

Gunnars, A., Blomqvist, S. and Martinsson, C., 2004, Inorganic formation of apatite in brackish seawater from the Baltic Sea: An experimental approach. Marine Chemistry, v. 15-26. p. 91, https://doi.org/10.1016/j.marchem.2004.01.008

Halverson, G. P., 2006, A Neoproterozoic chronology, in Xiao, S., and Kaufman, A. J., eds., Neoproterozoic Geobiology and Paleobiology, Volume Topics in Geobiology 27: New York, NY, Springer, p. 231-271.

Halverson, G. P., 2006, A Neoproterozoic chronology, in Xiao, S., and Kaufman, A. J., eds., Neoproterozoic Geobiology and Paleobiology, Volume Topics in Geobiology 27: New York, NY, Springer, p. 231-271.

Halverson, G., Maloof, A., Schrag, D. ,Dudás, F. and Hurtgen M. 2007, Stratigraphy and geochemistry of a ca. 800 Ma negative carbon isotope interval in northeastern Svalbard Chemical Geology, vol. 237, pp. 23-45. https://doi.org/10.1130/B25630.1.

Halverson, G.P., Dudás, F.Ö., Maloof, A.C., and Bowring, S.A., 2007, Evolution of the 87Sr/86Sr composition of Neoproterozoic seawater, Palaeogeography, Palaeoclimatology, Palaeoecology, vol. 256(3–4), pp. 103-129, https://doi.org/10.1016/j.palaeo.2007.02.028.

Hao, J., Sverjensky, D.A., Hazen, R.M., 2017, Mobility of nutrients and trace metals during weathering in the late Archean, Earth and Planetary Science Letters, vol. 471, pp. 148-159, http://dx.doi.org/10.1016/j.epsl.2017.05.003.

Hardie, L.A., 1987. Dolomitization; a critical view of some current views. Journal of Sedimentary Research, v. 57(1), v. 166–183, https://doi.org/10.1306/212F8AD5-2B24-11D7-8648000102C1865D

Harlan, S.S., Heaman, L., LeCheminant, A.N., Premo, W.R., 2003, Gunbarrel mafic magmatic event: A key 780 Ma time marker for Rodinia plate reconstructions. Geology, v. 32(2), p. 1053-1056, https://doi.org/10.1130/G19944.1

Harland, W.B., Wilson, C.B., 1956. The Hecla Hoek succession in Ny Friesland, Spitsbergen. Geological Magazine, v. 93, p. 265–286. https://doi.org/10.1017/S0016756800066693

Harries, J.E., Hasnain, S.S and Shah, J.S., 1987, EXAFS study of structural disorder in carbonate containing hydroxyapatites. Calcified Tissues International, v. 41, p. 346–50, https://doi.org/10.1007/BF02556675

He, S., and Morse, J.W., 1993, The carbonic acid system and calcite solubility in aqueous Na-K-Ca-Mg-Cl-SO4 solutions from 0 to 90°C: Geochimica et Cosmochimica Acta, v. 57(15), p. 3533-3554, https://doi.org/10.1016/0016-7037(93)90137-L

Henry, W., 1803, Experiments on the quantity of gases absorbed by water, at different temperatures, and under different pressures. Phil. Trans. R. Soc. London, v. 93, p. 29–274, https://doi.org/10.1098/rstl.1803.0004

Herbst, D.B., 1998, Potential salinity limitations on nitrogen fixation in sediments from Mono Lake, California. International Journal of Salt Lake Research, v. 7, p. 261–274 https://doi.org/10.1023/A:1009001514449

Higgins, J.A. et al., 2018, Mineralogy, early marine diagenesis, and the chemistry of shallow-water carbonate sediments: Geochimica et Cosmochimica Acta, vol. 220, pp. 512–534, doi:10.1016/j.gca.2017.09.046. https://doi.org/10.1016/j.gca.2017.09.046.

Higgins, J.A., Blättler, C.L., Lundstrom, E.A., Santiago-Ramos, D., Akhtar, A., Ahm, A-S.C., Bialik, O., Holmden, C., Bradbury, H., Murray S.T., and P. Swart, 2018, Mineralogy, early marine diagenesis, and the chemistry of shallow water carbonate sediments, Geochimica. Cosmochimica Acta, v. 220, p. 512-534, https://doi.org/10.1016/j.gca.2017.09.046

Hoffman, P.F., Kaufman, A., Halverson, G.P., and Schrag D. P., 1998, A Neoproterozoic Snowball Earth, Science, v. 281(5381), p. 1342-1346, https://doi.org/0.1126/science.281.5381.1342

Holm, N.G., 2012, The significance of Mg in prebiotic geochemistry. Geobiology, v. 10, p. 269-279, https://doi.org/10.1111/j.1472-4669.2012.00323.x

Horton, F., 2015, Did phosphorus derived from the weathering of large igneous provinces fertilize the Neoproterozoic ocean? Geochem. Geophysical Geosystems, v. 16, p. 1723–1738, https://doi.org/10.1002/2015GC005792

House, W.A. and Donaldson, L., 1986, Adsorption and coprecipitation of phosphate onto calcite. Journal of Colloid Interface Sci. v. 112, p. 309-324, https://doi.org/10.1016/0021-9797(86)90101-3,

Michalski, J. and Niles, P., 2010, Deep crustal carbonate rocks exposed by meteor impact on Mars. Nature Geoscience, v. 3, p. 751–755, 201, https://doi.org/10.1038/ngeo971

Huguet, L., Le Dudal, M., Livrozet, M., Bazin, D., Frochot, V., Joëlle., Haymann, J., Brocheriou, I., Daudon, M., and Letavernier, E, 2018, High frequency and wide range of human kidney papillary crystalline plugs. Urolithiasis. 46. https://doi.org/10.1007/s00240-017-1031-9

Ingall, E. and Jahnke, R., 1997, Influence of water-column anoxia on the elemental fractionation of carbon and phosphorus during sediment diagenesis. Marine Geology, v.139, p. 219–229, https://doi.org/10.1016/S0025-3227(96)00112-0

Ingall, E.D., Bustin, R.M. and Van Cappellen, P., 1993, Influence of water column anoxia on the burial and preservation of carbon and phosphorus in marine shales, Geochimica et Cosmochimica Acta, vol. 57(2), 1993, pp. 303-316, https://doi.org/10.1016/0016-7037(93)90433-W.

Ingall, E.D., Bustin, R.M., and Van Cappellen, P., 1993, Influence of water column anoxia on the burial and preservation of carbon and phos-phorus in marine shales: Geochimica et Cos-mochimica Acta, v. 57, p. 303–316, https://doi.org/10.1016/0016-7037(93)90433-W.

Ishikawa, M. and Ishikuni, M., 1981 Coprecipitation of phosphate with calcite. Geochemical Journal, v. 15, p. 283-288, https://doi.org/10.2343/geochemj.15.283

James, N.P., Narbonne, G.M., and Sherman, A.G., 1998, Molar-tooth carbonates: Shallow subtidal facies of the mid- to late Proterozoic: Journal of Sedimentary Research, v. 68, p. 716–722, https://doi.org/10.2110/jsr.68.716

Jasielec, J.J., Filipek, R., Dołowy, K., and Lewenstam, A., 2020, Precipitation of Inorganic Salts in Mitochondrial Matrix. Membranes, v. 10(5), p. 81. https://doi.org/10.3390/membranes10050081

Jellison R., and Melack J.M., 2001, Nitrogen limitation and particulate elemental ratios of seston in hypersaline Mono Lake, California, U.S.A.. In: Melack J.M., Jellison R., Herbst D.B. (eds) Saline Lakes. Developments in Hydrobiology, v. 162. Springer, Dordrecht. https://doi.org/10.1007/978-94-017-2934-5_1

Jensen, A.C.S., Imberti, S., Habraken, J.E.M. and Bertinetti, L., 2020, Small Ionic Radius Limits Magnesium Water Interaction in Amorphous Calcium/Magnesium Carbonates, Journal of Physical Chemistry, v. 124, p. 6141−6144, https://dx.doi.org/10.1021/acs.jpcc.9b11594

Jensen, A.C.S.; Rodriguez, I., Habraken, W.J.E.M., Fratzl, P. and Bertinetti, L. Mobility of hydrous species in amorphous calcium/ magnesium carbonates. Physical Chemistry Chemical Physics, v. 20, p. 19682− 19688, https://doi.org/10.1039/C8CP01782D

Johnsson, M.S., Nancollas, G.H., 1992, The role of brushite and octacalcium phosphate in apatite formation. Crit Rev Oral Biol Med., v. 1-2, p. 61-82. https://doi.org/10.1177/10454411920030010 60

Kah, L.C., Lyons, T.W. and Frank, T.D., 2004, Low Marine Sulphate and Protracted Oxygenation of the Proterozoic Biosphere, Nature v. 431, p. 834-838; doi:10.1038/nature02974

Kanazawa, M., Tsuru, K., Fukuda, N., Sakemi, Y., Nakashima, Y. and Ishikawa, K., 2017, Evaluation of carbonate apatite blocks fabricated from dicalcium phosphate dihydrate blocks for reconstruction of rabbit femoral and tibial defects. Journal of Materials Scientific Material Medicine, v. 28(6), p. 85. https://doi.org/10.1007/s10856-017-5896-5

Kebede, E. and Willén, K., 1998, Phytoplankton in a salinity–alkalinity series of lakes in the Ethiopian Rift Valley, Algol Stud, Phycologia v. 89, p. 63–96, https://doi.org/10.1127/algol_stud/89/1998/63

Keith, H. D., and Padden, F. J., 1963, A phenomenological theory of spherulitic crystallization: Journal of Applied Physics, v. 34, p. 2409–242, https://doi.org/10.1063/1.1702757

Kile, D.E., and Eberl, D.D., 2003, On the origin of size-dependent and size-independent crystal growth: Influence of advection and diffusion: The Ameri-can Mineralogist, v. 88, p. 1514–1521, https://doi.org/10.2138/am-2003-1014

Kiriukhin, M.Y. and Collins, K.D., 2002, Dynamic hydration numbers for biologically important ions, Biophysical Chemistry, v. 99, p. 155–168, https://doi.org/10.1016/s0301-4622(02)00153-9

Knoll A. H., 2015, Paleobiological Perspectives on Early Microbial Evolution. Cold Spring Harbor perspectives in biology, 7(7), a018093. https://doi.org/10.1101/cshperspect.a018093

Konhauser, K.O., Lalonde, S.V., Amskold, L. Holland, H.D., 2007, Was there really an Archean phosphate crisis?, Science, v. 315(5816), p. 1234, https://doi.org/10.1126/science.1136328

Krissansen-Totton, J., Arney, G.N. and Catling, D.C., 2018, Constraining the climate and ocean pH of the early Earth with a geological carbon cycle model, Proceedings of the National Academy of Sciences, v. 115(16), p. 4105-4110; https://doi.org/10.1073/pnas.1721296115

Krissansen-Tottona, J., Arney, G.N. and Catling, D.C., Constraining the climate and ocean pH of the early Earth with a geological carbon cycle model, PNAS, v. 115(16), p. 4105–4110, https://doi/10.1073/pnas.1721296115

Krom, M., Kress, N., Brenner, S. and Gordon, L., 1991, Phosphorus limitation of primary productivity in the eastern Mediterranean Sea. Limnology and Oceanography, p. 36, v. 424–432, https://doi.org/10.4319/lo.1991.36.3.0424

Kunzmann, M, Halverson, G.P. Scott, C., Minarik, W.G., Wing A., 2015, Geochemistry of Neoproterozoic black shales from Svalbard: Implications for oceanic redox conditions spanning Cryogenian glaciations, Chemical Geology, vol. 417, pp. 383-393, https://doi.org/10.1016/j.chemgeo.2015.10.022.

Laakso, T. and Schrag, D., 2014, Regulation of atmospheric oxygen during the Proterozoic. Earth and Planetary Science Letters, v. 388, p. 81–91. https://doi.org/10.1016/j.epsl.2013.11.049

Laakso, T.A., and Schrag, D.P., 2018a, A small marine biosphere in the Proterozoic: Geobiology, v. 17, p. 1–11, https://doi.org/10.1111/gbi.12323.

Laakso, T.A., and Schrag, D.P., 2018b, Limitations on limitation: Global Biogeochemical Cycles, v. 32, p. 486–496, https://doi.org/10.1002/2 017GB005832.

Laakso, T.A., Sperling, E.A., Johnston, D.T., and Knoll, A.H., 2020, Ediacaran reorganization of the marine phosphorus cycle: Proceedings of the National Academy of Sciences of the United States of America, v. 117(22), p. 11961–11967, https://doi.org/10.1073/pnas.1916738117

Land, L.S., 1998. Failure to Precipitate Dolomite at 25 ◦C from Dilute Solution Despite 1000-Fold Oversaturation after 32 Years. Aquatic Geochemistry v. 4, p. 361–368, https://doi.org/10.1023/A:1009688315854.pdf

Larson, A.C., and Von Dreele, R.B., 2004, General Structure Analysis System (GSAS): Los Alamos National Laboratory Report-LAUR, p. 86-748, https://doi.org/10.1103/PhysRevLett.101.107006

Last, W.M., and De Deckker, P., 1990, Modern and Holocene carbonate sedimentology of two saline volcanic maar lakes, southern Victoria. Sedimentology, v. 37, p. 967–981, https://doi.org/10.1111/j.1365-3091.1990.tb01839.x

Leckie, J. and Stumm, W., 1970. Phosphate precipitation E.F. Gloyna, W.W. Eckenfelder Jr. (Eds.), Water Quality Improvement by Physical and Chemical Processes, Univ. of Texas Press, v.3, p. 237-249.

Lee, J., and Morse, J.W., 2010, Influences of alkalinity and pCO2 on CaCO3 nucleation from estimated Cretaceous composition seawater representative of "calcite seas": Geology, v. 38, p. 115–118, https://doi.org/10.1130/G30537.1.

LeGeros, R.Z., 1965, Effect of carbonate on the lattice parameters of apatite, Nature, v. 206, p. 403–404, https://doi.org/10.1038/206403a0

Lenton, T.M. and Daines, S.J., 2018, The effects of marine eukaryote evolution on phosphorus, car-bon and oxygen cycling across the Proterozoic-Phanerozoic transition: Emerging Topics in Life Sciences, v. 2, p. 267–278, https://doi.org/10.1042/ETLS20170156

Lenton, T.M., 2020, On the use of models in understanding the rise of complex life. Interface Focus v. 10: 20200018. https://doi.org/10.1098/rsfs.2020.0018

Lenton, T.M., Boyle, R.A., Poulton, S.W., Shields-Zhou, G.A. and Butterfield, N.J., 2014. Co-evolution of eukaryotes and ocean oxygenation in the Neoproterozoic era. Nature Geoscience, v. 7(4), p. 257-265, https://doi.org/10.1038/ngeo2108

Lin, C.Y., Turchyn, A.V., Steiner, Z., Bots, P., Lam-pronti, G.I., and Tosca, N.J., 2018, The role of microbial sulfate reduction in calcium carbon-ate polymorph selection: Geochimica et Cos-mochimica Acta, v. 237, p. 184–204, https://doi.org/10.1016/j.gca.2018.06.019

Littlewood, J.L., Shaw, S., Peacock, C.L., Bots, P., Trivedi, D., and Burke, I.T., 2017, Mechanism of enhanced strontium uptake into calcite via an amorphous calcium carbonate crystallization path-way: Crystal Growth and Design, v. 17, p. 1214–1223, https://doi.org/10.1021/acs.cgd.6b01599

Lucas. J. and Prevot-Lucas, L., 1997. On the Genesis of Sedimentary Apatite and Phosphate-Rich Sediments. pp 249-268. In: Soils and Sediments. Springer, Berlin, Heidelberg. https://doi.org/10.1007/978-3-642-60525-3_12.

Macdonald, F. A., and Cohen, P. A., 2011, The Tatonduk inlier, Alaska-Yukon border, in E., A., Halverson, G. P., and Shields-Zhou, G., eds., The Geological Record of Neoproterozoic Glaciations, Volume 36: London, Geological Society of London, pp. 389-396.

Macdonald, F. A., Schmitz, M. D., Crowley, J. L., Roots, C. F., Jones, D. S., Maloof, A. C., Strauss, J. V., Cohen, P. A., Johnston, D. T., and Schrag, D. P., 2010b, Calibrating the Cryogenian: Science, v. 327, p. 1241-1243.

Macdonald, F.A., Halverson, G.P., Strauss, J.V., Smith, E.F., Cox, G.M., Sperling, E.A.,Roots, C.F., 2012. Early Neoproterozoic basin formation in Yukon, Canada: impli-cations for the make-up and break-up of Rodinia. Geosci. Can. 39, 77–99.

Macdonald, F.A., Mark D.Schmitz,Justin V.Strauss, Galen P.Halverson, Timothy M.Gibson, Athena Eyster, Grant Cox, Peter Mamrol, James L.Crowley, 2018, Cryogenian of Yukon, Precambrian Research, Volume 319, Pages 114-143 http://dx.doi.org/10.1016/j.precamres.2017.08.015

Macdonald, F.A., Schmitz, M.D., Crowley, J.L., Roots, C.F., Jones, D.S., Maloof, A.C.,Strauss, J.V., Cohen, P.A., Johnston, D.T., Schrag, D.P., 2010. Calibrating the Cryo-genian. Science 327, 1241–1243.

Marian, M. L., and Osborne, L. H., 1992. Petrology, petrochemistry, and stromatolites of the middle to late Proterozoic Beck Spring Dolomite, eastern Mojave Desert, California. Canadian Journal of Earth Sciences, v. 29, p. 2595–2609, https://doi.org/10.1139/e92-206

März, C., Poulton, S.W., Beckmann, B., Küster, K., Wagner, T. and Kasten, S., 2008, Redox sensitivity of P cycling during marine black shale formation: Dynamics of sulfidic and anoxic, non-sulfidic bottom waters. Geochimica et Cosmochimica Acta, v. 72(15), p. 3703-3717, https://doi.org/10.1016/j.gca.2008.04.025

Mason H. E., Frisia S., Tang Y., Reeder R. J. and Phillips B. L. (2007) Phosphorus speciation in calcite speleothems determined from solid-state NMR spectroscopy. Earth Planet. Sci. Lett. 254, 313–322.

Mason H. E., Frisia S., Tang Y., Reeder R. J. and Phillips B. L., 2007, Phosphorus speciation in calcite speleothems determined from solid-state NMR spectroscopy. *Earth Planet. Sci. Lett.* **254**, 313–322.

Mason H. E., Mccubbin F. M., Smirnov A. E. and Phillips B. L. (2009) Solid-state NMR and IR spectroscopic investigation of the role of structural water and F in carbonate-rich fuorapatite. American Mineralogist, v. 94, p. 507–516.

McKirdy, D. Thorpe, C., Haynes, D., Grice, K., Krull, E.S., Halverson, G.P. and Webster, L. 2010, The biogeochemical evolution of the Coorong during the mid- to late Holocene: An elemental, isotopic and biomarker perspective. Organic Geochemistry, v. 41(2), p. 96-110, https://doi.org/10.1016/j.orggeochem.2009.07.010

Mehrbach, C., Culberson, C. H., Hawley, J. E., Pytkowicx, R. M., 1973, Constants of Carbonic Acid in Seawater at Atmospheric Pressure, Article in Limnology and Oceanography, v. 18(6), p. 897-907, https://doi.org/10.4319/lo.1973.18.6.0897

Meyer, H.J., 1984, The influence of impurities on the growth rate of calcite: Journal of Crystal Growth, v. 66, p. 639–646, https://doi.org/10.1016/0022-0248(84)90164-7

Millero, F., and Schreiber, R. D., 1982, Use of the ion pairing model to estimate activity coefficients of the ionic components of natural waters. American Journal of Science, v. 282, p. 1508-1540. https://doi.org/10.2475/ajs.282.9.1508

Moczydłowska M., Pease V., Willman S., Wickström L. and Agić H. (2018) A Tonian age for the Visingsö Group in Sweden constrained by detrital zircon dating and biochronology: Implications for evolutionary events. Geol. Mag. 155, 1175–1189. Available at: https://doi.org/10.1017/S0016756817000085

Morris, R.V. Ruff, S.W. Gellert, R. Ming, D.W. Arvidson, R.E. Clark, B.C. Golden, D.C. Siebach, K. Klingelhofer, G. Schroder, C. Fleischer, I. Yen, A.S. Squyres S.W., Identification of carbonate-rich outcrops on Mars by the Spirit Rover, Science, v. 329, 2010, p. 421-424, https://doi.org/10.1126/science.1189667

Morse, J.W., 1985, Chemistry of calcium carbonate–rich shallow water sediments in the Bahamas: American Journal of Science, v. 285, p. 147–185, https://doi.org/10.2475/ajs.285.2.147.

Mort, H.P., Slomp, C.P., Gustafsson, B.G. and T.J. Andersen, 2010, Phosphorus recycling and burial in Baltic Sea sediments with contrasting redox conditions, Geochimica et Cosmochimica Acta, v. 74(4), p. 1350-1362, https://doi.org/10.1016/j.gca.2009.11.016

Mucci, A., 1983, The solubility of calcite and arago-nite in seawater at various salinities, tempera-tures temperatures, and one atmosphere total pressure: Ameri-can Journal of Science, v. 283, no. 7, p. 780–799, https://doi.org/10.2475/ajs.283.7.780

Mucci, A., 1983, The solubility of calcite and arago-nite in seawater at various salinities, tempera-tures, and one atmosphere total pressure: Ameri-can Journal of Science, v. 283, no. 7, p. 780–799, https://doi.org/10.2475/ajs.283.7.780.

Mucci, A., 1986, Growth kinetics and composi-tion of magnesian calcite overgrowths precipi-tated from seawater: Quantitative influence of orthophosphate ions: Geochimica et Cosmochimica Acta, v. 50, p. 2255–2265, https://doi.org/10.1016/0016-7037(86)90080-3

Nash, M.C., Wu, Zhongwei, Trafford, J.M., Opdyke,B.N. and Xu, H., 2013, Simple X-Ray Diffraction Techniques To Identify MG Calcite, Dolomite, and Magnesite In Tropical Coralline Algae and Assess Peak Asymmetry. Journal of Sedimentary Research, Research Methods, v.83, p.1084–1098. https://doi.org/10.2110/jsr.2013.67

Nash. W.P., 1984, Phosphate minerals in terrestrial igneous and metamorphic rocksIn: Phosphate Minerals. Editors: Nriagu, J.O., Moore, P.H. Springer-Verlag Berlin Heidelberg, pp. 444. ISBN. 978-3-642-61736-2. https://doi.org/10.1007/978-3-642-61736-2

Nelson, A. S., 2019, Twinning, Polymorphism, Polytypism, Pseudomorphism Mineralogy, Tulane University, EENS 2110, http://www.tulane.edu/~sanelson/eens211/twinning.htm (accessed 23 September 2021)

Nielsen, A.N. and Toft, J.M., 1984, Electrolyte crystal growth kinetics, Journal of Crystal Growth, v. 67(2), p. 278-288, https://doi.org/10.1016/0022-0248(84)90188-X

Notholt, A.J.G and Jarvis, I., 1984, (Eds.), Phosphorite Research and Development. Geological Society Special Publication, London, U.K., v. 52, p. 119-124.

Notholt, A.J.G., Sheldon, R.P. and Davidson, D.F., 1989. Phosphate Deposits of the World: vol. 2. Phosphate Rock Resources. Cambridge Univ. Press, United Kingdom, pp. 566. ISBN:9780521673334

Obst, M., Wehrli, B., and Dittrich, M., 2009, CaCO3 nucleation by cyanobacteria: Laboratory evidence for a passive, surface-induced mechanism: Geobi-ology, v. 7, p. 324–347, https://doi.org/10.1111/j.1472-4669.2009.00200.x.

Och, L. and Shields-Zhou, G., 2012, The Neoproterozoic Oxygenation Event: Environmental perturbations and biogeochemical cycling. Earth-Science Reviews, v. 110, p. 26-57, https://doi.org/10.1016/j.earscirev.2011.09.004.

Olli K, Ptacnik R, Klais R, Tamminen T., 2019, Phytoplankton Species Richness along Coastal and Estuarine Salinity Continua. The American Society of Naturalists, v. 194(2), p. E41-E51. https://doi.org/0.1086/703657

Oxmann J.F. Schwendenmann, L., 2014, Quantification of octacalcium phosphate, authigenic apatite and detrital apatite in coastal sediments using differential dissolution and standard addition Ocean Science, v. 10, p. 571–585, 2014, https://doi.org/10.5194/os-10-571-2014

Pan, Y. and Fleet, M.E., 2002, Compositions of the Apatite-Group Minerals: Substitution Mechanisms and Controlling Factors, Reviews in Mineralogy and Geochemistry, v. 48, p. 13–49, https://doi.org/10.2138/rmg.2002.48.2

Papineau, D., De Gregorio, B., Fearn, S., Kilcoyne, D., McMahon, G., Purohit, R. and Fogel, M. (2016), Nanoscale petrographic and geochemical insights on the origin of the Palaeoproterozoic stromatolitic phosphorites from Aravalli Supergroup, India. Geobiology, 14: 3-32. https://doi.org/10.1111/gbi.12164

Paquet, H. and Clauer, N., 1997. Soils and Sediments: Mineralogy and Geochemistry. 1997. Springer-Verlag Berlin Heidelberg. https://doi.org/10.1007/978-3-642-60525-3

Paquette, J., Reeder, R.J., 1990, Single-crystal X-ray structure refinements of two biogenic magnesian calcite crystals: American Mineralogist, v. 75(9-10), p. 1151–1158.

Pasek, Ma. Omran, A. Lang, C. Gull, M. and Abbatiello, J. Feng, T. G, Lyle, Abbott-Lyon, H., 2020, Serpentinization as a route to liberating phosphorus on habitable worlds. https://doi.org/110.21203/rs.3.rs-37651/v1.

Pérez, A., Luzón, A., Roc, A.C., Soria, A.R., Mayayo, M.J., Sánchez, J.A., 2002, Sedimentary facies distribution and genesis of a recent carbonate-rich saline lake: Gallocanta Lake, Iberian Chain, NE Spain. Sedimentary Geology, v. 148, p. 185–202, https://doi.org/10.1016/S0037-0738(01)00217-2

Petrash, D.A. Bialik, O.M., Bontognali, T.R.R., Vasconcelos, C., Roberts, J.A., McKenzie, J.A. and Konhauser, K.O. 2017. Microbially catalysed dolomite formation: From near-surface to burial. Earth-Science Reviews 171, 558–582, https://doi.org/10.1016/j.earscirev.2017.06.01

Phillips, B.L., Zhang, Z., Kubista, L., Frisia, S., Borsato, A., 2016, NMR spectroscopic study of organic phosphate esters coprecipitated with calcite, Geochimica et Cosmochimica Acta, v. 183, p. 46-62, https://doi.org/10.1016/j.gca.2016.03.022.

Pierrehumbert, R.T., Abbot, D.S., Voigt, A., Koll, D., 2011, Climate of the Neoproterozoic, Annual Review of Earth and Planetary Sciences, v. 39(1), p. 417-460, https://doi.org/10.1146/annurev-earth-040809-152447

Pilson, M. E. Q., 2012, An Introduction to the Chemistry of the Sea, (2nd ed.). Cambridge: Cambridge University Press. https://doi.org/10.1017/CBO9781139047203

Planavsky, N. J. et al. 2010, The evolution of the marine phosphate reservoir. Nature v. 467, p. 1088–1090, 1 https://doi.org/0.1038/nature09485

Planavsky, N.J, McGoldrick, P, Scott C.T., Li, C., Reinhard, C.T., Kelly, A.E., Chu, X., Bekker, A, Love, G.D. and Lyons, T.W., 2011, Widespread iron-rich conditions in the mid-Proterozoic ocean., Widespread iron-rich conditions in the mid-Proterozoic ocean. Nature, v. 447, p. 448-451, https://doi.org/10.1038/nature10327

Planavsky, N.J., Rouxel, O., Bekker, A., Lalonde, S.V., Konhauser, K.O., Reinhard, C.T. and Lyons, T.W. 2010. The evolution of the marine phosphate reservoir. Nature v. 467, p. 1088–1090. https://doi.org/10.1038/nature09485.

Plummer, N. L., and Busenberg, E., 1982, The solubilities of calcite, aragonite and vaterite in CO2-H2O solutions between 0 and 90°C, and an evaluation of the aqueous model for the system CaCO3-CO2-H2O. Geochimica et Cosmochimica Acta, v. 46(6), p. 1011-1040, https://doi.org/10.1016/0016-7037(82)90056-4

Pokrovsky, O.S., 1998, Precipitation of calcium and magnesium carbonates from homogeneous supersaturated solutions: Journal of Crystal Growth, v. 186, p. 233–239, https://doi.org/10.1016/S0022-0248(97)00462-4.

Pollack, J.B. Kasting, J.F. Richardson, S.M. Poliakoff, K., 1987, The case for a wet, warm climate on early Mars, Icarus, v. 71(2), p. 203-224, https://doi.org/10.1016/0019-1035(87)90147-3

Pollack, J.B., Haberle, R.M., Schaeffer, J., and Lee, H., 1990, Simulations of the general circulation of the Martian atmosphere: 1. Polar processes, Journal of Geophysical Research, v. 95 B2), p. 1447– 1473, doi: https://doi.org/110.1029/JB095iB02p01447

Pollock, M.D., Kah, L.C., and Bartley, J.K., 2006, Morphology of molar-tooth structures in Pre-cambrian carbonates: Influence of substrate rhe-ology and implications for genesis: Journal of Sedimentary Research, v. 76, p. 310–323, https://doi.org/10.2110/jsr.2006.021

Poulton, S. Early phosphorus redigested, 2017, Nature Geoscience, v. 10, p. 75–76, https://doi.org/10.1038/ngeo2884

Poulton, S.W. and Canfield, D.E. 2011, Ferruginous conditions: a dominant feature of the ocean through Earth's history. Bements, v. 7, p. 107-112, https://doi.org/10.2113/gselements.7.2.107

Power, I.A., Wilson, S.A., Thom, J.M., Dipple, G.M., Gabites, J.E., Southam, G., 2009. The hydromagnesite playas of Atlin, British Columbia, Canada: a biogeochemical model for CO2 sequestration. Chemical Geology, v. 260, p. 286–300, https://doi.org/10.1016/j.chemgeo.2009.01.012

Power, I.M., Kenward, P.A., Dipple, G.M., and Raudsepp, M., 2017, Room temperature magnesite precipitation. Crystal Growth Design 17, 5652–5659. doi: https://doi.org/10.1021/acs.cgd.7b00311

Purgstaller, B., Goetschl, K. E., Mavromatis, V., Dietzel, M., 2019, Solubility investigations in the amorphous calcium magnesium carbonate system, v. 21, p. 155–164, https://doi.org/10.1039/C8CE01596A

Purgstaller, B., Goetschl, K.E., Mavromatis, V., and Dietzel, M., 2019, Solubility investigations in the amorphous calcium magnesium carbonate sys-tem: CrystEngComm, v. 21, p. 155–164, https://doi.org/10.1039/C8CE01596A

Purgstaller, B., Mavromatis, V., Goetschl, K.E., Steindla, F.R. and Dietzel, M., 2021, Effect of temperature on the transformation of amorphous calcium magnesium carbonate with near-dolomite stoichiometry into high Mg-calcite, Crystal Engineering Communications, v. 23, p. 1969, https://doi.org/10.1039/D0CE01679A

Purgstaller, B., Mavromatis, V., Immenhauser, A. and Dietzel, M., 2016, Transformation of Mg-bearing amorphous calcium carbonate to Mg-calcite – In situ monitoring, Geochimica Cosmochimica Acta, v. 174, p. 180–195, https://doi.org/10.1016/j.gca.2015.10.030

Radha A. V., Forbes T. Z., Killian C. E., Gilbert P. U. P. A. and Navrotsky A., 2010 Transformation and crystallization energetics of synthetic and biogenic amorphous calcium carbonate. Proceedings of the National Academy of Sciences of the United States of America, v. 107, p. 16438 – 16443, https://doi.org/10.1073/pnas.1009959107

Reddy, M.M., 1977. Crystallization of calcium carbonate in the presence of trace concentrations of phosphorus-containing anions: I. Inhibition by phosphate and glycerophosphate ions at pH 8.8 and 25°C. Journal of Crystal Growth, v. 41(2), p. 287-295, https://doi.org/10.1016/0022-0248(77)90057-4

Reddy, M. M. and Hoch, A. R., 2001, Calcite Crystal Growth Rate Inhibition by Polycarboxylic Acids. J Colloid Interface Sci. 15;235(2):365-370. https://doi.org/10.1006/jcis.2000.7378. PMID: 11254315.

Reddy, M.M., and Hoch, A., 2012, Calcium carbon-ate nucleation in an alkaline lake surface water, Pyramid Lake, Nevada, USA: Aquatic Geochem-istry, v. 18, p. 95–113, https://doi.org/10.1007/s10498-011-9150-3

Reinhard, C., Planavsky, N., Gill, B., Ozaki, K., Robbins, L., Lyons, T., Fischer, W., Wang, C., Cole, D. and Konhauser, K., 2017, Evolution of the global phosphorus cycle. Nature Letter, Nature, v. 541(7637), p. 386-389, https://doi.org/10.1038/nature20772

Renaut, R.W., 1993, Morphology, distribution, and preservation potential of microbial mats in the hydromagnesite-magnesite playas of the Cariboo Plateau, British-Columbia, Canada. Hydrobiologia, v. 267, p. 75–98. https://doi.org/10.1007/Bf00018792

Reynolds, C.S. and Davies, P.S., 2001, Sources and bioavailability of phosphorus fractions in freshwaters: a British perspective, Biological Reviews, v. 76(1), p. 27-64, https://doi.org/10.1017/s1464793100005625.

Richard A. Jahnke, 1984. The synthesis and solubility of carbonate fluorapatite, Am J Sci vol. 284, pp. 58-78.

Robbins, L.L., and Blackwelder, P.L., 1992, Biochemical and ultrastructural evidence for the origin of whitings: A biologically induced calcium carbonate precipitation mechanism: Geology, v. 20, p. 464–468, https://doi.org/10.1130/0091-7613(1992)020<0464:BAUEFT>2.3.CO;2.

Roberts, J.A., Kenward, P.A., Fowle, DA., Goldstein, R.H.. González, L.A. and Moore, D.S., Surface chemistry allows for abiotic precipitation of dolomite at low temperature. Proceedings of the National Academy of Sciences of the United States of America, v. 10(36), p. 14540 – 14545, https://doi.org/10.1073/pnas.1305403110

Rodriguez-Blanco, J.D. Shaw, S. Bots, P. Roncal-Herrero, and T. Benning, L. G., 2012,The role of pH and Mg on the stability and crystallization of amorphous calcium carbonate. Journal of Alloys and Compounds, v. 536, p. S477−S479, https://doi.org/10.1016/j.jallcom.2011.11.057

Rodriguez-Blanco, J.D.; Shaw, S. Bots, P. Roncal-Herrero, T. and Benning, L.G., 2014, The role of Mg in the crystallization of monohydrocalcite. Geochimica Cosmochimica Acta, v. 127, p. 204−220, https://doi.org/10.1016/j.gca.2013.11.034

Romain Guilbaud, Simon W. Poulton , Jennifer Thompson , Kathryn F. Husband , Maoyan Zhu, Ying Zhou , Graham A. Shields and Timothy M. Lenton, 2020, Nature Geoscience, 296–301, https://doi.org/10.1038/s41561-020-0548-7

Romero, J. Jellison, R. and Melack. J.M., 1998, Stratification, Vertical Mixing, And Upward Ammonium Flux In Hypersaline Mono Lake, California. Arch. Hydrobiology, v. 142, p. 283–315, https://doi.org/10.1127/archiv-hydrobiol/142/1998/283

Rosen, M.R., Miser, Donald.E., Starcher, M.A. and Warren, J.K., 1989, Formation of dolomite in the Coorong region, South Australia. Geochimica et Cosmochimica Acta, v. 53(3), p. 661-669, https://doi.org/10.1016/0016-7037(89)90009-4

Roy, R.N., Roy, L.N., Vogel, K.M., Porter-Moore, C., Pearson, T., Good, C.E., Millero, F. J., Campbell, D.M. 1993, The dissociation constants of carbonic acid in seawater at salinities 5 to 45 and temperatures 0 to 45°C, Marine Chemistry, v. 44(2 – 6), p. 249-267, https://doi.org/10.1016/0304-4203(93)90207-5

Russell, M.J., Ingham, J.K., Zedef, V., Maktav, D., Sunar, F., Hall, A.J., Fallick, A.E., 1999. Search for signs of ancient life on Mars; expectations from hydromagnesite microbialites, Salda Lake, Turkey. Journal of the Geological Society of London 156, 869–888. Salvany,

Ruttenberg, K.C. and Berner, R.A., 1993, Authigenic apatite formation and burial in sediments from non-upwelling, continental margin environments. Geochim. Cosmochim. Acta, vol. 57, pp. 991-1007.

Saldi, G.D., 2009, 'Les cinétiques de dissolution et précipitation de la magnesite aux conditions hydrothermales'. PhD thesis. Thèse de l'Université Paul-Sabatier, Toulouse, France p. 184.

Saldi, G.D., et al., 2009, Magnesite growth rates as a function of temperature and saturation state, In: Geochimica et Cosmochimica Acta, v. 73(19), p. 5646–5657.doi: https://doi.org/10.1016/j.gca.2009.06.035.

Saller, A. Rushton, S. Buambua, L., Inman, K. McNeil, R. Dickson, J.A.D., 2016, Presalt stratigraphy and depositional systems in the Kwanza Basin, offshore Angola. AAPG Bulletin, v. 100, p.1135-1164. https://doi.org/10.1306/02111615216

Sánchez-Román, M., McKenzie, M.J., Rebello, A., Wagener, d.L., Rivadeneyra, M.,Vasconcelos, C, 2009. Presence of sulfate does not inhibit low-temperature dolomite precipitation., v. 85(1-2), p. 131-139, https://doi.org/10.1016/j.epsl.2009.06.003

Sandford, K.S., 1956, The stratigraphy and structure of the Hecla Hoek formation and its relationship to a subjacent metamorphic complex in North-East Land (Spitsbergen), Quarterly Journal of the Geological Society, v. 112, p. 339-362, https://doi.org/10.1144/GSL.JGS.1956.112.01-04.16

Sanz-Montero M.E., Cabestrer, O., Sánchez-Román, M., 2019, Microbial Mg-rich Carbonates in an Extreme Alkaline Lake (Las Eras, Central Spain), Frontiers in Microbiology, v. 10, p. 148,

Sanz-Montero, M.E. and Rodríguez-Aranda, J.P., 2012, Magnesite formation by microbial activity: evidence from a Miocene hypersaline lake. Sedimentary Geology, v. 263, p. 6–15. https://doi.org/10.1016/j.sedgeo.2011.08.004

Sato, S., Solomon, D., Hyland, C., Ketterings Q.M. and Lehmann, J., 2005, Phosphorus speciation in manure and manure-amended soils using XANES spectroscopy, Environmental Science and Technology, v. 39, p. 7485–7491, https://doi.org/10.1021/es0503130

Sayles, F.L. and Fyfe W.S., 1973, The crystallization of magnesite from aqueous solution, Geochimica et Cosmochimica Acta, v. 37(1), p. 87–99, https://doi.org/10.1016/0016-7037(73)90246-9.

Schwartz, A. W., 2006. Phosphorus in prebiotic chemistry. Philos. Trans. R. Soc. Lond. B Biol. Sci. vol. 361, pp. 1743–1749.

Selvama, N.C.S., Kumar, S.R.T., Kennedy, J., Vijayaa, J.J., 2011, Comparative study of microwave and conventional methods for the preparation and optical properties of novel MgO-micro and nano-structures, Journal of Alloys and Compounds, v. 509 p. 9809–9815, https://doi.org/10.1016/j.jallcom.2011.08.032

Shuster, A.M., Wallace, M.W., Hood, A.v.S., and Jiang, G., 2018. The Tonian Beck Spring Dolomite: Marine dolomitization in a shallow, anoxic sea. Sedimentary Geology, v. 368, p. 83–104, https://doi.org/10.1016/j.sedgeo.2018.03.003

Sibley, D.F., Dedoes, R.E., Bartlett .T.R.. Kinetics of dolomitization. Geology 1987, v. 15(12), p. 1112–1114. doi: https://doi.org/10.1130/0091-7613(1987)15<1112:KOD>2.0.CO;2

Slomp, C. P., Thomson, J. and de Lange, G. J., 2004, Controls on phosphorus regeneration and burial during formation of eastern Mediterranean sapropels. Marine Geology, v. 203, p 141–159 https://doi.org/10.1016/S0025-3227(03)00335-9

Slomp, C.P., Epping, E.H.G., Helder, W. and VanRaaphorst, W., 1996. A key role for iron-bound phosphorus in authigenic apatite formation in North Atlantic continental platform

sediments. J. Mar. Research, v. 54, p. 1179–1205. https://doi.org/10.1357/0022240963213745

Smith, G.I., 1927, Subsurface Stratigraphy and Geochemistry of Late Quaternary Evaporites, Searles Lake, California, Geological Survey Professional Paper 1043, https://doi.org/10.3133/pp1043

Smith, P., 1982, Was Precambrian seawater different?. Nature, v. 296, p. 309–310, https://doi.org/10.1038/296309a0

Spear, N., Holland, H.D., Garcia-Veígas, J., Lowen-stein, T.K., Giegengack, R., and Peters, H., 2014, Analyses of fluid inclusions in Neoproterozoic marine halite provide oldest measurement of seawater chemistry: Geology, v. 42, p. 103–106, https://doi.org/10.1130/G34913.1

Spence, G.H., Le Heron, D.P., and Fairchild, I.J., 2016, Sedimentological perspectives on climatic, atmospheric and environmental change in the Neoproterozoic Era, Sedimentology, v.63, p. 253-306.

Sperling, E.A., Halverson, G.P., Knoll, A.H., Macdonald, F.A. and Johnston, D.T., 2013, A basin redox transect at the dawn of animal life. Earth Planet. Sci. Lett. Vol. 371–372, pp. 143–155. https://doi.org/10.1016/j.epsl.2013.04.003.

Stone, D., Palmer, D., Hamilton, B., Cooney C. and Mosley, L., 2016. Coorong, Lower Lakes and Murray Mouth water quality monitoring program 2009—2016 Summary report, South Australian Environment Protection, University of Adelaide, ISBN 978-1-921495-75-5

Strauss, J.V., and Tosca, N.J., 2020, Mineralogical constraints on Neoproterozoic pCO2 and marine carbonate chemistry: Geology, v. 48, p. 599–603, https://doi.org/10.1130/G47506.1

Strauss, J.V., and Tosca, N.J., 2020, Mineralogical constraints on Neoproterozoic p CO2 and 336 marine carbonate chemistry: Geology, vol. 48, pp. 1-5, https://doi.org/10.1130/G47506.1.

Stumm, W. Leckie, J.O., 1970, Phosphate exchange with sediments: its role in the productivity of surface water, Advances in Water Pollution Research, Part III 2, Pergamon Press, New YorK, 1970, pp. 26/1–26/16

Sumner, D.Y. and Grotzinger, J.P., 1996, Were kinetics of Archean calcium carbonate precipitation related to oxygen concentration? Geology; v. 24(2), p. 119–122, https://doi.org/10.1130/0091-7613(1996)024<0119:WKOACC>2.3.CO;2

Sumner, D.Y., and Grotzinger, J.P., 1996, Were kinet-ics of Archean calcium carbonate precipitation related to oxygen concentration?: Geology, v. 24, no. 2, p. 119–122, https://doi .org/10.1130/0091-7613(1996)024<0119:WKOACC>2.3.CO;2.

Tadier, S., Rokidi, S., Rey, C., Combes, C. and Koutsoukos, P.G., 2017. Crystal growth of aragonite in the presence of phosphate. Journal of Crystal Growth, v. 458, p. 44-52, https://doi.org/10.1016/j.jcrysgro.2016.10.046

Tas, A., 2009, Use of Vaterite and Calcite in Forming Calcium Phosphate Cement Scaffolds, https://doi.org/10.1002/9780470339749.CH14

Thompson, J.B., and Ferris, F.G., 1990, Cyanobacterial precipitation of gypsum, calcite, and magnesite from natural alkaline lake water. Geology, v. 18, p. 995–998. https://doi.org/10.1130/0091-7613(1990)018<0995:CPOGCA>2.3.CO;2

Titschack, J., Goetz-Neunhoeffer F. and Neubauer J. (2011) Magnesium quantifcation in calcites [(Ca, Mg)CO3] by Rietveld-based XRD analysis: Revisiting a well-established method. Am. Mineral. v. 96, p. 1028–1038, https://doi.org/10.2138/am.2011.3665

Toner, J. and Catling, D., 2020. A carbonate-rich lake solution to the phosphate problem of the origin of life. PNAS, 117(2), pp. 883-888, https://doi.org/10.1073/pnas.1916109117.

Trautz, O., 1960, Crystallographic Studies of Calcium Carbonate Phosphate. Annals New York Academy of Science, v. 85, p. 145-60, https://doi.org/10.1111/J.1749-6632.1960.Tb49953.X

Trower, E.J., 2020, The enigma of Neoproterozoic giant ooids—Fingerprints of extreme climate?: Geo-physical Research Letters, v. 47, e2019GL086146, https://doi.org/10.1029/2019GL086146.

Tucker, M.E., 1982. Precambrian dolomites: Petrographic and isotopic evidence that they differ from Phanerozoic dolomites. Geology, v. 10(1), p. 7-12, https://doi.org/10.1130/0091-7613(1982)10<7:PDPAIE>2.0.CO;2

Turner et al., 1993, Elizabeth C. Turner, Guy M. Narbonne, Noel P. James; Neoproterozoic reef microstructures from the Little Dal Group, northwestern Canada. *Geology* 1993;; 21 (3): 259–262. doi: https://doi.org/10.1130/0091-7613(1993)021<0259:NRMFTL>2.3.CO;2

Turner, E. C., 2011, Stratigraphy of the Mackenzie Mountains supergroup in the Wernecke Mountains, Yukon, *in* MacFarlane, K. E., Weston, L. H., and Relf, C., eds., Yukon Exploration and Geology 2010: Whitehorse, Yukon, Yukon Geological Survey, p. 207-231.

Tutolo, B.M. and Tosca, N.J. 2018, Experimental examination of the Mg-silicate-carbonate system at ambient temperature: Implications for alkaline chemical sedimentation and lacustrine carbonate formation, Geochimica et Cosmochimica Acta, v. 225, p. 80-101, https://doi.org/10.1016/j.gca.2018.01.019

Tyrrell, T., 1999. The relative influences of nitrogen and phosphorus on oceanic primary production. Nature vol. 400, pp. 525–531.

Van Cappellen, P. and Berner, R.A.A, 1988. A mathematical model for the early diagenesis of phosphorus and fluorine in marine sediments: apatite precipitation. Am. J. Sci. vol. 288, pp. 289–333.

Van Cappellen, P. and Ingall, E.D., 1994, Benthic phosphorus regeneration, net primary production, and ocean anoxia: a model of the coupled marine biogeochemical cycles of carbon and phosphorus. Paleoceanography, v. 9, p. 677–692, https://doi.org/10.1029/94PA01455

Van Cappellen, P.S., 1991, Thesis: The formation of marine apatite, a kinetic study, Yale University, USA.

Van Cappellen, P. and Ingall, E.D, 1996, Redox Stabilization of the Atmosphere and Oceans by Phosphorus-Limited Marine Productivity, Science, v. 271(5248), p. 493-496, https://doi.org/10.1126/science.271.5248.493

Vasconcelos, C. and Mckenzie, J.A., 1997, Microbial mediation of modern dolomite precipitation and diagenesis under anoxic conditions (Lagoa Vermelha, Rio de Janeiro, Brazil). Journal of Sedimentary Research, v. 67(3), p. 378–390, https://doi.org/10.1306/D4268577-2B26-11D7-8648000102C1865D

Vasconcelos, C., Mckenzie, J.A., Bernasconi, S., Grujic, D. and Tien, A.J., 1995, Microbial mediation as a possible mechanism for natural dolomite formation at low temperatures. Nature, v. 377, p. 220–222, https://doi.org/10.1038/377220a0

Vignoles, M., Bonel, G., Holcomb, D.W., 1988, Influence of preparation conditions on the composition of type B carbonated hydroxyapatite and on the localization of the carbonate ions, Calcified Tissues International, 43, p. 33–40, https://doi.org/10.1007/BF02555165

Von Der Borch, C.C. and Lock, D., 1979.Geological significance of Coorong dolomites. Sedimentology, v. 26(8), p. 13-824, https://doi.org/10.1111/j.1365-3091.1979.tb00974.x

Wacey, D., 2002. The origin of dolomite in distal ephemeral lakes of the Coorong region of South Australia. D. Phil. Thesis, University of Oxford, Oxford, p.279.

Walker, L.J., Wilkinson, B.H. and. Ivany, L.C., 2002, Continental Drift and Phanerozoic Carbonate Accumulation in Shallow-Shelf and Deep-Marine Settings, The Journal of Geology, vol. 110(1), p. 75-87, https://doi:10.1086/324318

Wallace, A.F., Hedges, L.O., Fernandez-Martinez, A., Raiteri, P., Gale, J.D., Waychunas, G.A., Whitelam, S., Banfield, J.F., and De Yoreo, J.J., 2013, Microscopic evidence for liquid-liquid separation in supersaturated CaCO3 solutions: Science, v. 341, no. 6148, p. 885–889, https://doi.org/10.1126/science.1230915.

Walter L.M. and Hanor J.S., 1979, Effect of orthophosphate on the dissolution kinetics of biogenic magnesian calcites. Geochim. Cosmochim. Acta v. 43, p. 1377- 1385, https://doi.org/10.1016/0016-7037(79)90128-5

Walter, M.R., Golubic, S., Preiss, W.V., 1973. Recent stromatolites from hydromagnesite and aragonite depositing lakes near Coorong Lagoon, South Australia. Journal of Sedimentary Petrology, v.43, p. 10021–11030, https://doi.org/10.1306/74D728DD-2B21-11D7-8648000102C1865D

Wang, J., Zhou W., Chen H., Zhan J., He C. and Wang Q., 2019, Ammonium Nitrogen Tolerant Chlorella Strain Screening and Its Damaging Effects on Photosynthesis, Frontiers in Microbiology, v. 9, p. 3250, https://doi.org/10.3389/fmicb.2018.03250

Warren, J. K., 1990, Sedimentology and mineralogy of dolomitic Coorong lakes, South Australia: Journal of Sedimentary Petrology, v. 60, p. 843-858, https://doi.org/10.1306/212F929B-2B24-11D7-8648000102C1865D

Webb, S.M., 2005. SIXPACK a graphical user interface for XAS analysis using IFEFFIT. Phys. Scr. 2005, 1011, https://doi.org/10.1238/Physica.Topical.115a01011

Webb, S.M., McNulty, I., Eyberger, C., Lai, B., 2011. The MicroAnalysis toolkit: X-ray fluorescence image processing software. In: AIP Conference Proceedings. American Institute of Physics. p. 196–199. https://doi.org/10.1063/1.3625338.

Weiner, S. and Dove, P. M., 2003, An overview of biomineralization processes and the problem of the vital effect. In: Dove, P.M., de Yoreo, J.J., and Weiner, S. Editors., Biomineralization, Mineralogical Society of America, Washington, DC., p. 381, ISBN13 978-0-939950-66-9

Weiner, S., Levi-Kalisman, Y., Raz, S., Addadi, L., 2003, Biologically formed amorphous calcium carbonate, Connective Tissue Research, v. 44, p. 214-218, https://doi.org/10.1080/03008200390181681

Westphal,H. et al. Differential Diagenesis of Rhythmic Limestone Alternations Supported by Palynological Evidence Journal of Sedimentary Research(2000),70(3):715

White, A.H. and Youngs, B.Y, 1980, Cambrian alkali playa-lacustrine sequence in the northeastern Officer Basin, South Australia. Journal of Sedimentary Research, v. 50(4), p. 1279–1286. doi: https://doi.org/10.1306/212F7BD0-2B24-11D7-8648000102C1865D

Wilson, C.B., 1961, The Upper Middle Hecla Hoek Rocks of Ny Friesland, Spitsbergen, Geological Magazine, v. 98 (2), p. 89-116, https://doi.org/10.1017/S0016756800060325

Wolf-Gladrow, D. A., Zeebe, R. E. Klaas, C., Koertzinger, A., and Dickson, A. G., 2007, Total alkalinity: the explicit conservative expression and its application to biogeochemical processes. Marine Chemistry, v. 106(1–2), p. 287-300, https://doi.org/10.1016/j.marchem.2007.01.006

Wood, R., Bowyer, F., Penny, A. and Poulton, S.W., 2018, Did anoxia terminate Ediacaran benthic communities? Evidence from early diagenesis, Precambrian Research, v. 313, p. 134-147, https://doi.org/10.1016/j.precamres.2018.05.011

Wright D.T. and Wacey, D., 2005, Precipitation of dolomite using sulphate-reducing bacteria from the Coorong Region, South Australia: Significance and implications International Association of Sedimentologists, Sedimentology, v. 52(5), p. 987–1008 https://doi.org/10.1111/j.1365-3091.2005.00732.x

Wright, P.V. and Barnett, A.J., 2015, An abiotic model for the development of textures in some South Atlantic early Cretaceous lacustrine carbonates,Geological Society, London, Special Publications, v. 418, p. 209-219, https://doi.org/10.1144/SP418.3

Wright, V.P., Barnett, A.J., 2020, The textural evolution and ghost matrices of the Cretaceous Barra Velha Formation carbonates from the Santos Basin, offshore Brazil. Facies, v. 66, p. 7, https://doi.org/10.1007/s10347-019-0591-2

Xu, N., Li, Y., Zheng, L., Gao, Y., Yin, H., Zhao, J., Chen, Z., Chen, J. and Chen, M., 2014, Synthesis and application of magnesium amorphous calcium carbonate for removal of high concentration of phosphate, Chemical Engineering Journal, v. 251, p. 102–110, https://doi.org/10.1016/j.cej.2014.04.037

Xu, J., Yan, C., Zhang, F., Konishi,H.,Xu,, H.,Henry H.,Teng, Crystallization of Mg–Ca–CO3 at ambient conditions, Proceedings of the National Academy of Sciences Oct 2013, 110 (44) 17750-17755; https://doi.org/10.1073/pnas.1307612110

Yang, Y-N., Zhu, X-L, Kong, X-Z., 2013, Controls of Crystal Morphology, Size and Structure in Spontaneous Precipitation of Calcium Carbonate: Controls of Crystal Morphology, Size and Structure in Spontaneous Precipitation of Calcium Carbonate, Journal of Inorganic Materials, 28, 1313-1320. https://doi.org/10.3724/SP.J.1077.2013.13163

Yang, J., Junium, C.K., Grassineau, N.V., Nisbet, E.G. Izon, G.I., Mettam, C., Martin, A. and Zerkle A. L. 2019 Ammonium availability in the Late Archaean nitrogen cycle. Nature Geoscience, v. 12, p. 553–557 https://doi.org/10.1038/s41561-019-0371-1

Yi et al., 2013, A carbonate-fluoride defect model for carbonate-rich fluorapatite. Am. Mineral. V. 98, p. 1066–1069.

Yi, et al., 2020, A continuous reaction network that produces RNA precursors, Proceedings of the National Academy of Sciences . https://doi.org/10.1073/pnas.1922139117

Z.X. Li, S.V. Bogdanova, A.S. Collins, A. Davidson, B. De Waele, R.E. Ernst, I.C.W. Fitzsimons, R.A. Fuck, D.P. Gladkochub, J. Jacobs, K.E. Karlstrom, S. Lu, L.M. Natapov, V. Pease, S.A. Pisarevsky, K. Thrane, V. Vernikovsky, Assembly, configuration, and break-up history of Rodinia: A synthesis, Precambr. Res., 160 (2008), pp. 179-210

Zeebe, R. E., Wolf-Gladrow, D., 2001, CO2 in Seawater: Equilibrium, Kinetics, Isotopes, Elsevier Oceanography Series, Elsevier Science, 65. p. 365, ISBN: 9780444509468

Zegeye, A. et al., 2012, Green rust formation controls nutrient availability in a ferruginous water column. Geology, v. 40(7), p. 599–602, https://doi.org/10.1130/G32959.1

Zhang, F., Xu, H., Konishi, H and Roden, E.E., 2010, A relationship between d104 value and composition in the calcite-disordered dolomite solid-solution series, American Mineralogist, v. 95, p.1650–1656, https://doi.org/10.2138/am.2010.3414 Temperature- and pH-Dependent Morphology and FT−IR Analysis of Magnesium Carbonate Hydrates

Zhang, P., Anderson, H.L., Kelly, J., Krumhansl, J., and Papenguth, H. 2000, Kinetics and Mechanisms of Formation of Magnesite from Hydromagnesite in Brine. Applied Geochemistry, https://www.osti.gov/servlets/purl/764025/

Zhang, Y., Dawe, R., 2000, Influence of Mg2+ on the kinetics of calcite precipitation and calcite crystal morphology, Chemical Geology, v. 163(1–4), p. 129-138, https://doi.org/10.1016/S0009-2541(99)00097-2

Zhang, Z., Zheng, Y., Ni, Y., Liu, Z., Chen, J. and Liang, X., 2006, The Journal of Physical Chemistry B, v. 110(26), p. 12969-12973, https://doi.org/10.1021/jp061261j

Zhao, M., Zhang, S., Tarhan, L.G., Reinhard, C.T., and Planavsky, N., 2020, The role of calcium in regulating marine phosphorus burial and atmospheric oxygenation: Nature Communica-tions, v. 11, p. 2232, https://doi.org/10.1038/s41467-020-15673-3

Zumberge, J.A., Rocher, D., Love, G.D., 2020, Free and kerogen-bound biomarkers from late Tonian sedimentary rocks record abundant eukaryotes in mid-Neoproterozoic marine communities. Geobiology, v. 8, p. 326– 347. https://doi.org/10.1111/gbi.12378

Supplement 1

S1 Introduction to supplementary material

Additional relevant data, extended methodologies and geochemical calculations are provided in the supplementary material. The supplement number corresponds to the chapter number in the thesis i.e., Chapter 1 – Supplement 1; Chapter 2; Supplement 2; Chapter 3 – Supplement 3; Chapter 4 – Supplement 4.

Supplement 2

S2 Supplementary material Chapter 2

S2 1.1 Additional FTIR and XRD data

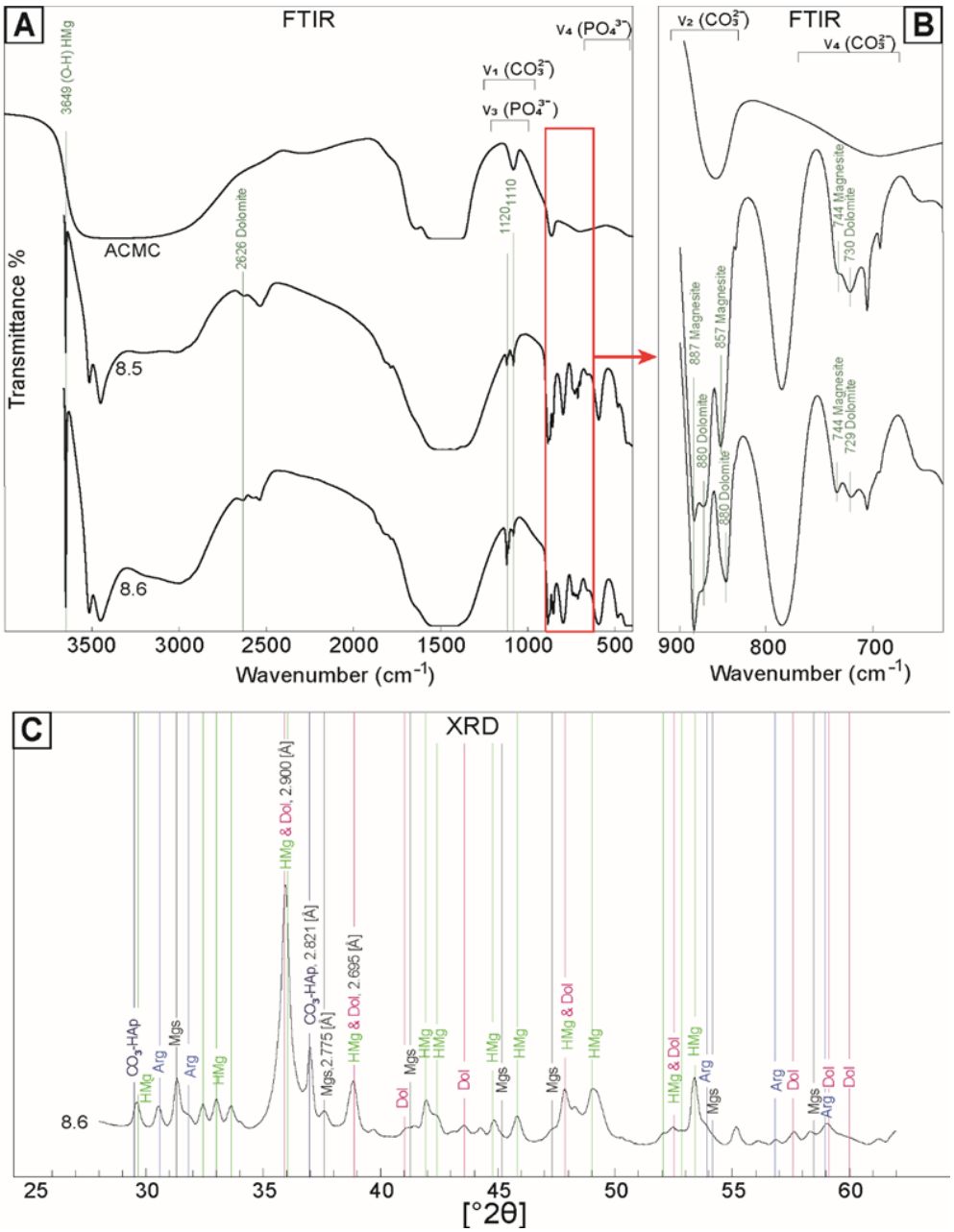

Figure S2. 1 Representative FTIR and XRD diagrams from the homogenous nucleation experiments. Interpretations are labelled. A: FTIR indicates an ACMC spectrum from a sample that was nucleated at room temperature (22 ºC), vacuum filter dried and analyzed immediately

without subject to recrystallization in the water-bath. The ACMC spectra presents no observable crystalline bands. The remaining spectra are taken from homogenous nucleation experiments 8.5 and 8.6 (i.e., Table S2). These solids precipitated from *higher PO_4* experiments in highly alkaline and supersaturated solutions (Ω_{ACMC} = 228) that contain [PO_{4tot}] = 14 m*M*/L, Mg/Ca = 5, ([Ca^{2+}] 9; [Mg^{2+}] 43 m*M*), CO_3/Ca = 12 ([CO_3^{2-}] 103; [Ca^{2+}] 9 m*M*) at pH 10 in 50 ºC temperatures. The increase in salinity in 8.6 appears to result in a greater degree of crystallinity of magnesite peaks and the lower salinity appears to result in a greater degree of crystallinity of dolomite peaks. B: A representative XRD diagram of the sample, 8.6. The XRD peaks positions (°2θ) and d-spacing (Å) are labelled for the dominant mineral phases.

S2 1.2 XRD characterization of ACMC

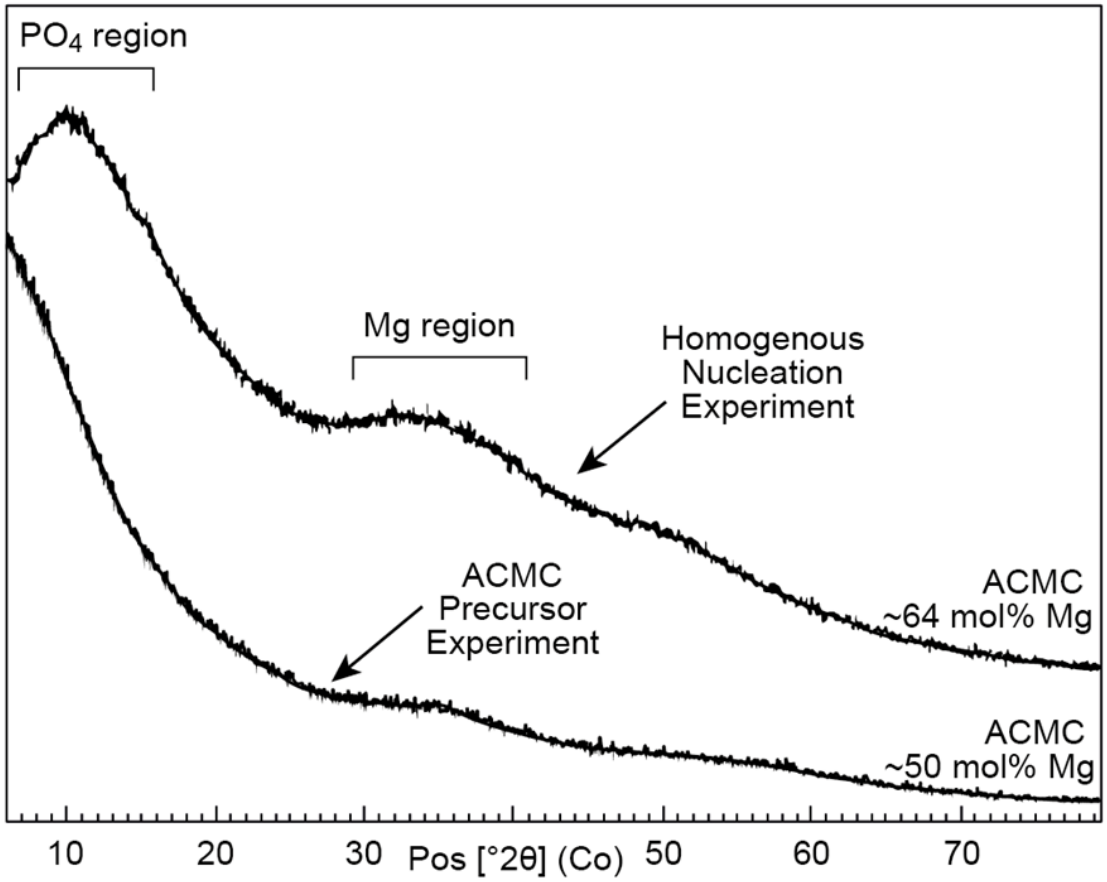

Figure S2. 2 XRD diagrams of initial ACMC precursor and homogenous nucleation phases. The absence of peaks is indicative of amorphous material. The homogenous nucleation experiment ACMC is notably different from the controlled ACMC precursor with a distinct hump positioned at approximately 12º 2Θ. Indicating that this phase may contain mixed amorphous Mg-carbonate (AMC) and/or amorphous Ca-phosphate (ACP). The homogenous nucleation Mg mol% is based on ICP-AES solid analyses and FTIR ν_1 peak values. The ACMC precursor material precipitated through steady state conditions contained approximately 50 % mol Mg based on FTIR ν_1 peak values (Blue and Dove, 2015)

S2 1.3 XRD results from homogenous nucleation experiments

Initial conditions summary					XRD Results (approx. %) – Homogenous Nucleation Experiments														
					$MgCO_3$ minerals			$MgCaCO_3$ minerals		$CaCO_3$ minerals				PO_4 minerals					Other
Exp. ID	$CaCl_2$ m*M*/kg	$MgCl_2$ m*M*/kg	CO_3 m*M*/kg	PO_4 m*M*/L	HMGs	Magnesite	NSQh	Dolomite	Huntite	Calcite	Aragonite	Northupite	Monetite	HAp	CO_3-Ap	CLAp	Mg-PO_4	Trömelite	Halite
6.6	9	43	132	7	ACMC														
7.0	28	24	132	7	35	0	0	13	0	0	15	0	37	0	0	0	0	0	0
7.1	17	43	132	7	58	0	0	6	0	18	9	5	0	0	0	0	0	9	0
7.2	9	38	132	7	80	0	0	8	0	0	5	3	0	0	0	0	0	0	3
7.3	6	38	132	7	83	0	0	0	0	7	4	5	0	0	0	0	0	0	0
7.4	5	43	132	7	76	0	0	0	0	0	11	0	0	4	0	0	0	0	3
7.5	4	43	132	7	80	0	0	6	0	7	4	0	0	0	0	0	0	0	0
7.6	3	43	132	7	91	0	0	0	0	0	4	0	0	5	0	0	0	0	0
7.7	3	43	132	7	89	0	0	3	0	0	0	0	0	0	0	8	0	0	0
7.8	3	48	132	7	84	0	0	6	0	0	3	3	0	0	0	0	0	0	3
7.9	9	43	132	7	70	0	0	2	0	0	19	0	0	6	0	0	0	0	3
8.0	9	43	132	7	85	0	0	2	0	0	5	0	0	0	0	2	0	0	6
8.1	9	43	132	7	59	0	0	0	0	0	4	0	0	0	0	0	29	0	2
8.2	9	43	132	7	79	0	0	7	0	0	13	0	0	0	0	13	0	0	0
8.3	9	43	132	14	69	0	0	6	0	0	6	0	20	0	0	0	0	0	0
8.4	9	43	132	14	85	0	0	3	0	0	5	0	7	0	0	0	0	0	0
8.5	9	43	132	14	78	3	0	11	0	0	4	0	0	4	0	0	0	0	1
8.6	9	43	132	14	57	6	0	11	0	0	21	0	0	0	5	0	0	0	1
8.7	9	43	132	14	59	7	0	13	0	0	5	0	0	8	0	0	0	0	1
Chemical formula					$MgCO_3 \bullet H_2O$	$MgCO_3$	$Mg(OH)(HCO_3) \bullet 2H_2O$	$CaMg(CO_3)_2$	$CaMg_3(CO_3)_4$	$CaCO_3$	$Ca_{0.94}Mg_{0.064}(CO_3)_2$	$(Na_3Mg(CO_3)_2Cl)$	$CaHPO_4$	$Ca_{10}(PO_4)_6(OH)_2$	$Ca_{10}(PO_4)_6(CO_3) \bullet 2H_2O$	$(Ca_{9.63}Na_{0.40})5Cl(PO_4)_3$	$Mg_2(PO_4)(OH)$	$Ca_4P_6O_{19}$	NaCl
Reference code (XRD)					01-079-9948	01-080-3274	04-011-2636	01-083-5728	04-007-8886	04-012-8072	04-015-6307	01-076-6232	04-011-3070	04-016-1647	01-072-9862	01-077-4348	04-009-5640	04-011-7772	04-006-5357
HMGs: hydromagnesite, NSQh: nesquehonite, HAp: hydroxyapatite, CO_3Ap: carbonate apatite, CLAp: chlorapatite, DCP: dicalcium-PO_4																			

Table S2 1 Summary of the semi quantitative XRD results from the homogenous nucleation expetiments. The values given are for the closest XRD reference matches corresponding with

the analyzed XRD diffraction peaks of the experimental samples. The approximate percentage of the minerals present, chemical formula of the identified minerals and representative reference codes are indicated. It is important to note that many of the samples contained disordered crystallography, polyphase mixtures of minerals and possible ionic substitution within the crystals and/or inclusions within the crystals or contain hydrated ions. These impurities may have resulted in altered or atypical XRD diffraction data and contributed to challenges with identification. Therefore, the reference codes for minerals are not often a 'good' match and this table represents a summary of the closest matches. The dataset would benefit from more extensive Rietveld refinement.

In addition to the Mg-and Mg-Ca carbonate minerals produced in the homogenous nucleation experiments, XRD spectra identify the presence of rare mineral northupite $Na_3Mg(CO_3)_2Cl$ from several samples, which may be explained by the excess of magnesium, sodium and chlorine in the solutions (Deelman, 2011). Although northupite is uncommon, it is most notably identified in evaporative sediments from Searles Lake, California; an alkaline carbonate-rich lake that produces primary dolomite (Smith and Haines, 1964) and contains uniquely high [PO_{4tot}], dissolved inorganic carbon ([DIC]) (i.e., Toner and Catling, 2020) and hosts primary dolomite sediments (Smith, 1978). Northupite is a metastable mineral that forms from an amorphous precursor and alongside witherite ($BaCO_3$) can ripen via dissolution–crystallization process into dolomite-group mineral norsethite ($BaMg(CO_3)_2$) (Pimentel and Pina, 2014). Although Ba and Mn are absent in our experiment, this process may be similar to that which forms primary dolomite at the expense of two metastable precursor minerals such as ACMC and AMC or hydromagnesite in similar environmental settings. Although previous studies indicate that northupite may form resulting from high [Cl] in solution that may favour northupite over hydromagnesite and nesquehonite (Deelman, 2011) we observe predominantly hydromagnesite with only minor northupite indicated. This may indicate that northupite postdates the formation of hydromagnesite in solution.

S2 1.4 FTIR results from homogenous nucleation experiments

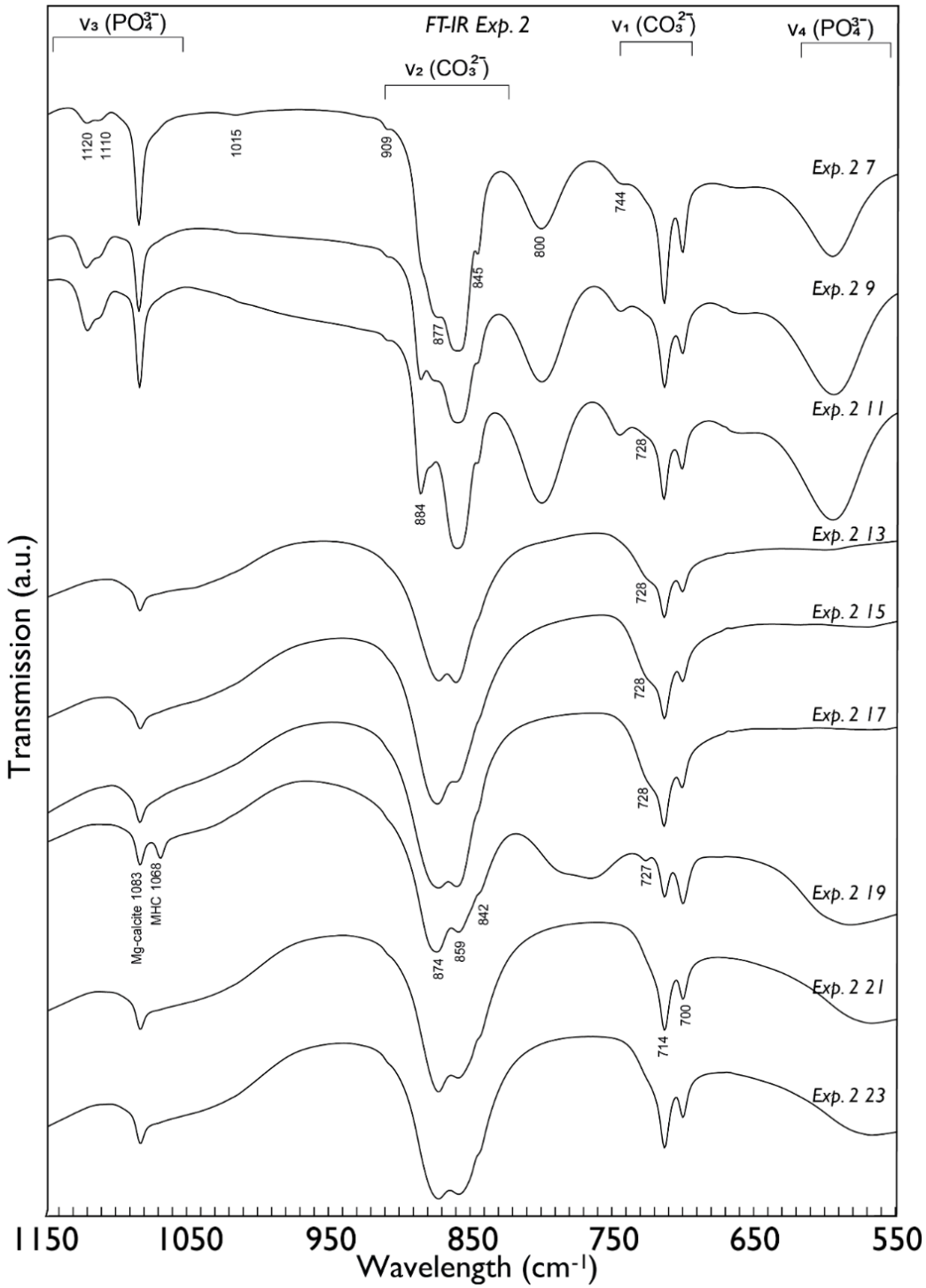

Figure S2. 3 FTIR results from ACMC precursor experiments with vibrational bands assigned and mineralogical interpretations based on peaks.

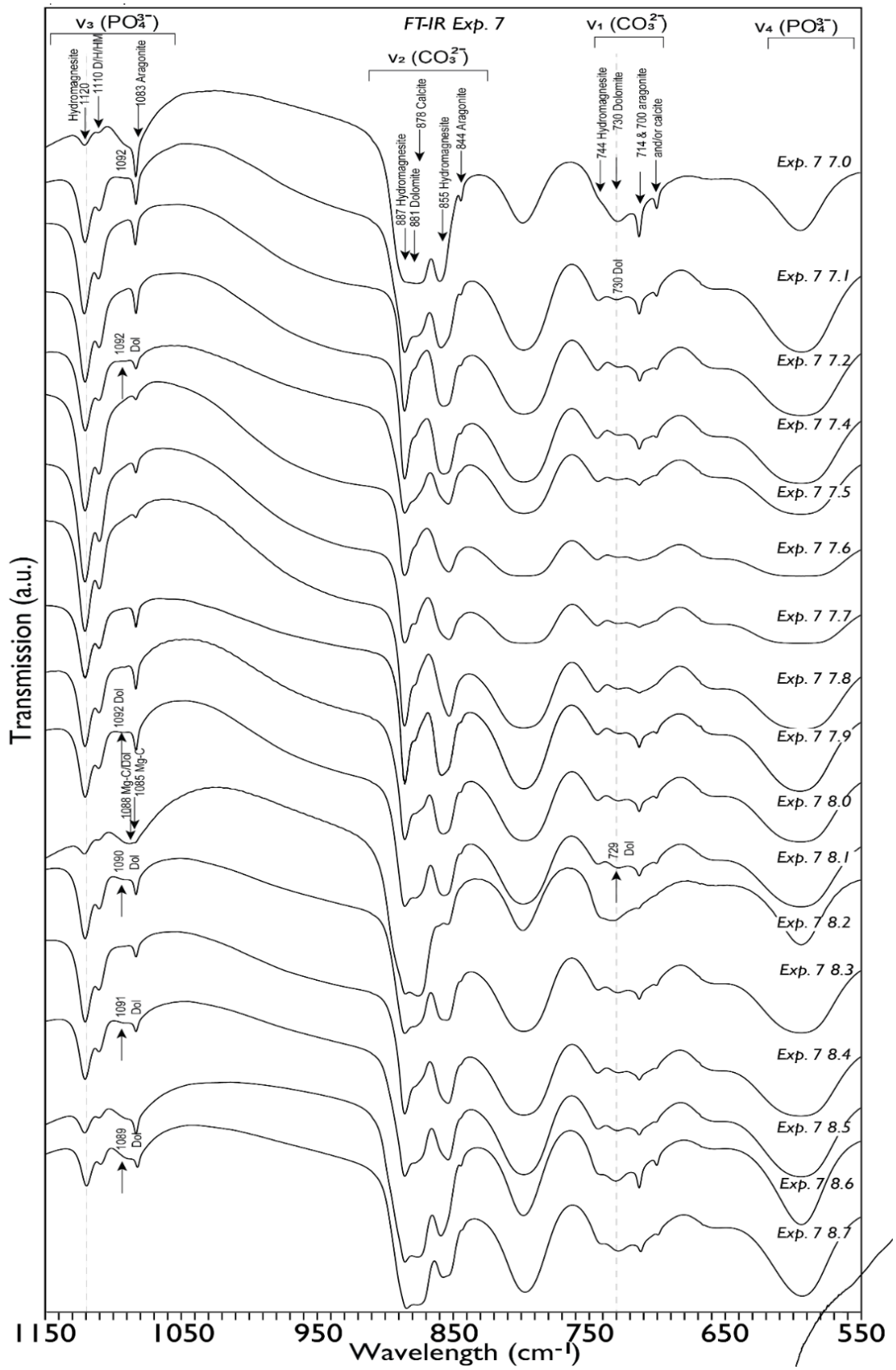

Figure S2. 4 FTIR results from homogenous nucleation experiments with vibrational bands assigned and mineralogical interpretations based on peaks.

S2 2 Homogenous Nucleation Experiments

S2 2.1 ICP-MS solid sample analyses

During the homogeneous nucleation experiments (Exp. 7), the aqueous Ca and Mg concentrations of experimental solution samples were extracted, syringe-filtered (0.22 μm), and acidified (HNO_3, 4 %). When the experiments were terminated, the bulk solid samples were syringe-filtered (0.22 μm), vacuum-filtered, rinsed with isopropanol, and dried in a vacuum-desiccator at 25 °C for 24 h before digestion (HNO_3, 4 %). The Ca, Mg and P elemental concentrations were then measured using ICP-AES performed using an Ultima 2C Horiba Jobin Yvon inductively coupled plasma optical emission spectrometer (ICP-AES) at Kingston University. Samples were randomized, replicates were analyzed every 10 samples, 8 calibration standards were used and 1 ppm, quality control (QC) standards were analyzed every 10 samples. In addition, 10 matrix matched standards were produced and analyzed along with blank samples with no Ca, Mg or P were analyzed every 10 samples and reference standards: SPS-SW2; NASS-7; SLRS-6_R2_5xdil and a synthetic seawater with no calcium. The analytical precision for the bulk solid samples was ± 4% for Mg and ±5% for Ca and the analytical precision for the aqueous solution samples was ± 6%.

EXP 7 No.	EXP 7 No.2	Mg (ppb)	Ca (ppb)	Total Mg + Ca	Mg:Ca overall of solid	Mg mol %	Ca mol %
Exp 7	6.6	123603.96	114974.55	238578.51	1.08	63.9	4.5
Exp 7	7.0	114356.65	171127.08	285483.72	0.67	52.4	8.1
Exp 7	7.1	152817.29	140309.95	293127.25	1.09	64.2	5.5
Exp 7	7.2	201725.20	71414.95	273140.15	2.82	82.3	2.2
Exp 7	7.3	237046.76	49590.60	286637.36	4.78	88.7	1.4
Exp 7	7.4	244068.28	38454.36	282522.64	6.35	91.3	1.1
Exp 7	7.5	240155.21	38497.83	278653.04	6.24	91.1	1.1
Exp 7	7.6	237132.05	29852.91	266984.97	7.94	92.9	0.8
Exp 7	7.7	250298.21	21687.69	271985.91	11.54	95.0	0.6
Exp 7	7.8	241293.30	21873.40	263166.70	11.03	94.8	0.6
Exp 7	7.9	199581.51	77669.83	277251.34	2.57	80.9	2.4
Exp 7	7.9 d.	203376.06	78243.36	281619.42	2.60	82.0	2.4
Exp 7	8.0	218020.64	79144.07	297164.71	2.75	79.1	2.6
Exp 7	8.1	188548.35	81968.06	270516.41	2.30	82.1	2.4
Exp 7	8.2	218260.46	78306.57	296567.04	2.79	81.4	2.4
Exp 7	8.4	207650.93	78148.70	285799.63	2.66	83.3	2.2
Exp 7	8.5	219863.06	72862.72	292725.78	3.02	82.8	1.8
Exp 7	8.6	171782.85	58797.41	230580.26	2.92	86.0	1.7
Exp 7	8.7	215607.84	57801.96	273409.80	3.73	63.9	4.5

Table S2 2 Results of the bulk solid samples from homogenous nucleation experiments following digestion and analysis by ICP-AES to determine Mg, Ca and P concentration. P was below the detection limit in all solid sample analyses and is not shown. Mg/Ca ratio. Mg and Ca mol % were estimated from the calculation shown in Eq. 2.25.

S2 2.2 ICP-AES solution analyses

ICP-AES results				
Average Sample	**Days in bath**	**Mg m*M*/L**	**Ca m*M*/L**	**P m*M*/L**
7.0	0	5.79	0.01	2.67
7.0	22	0.08	0.00	2.28
7.0	54	0.06	0.00	2.41
7.0	64	0.04	0.00	3.81
7.1	0	0.69	0.01	3.37
7.1	22	0.07	0.00	2.37
7.1	54	0.06	0.00	3.31
7.1	64	0.03	0.00	3.36
7.2	0	0.30	0.00	1.49
7.2	54	0.07	0.00	1.72
7.2	64	0.01	0.00	1.99
7.3	0	0.25	0.00	4.88
7.3	22	-	-	-
7.3	54	0.06	0.00	3.74
7.3	64	0.04	0.00	1.50
7.4	0	0.77	0.00	2.48
7.4	22	0.02	0.00	2.59
7.4	54	0.05	0.01	1.35
7.4	64	0.04	0.00	1.75
7.5	0	1.39	0.01	1.61
7.5	22	0.05	0.00	3.43
7.5	54	0.06	0.00	3.54
7.5	64	0.03	0.00	4.37
7.6	0	0.67	0.01	3.56
7.6	22	0.06	0.00	4.09
7.6	54	0.05	0.00	3.22
7.6	64	0.05	0.01	2.60
7.7	0	0.69	0.00	4.19
7.7	22	0.10	0.00	3.74
7.7	54	0.06	0.00	2.25
7.7	64	0.06	0.00	4.08
7.8	0	0.33	0.01	3.03
7.8	22	0.06	0.00	2.12
7.8	54	0.02	0.00	2.59
7.8	64	0.06	0.00	2.31
7.9	0	0.66	0.00	1.89
7.9	22	0.04	0.00	3.96
7.9	54	0.07	0.01	1.54
7.9	64	0.05	0.00	4.10
8.0	0	0.39	0.02	2.79
8.0	22	0.05	0.00	3.06
8.0	54	0.07	0.01	3.01
8.0	64	0.05	0.00	2.03
8.1	0	3.41	0.01	5.02

8.1	22	0.06	0.01	2.04
8.1	54	0.05	0.00	2.69
8.1	64	0.04	0.00	4.38
8.2	0	0.47	0.01	1.69
8.2	22	0.12	0.02	2.39
8.2	54	0.04	0.00	2.73
8.2	64	0.10	0.01	2.11
8.3	0	0.50	0.00	3.58
8.3	22	0.03	0.00	5.25
8.3	54	0.05	0.00	2.86
8.3	64	0.05	0.01	1.73
8.4	0	0.53	0.01	2.27
8.4	22	0.06	0.00	1.57
8.4	54	0.11	0.02	3.25
8.4	64	0.03	0.00	2.37
8.5	0	0.73	0.01	1.54
8.5	22	0.07	0.01	2.72
8.5	54	0.08	0.01	1.85
8.5	64	0.58	0.00	5.20
8.6	0	0.14	0.01	3.31
8.6	22	0.15	0.01	1.97
8.6	54	0.05	0.00	3.04
8.6	64	0.05	0.00	0.48
8.7	0	0.36	0.00	2.61
8.7	22	0.08	0.01	4.42
8.7	54	0.07	0.01	3.42
8.7	64	0.10	0.01	2.02

Table S2 3 Results of the solution samples taken through the course of the homogeneous nucleation experiments following digestion and analysis by ICP-AES to determine changes in Mg, Ca and P concentration.

ICP-AES matrix-matched standard results				
Sample	**MgO m*M*/L**	**CaO m*M*/L**	**PO_4 m*M*/L**	**P_2O_5 µ*M*/L**
STD1_SW1	0.0012	0.0003	0.0004	0.3544
STD1_SW1	0.0050	0.0009	0.0014	1.4149
STD1_SW1	0.0065	0.0008	0.0018	1.8341
STD1_SW1	0.0079	0.0011	0.0023	2.2521
STD1_SW2	0.0010	0.0002	0.0003	0.2884
STD1_SW2	0.0004	0.0002	0.0001	0.1132
STD1_SW2	0.0016	0.0001	0.0005	0.4512
STD1_SW2	0.0032	0.0001	0.0009	0.8986
STD1_SW3	0.0034	0.0001	0.0010	0.9610
STD1_SW3	0.0017	0.0004	0.0005	0.4707
STD1_SW3	0.0029	0.0003	0.0008	0.8336
STD1_SW4	0.0015	0.0003	0.0004	0.4346
STD1_SW4	0.0014	0.0003	0.0004	0.3953
STD1_SW4	0.0008	0.0003	0.0002	0.2410
STD1_SW4	0.0011	0.0002	0.0003	0.3016
STD1_SW5	0.0018	0.0001	0.0005	0.5019
STD1_SW5	0.0027	0.0002	0.0008	0.7628
STD1_SW5	0.0004	0.0001	0.0001	0.1219
STD1_SW5	0.0009	0.0003	0.0003	0.2620
STD1_SW3	0.0077	0.0053	0.0022	2.1974
STD6_SW1	0.0097	0.0075	0.0027	2.7445
STD6_SW1	0.0035	0.0026	0.0010	0.9837
STD6_SW1	0.0088	0.0068	0.0025	2.4995
STD6_SW1	0.0135	0.0090	0.0038	3.8431
STD6_SW2	0.0088	0.0065	0.0025	2.5025
STD6_SW2	0.0080	0.0056	0.0023	2.2639
STD6_SW2	0.0031	0.0024	0.0009	0.8872
STD6_SW2	0.0038	0.0022	0.0011	1.0686
STD6_SW3	0.0044	0.0033	0.0013	1.2536
STD6_SW3	0.0126	0.0095	0.0036	3.5831
STD6_SW3	0.0060	0.0040	0.0017	1.7135
STD6_SW3	0.0069	0.0050	0.0020	1.9652
STD6_SW4	0.0096	0.0070	0.0027	2.7362
STD6_SW4	0.0070	0.0055	0.0020	1.9975
STD6_SW4	0.0053	0.0038	0.0015	1.4929
STD6_SW4	0.0064	0.0043	0.0018	1.8110
STD6_SW5	0.0048	0.0036	0.0014	1.3507
STD6_SW5	0.0041	0.0030	0.0012	1.1655
STD6_SW5	0.0062	0.0047	0.0017	1.7469
STD6_SW5	0.0052	0.0041	0.0015	1.4756
U.S. Geological Survey (U.S.G.S.) W-2 standard material was also used for geochemical reference				

Table S2 4 Results of the ICP-AES matrix-matched solution standards following digestion and analysis by ICP-AES. These results were used to determine precision and error.

S2 3 Geochemical calculations

S2 3.1 Carbonate speciation

The sum of inorganic carbon species dissolved in solution; carbon dioxide $CO_{2(aq)}$ (including H_2CO_3), bicarbonate HCO_3, and carbonate CO_3^{2-}, is referred to as total dissolved inorganic carbon (DIC). DIC can be determined from $CO_{2(g)}$ partial pressure (pCO_2) using Henry's law (Eq. 2.1). Henry's law is expressed by:

$$p = k_H\, C \qquad \text{(Eq. 2.1)}$$

The $CO_{2(g)}$ dissolution and dissociation, assuming water activity to be unity can be expressed by:

$$CO_{2(g)} \overset{K'_0}{\longleftrightarrow} \left[CO_{2(aq)} + H_2O \leftrightarrow H_2CO_3 \overset{K_1}{\longleftrightarrow} HCO_3^- + H^+ \overset{K_2}{\longleftrightarrow} CO_3^{2-} + 2H^+\right] \qquad \text{(Eq. 2.2)}$$

where p, represents the partial pressure of the solute above the solution, k_H is Henry's law constant, and C is the concentration of the solute in the solution. There are five equilibrium constants in seawater expressed by:

$$K'^{*}_0 = \frac{[CO_{2(aq)}]}{pCO_2} \qquad \text{(Eq. 2.3)}$$

$$K^*_1 = \frac{[HCO_3^-] \times [H^+]}{[CO_{2(aq)}]} \qquad \text{(Eq. 2.4)}$$

$$K^*_2 = \frac{[CO_3^{2-}] \times [H^+]}{[HCO_3^-]} \qquad \text{(Eq. 2.5)}$$

$$K^*_3 = \frac{[OH^-] \times [H^+]}{H_2O} \qquad \text{(Eq. 2.6)}$$

$$K^*_B = \frac{[(OH)_4^-] \times [H^+]}{[B(OH)_3]} \qquad \text{(Eq. 2.7)}$$

To account for salinity dependence in seawater, 'apparent' dissociation constants are used (Mehrbach et al., 1973), these stoichiometric constants expressed in terms of concentration denoted by (*) rather than ion activity. K'^{*}_0 represents the Henry's law constant for $CO_{2(g)}$ in equilibrium with the $CO_{2(aq)}$ (0.034 $molkg^{-1}bar^{-1}$ at 298 k; Henry, 1803; Zeebe and Wolf-Gladrow,

2007), (Eq. 2.1). K_1^* and K_2^* represent the apparent dissociation constants of carbonic acid, K_w^* of water, and K_B^* of boric acid.

S2 3.2 Carbonate reaction system

The reaction between CO_2 and H_2O, results in 6 species that are strongly pH dependant; together these make up the carbonate system: $CO_{2(g)}$; H_2CO_3 (carbonic acid); HCO_3^- (bicarbonate); CO_3^{2-} (carbonate); H^+ (proton); and OH^- (hydroxyl) ions. The reaction of a carbonate system is expressed by:

$$CO_{2(aq)} + H_2O_{(aq)} \longleftrightarrow H_2CO_{3(aq)} \rightleftharpoons H^+_{(aq)} + HCO^-_{3(aq)} \longleftrightarrow 2H^+_{(aq)} + CO_3^{2-}{}_{(aq)} \qquad \text{(Eq. 2.8)}$$

S2 3.3 Total alkalinity

An excess of proton acceptors over donors with respect to the zero level of protons is defined as the total alkalinity (TA) (Dickson, 1981). The simplified total alkalinity (based on carbonate alkalinity) (Wolf-Gladrow et al., 2007) is expressed by:

$$\text{Total alkalinity} = HCO_3^-{}_{(aq)} + 2CO_3^{2-}{}_{(aq)} + OH^-_{(aq)} - H^+_{(aq)} \qquad \text{(Eq. 2.9)}$$

The total alkalinity of a sample is dominated by the contributions of HCO_3^- (which is the dominant species of carbonic acid at *p*H = 8.2) and CO_3^{2-}. The OH^- contributes less than 1% to total alkalinity and H^+ even less. Present day seawater has a pH value ~8.2 and a total alkalinity dominated by HCO_3^- and CO_3^{2-} and total alkalinity>DIC (Wolf-Gladrow et al., 2007). However alkaline lakes and Neoproterozoic seawater may have had an increased DIC pool, as supersaturation states appear high.

When CO_2 dissolves in water, it is buffered by *p*H, therefore, the species concentration changes. Therefore, TA is expressed by:

$$TA = CO_2\left(\frac{K_1^*}{H^+} + 2\frac{K_1^* K_2^*}{H^+}\right) + \frac{B_T K_B^*}{K_B^* + H^+} + \frac{K_w^*}{H^+} - H^+ \qquad \text{(Eq. 2.10)}$$

Where K_1^*, K_2^*, K_w^*, and K_B^*, represent equilibrium constants expressed in terms of concentration rather than ion activities (see Eq. 2.3–6), H^+ represents a proton, and B_T represents total dissolved boron. Stoichiometric constants are not 'true thermodynamic constants' and therefore are salinity dependent. We know the starting TA concentration of our experiments because we know the composition of the solution including the amount of salt added and the pH. TA was also calculated based on calculations from Geochemists Workbench (Bethke and Yeakel, 2015) and known amount solution composition.

$$\mathrm{DIC} = \mathrm{CO_2}\left(1 + \frac{K_1^*}{H^+} + \frac{K_1^* K_2^*}{(H^+)^2}\right) \quad \text{(Eq. 2.11)}$$

The effect of ionic strength of the solution on the dissociation constants can be simplified to K_1'* and K_2'*, however K_0* does not vary with ionic strength as the activity coefficient for uncharged $CO_{2(aq)}$ is assumed to be unity. K_1'* and K_2'* are expressed by:

$$K_1'^* = K_1^*\left(\frac{\gamma_{H^+}\gamma_{HCO_3^-}}{\gamma_{CO_2}}\right) \quad \text{(Eq. 2.12)}$$

$$K_2'^* = K_2^*\left(\frac{\gamma_{H^+}\gamma_{CO_3^{2-}}}{\gamma_{HCO_3^-}}\right) \quad \text{(Eq. 2.13)}$$

where γ represents the activity coefficient in seawater with ionic strength of 0.714.

Obtaining K_1'* and K_2'* values allows CO_3^{2-} concentrations to be determined at a specific *p*H and DIC concentration (summarized from Zeebe and Wolf-Gladrow, 2001). The calculation of CO_2 from *p*H and DIC can be expressed by:

$$\mathrm{CO_2} = \mathrm{DIC} \Big/ \left(1 + \frac{K_1'^*}{H^+} + \frac{K_1'^* K_2'^*}{(H^+)^2}\right) \quad \text{(Eq. 2.14)}$$

this equation can be used to calculate pCO^2 (ppm), where K_H represents Henry's gas constant ($10^{-1.5468}$ M/atm) and increases with increasing ionic strength at constant temperature (Henry, 1803). pCO^2 is expressed by:

$$pCO_2 = \left(\frac{CO_2}{K_H}\right) \times 1000000 \quad \text{(Eq. 2.15)}$$

Because we have known DIC concentrations and pH of the initial solution, we can calculate $[CO_3^{2-}]$ which is expressed by:

$$[CO_3^{2-}] = DIC \times \left(\frac{K_1'^* K_2'^*}{[H^+]^2 + K_1'^*[H^+] + K_1'^* K_2'^*} \right) \quad \text{(Eq. 2.16)}$$

The change in Mg^{2+} and Ca^{2+} concentration during nucleation can be calculated from ICP-AES or ICP-MS elemental measurements of solution samples. By combining the Mg^{2+} and Ca^{2+} concentrations, the stoichiometric equivalent of $[CO_3^{2-}]$ is subtracted from the total DIC, before the remaining $[CO_3^{2-}]$ is calculated using Eq. 2.16 (assuming spontaneous carbonate speciation and no degassing). This allows saturation state estimations of the solution with respect to a mineral phases.

S2 3.4 ACMC mineral pathway

Although more common for ACC (Brecevic and Nielsen, 1989), thermodynamic datasets for ACMC are not widely available. However, constraints on solubility data of ACMC (Purgstaller et al., 2016, 2019, 2021) and AMC (Chang et al., 2021) have recently been published. The formation reaction for Mg-calcite and ACMC can be used according to Purgstaller et al., (2016), which is expressed by:

$$_{(1-x)}Ca^{2+} + {}_{(x)}Mg^{2+} + CO_3^{2-} \longleftrightarrow Ca_{(1-x)}Mg_{(x)}CO_3 \quad \text{(Eq. 2.17)}$$

In order to yield thermodynamic data from our experiments and assess the effect of changes to the chemical conditions of the solutions on the solubility (K) of ACMC, we calculated the activities of Ca^{2+}, Mg^{2+} and CO_3^{2-} ions in the initial solution. We also calculated the bulk ACMC stoichiometry from the resultant solid (Mg and Ca $Mol\%_{ACMC}$), which were used to calculate K_{ACMC} values (described below).

S2 3.5 Ion activity

Firstly, to calculate the activity (a) of ions in experimental solutions, ion activity coefficient values (γ) for the solute species can be calculated using the Extended Debye-Huckel equation expressed by:

$$log_{\gamma i}\frac{-0.509z_i^2\sqrt{I_c}}{1+(3.28d_i\sqrt{I_c}} \quad \text{(Eq. 2.18)}$$

where γi is the activity coefficient, z_i is the charge number of ion species, I is the ionic strength of the solution (expressed by Eq. 2.23 below) and d_i is the ion size parameter. Ionic strength of 0.65673 was used at 25 °C. d_i values are from (Kielland, 1937). Ion activity values (a) can be determined from the concentration of the solute species in the synthetic solutions which are measured by ICP or calculated, multiplied by the activity coefficient values (γ) and expressed by:

$$a\mathrm{H} = 10^{(-1\times pH)} \quad \text{(Eq. 2.19)}$$

$$a\mathrm{Ca} = \gamma\,\mathrm{Ca} \times \mathrm{Ca} \quad \text{(Eq. 2.20)}$$

$$a\mathrm{Mg} = \gamma\,\mathrm{Mg} \times \mathrm{Mg} \quad \text{(Eq. 2.21)}$$

$$a\mathrm{CO_3} = \gamma\,\mathrm{CO_3} \times \mathrm{CO_3} \quad \text{(Eq. 2.22)}$$

where a represents the ion activity from the calculated initial composition or the ion activity using measured values from ICP. Where (γ) represents activity coefficients of γ Ca = 0.297, γ CO_3 = 0.195, γ Mg = 0.401, and γ H = 0.756, (alternative values of γ Ca = 0.256, γ CO_3 = 0.205, γ Mg = 0.285, and γ H = 0.709 at 35 permil salinity for modern seawater (Millero and Schrieber 1982; Pilson, 2013) were also used but gave a difference of <0.68 %). The $a$$H_2O$ values of the experimental solutions remained constant, therefore, $a$$H_2O$ of water activity was assumed to be unity in accordance with (Purgstaller et al., 2016; 2019; 2021). However, as the calculations are based on ions in seawater/ saline solutions, stoichiometric constant values are dependent on ionic strength, which is expressed by:

$$\mathrm{I} = {}^1/_2 \sum_i \mathrm{m}_i \mathrm{z}_i^2 \quad \text{(Eq. 2.23)}$$

where m*i* is the molality of the *i*th ion, *Z*i is the integer number of charges on the *i*th ion, and the summation is over all ions. Ionic strength in our experimental solutions ranges from = 0.415 to 1.21 M/kg.

S2 3.6 Solubility product

Mineral nucleation is predicted when the ionic activity product (IAP) (Eq. 2.28 below) of the dissolved ions in solution exceeds the mineral solubility product K (or K_{sp}) (Eq. 2.24). The estimation of the apparent mineral solubility product (K) with respect to ACMC was calculated and is expressed by:

$$K = (a\mathrm{Ca}^{2+})^{1-x}(a\mathrm{Mg}^{2+})^{x}(a\mathrm{CO}_3^{2-})(\mathrm{H_2O})^{n} \qquad (\mathrm{Eq.}\ 2.24)$$

Although the term K is widely accepted for crystalline phases, it is not necessarily valid for amorphous phases (Brečević and Nielsen, 1989), particularly as amorphous phases are more sensitive to thermal variability, instability and structural disorder. However, it provides a useful constraint.

The Mg content ($[\mathrm{Mg}]_{\mathrm{ACMC}}$) was calculated according to the equation where $[\mathrm{Mg}]_{\mathrm{solid}}$ and $[\mathrm{Ca}]_{\mathrm{solid}}$ are the measured concentrations of Ca and Mg of the solids from the ICP-AES results with units *M*l/kg:

$$[\mathrm{Mg}]_{\mathrm{solid}} = \frac{[\mathrm{Mg}]_{\mathrm{s}}}{[\mathrm{Mg}]_{\mathrm{solid}} + [\mathrm{Ca}]_{\mathrm{solid}}}\ \mathrm{X}\ 100 \qquad (\mathrm{Eq.}\ 2.25)$$

The results for the bulk solid sample characterization are presented in Table. S2.2 and the results for the aqueous solution concentrations are presented in Table S3.3. The [Mg mol%] of the resultant bulk solid ranged from 54.2 – 95.0% (however, this resultant phase is a mixture of phases including crystalline hydromagnesite).

At a given temperature, the linear increase of the solubility (K) of ACMC as a function of the Mg content [Mg]solid (in mol%) is expressed according to Purgstaller et al., (2021) by:

$$K_{ACMC} = m\,[Mg]solid + y0 \quad \text{(Eq. 2.26)}$$

where *m* = slope and y0 = intercept. Based on our experimental conditions of ~50 °C, we used K values published by Purgstaller et al., (2021) for ACMC nucleation at 60 °C where *m* = 0.01632 and y0 = -6.910. This yielded the equation:

$$K = 10^{(0.01632[Mg\ mol\%])+ -6.91} \quad \text{(Eq. 2.27)}$$

K is often expressed as Log(K). The results from this study yielded $Log(K)_{ACMC}$ = -5.36 to -6.05 with less negative values corresponding to higher Mg content. These values are in accordance with values of ACMC at 60 °C of $Log(K)_{ACMC}$ = -6.13 (Purgstaller et al., 2021); however, these values are closer to Mg-rich ACMC where Mg-rich solubility product $Log(K_{ACMC})$ = -4.54 and -Ca-rich solubility product $Log(K_{CMC})$ = -6.28 (Purgstaller et al., (2019). These values also correspond more closely with AMC values published by Chang et al., (2021) of Log(K) = -5.201 than values of ACC at 60 °C of $Log(K)_{ACC}$ = -6.91 Brečević and Nielsen, (1989); values of ACC at 60 °C of $Log(K)_{ACC}$ = -7.510 (Gebauer et al., 2008). For reference, the solubility product for calcite in seawater at 25°C is $Log(K)_{calcite}$ = -6.3693 (based on concentration not activity (Mucci, 1983).

S2 3.7 Ion activity product

The estimation of the apparent ion activity product (IAP) with respect to ACMC is based on activities (*a)* and is expressed by:

$$IAP_{ACMC} = (aCa^{2+})^{x}(aMg^{2+})^{1-x}(aCO_3^{2-})^{n} \quad \text{(Eq. 2.28)}$$

where activities were calculated from the aqueous solution concentrations and where $(1-x) = [Mg]_{ACMC}/100$) determined by the ICP measurements of Mg and Ca mol% and *n* indicates the number of H_2O in the ACMC (assumed to be unity). This research obtained a range of ion activity product values from $Log(IAP_{ACMC})$ = -3.41 to -2.88 in homogeneous nucleation experiments and

$Log(IAP_{ACMC})$ = -2.62 to -4.13 in ACMC precursor experiments. IAP_{ACMC} increased as a function of Mg content ($[Mg]_{ACMC} = (1-x) \times 100$ in mol %, which can be explained by the increasing water content and changes in short-range order, as Ca is substituted by Mg in the ACMC structure as observed by (Purgstaller et al., 2019). IAP_{ACMC} values also decrease as a function of increasing temperature according to Purgstaller et al., (2021). In a similar manor, values obtained for $Log(IAP_{AMC})$ = -2.72 to -3.39 in homogeneous nucleation experiments and $Log(IAP_{AMC})$ = -2.63 to -4.15 in ACMC precursor experiment solutions.

S2 3.8 Saturation State

Using the calculated ion activity product (IAP_{ACMC}: Eq. 2.28) and the apparent mineral solubility product (K_{ACMC}: Eq. 2.26) of the experimental solution we estimated the apparent saturation state (Ω) with respect to ACMC (Ω_{ACMC}), which is expressed by:

$$\Omega_{ACMC} = \frac{IAP_{ACMC}}{K} \qquad \text{(Eq. 2.29)}$$

which yielded Ω_{ACMC} = 176 to 1512 (see Table S2.5). The logarithm of the Ω_{ACMC} values provides the Saturation Index (SI) which produced values of 2.0 to 3.18 in homogeneous nucleation experiments and 1.9 to 3.5 in ACMC precursor experiment solutions. In a similar manor, values obtained for Ω_{AMC} = 305 to 65 in homogeneous nucleation experiments and Ω_{AMC} = 379 to 6 in ACMC precursor experiment solutions based on K values obtained from Chang et al., (2021).

ACMC Precursor Experiments															
Aqueous conc. initial				Measured		Calculated									
EXP 2 No.	[Mg] m*M*	[Ca] m*M*	[CO_3] m*M*	Mg_{solid} mol%	Ca_{solid} mol%	*a* (Mg^{2+})	*a* (Ca^{2+})	*a* (CO_3^{2-})	[Mg] $_{ACMC}$	[Ca] $_{ACMC}$	IAP $_{ACMC}$	K	Log(K)	Ω_{ACMC}	SI
7	47.6	11.1	103.1	50	50	0.297	0.401	0.195	0.119	0.973	0.0023	8.1E-07	**-6.09**	**2888**	3.5
9	47.6	11.1	103.1	50	50	0.297	0.401	0.195	0.119	0.973	0.0023	8.1E-07	**-6.09**	**2888**	3.5
11	47.6	11.1	103.1	50	50	0.297	0.401	0.195	0.119	0.973	0.0023	8.1E-07	**-6.09**	**2888**	3.5
13	47.6	11.1	10.6	50	50	0.297	0.401	0.195	0.119	0.973	0.0002	8.1E-07	**-6.09**	**298**	2.5
15	47.6	11.1	10.6	50	50	0.297	0.401	0.195	0.119	0.973	0.0002	8.1E-07	**-6.09**	**298**	2.5
17	47.6	11.1	10.6	50	50	0.297	0.401	0.195	0.119	0.973	0.0002	8.1E-07	**-6.09**	**298**	2.5
19	47.6	11.1	3.2	50	50	0.297	0.401	0.195	0.119	0.973	0.0001	8.1E-07	**-6.09**	**89**	1.9
21	47.6	11.1	3.2	50	50	0.297	0.401	0.195	0.119	0.973	0.0001	8.1E-07	**-6.09**	**89**	1.9
23	47.6	11.1	3.2	50	50	0.297	0.401	0.195	0.119	0.973	0.0001	8.1E-07	**-6.09**	**89**	1.9

Table S2 5 Table presents [Mg], [Ca] and [CO_3] initial concentrations along with Mg and Ca mol% that. For the ACMC nucleation experiments, the ACMC precursor was ~50 mol% Mg and this was the value used for these calculations. K_{ACMC} is determined by Eq. 2.27, IAP_{ACMC} is determined by Eq. 2.28, Ω_{ACMC} is determined by Eq. 2.29. Changes in salinity had a negligible effect on K values with ~1.27% change.

Homogenous Nucleation Experiments														
Aqueous conc. initial				Measured		Calculated								
EXP 7 No.	[Mg] m*M*	[Ca] m*M*	[CO_3] m*M*	Mg_{solid} mol%	Ca_{solid} mol%	*a* (Mg^{2+})	*a* (Ca^{2+})	*a* (CO_3^{2-})	$[Mg]_{ACMC}$	$[Ca]_{ACMC}$	IAP_{ACMC}	K	Log(K)	Ω_{ACMC}	SI
6.6	40.1	8.25	132	63.9	4.5	0.012	0.003	0.026	63.9	4.5	0.0012	1.4E-06	-5.87	864	2.9
7.0	23.80	27.75	132	52.4	8.1	0.007	0.011	0.026	0.075	0.693	0.0013	8.8E-07	**-6.05**	**1512**	3.2
7.1	42.84	16.65	132	64.2	5.5	0.013	0.007	0.026	0.061	0.761	0.0012	1.4E-06	**-5.86**	**866**	2.9
7.2	38.08	8.88	132	82.3	2.2	0.011	0.004	0.026	0.025	0.885	0.0006	2.7E-06	**-5.57**	**210**	2.3
7.3	38.08	5.55	132	88.7	1.4	0.011	0.002	0.026	0.019	0.918	0.0004	3.5E-06	**-5.46**	**129**	2.1
7.4	42.84	4.99	132	91.3	1.1	0.013	0.002	0.026	0.019	0.937	0.0004	3.8E-06	**-5.42**	**118**	2.1
7.5	43.32	3.88	132	91.1	1.1	0.013	0.002	0.026	0.019	0.934	0.0005	3.8E-06	**-5.42**	**121**	2.1
7.6	42.84	3.33	132	92.9	0.8	0.013	0.001	0.026	0.017	0.948	0.0004	4.0E-06	**-5.39**	**105**	2.0
7.7	42.84	2.77	132	95.0	0.6	0.013	0.001	0.026	0.016	0.962	0.0004	4.4E-06	**-5.36**	**90**	2.0
7.8	47.61	2.77	132	94.8	0.6	0.014	0.001	0.026	0.018	0.962	0.0004	4.3E-06	**-5.36**	**101**	2.0
7.9	42.84	8.88	132	80.9	2.4	0.013	0.004	0.026	0.029	0.874	0.0007	2.6E-06	**-5.59**	**257**	2.4
8.0	42.84	8.88	132	82.0	2.4	0.013	0.004	0.026	0.028	0.873	0.0006	2.7E-06	**-5.57**	**235**	2.4
8.1	42.84	8.88	132	79.1	2.6	0.013	0.004	0.026	0.032	0.864	0.0007	2.4E-06	**-5.62**	**293**	2.5
8.2	42.84	8.88	132	82.1	2.4	0.013	0.004	0.026	0.028	0.874	0.0006	2.7E-06	**-5.57**	**232**	2.4
8.3	42.84	8.88	132	82.1	2.4	0.013	0.004	0.026	0.029	0.874	0.0006	2.6E-06	**-5.58**	**246**	2.4
8.4	42.84	8.88	132	81.4	2.4	0.013	0.004	0.026	0.029	0.874	0.0006	2.6E-06	**-5.58**	**246**	2.4
8.5	42.84	8.88	132	83.3	2.2	0.013	0.004	0.026	0.026	0.884	0.0006	2.8E-06	**-5.55**	**214**	2.3
8.6	42.84	8.88	132	82.8	1.8	0.013	0.004	0.026	0.027	0.905	0.0006	2.8E-06	**-5.56**	**228**	2.4
8.7	42.84	8.88	132	86.0	1.7	0.013	0.004	0.026	0.023	0.910	0.0005	3.1E-06	**-5.51**	**176**	2.2

Table S2 6 Table presents [Mg], [Ca] and [CO_3] initial concentrations along with Mg and Ca mol % of the resultant bulk solid samples, which were estimated from the calculation shown in Eq. 2.17 for homogenous nucleation experiments following digestion and analysis by ICP-AES to determine Mg and Ca within the solid phase. K_{ACMC} is determined by Eq. 2.27, IAP_{ACMC} is determined by Eq. 2.28 and Ω_{ACMC} is determined by Eq. 2.29. Changes in salinity had a negligible effect on K values with ~1.27% change.

Homogenous Nucleation Experiment			
Exp. 7 No.	**d_{104} (Å)**	**[Mg] $\%_{XRD}$**	**$[Mg]_{solid}$ mol% (bulk -ICP)**
7.0	2.933	**36.1**	52.4
7.0	2.908	**44.9**	52.4
7.1	2.908	**45.0**	64.2
7.2	2.899	**48.3**	82.3
7.3	2.885	**53.2**	88.7
7.4	2.882	**54.3**	91.3
7.5	2.888	**52.2**	91.1
7.6	2.898	**48.6**	92.9
7.7	2.900	**47.9**	95.0
7.8	2.888	**52.2**	94.8
7.9	2.906	**45.8**	82.0
7.9	2.899	**48.3**	82.0
8.0	2.908	**45.1**	79.1
8.1	2.903	**46.9**	82.1
8.2	2.901	**47.6**	81.4
8.3	2.902	**47.2**	-
8.4	2.898	**48.6**	83.3
8.5	2.902	**47.2**	82.8
8.6	2.901	**47.6**	86.0
8.7	2.914	**42.8**	63.9
8.7	2.901	**47.6**	63.9

ACMC Precursor Experiment		
Exp. 2 No.	**d_{104} (Å)**	**[Mg] $\%_{XRD}$**
7	3.0200	0.0
7	3.0060	10.1
7	2.9000	**47.9**
9	3.0410	0.0
9	3.0150	6.9
9	2.9080	**45.1**
11	2.9050	**46.1**
11	3.0140	**7.2**
13	2.9000	**47.9**
13	2.9107	44.1
15	3.0349	0.0
15	2.9963	13.5
15	2.9692	23.2
15	2.9081	**45.1**
17	3.0363	0.0
17	2.9924	14.9
19	3.0780	0.0
19	3.0150	6.9
21	3.0181	5.7
21	2.9962	13.6
23	3.0192	5.3

Table S2 7 Table of estimated [Mg] $\%_{XRD}$ based on d_{104} spacing (Å) values from XRD results. Estimates of the Mg content of the dominant Mg-Ca-CO_3 phase were calculated according to the calculations from Goldsmith et al., (1961) and updated with Mg results from (Zhang and Dave, 2000; dos Santos et al., 2017). In the homogenous nucleation experiments the mean content of Mg is 47 % and reaches 54 % in the high Mg/Ca experiments. In the ACMC precursor experiments the average content was calculated for the highest d_{104} values, where the mean content of Mg is 42 % and reaches 48 % in experiments $\Omega_{ACMC} \geq 298$. However, it is important to note that the validity of this calculation is somewhat unreliable especially for high-Mg content due to variations in Mg-calcite, disordered dolomite and amorphous phases. The data would benefit from Rietveld refinement using lattice parameters and cell volumes of disordered and ordered dolomite (i.e., Zhang et al., 2010).

Supplement 3

S3 1 Supplementary methods – published

CITATION: Roest-Ellis, S., Strauss, J.V., and Tosca, N.J., 2021, Experimental constraints on non-skeletal $CaCO_3$ precipitation from Proterozoic seawater: Geology, Geological Society of America, v. 49, p. XX, https://doi.org/10.1130/G48044.1.

Please visit https://doi.org/10.1130/GEOL.S.13377239 to access the supplemental material

S3 1.1 Experimental design

$CaCO_3$ nucleation in the presence of PO_4 was examined with two types of experiments (Figure S3. 1) conducted in synthetic Tonian composition seawater (Table S3. 1) that was based on fluid inclusion constraints; Spear et al., (2014) as described in the main text). $CaCO_3$ nucleation was first examined with *degassing* experiments (Figure S3. 1) where CO_2 was degassed to increase the $CaCO_3$ supersaturation (Ω_{Cal}) until nucleation occurs based on He and Morse, (1993) and Lee and Morse, (2010) as described in the main text. Continuous monitoring of pH, in combination with known [Ca^{2+}] and total alkalinity (TA), constrained the carbonate chemistry at the point of nucleation (Table S3. 1). $CaCO_3$ nucleation was also examined with *constant composition* experiments (Figure S3. 1) based on Beck et al., (2013), where the desired $\Omega_{calcite}$, dissolved inorganic carbon (DIC), ionic strength, and TA were maintained via autotitration as described the main text. Continuous monitoring of pH and [Ca^{2+}], with ion selective and AgCl reference electrodes, constrained carbonate chemistry at the point of nucleation as described the main text.

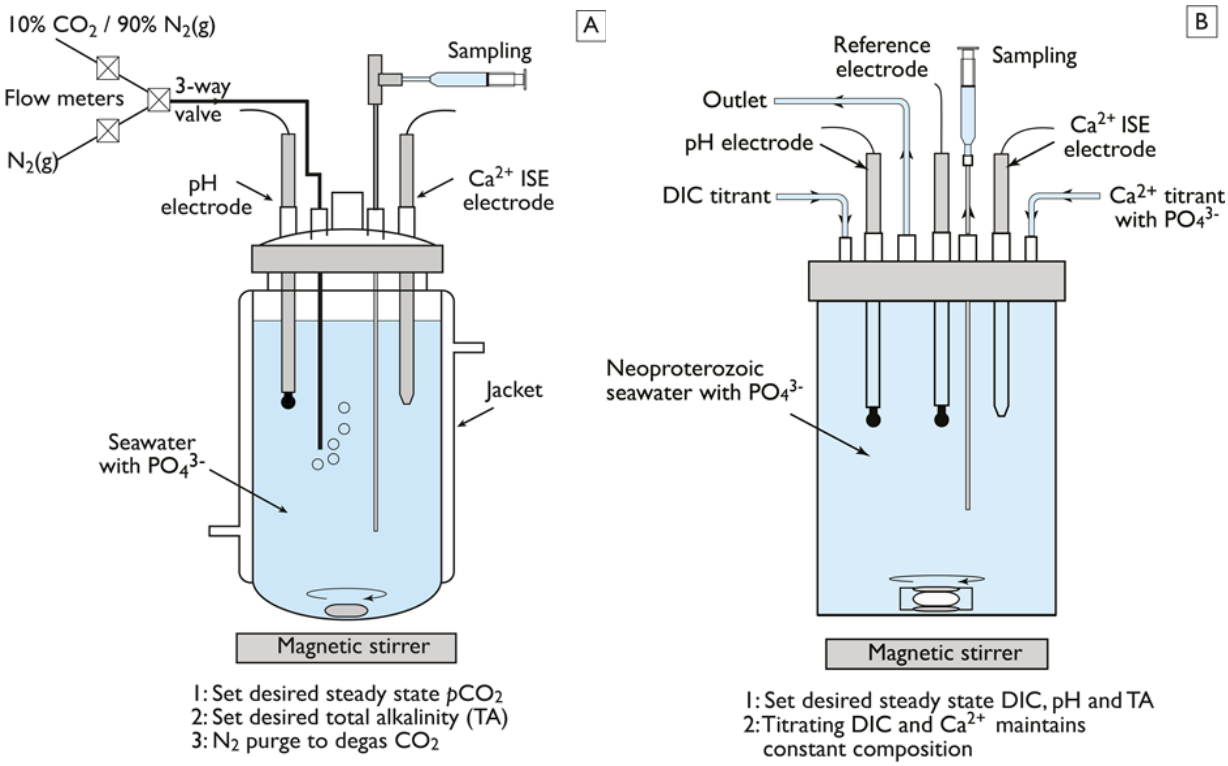

Figure S3. 1 Schematic diagram of A: *degassing experiment* set up indicating the CO_2 and N_2 gas inlet and measurement electrodes and B: *constant composition experiment* set up indicating the DIC and Ca^{2+} titrant inlets and measurement electrodes as described in the main text. Arrows indicate direction of flow.

S3 1.2 Bulk PO_4 method

During constant composition experiments, solution samples (1.5 ml) were syringe-filtered (0.22 μm) and acidified (6 ml HNO_3, 4 %) for solution sample total PO_4 concentration ($[PO_{4tot}]$), determined by spectrophotometry using the ascorbic acid method (phosver3 Ascorbic Acid Method 8048, Hach Lange) that determines the PO_4 concentration by detecting the absorbance at a wavelength of 680nm of the reduced phosphate-molybdate complex in solution (Baird et al., 2017).

S3 3.1 Experiment solution chemistry

Neoproterozoic Seawater Experiments - Table A							
EXP ID	pH	DIC molal	Ω_{cal}	Mg^{2+}/Ca^{2+}	CO_3^{2-}/Ca^{2+}	TA molal	Ionic strength molal
1-A 310718	9.2	0.025	301	5.56	1.59	0.039	0.67
1-B 101018R	8.8	0.025	183	5.56	0.96	0.034	0.65
1-C 210818	8.3	0.025	75	5.56	0.40	0.028	0.66
1-D 170918	7.7	0.025	21	5.56	0.11	0.026	0.65
1-E 241018R	9.2	0.015	181	5.56	0.95	0.024	0.66
1-F 301018	8.8	0.015	110	5.56	0.58	0.020	0.65
1-G 061110	8.3	0.015	45	5.56	0.24	0.017	0.65
2-MB 300419	8.7	0.010	83	3.33	0.25	0.013	0.63
2-MBR 040619	8.7	0.010	83	3.33	0.25	0.013	0.63
2-MCR 170619	8.7	0.010	83	3.33	0.25	0.013	0.63
2-SI 290719	8.5	0.014	83	3.33	0.25	0.013	0.63
2-EB 100419	8.1	0.024	60	3.33	0.18	0.026	0.64
2-F 211118	9.2	0.014	169	5.56	0.89	0.022	0.66
2-H 240119	8.7	0.014	117	3.33	0.35	0.018	0.64
2-I 140119	8.5	0.014	83	3.33	0.25	0.013	0.63
2-I-R 170118	8.5	0.014	83	3.33	0.25	0.013	0.63
2-J 280119	8.3	0.014	56	3.33	0.17	0.016	0.63
2-MR 190219	8.7	0.010	83	3.33	0.25	0.013	0.63
2-N 270219	8.5	0.010	59	3.33	0.17	0.012	0.63
2-Q 050319	8.9	0.025	113	3.33	0.33	0.014	0.63
2-X 270220	8.7	0.014	117	2.86	0.21	0.013	0.63

Neoproterozoic Seawater Experiments - **Table B**											
EXP ID	**[Na] molal**	**[K] molal**	**[Mg] molal**	**[Ca] molal**	**[Si] molal**	**[SO_4] molal**	**[Cl] molal**	**[PO_4] umolal**	**[HCO_3] molal**	**[CO_3] molal**	**[CO_2]**
1-A 310718	0.452	0.010	0.050	0.009	0.00	0.003	0.565	50	0.0107	0.0143	0.00001
1-B 101018R	0.452	0.010	0.050	0.009	0.00	0.003	0.565	50	0.0163	0.0087	0.00003
1-C 210818	0.452	0.010	0.050	0.009	0.00	0.003	0.565	50	0.0213	0.0036	0.00011
1-D 170918	0.452	0.010	0.050	0.009	0.00	0.003	0.565	50	0.0235	0.0010	0.00048
1-E 241018R	0.452	0.010	0.050	0.009	0.00	0.003	0.565	50	0.0064	0.0086	0.00000
1-F 301018	0.452	0.010	0.050	0.009	0.00	0.003	0.565	50	0.0098	0.0052	0.00002
1-G 061110	0.452	0.010	0.050	0.009	0.00	0.003	0.565	50	0.0128	0.0022	0.00006
2-MB 300419	0.452	0.010	0.040	0.012	0.00	0.003	0.565	100	0.0070	0.0030	0.00001
2-MBR 040619	0.452	0.010	0.040	0.012	0.00	0.003	0.565	100	0.0070	0.0030	0.00001
2-MCR 170619	0.452	0.010	0.040	0.012	0.00	0.003	0.565	25	0.0070	0.0030	0.00001
2-SI 290719	0.452	0.010	0.040	0.012	0.00	0.003	0.565	50	0.0070	0.0030	0.00001
2-EB 100419	0.452	0.010	0.040	0.012	0.00	0.003	0.565	50	0.0217	0.0021	0.0002
2-F 211118	0.452	0.010	0.050	0.009	0.00	0.003	0.565	50	0.0060	0.0080	0.0000
2-H 240119	0.452	0.010	0.040	0.012	0.00	0.003	0.565	50	0.0098	0.0042	0.0000
2-I 140119	0.452	0.010	0.040	0.012	0.00	0.003	0.565	50	0.0070	0.0030	0.00001
2-I-R 170118	0.452	0.010	0.040	0.012	0.00	0.003	0.565	50	0.0070	0.0030	0.00001
2-J 280119	0.452	0.010	0.040	0.012	0.00	0.003	0.565	50	0.0119	0.0020	0.0001
2-MR 190219	0.452	0.010	0.040	0.012	0.00	0.003	0.565	50	0.0070	0.0030	0.0000
2-N 270219	0.452	0.010	0.040	0.012	0.00	0.003	0.565	50	0.0079	0.0021	0.0000
2-Q 050319	0.452	0.010	0.040	0.012	0.00	0.003	0.565	50	0.0060	0.0040	0.0000
2-X 270420	0.452	0.010	0.040	0.014	0.00	0.003	0.565	50	0.0070	0.0030	0.0000

Note: HCO_3, CO_3 and CO_2 were computed using relationships and constants in Zeebe and Wolf-Gladrow (2001).

Neoproterozoic Seawater Experiments - Table C						
EXP ID	pH	DIC molal	Ω_{cal}	Mg^{2+}/Ca^{2+}	CO_3^{2-}/Ca^{2+}	TA molal
110716	8.56	0.0115	21.37	5.55	0.300	0.0142
130716	8.70	0.0039	25.83	5.55	0.165	0.0054
140716	8.86	0.0028	22.42	5.55	0.119	0.0039
190716	7.63	0.0229	17.65	5.55	0.228	0.0248
250716	9.21	0.0076	92.69	5.55	0.490	0.0120
260916	8.87	0.0145	117.33	5.55	0.620	0.0201
101016	8.51	0.0265	118.97	5.55	0.629	0.0320
311017	8.76	0.0215	147.62	5.55	0.780	0.0285
021117	8.60	0.0218	114.89	5.55	0.608	0.0272
061117	8.48	0.0232	98.79	5.55	0.522	0.0278
241016	8.87	0.0087	117.40	2.67	0.223	0.0120
191016	8.33	0.0156	83.10	2.67	0.158	0.0179
171016	8.42	0.0236	150.11	2.67	0.285	0.0278
131117	8.64	0.0196	184.29	2.67	0.350	0.0248
141117	8.64	0.0196	184.29	2.67	0.350	0.0248

Neoproterozoic Seawater Experiments - Table C						
EXP ID	[Ca] molal	[Mg] molal	KH_2PO_4 umolal	SiO_2 molal	pCO_2 uatm	$[CO_3^{2-}]$ molal
110716	0.0090	0.0499	0	0.0017	866	0.0027
130716	0.0090	0.0499	0	0.0017	120	0.0015
140716	0.0090	0.0499	0	0.0017	86	0.0011
190716	0.0090	0.0499	0	0.0017	6282	0.0020
250716	0.0090	0.0499	50	0.0017	71	0.0044
260916	0.0090	0.0499	50	0.0017	430	0.0056
101016	0.0090	0.0499	50	0.0017	2286	0.0057
311017	0.0090	0.0499	23	0.0017	897	0.0070
021117	0.0090	0.0499	12	0.0017	1459	0.0055
061117	0.0090	0.0499	6	0.0017	2180	0.0047
241016	0.0150	0.0400	50	0.0017	258	0.0033
191016	0.0150	0.0400	50	0.0017	2192	0.0024
171016	0.0150	0.0400	50	0.0017	2617	0.0043
131117	0.0150	0.0400	75	0.0017	1167	0.0053
141117	0.0150	0.0400	100	0.0017	1167	0.0053

Table S3. 1 Details of carbonate chemistry at the point of nucleation. A: constant composition experimental parameters. B: constant composition solution chemistry. C: degassing experimental parameters. D: degassing solution chemistry. HCO_3, CO_3 and CO_2 were computed using relationships and constants in Zeebe and Wolf-Gladrow, (2001). Mg/Ca and CO_3/Ca are molar ratios.

S3 1.3 Rietveld refinement

The Mg content of the solids was estimated by Rietveld refinement (Table S3. 2) using GSAS-II (Larson and Von Dreele, 2004) with structural models for Mg-calcite reported in Paquette and Reeder (1990) and calibrations determined by Titschack et al. (2011). X-ray diffraction patterns (XRD) (Figure S3. 2) represent amorphous calcium magnesium carbonate (ACMC) and resultant solids.

Rietveld refinement - Table A

			Calcite				
EXP ID	Phases	Residual wR	wt. %	a (Å)	c (Å)	volume (Å^3)	Estimated Mg content (mol %)
2Q-050319	Mg-calcite + MHC	4.198%	75.0	4.97789	16.96770	364.120	3.34
2I-140219	Mg-calcite	9.666%	100.0	4.97614	16.98467	364.228	3.23
2M-190219	Mg-calcite + MHC	4.259%	87.5	4.96822	16.93305	361.966	5.65
1C-210818	Mg-calcite	5.935%	100.0	4.97335	16.97488	363.610	3.89
2I-140119	Mg-calcite	8.354%	100.0	4.97634	16.99683	364.517	2.92
A-171016	Mg-calcite + MHC	5.014%	96.8	4.96725	16.95286	362.247	5.35
A-141117	Mg-calcite + MHC + arag	9.55%	86.0	4.96884	16.95949	362.621	4.95
A-241016	Mg-calcite + MHC	13.10%	77.5	4.94545	16.87389	357.402	10.5

Rietveld refinement - Table B

		Monohydrocalcite			
EXP ID	Phases	wt. %	a (Å)	c (Å)	volume (Å^3)
2Q-050319	Mg-calcite + MHC	25.0	10.59414	7.53753	732.642
2I-140219	Mg-calcite	--	--	--	--
2M-190219	Mg-calcite + MHC	12.5	10.58886	7.52948	731.128
1C-210818	Mg-calcite	--	--	--	--
2I-140119	Mg-calcite	--	--	--	--
A-171016	Mg-calcite + MHC	3.2	10.57972	7.54315	731.192
A-141117	Mg-calcite + MHC + arag	2.7	10.52771	7.41047	711.286
A-241016	Mg-calcite + MHC	22.5	10.56369	7.47366	722.263

Table S3. 2 Rietveld refinement of synthetic samples produced from experiments that contain Mg-calcite, monohydrocalcite (MHC) and aragonite (arag). A: Rietveld refinement values for Mg-calcite. B: Rietveld refinement values for monohydrocalcite.

S3 1.4 XRD diagrams

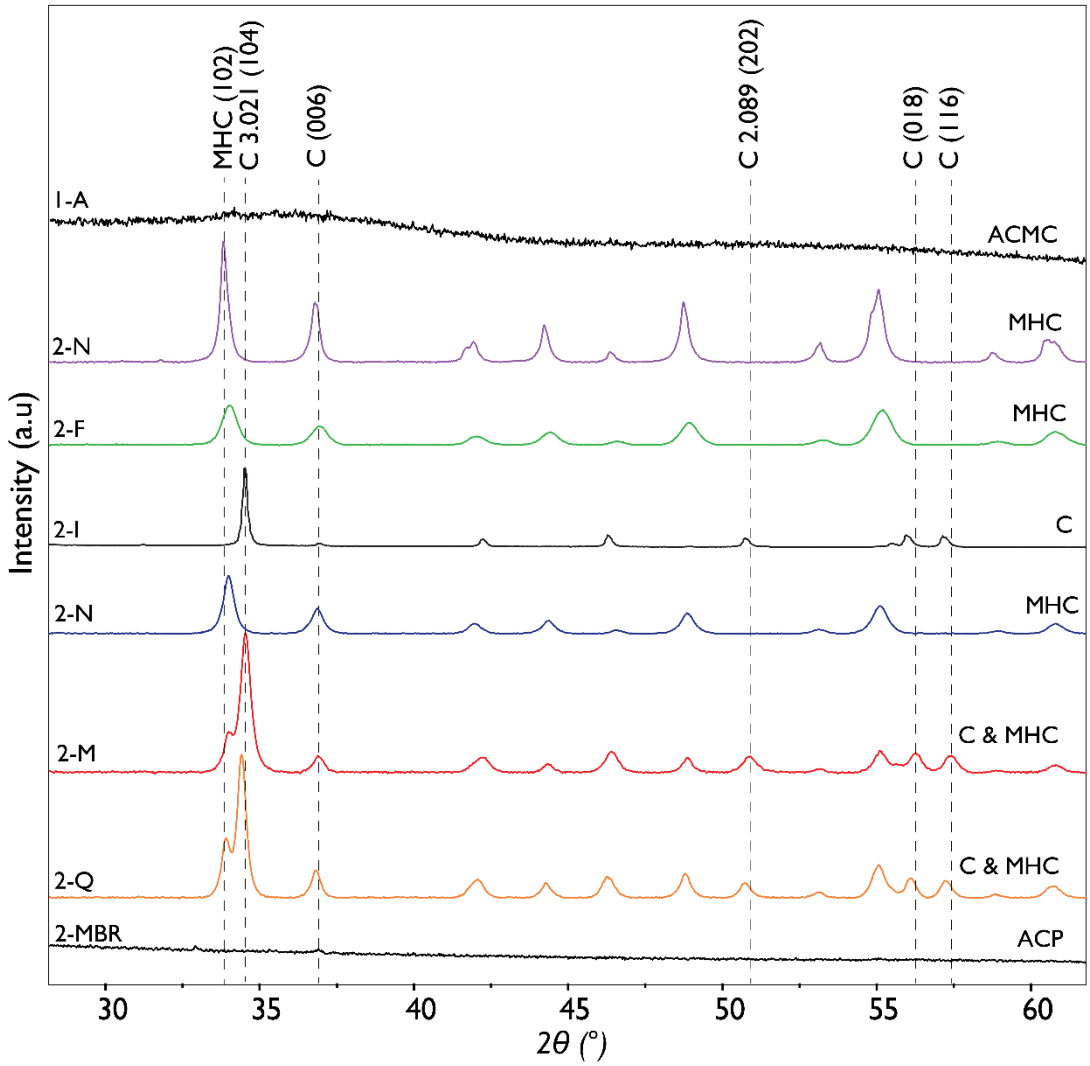

Figure S3. 2 XRD solid sample characterization from experimental solutions with Bragg peaks assigned. Amorphous-Ca-Mg-carbonate (ACMC), monohydrocalcite (MHC), calcite (C) and amorphous calcium phosphate (ACP).

S3 1.5 Spectroscopy

Ex-situ FT-IR analyses display diagnostic absorbance features in vibrational spectroscopy (Figure S3. 3). Amorphous calcium phosphate (ACP) also nucleates in experiments where PO_{4tot} approached 100 μmolal (along with ACMC), which recrystallized to octacalcium phosphate (OCP) over 48 hours (Figure S3. 3). FTIR spectra also indicate that poorly crystalline calcium

phosphate phases may be present and associated with samples containing monohydrocalcite and calcite (Figure S3. 3).

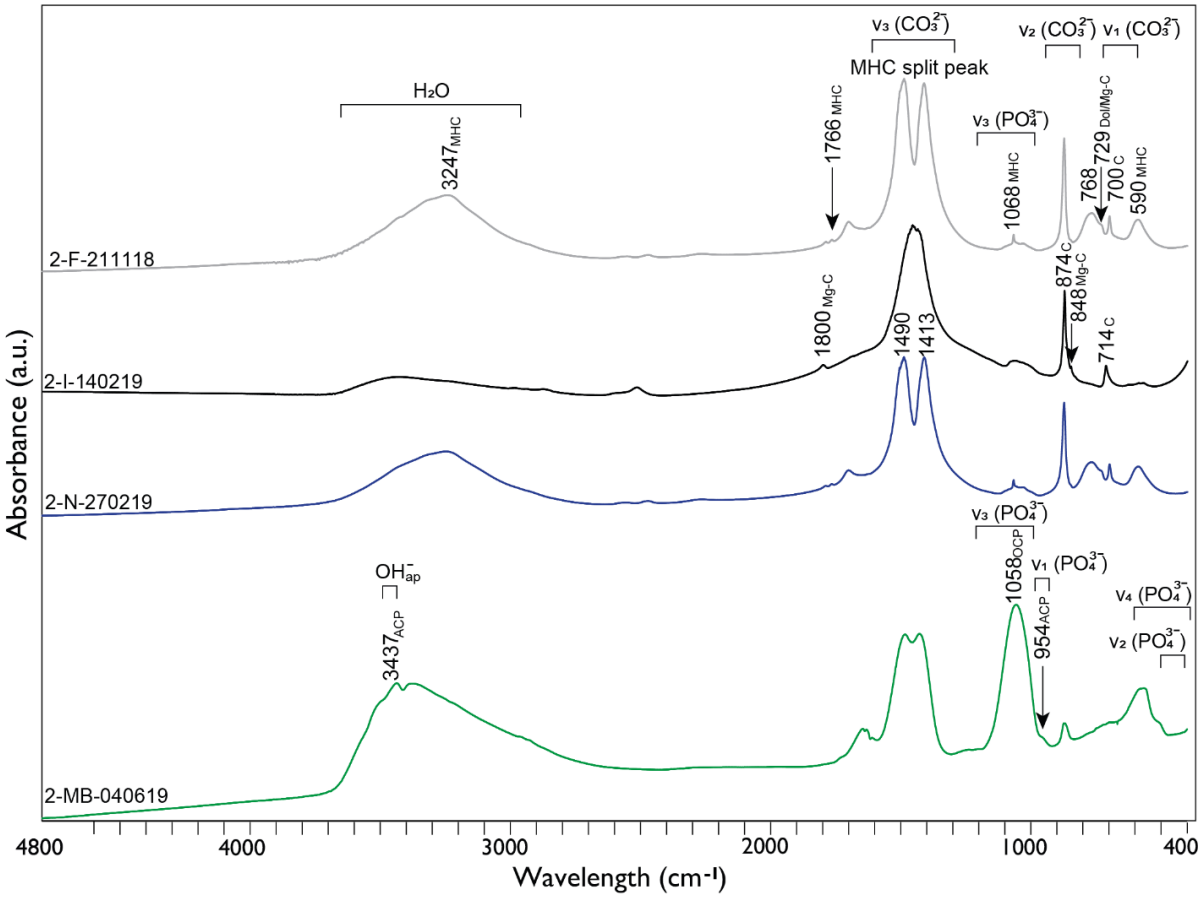

Figure S3. 3 FTIR sample characterization of monohydrocalcite (MHC), calcite (C) and octacalcium phosphate (OCP) with peaks representing apatite (ap) and amorphous calcium phosphate (ACP) also labelled.

S3 2 Additional supplemental material – unpublished

S3 2.1 Constant composition titration data

The constant composition procedures based on Beck et al., (2013) mimic supersaturated natural seawater systems by constantly replenishing depleted ions controlled using a Metrohm Titrino 920 dual-direction autotitrator (Tiamo 2.2 software) via a pH electrode and paired Ca^{2+} ISE and AgCl reference electrodes. Degassing of dissolved $CO_{2(aq)}$ and gaseous ρCO_2 absorption were minimized to prevent carbonate speciation. Once DIC-pH conditions were established, nucleation experiments were initiated by adding $CaCl_2$ to reach the desired $\Omega_{calcite}$. An example of the titration data collected from the *Constant Composition* experiments is presented in Figure S3. 4.

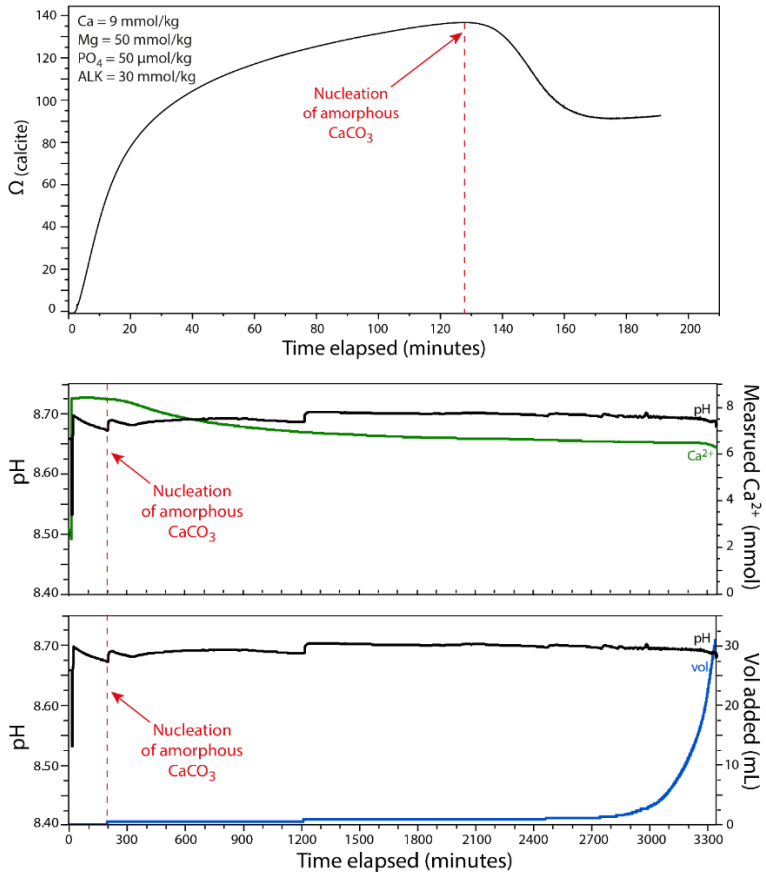

Figure S3. 4 Plotted data showing the reaction progression from the titration data for A: degassing experiment and B: Neoproterozoic experiment Exp. 2-X with pH and calcium electrode data. Experimental solution conditions and solid sample characterization for Exp. 2X can be found in Roest-Ellis et al., (2021) Supplementary Methods, Table S3.1,S3.2) which can be viewed in Chapter 3.

S3 2.2 Induction time calculations

The induction time (τ) (minutes) is the time taken for a supersaturated steady state system to begin precipitating material as the nuclei cluster crosses a critical threshold. In these experiments, pH measurements were used to determine the time elapsed from the preparation of the solution by adding the $CaCl_2$ to the NPZ-seawater, through to precipitation (of ACC). Nucleation was characterized by a pH decline (rate), and rapid dosing of the titrant to maintain constant composition, as well as visible changes to the solution as a white, opaque colour characterized solid precipitation. The reaction is characterized by (Eq. 3.1) (Pokrovsky, 1998). The induction time was used for calculating nucleation rates.

$$Ca^{2+} + HCO_3^- = CaCO_{3(s)} + H^+ \qquad (Eq.\ 3.1)$$

Homogeneous nucleation occurs spontaneously without preferential nucleation sites or surfaces (i.e. no seed). The induction period can be measured from homogeneous nucleation experiments and used to calculate nucleation rates and estimate the surface energy of ACC (Figure S3. 5). The induction time (τ, minutes) is the time taken for a supersaturated steady state system to begin precipitating material. pH measurements were obtained from the constant composition experiments and used to determine the time elapsed from the addition of Ca to seawater to precipitation of ACC. Nucleation was characterized by pH decline (initial pH – 2.5 %) and the onset titration to maintain constant composition. The theory of homogeneous nucleation, states that a plot of the logarithm of induction time (τ), as a function of the logarithm of the supersaturation (Ω) must yield a straight line (Nielsen and Toft, 1984; Pokrovsky, 1998).

$$\log_\tau = A + n\log_\Omega \qquad (Eq.\ 3.2)$$

The observed induction time displays a linear dependence, decreasing with increasing supersaturation according to Eq. 3.2, Figure S3. 5. The slope and y-intercept (A) of the regression line from Eq. 3.2 are used to calculate estimates of surface energy (σ) between ACMC and the seawater solution. Using the observed induction time, an equation relating to the solid-solution

surface energy and the degree of supersaturation (S) can be derived according to Eq. 3.3 (van Cappellen, 1991).

$$\ln t_{ind} = A + \frac{\pi a^4 \sigma^2}{(k_b T)^2 \ln S} \qquad \text{(Eq. 3.3)}$$

where mean ionic diameter estimate a of $3.4315e^{-10}$, Boltzmann constant k_b $1.380658e^{-23}$, and T (Kelvin) 298.15 are used. However, replotting Eq. 3.2 as the logarithm of induction time against the inverse of the logarithm of the saturation ratio (S) with respect to ACMC, incorporating the new value for S calculated from (Eq. 3.3) we observe a positive correlation (Figure S3. 5). We then use the recalculated Eq. 3.2 to calculate the surface energy (σ) of ACMC with better constraints, see Table S1 for values.

ID	Sample	PO_4 μmol	Si mmol	Mg:Ca	Ind. Time (mins)	Ωcalcite	Slope	A	Energy (σ) mJ/m^2
280119	2-J	50	0	3.33	2553	56	28.049	-13.455	0.105
270219	2-N				1392	59			
110219	2-I				198	83			
140119	2-I				233	83			
190219	2-M				135	83			
050319	2-Q				150	113			
301018	1-F	50	0	5.56	185	110	14.661	-4.2091	0.076
211118	2-F				66	169			
221018	1-E				70	181			
101018	1-B				243	183			
310718	1-A				15	301			
210818	1-C				277	75			
040619	2-MBR	100	0	3.33	185	83			
170619	2-MCR	25	0	3.33	28	83			
290719	2-SI	50	2	3.33	125	83			
All Results							14.987	-4.6715	0.076

Table S3. 3 Induction time data measured from experiments, with calculated slope and y-intercept (A) values of the regression line from Eq. 3.2 used to calculate estimates of surface energy (σ) between ACMC and the solution.

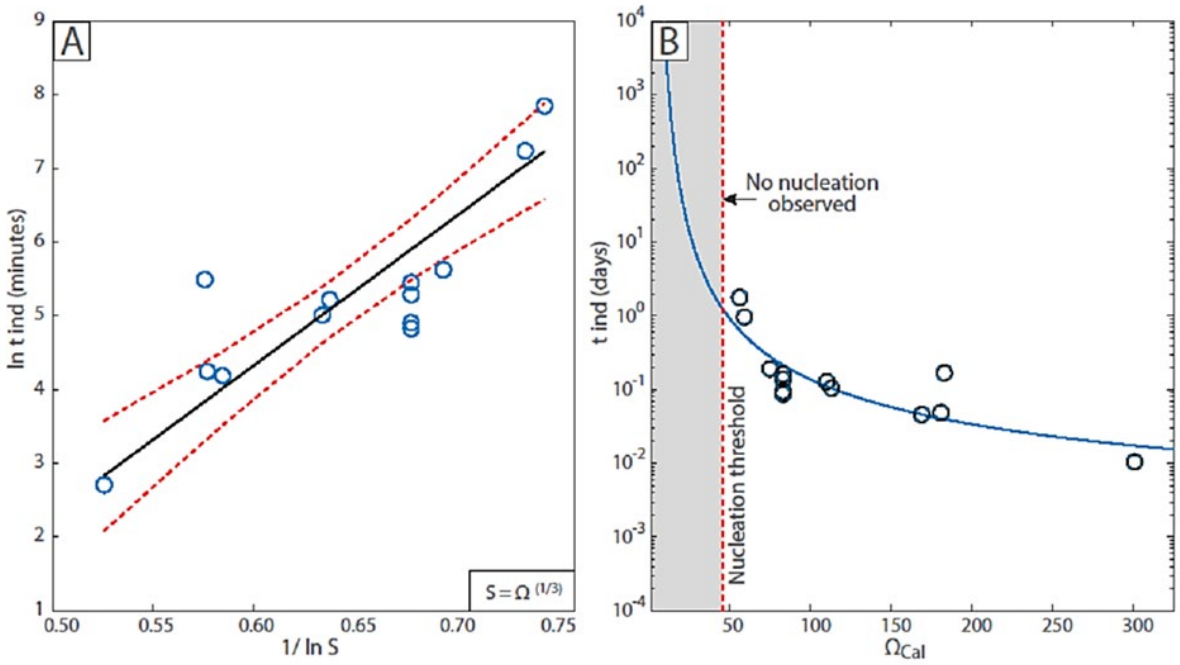

Figure S3. 5 Figure from Roest-Ellis et al., (2020) indicates results of the induction time measurements (τ) from all data combined (A) Relationship between natural logarithm of measured $CaCO_3$ nucleation induction time (t_{ind}) and calculated saturation ratio, $S = \Omega_{(1/N)}$, where N = number of ions in ACMC = 3(Ca^{2+}, Mg^{2+}, and CO_3^{2-}). (B) Relationship between calculated induction time (τ) and $\Omega_{calcite}$. Grey shaded area indicates minimum nucleation threshold of $\Omega_{calcite} = 45$ in seawater with elevated [PO_{4tot}]. The plot of the logarithm of induction time (τ), as a function of the logarithm of the supersaturation (Ω) must yield a straight line (Nielsen and Toft, 1984; Pokrovsky, 1998) represented by Eq. 3.2 in plot A).

These experiments as published in Roest-Ellis et al., (2020) show that in synthetic seawater with elevated [PO_{4tot}], no nucleation occurs below an $\Omega_{calcite}$ threshold of 45 (Figure S3. 4), even over time scales where nucleation should have occurred according to CNT (Pokrovsky, 1998). This result is consistent with molecular dynamic calculations of supersaturated CaCO3 solutions (Wallace et al., 2013), which show that once a key $\Omega_{calcite}$ threshold is crossed, amorphous CaCO3 can form through the rapid production of dense liquid droplets. This liquid-liquid separation process occurs in a compositional regime that may only be accessed if the precipitation of crystalline polymorphs is suppressed.

S3 2.3 FTIR results

FTIR results for the remaining Neoproterozoic seawater experiments.

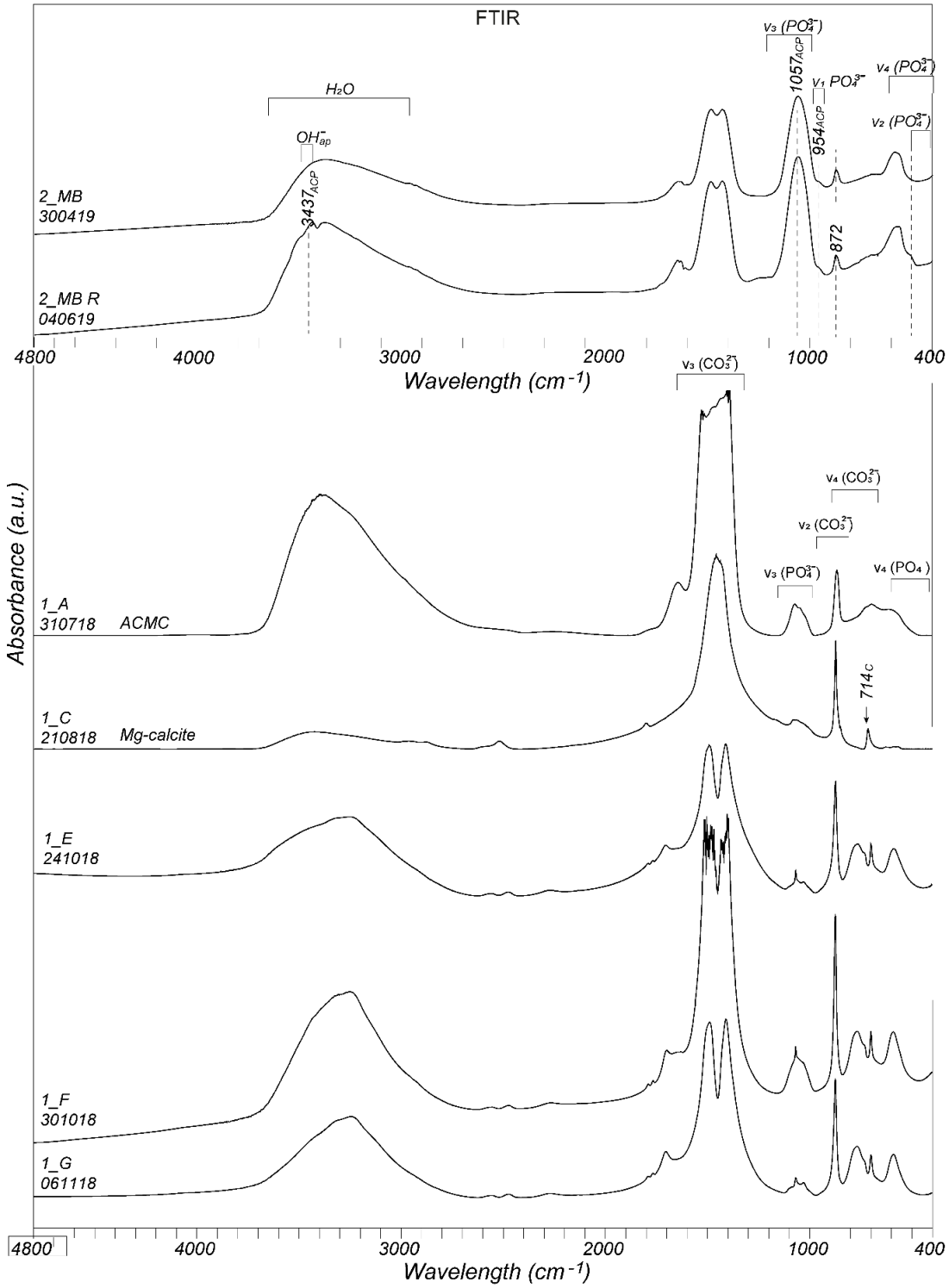

Figure S3. 6 Plotted FTIR data showing Neoproterozoic seawater experiments Exp. 1 and Exp 2_MB that contain 100 µmol [PO_4] compared with 50 µmol [PO_4] in the rest of the experiments. CO_3^{2-} and PO_4^{3-} vibrational modes are labelled and interpretations of Ca-Mg- CO_3^{2-}

and PO_4 minerals are labelled. Labels: MHC – monohydrocalcite, C – calcite and Mg-C – Mg-calcite and ACP – amorphous calcium phosphate.

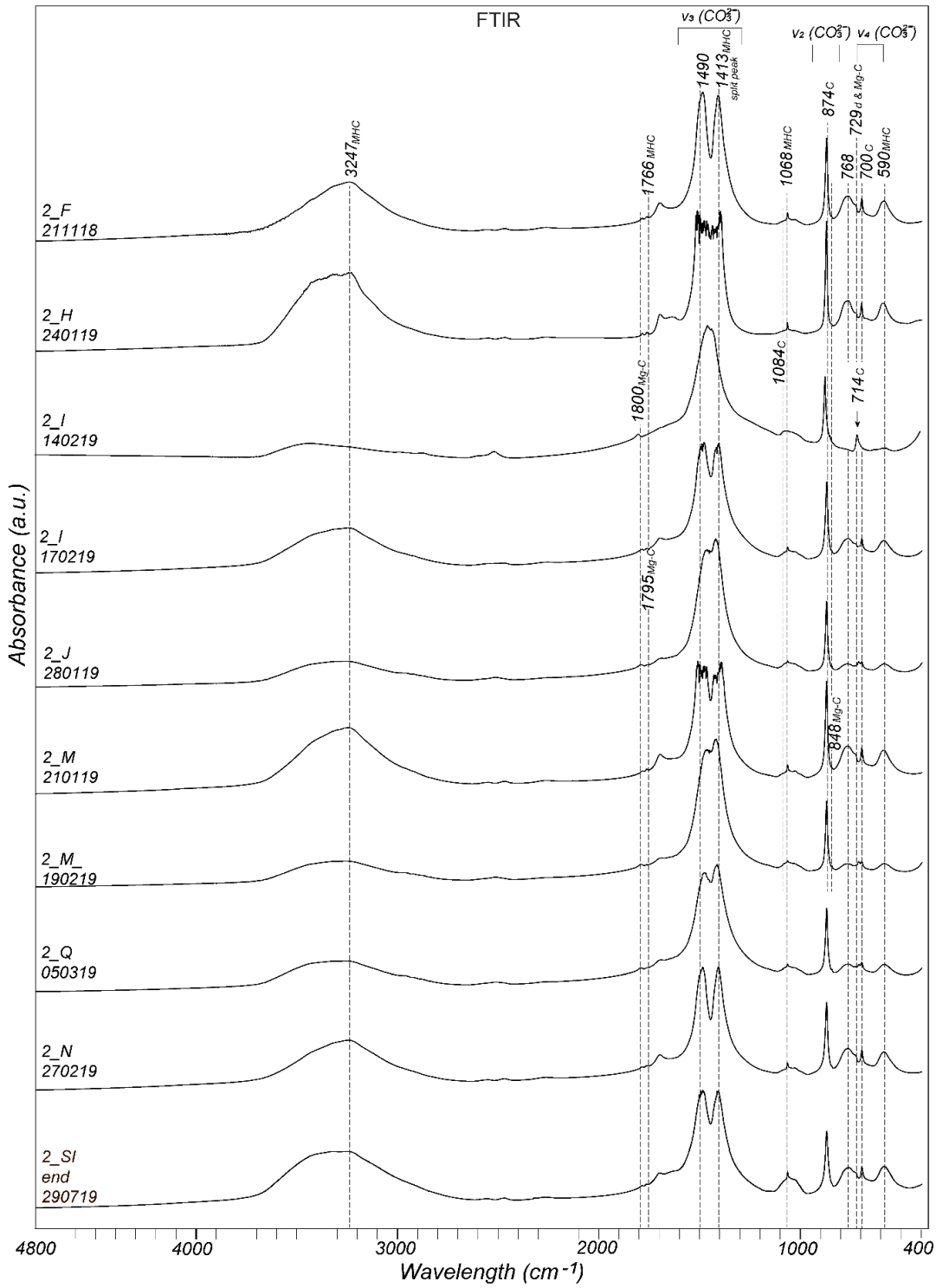

Figure S3. 7 Plotted FTIR data showing Neoproterozoic seawater experiments Exp. 2. CO_3^{2-} vibrational modes are labelled and interpretations of Ca-Mg- CO_3^{2-} minerals are labelled. Labels: MHC – monohydrocalcite, C – calcite and Mg-C – Mg-calcite.

S3 2.4 ICP-MS solid sample results

During experiments, the aqueous Ca and Mg concentrations of experimental solution samples were extracted, syringe-filtered (0.22 μm), and acidified (HNO_3, 4 %). When the experiments were terminated, the bulk solid samples were syringe-filtered (0.22 μm), vacuum-filtered, rinsed with isopropanol, and dried in a vacuum-desiccator at 25 °C for 24 h before digestion (HNO_3, 4 %). The Ca, Mg, P, and Si concentrations were then measured via a PerkinElmer NexION 350D inductively coupled plasma–mass spectrometer (ICP-MS). Samples were randomized, replicates were analyzed every 10 samples, 8 calibration standards were used and 1 ppm quality control (QC) standards were analyzed every 10 samples. In addition, blank samples with no Ca, Mg or P were analyzed every 10 samples and reference standards: SPS-SW2; NASS-7; SLRS-6_R2_5xdil and a synthetic seawater with no calcium. The analytical precision for the bulk solid samples was ± 2% for Mg and ±5% for Ca. Based on the ICP-MS results, the Mg content of the bulk solid was calculated according to the equation where $[Mg]_{solid}$ and $[Ca]_{solid}$ are the measured concentrations of Ca and Mg of the solid with units Mol/kg:

$$[Mg]_{solid} = \frac{[Mg]_s}{[Mg]_{solid} + [Ca]_{solid}} \text{ X } 100 \qquad \text{(Eq. 3.4)}$$

The results are presented in Table S3.4. In addition, approximate mass-balanced Mg and Ca mol $\%_{wt}$ were calculated from ICP-MS for the dominant mineral phase (i.e., Mg-calcite, high Mg-calcite, monohydrocalcite and ACMC) present in the solid precipitates detected by XRD from the Neoproterozoic seawater nucleation experiments and accounts for mass balance for Ca, Mg, C, O and H mol $\%_{wt}$.

It is important to note that in our experiments, the molar Mg/Ca of the solids and the mass balance calculated from the solution Mg and Ca concentrations indicates that substantial Mg content must have incorporated into the monohydrocalcite solid phases. According to XRD analyses, there were no crystalline phases other than monohydrocalcite present in most experiments (i.e., Table S2.A). This discrepancy was also noted by Fukushi and Matsumiya, (2018) and Fukushi et al.,

(2017), the latter of whom examined the speciation of Mg associated with monohydrocalcite using XANES, calculations and geochemical modelling and concluded that most Mg was present as a discrete amorphous phase with a stoichiometry of $MgCO_3 \cdot$ This may explain the high Mg content of monohydrocalcite in our examples.

ID	Sample	Dominant mineral	P 31 (ppb)	Mg 24 Helium KED (ppb)	Ca 40 Ammonia DRC (ppb)	Mg:Ca overall of solid	Mg mol %	Ca mol %	Mineral Mg mol %*	Mineral Ca mol %*
310718-0	1-A	ACMC	13143	30399	275409	0.11	**9.94**	**90.06**	4.50	24.71
210818-0	1-C	Mg-cal	7812	6643	369028	0.02	**1.77**	**98.23**	0.59	20.01
101018-0	1-B	MHC	3677	1555	239113	0.01	**0.65**	**99.35**	0.22	30.48
241018-0	1-E	MHC	8436	6591	337019	0.02	**1.92**	**98.08**	0.96	29.84
301018-0	1-F	MHC	18599	20767	341660	0.06	**5.73**	**94.27**	2.81	28.00
061118-0	1-G	MHC	8208	595	292770	0.00	**0.20**	**99.80**	0.10	30.70
211118-0	2-F	MHC	8095	8051	343973	0.02	**2.29**	**97.71**	12.06	29.66
170119-0	2-I	Mg-cal	8756	8155	364269	0.02	**2.19**	**97.81**	0.72	19.62
240119-0	2-H	MHC	5563	25023	263635	0.09	**8.67**	**91.33**	4.17	26.63
280119-0	2-J	MHC	9183	448	304822	0.00	**0.15**	**99.85**	0.07	30.73
190219-0	2-M	Mg-cal, MHC	9002	11674	328012	0.04	**3.44**	**96.56**	1.13	19.21
270219-0	2-N	MHC	8507	593	324662	0.00	**0.18**	**99.82**	0.09	30.71
050319-0	2-Q	Mg-cal	7559	5245	327363	0.02	**1.58**	**98.42**	0.52	19.82
050319-0 d.	2-Q	Mg-cal	7207	5153	316870	0.02	**1.60**	**98.40**	0.53	19.81
300419-0	2-MB	MHC, Mg-cal	107061	80278	265260	0.30	**23.23**	**76.77**	-	-
40619-0	2-MBRE	-	68247	58782	147300	0.40	**28.52**	**71.48**	-	-
210519-0	2-MC	-	70972	54424	173433	0.31	**23.89**	**76.11**	-	-
170619-0	2-MCR	-	82279	56195	160588	0.35	**25.92**	**74.08**	-	-
290719-0	2-SI-Mid	-	14043	40351	224654	0.18	**15.23**	**84.77**	-	-
290719-0 d.	2-SI-End	-	14006	40621	224419	0.18	**15.33**	**84.67**	-	-

Table S3. 4 ICP-MS results of dissolved solid to determine Mg/Ca ratio. Mg and Ca mol % were estimated from the calculation shown in Eq. 3.4. (*) denotes approximate mass-balanced Mg and Ca mol $\%_{wt}$ that were calculated from ICP-MS for the dominant mineral phase present in the solid precipitates from the Neoproterozoic seawater nucleation experiments detected by XRD and accounts for estimated Ca, Mg, C, O and H mol $\%_{wt}$ according to theoretical mass-balance of the minerals (see Table S2.5). MHC – monohydrocalcite, ACMC – amorphous calcium magnesium calcite, Mg-cal – magnesium calcite, d. – duplicate.

S3 2.5 Theoretical Mol % of solid samples

Molar weight corrected theoretical composition of solid minerals precipitated in Neoproterozoic seawater nucleation experiments using approximate Mg and Ca Mol % that were calculated from ICP-MS (Table S3.4) for the dominant mineral phase present and approximate H_2O for the amorphous phases.

Theoretical Mol %		Atomic weight	Number of atoms	Molar weight	Molar weight %	Ca + Mg weight %
ACMC $Ca_{(0.5)}Mg_{(0.5)}(CO_3)_2 \cdot (H_2O)$						
Ca	Calcium	40.1	1	40.1	18.2	29.2
Mg	Magnesium	24.3	1	24.3	11.0	
C	Carbon	12.0	2	24.0	10.9	
O	Oxygen	16.0	8	128.0	58.1	
H	Hydrogen	1.0	4	4.0	1.8	
Total				220.4	100.0	
Monohydrocalcite $CaCO_3 \cdot (H_2O)$						
Ca	Calcium	40.1	1	40.1	30.8	30.8
C	Carbon	12.0	2	24.0	18.5	
O	Oxygen	16.0	4	64.0	49.2	
H	Hydrogen	1.0	2	2.0	1.5	
Total				130.1	100.0	
Low Mg-calcite $Ca_{(0.96)}Mg_{(0.04)}(CO_3)_2$						
Ca	Calcium	40.1	0.96	38.5	20.1	20.6
Mg	Magnesium	24.3	0.04	1.0	0.5	
C	Carbon	12.0	2	24.0	12.5	
O	Oxygen	16.0	8	128.0	66.9	
Total				191.5	100.0	
Mg-calcite $Ca_{(0.92)}Mg_{(0.08)}(CO_3)_2$						
Ca	Calcium	40.1	0.92	36.9	19.3	20.3
Mg	Magnesium	24.3	0.08	1.9	1.0	
C	Carbon	12.0	2	24.0	12.6	
O	Oxygen	16.0	8	128.0	67.1	
Total				190.8	100.0	
Calcite $CaCO_3$						
Ca	Calcium	40.1	1	40.08	40.04	
C	Carbon	12.0	1	12.01	12.00	
O	Oxygen	16.0	3	48.00	47.96	
Total				100.09	100.00	
ACMC $Ca_{(0.8)}Mg_{(0.2)}(CO_3)_2 \cdot (H_2O)$						
Ca	Calcium	40.1	**0.8**	**32.06**	**14.55**	**19.1**
Mg	Magnesium	24.3	**0.2**	**4.86**	**2.21**	
C	Carbon	12.0	2	**24.02**	**10.90**	
O	Oxygen	16.0	8	**128.00**	**58.07**	
H	Hydrogen	1.0	4	**4.03**	**1.83**	
Total				**192.97**	**87.54**	

Table S3. 5 Theoretical composition of solid minerals precipitated in Neoproterozoic seawater nucleation experiments using approximate Mg and Ca Mol % that were calculated from ICP-MS (Table S3.4) for the dominant mineral phase present.

S3 2.6 Isotopic analysis of solid samples using Gasbench

To investigate the isotopic $\delta^{13}C/^{12}C$ and $\delta^{18}O/^{16}O$ of the Neoproterozoic nucleation experiments, samples drawn from solutions, filtered and vacuum dried were analyzed. The solid sample and initial solution composition are summarized in Table S3.1. Multiple samples from the same experiment taken at different time intervals are presented here from the middle (*2_M_190219 mid*) of an experiment and at the end (*2_M_190219 end)* of an experiment (Table S3. 4). This progression in time means that the nucleated product was left in the solution to precipitate more or recrystallize. The summarized semi—quantitative mineralogy based on XRD analyses (Table S3. A) indicate that the earlier of the samples was dominantly calcite (87.5 %) with a smaller proportion of monohydrocalcite (12.5 %) with Mg wt% content that decrease correspondingly from 5.7 % to 3.9 %. There is not enough data for reliable interpretations or conclusions regarding the mineral progression, but one possibility is that monohydrocalcite with Mg incorporated was produced via ACMC which then recrystallizes to calcite with a slightly lower concentration of magnesium than the monohydrocalcite. The samples may recrystallize removing some Mg or incorporate more calcium as the titrator continues to titrate Ca^{2+} CO^{3-}- $PO4^{3-}$ solutions to maintain constant composition and further nucleation continues. The corresponding isotopic $\delta^{13}C/^{12}C$ data for these samples (presented in Table S3. 7.) becomes slightly more depleted from -2.122 to -2.360 during the experiment progression. This may be consistent with increased and rapid nucleation. Apparent changes in isotopic composition related to Mg-Ca-carbonate polymorphism are indicated (Table S3. 7), for example monohydrocalcite and calcite (Mg-calcite) have relatively similar $\delta^{13}C/^{12}C$ values of ~2.1 to ~2.5, yet high Mg ACMC has a more enriched (less negative) value ~ 0.8, however, this sample was taken earlier on in the experiment duration relative to the other samples and contains

	Solid sample composition		Initial solution conditions			
Sample	Calcite wt%	Monohydrocalcite wt %	Mg wt%	Ω (calicte)	DIC	pH
NOCZ_grain-250-355 ug	-	-	-	-	-	-
NOCZ_grain-250-355 ug	-	-	-	-	-	-
NOCZ_grain-250-355 ug	-	-	-	-	-	-
NOCZ_grain-250-355 ug	-	-	-	-	-	-
NBS19-grain	-	-	-	-	-	-
NBS19-grain	-	-	-	-	-	-
NBS18-grain	-	-	-	-	-	-
NBS18-grain	-	-	-	-	-	-
STD_NaHCO3	-	-	-	-	-	-
1_C_210818	75.0	25.0	3.3	75	25	8.3
2_I_140119	100.0	-	3.2	83	14	8.5
2_M_190219 mid	87.5	12.5	5.7	83	10	8.7
2_M_190219 end	100.0	-	3.9	83	10	8.7
2_Q_050319	100.0	-	2.9	113	6	8.9
1_A_310718	N/A (ACMC 100%)	-	-	301	25	9.2

Table S3. 6 Table summarizing the characteristics of the samples used for isotope data collection. Data are presented in **Table S3.7** below. The Mg wt% content of the solids presented here was estimated using XRD Rietveld refinement and these values are originally reported in Roest-Ellis et al., (2021) Supplementary Methods, Table S2.1; S2.2).

Sample	Ampl. 44	Mean $\delta^{13}C/^{12}C$	Std. dev.	Mean $\delta^{18}O/^{16}O$	Std. dev.	Correct * $\delta^{13}C/^{12}C$	Correct * $\delta^{18}O/^{16}O$	Correct ** $\delta^{13}C/^{12}C$	Correct ** $\delta^{18}O/^{16}O$
NOCZ_grain	6240	2.04	0.029	-2.351	0.03	2.110	-1.933	-	-
NOCZ_grain	6385	2.092	0.022	-2.335	0.036	2.164	-1.916	-	-
NOCZ_grain	6217	2.108	0.026	-2.326	0.029	2.180	-1.907	-	-
NOCZ_grain	6295	2.133	0.015	-2.337	0.018	2.206	-1.918	-	-
NBS19-grain	6086	1.876	0.015	-2.642	0.022	1.942	-2.226	-	-
NBS19-grain	5681	1.891	0.02	-2.59	0.034	1.958	-2.174	-	-
NBS18-grain	5229	-4.828	0.023	-23.252	0.045	-4.928	-23.021	-	-
NBS18-grain	5550	-4.988	0.024	-23.23	0.023	-5.092	-22.999	-	-
STDNaHCO3	6232	-2.763	0.023	-16.249	0.027	-2.812	-15.955	-	-
1_C_210818	4931	-5.144	0.043	-8.627	0.025	-5.252	-8.265	**-2.440**	**7.690**
2_I_140119	5825	-5.066	0.018	-13.507	0.03	-5.172	-13.189	**-2.360**	**2.767**
2_M_190219 mid	5139	-4.834	0.035	-12.982	0.045	-4.934	-12.659	**-2.122**	**3.296**
2_M_190219 end	5853	-5.066	0.021	-13.291	0.04	-5.172	-12.971	**-2.360**	**2.985**
2_Q_050319	6949	-4.954	0.021	-14.169	0.02	-5.057	-13.857	**-2.245**	**2.099**
1_A_310718	10306	-3.576	0.011	-9.072	0.029	-3.645	-8.714	**-0.833**	**7.241**

Table S3. 7. Isotope analyses of solid samples precipitated in Neoproterozoic seawater experiments. Isotopic analyses was conducted using Gasbench at the University of Oxford Department of Earth Sciences. The minimum voltage (mV) was 1000 and the maximum voltage was 12000. Peak count for each sample were 6. The data presented show data that were corrected using two standards (denoted by *) in which the corrected standard results were: NBS19-grain $\delta^{13}C/^{12}C$ 1.95 (mean), 0.01.87 (std. dev); $\delta^{18}O/^{16}O$ -2.2 (mean), 0.037099 (std. dev); and NBS18-grain $\delta^{13}C/^{12}C$ -5.01 (mean), 0.115944 (std. dev); $\delta^{18}O/^{16}O$ -23.01 (mean), 0.015696 (std. dev). The second set of data presented show data corrected using two standards as previously mentioned in addition to a sodium bicarbonate ($NaHCO_3$) powder standard that was used in the initial sample precipitation (denoted by **). The results here do not present enough data to warrant interpretations or conclusions, however, however the sample repeats from different stages in the same experiment (*2_M_190219 mid* and *2_M_190219 end*) indicate that the sample $\delta^{13}C/^{12}C$ becomes slightly more depleted from -2.122 to -2.360 during the experiment progression where the samples may recrystallize.

Supplement 4

S4 XANES and μXRF

S4. 1 Fe K-edge XANES and μXRF

XANES and μXRF data collected at the Fe K-edge demonstrate that the Fe present in these samples is almost exclusively bound up in detrital phases chlorite and biotite. This important observation indicates that microbial diagenetic re-processing, as an origin for the P cannot account for the enhanced P accumulations in these carbonates.

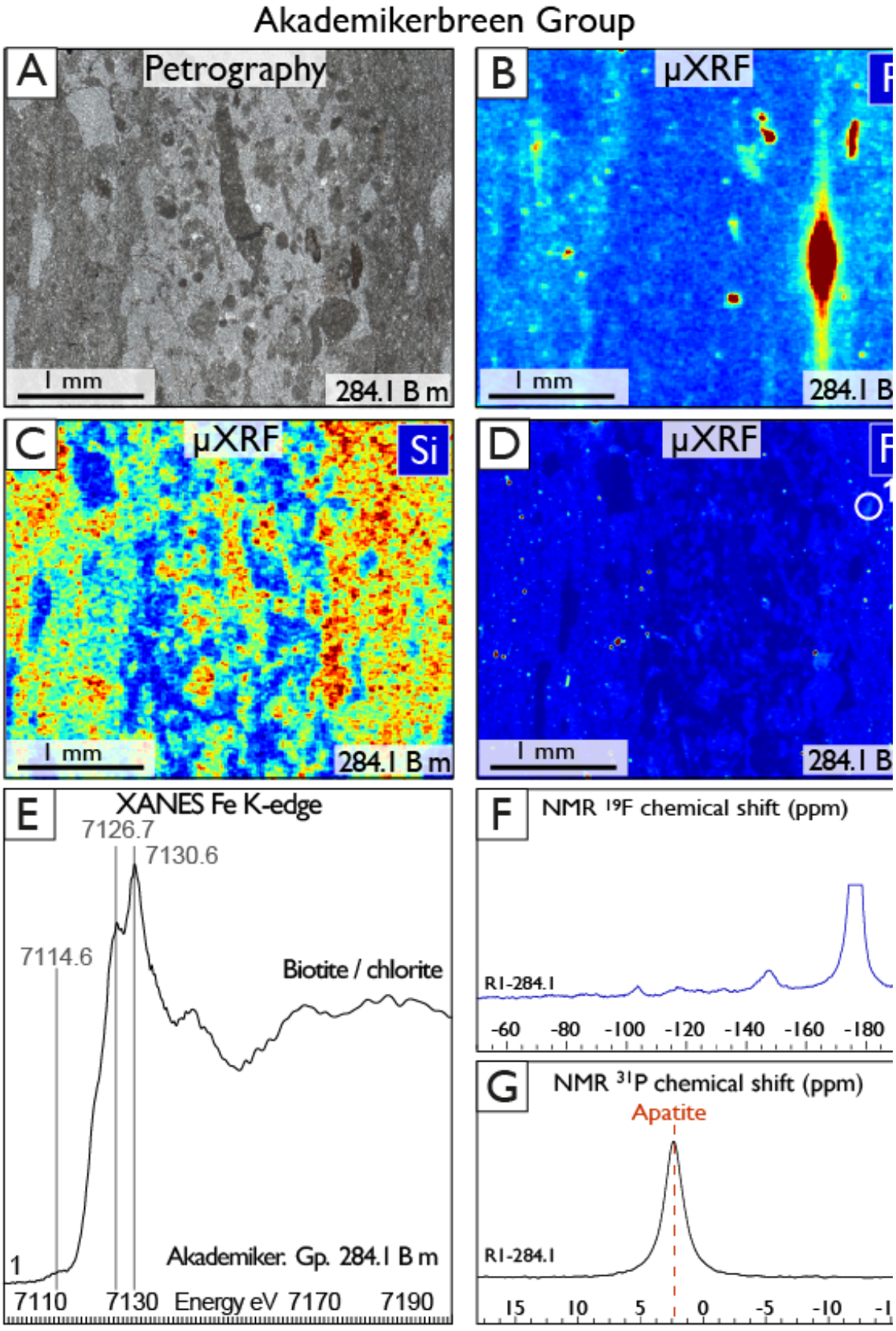

Figure S4 1. XANES and µXRF maps of Fe- K-edge indicating biotite and chlorite as the dominant minerals that bind Fe rather than Fe minerals associated with microbial reduction.

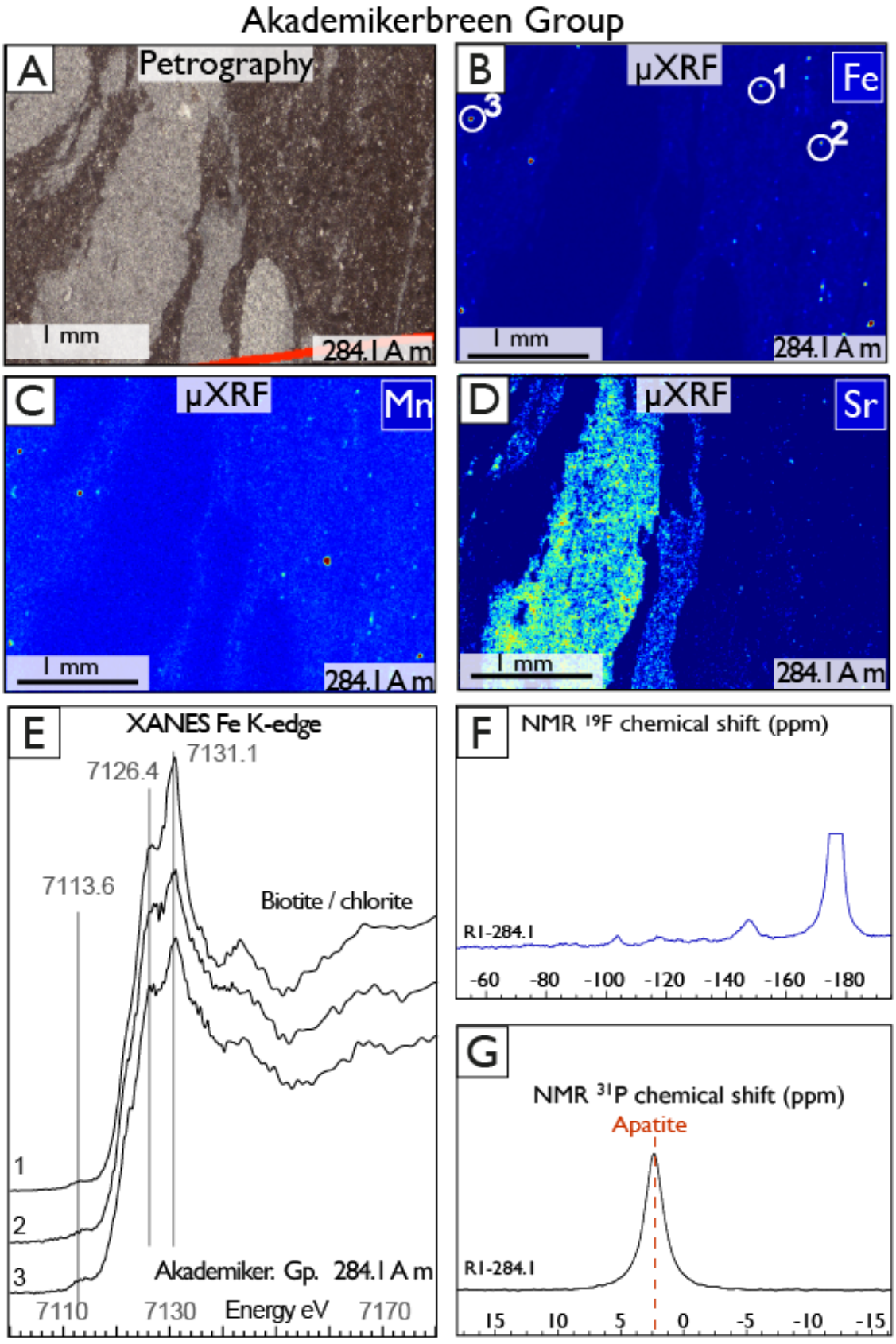

Figure S4 2. XANES and µXRF maps of Fe- K-edge indicating biotite and chlorite as the dominant minerals that bind Fe rather than Fe minerals associated with microbial reduction.

S4. 2 P K-edge XANES and µXRF Akademikerbreen Group

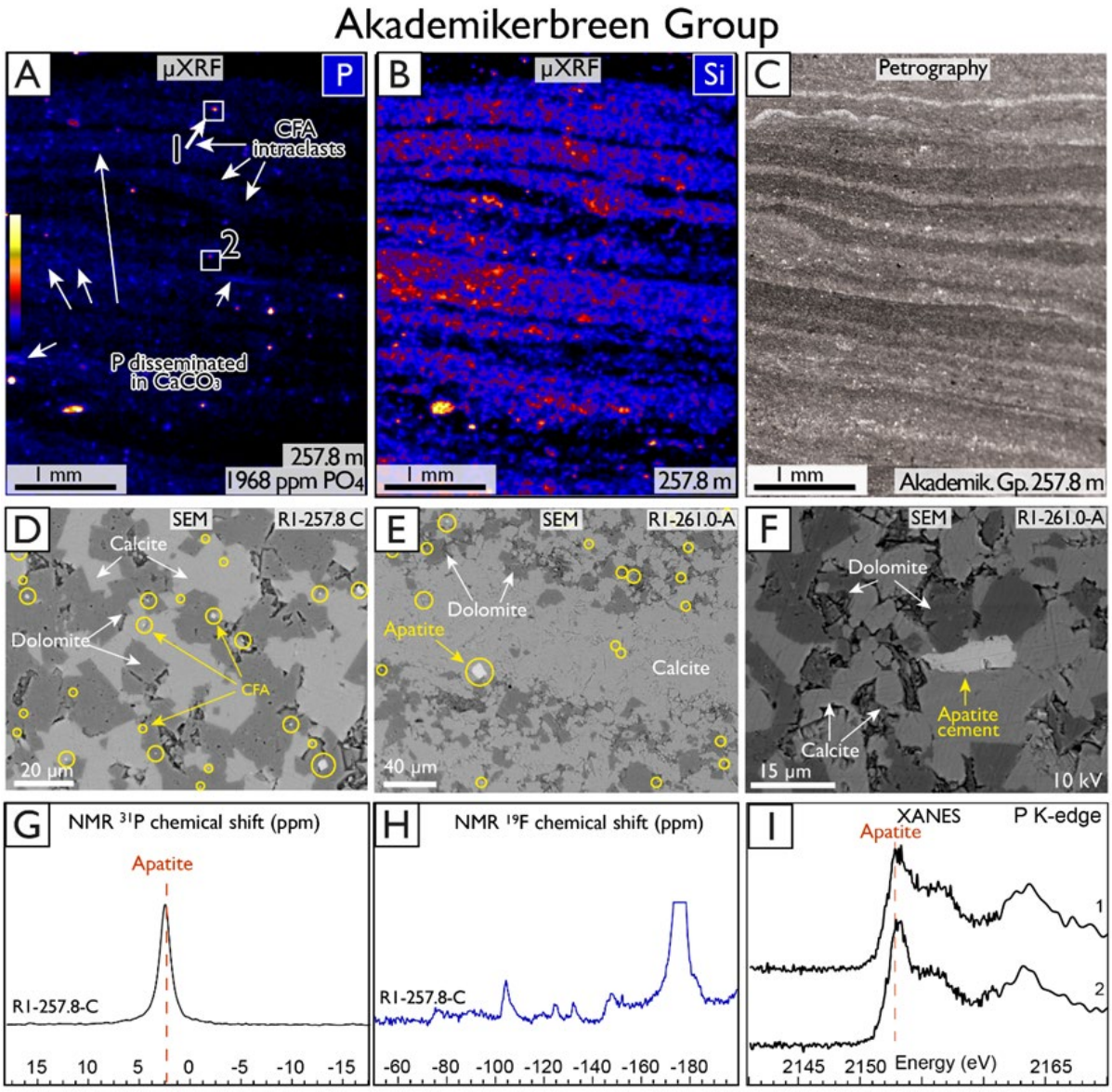

Figure S4 3. Additional P K-edge XANES and µXRF of Akademikerbreen Group stromatolite from the Svanbergfjellet Formation. SEM images of the same sample and additional sample 261.0-A are included and ^{31}P and ^{19}F NMR data are presented.

S4. 3 XANES reference compilation from BL 14-3, SSRL

Normalized XANES spectra of P-bearing minerals standards and references for comparison with samples. Spectra and processing obtained by Jocelyn Richardson and Sam Webb at SSRL Stanford Synchrotron Radiating Lightsource, USA.

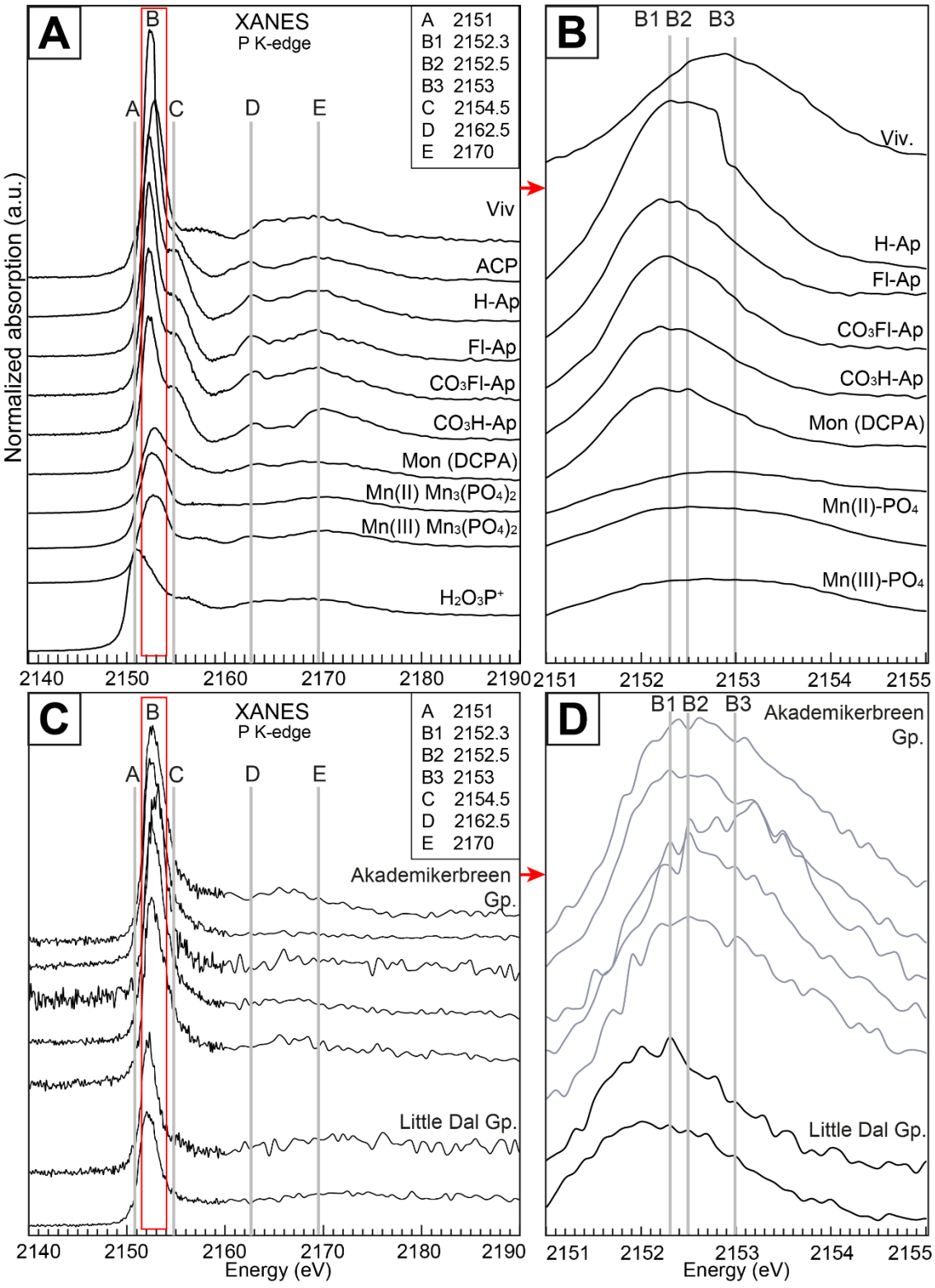

Figure S4 4. A: Normalized spectra of P-bearing minerals standards and references for comparison with samples. B: Zoomed in area highlighted by red box to display the dominant peak shifts observed between the samples. Spectra and processing obtained by Jocelyn Richardson and Sam Webb at SSRL Stanford Synchrotron Radiating Lightsource, USA. C: Selected XANES spectroscopy of Akademikerbreen Group and Little Dal Group that appear to characterize CO_3-associate lattice bound PO_4. D: Zoomed in area of (C) to show the dominant peak energy shifts.

S4. 4. Synthetic calcite – carbonate associated PO_4

XANES spectroscopy of synthetic calcite carbonate associated PO_4 (CAP) precipitated in PO_4-doped solutions using the ammonium carbonate gas diffusion method first described by Gruzensky, (1967). The resultant solids were analyzed to characterize the nature of PO_4 (see section S4 1.7 for further characterization). The three samples contain increasing measured bulk PO_4. The spectra are normalized and consist of the average of three XANES for each sample. The XANES spectra indicate carbonate-associated PO_4 which appears to be characterized by a featureless peak with no shoulder (as present in apatite) and a shift to higher energy values (~0.2–.3 eV) (Fig. S4 5). This may be explained because presence of CO_3 in apatite causes a decrease in crystallinity and crystal ordering (i.e. Harries et al., 1987), which, with high CO_3 concentrations leads to calcium carbonate phosphate phases with near-amorphous crystallinity that appears amorphous – poorly crystalline in XRD patterns (i.e., Trautz, 1960).

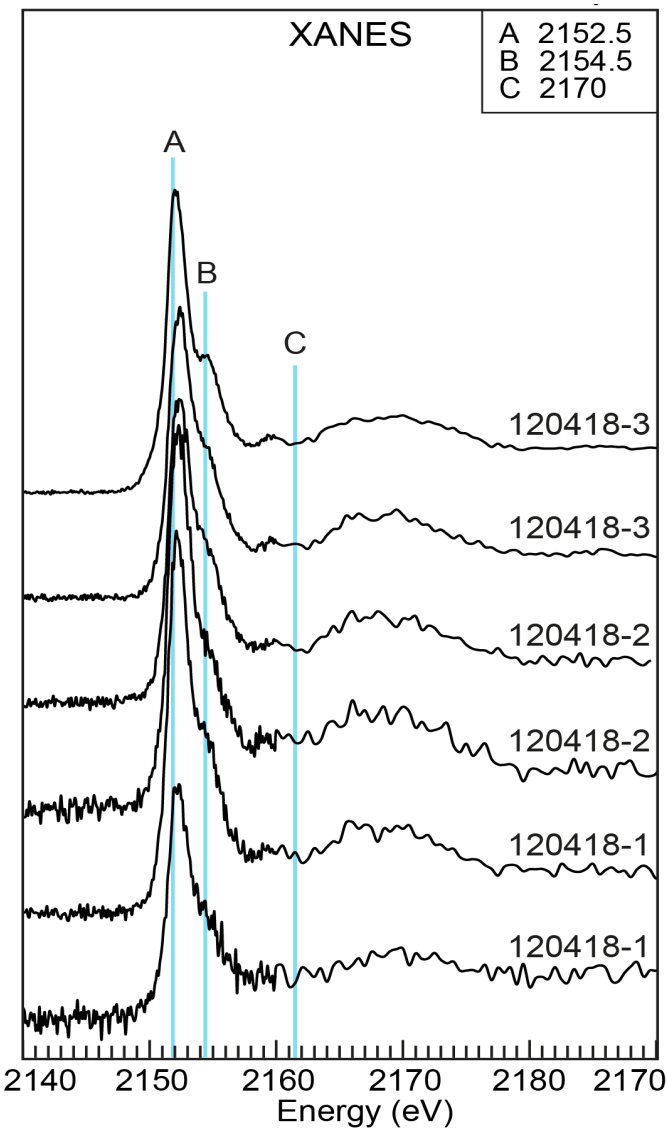

Figure S4 5. XANES spectroscopy of synthetic $CaCO_3$-PO_4 samples with increasing PO_4 from bottom to top. Each spectra is the average of three spectra.

S4. 5 Akademikerbreen Group ^{31}P NMR and ^{19}F NMR

NMR spectroscopy on Tonian aged carbonates from the Akademikerbreen Group and Little Dal Group were analyzed by Brian Phillips at Stony Brook University, New York. Based on solid-state NMR spectroscopy, incorporation of PO_4 in calcite can be observed by changes in the ^{31}P NMR chemical shift of the PO_4 group (Phillips et al., 2016) and $^{31}P/^{13}C$ rotational echo double resonance (REDOR) experiments that identify atomic-scale proximity of C-O-P of the PO_4 groups to C in the CO_3^{2-} ion of calcite providing. This can provide evidence that PO_4 is tightly

enclosed within the calcite lattice (Phillips et al., 2016) and not precipitated on the calcite surface for example. The orthophosphate is identified by a broad peak with a chemical shift near ~3.5 ppm with narrow resonance at = 2.9 ppm (Mason et al., 2007; Philips et al., 2016).

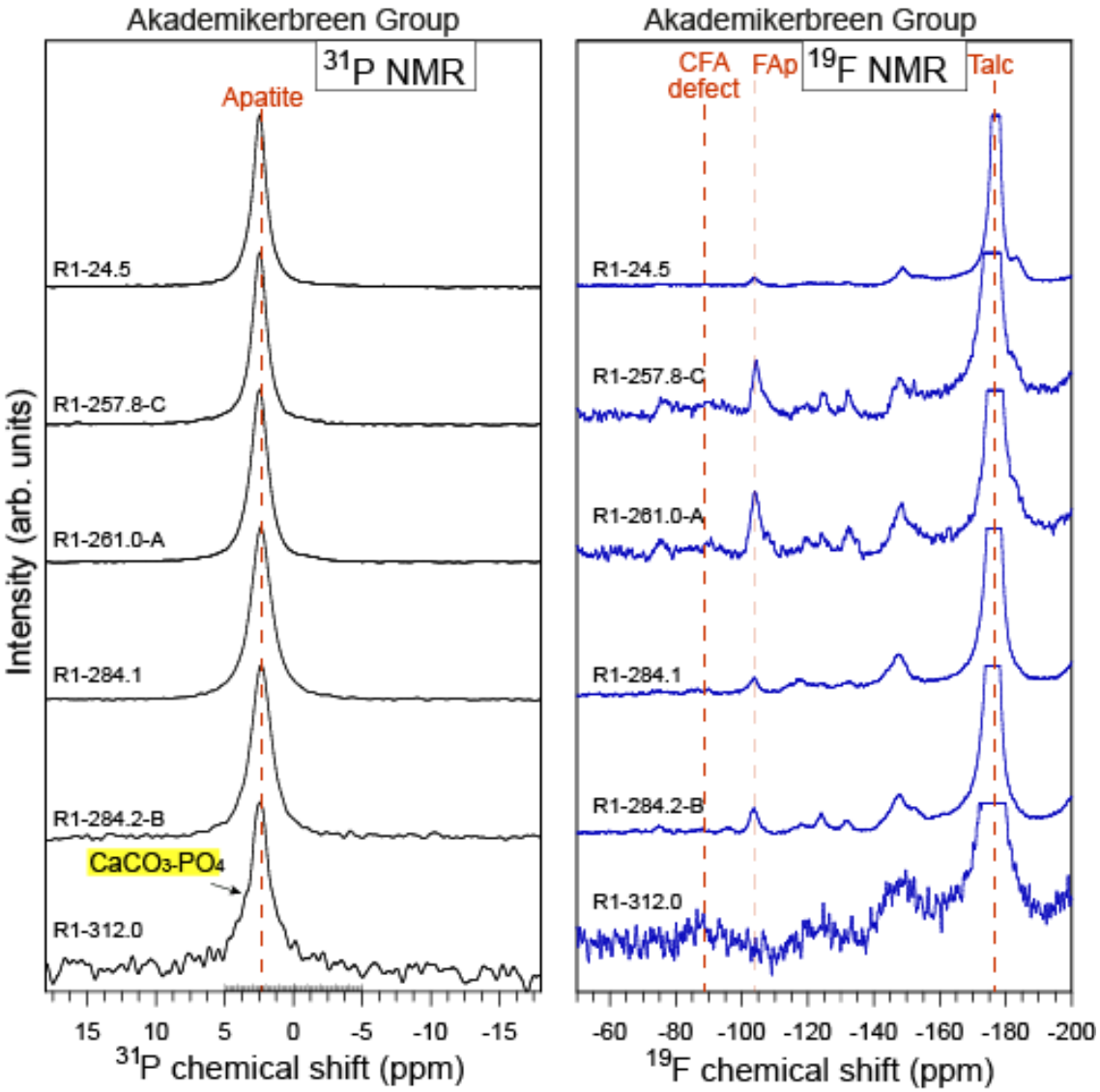

Figure S4 6. Solid state ^{31}P and ^{19}F NMR data indicate that the mineral phase that hosts PO_4 in the Akademikerbreen Group carbonates is almost entirely apatite, with a chemical shift of ca. 2.5-2.8 ppm. ^{19}F data further show that the dominant host of F is consistent with a trioctahedral silicate (likely talc given petrographic and XRD analyses. In addition, a chemical shift of -102 ppm highlights the presence of fluorapatite, while the presence of a weak band at -88 ppm further corresponds to a "francolite-type defect" arising from F-bonding environments sensitive to the substitution of carbonate for phosphate in francolite (Yi et al. 2013). Together, these data indicate that much of the P hosted within Akademikerbreen Group carbonates is CFA and P is dominantly CO_3–associated PO_4 within CFA. In addition, incorporation of PO_4 into the calcite lattice may be observed by minor changes in the ^{31}P NMR chemical shift of orthophosphate group identified by

a broad peak with a chemical shift ca. 3.5 ppm with narrow resonance at 2.9 ppm (Mason et al., 2007; Philips et al., 2016).

S4. 6 Little Dal Group ^{31}P NMR and ^{19}F NMR

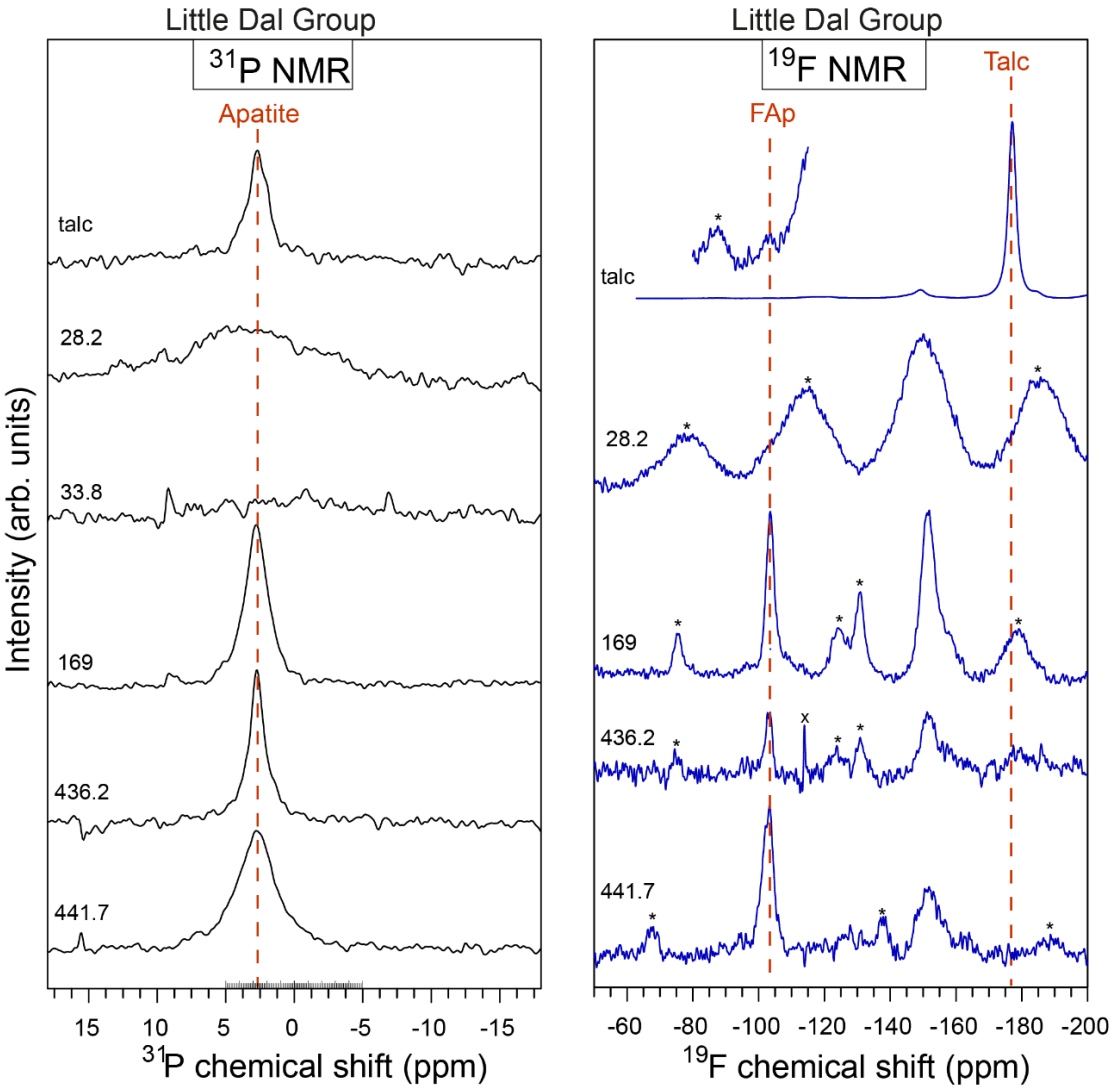

Figure S4 7. The ^{31}P NMR phosphorous speciation data generally yields an apatite-like ^{31}P signal ca. 2.8 ppm. ^{19}F data indicate a fluorapatite F peak, and some but not all of the Little Dal Group spectra contained a carbonate defect determined by a resonance peak shift in the NMR spectra that indicates CO_3 substitution for PO_4, known as β-type carbonate substitution (supplementary material Figure S4 6). However, the ^{19}F "francolite-type defect" is difficult to discern in these spectra due to the typically low fraction of F, which is sensitive to CO_3 substitution. The ^{19}F peak near -150 ppm likely arises from dioctahedral phyllosilicates. Sample 28.2 yielded very broad ^{31}P and ^{19}F peaks. This may result from high-Fe content as suggested by the broad peaks and wide spinning sideband pattern in the ^{19}F spectrum (supplementary material Figure S4 6). Additional PO_4 incorporation into the calcite lattice may be observed by minor changes in the ^{31}P NMR chemical shift of orthophosphate within the calcite lattice identified by

a broad peak with a chemical shift near ca. 3.5 ppm with narrow resonance at 2.9 ppm (Mason et al., 2007; Philips et al., 2016).

S4. 8 Little Dal Group SEM-EDS elemental maps

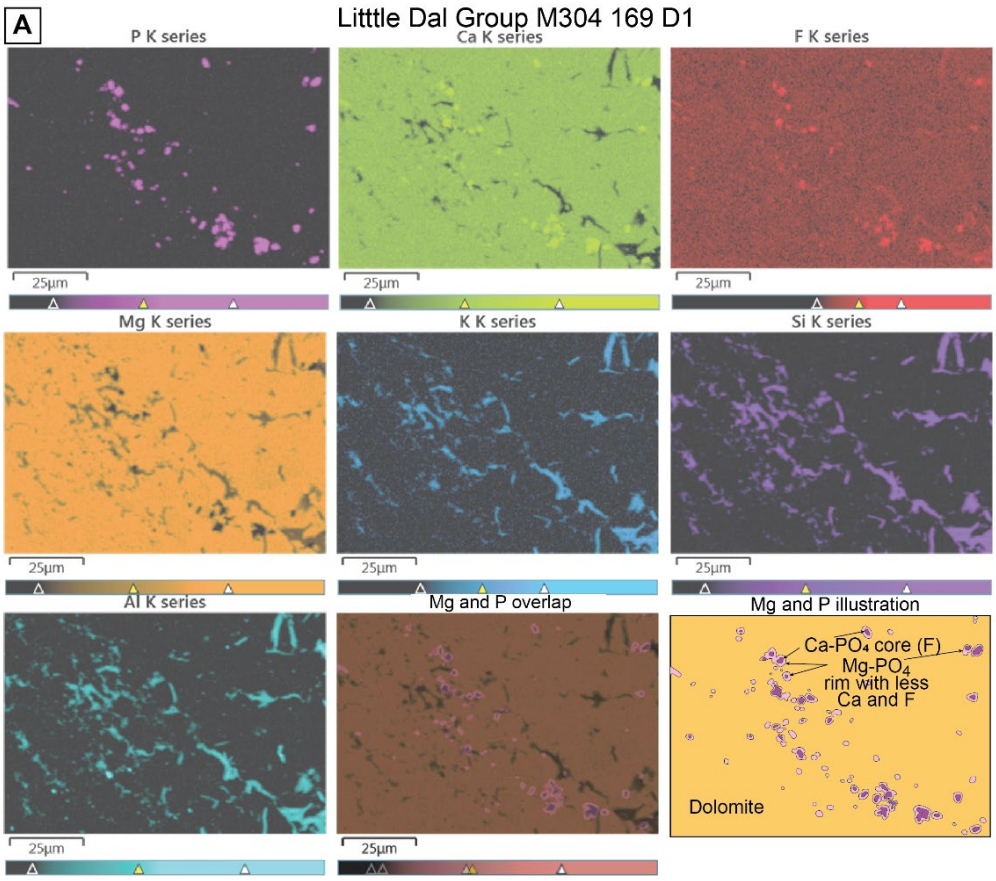

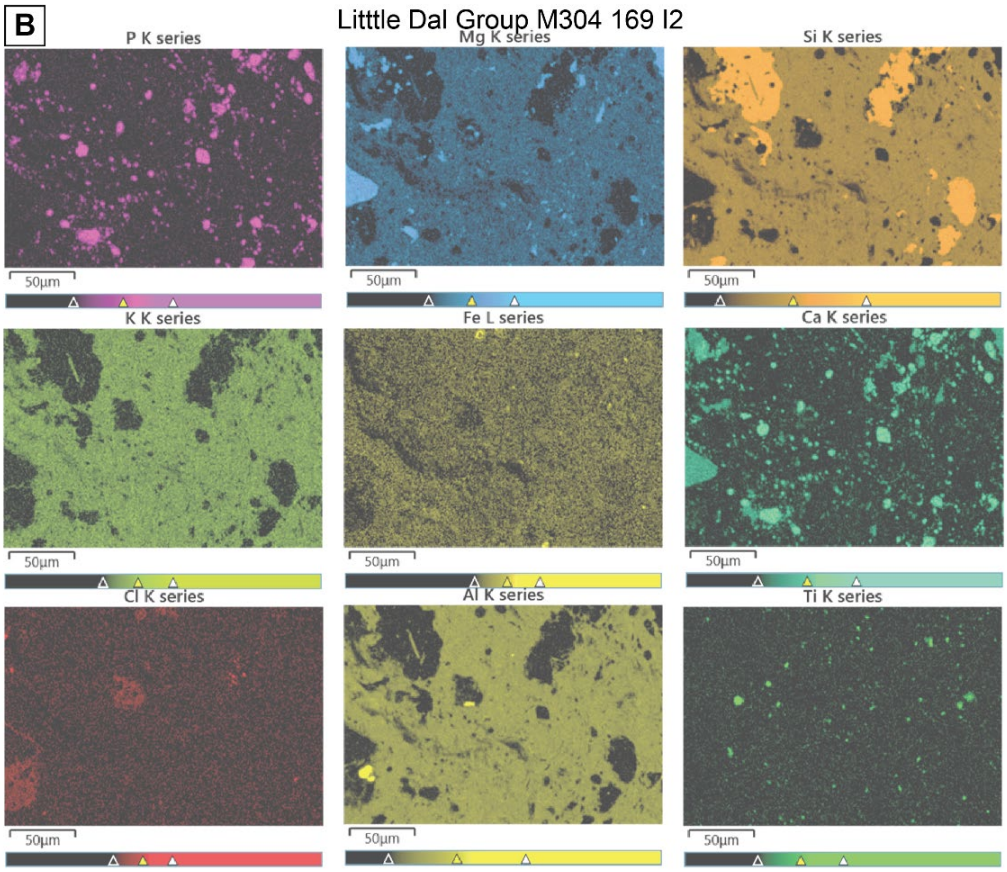
B
Litttle Dal Group M304 169 I2
P K series
Mg K series
Si K series
K K series
Fe L series
Ca K series
Cl K series
Al K series
Ti K series
50µm

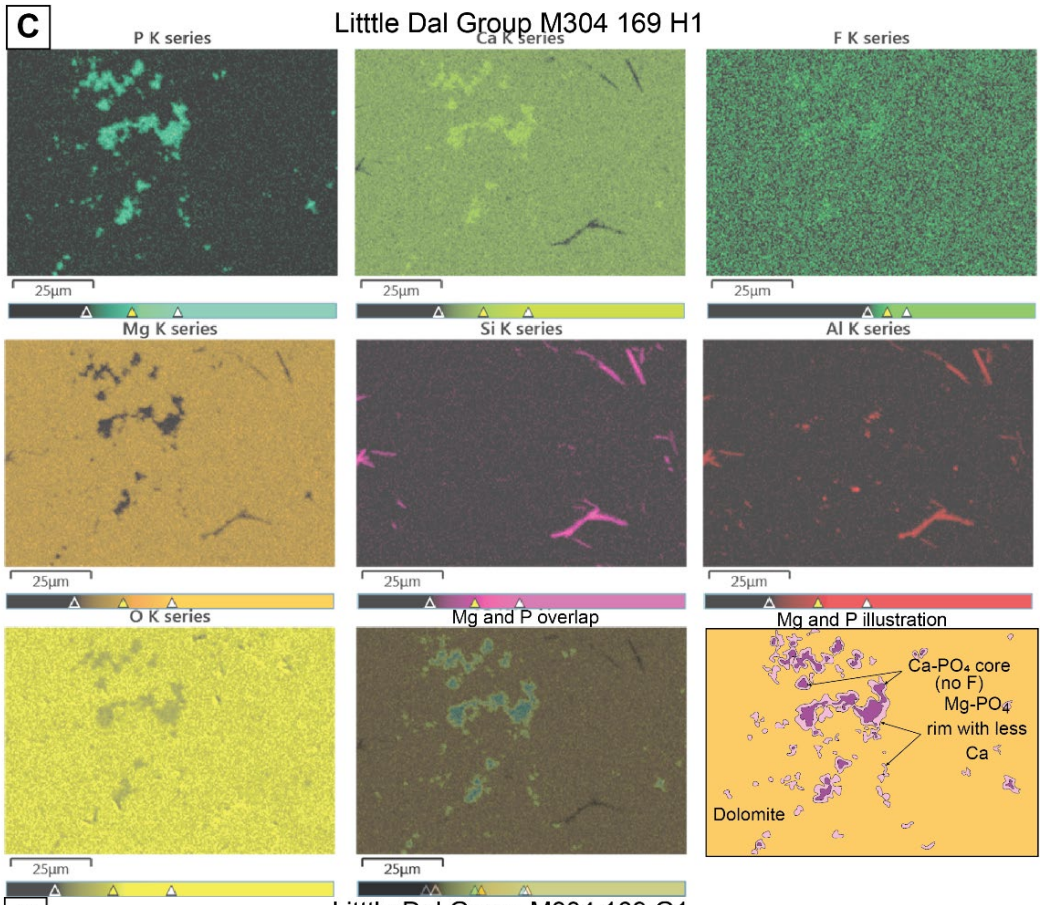
C
Litttle Dal Group M304 169 H1
P K series
Ca K series
F K series
Mg K series
Si K series
Al K series
O K series
Mg and P overlap
Mg and P illustration
Ca-PO4 core (no F)
Mg-PO4 rim with less Ca
Dolomite
25µm

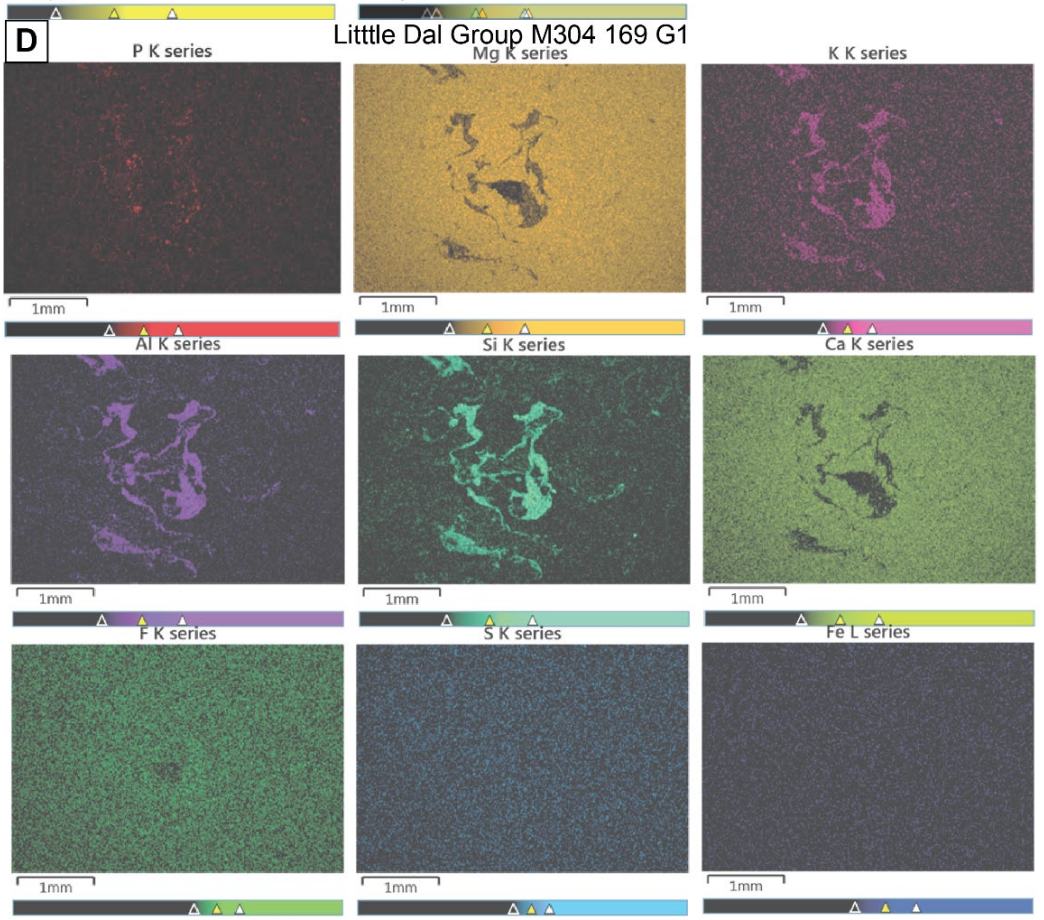
D
Litttle Dal Group M304 169 G1
P K series
Mg K series
K K series
Al K series
Si K series
Ca K series
F K series
S K series
Fe L series
1mm

Figure S4. 8. Little Dal Group SEM-EDS elemental maps that indicate multiple diffrernt chemical variations and styles of apatite present within carbonate sample 169.0 m. A: High F (possibly CFA) apatite embedded within dolomite but in close proximity to clays. Apatite has a Ca core with an Mg-PO_4 rich rim. B: Large, euhedral, low F apatite within K-Mg-Al-Si clays. Ti minerals also present. C: F-poor apatite present between dolomite crystal boundaries. No association with clays. Morphologically different characterized by clusters of apatite with elongated morphologies . D: PO_4 cement within dolomite matrix. Cement is of possible later stage diagenetic origin or syn-depositional fluid flow. Compositionally, the fluid is rich in O_4, Si, K, Al rich fluid. No F, S or Fe are observed

S4. 9 XRD, FTIR and SEM for synthetic calcite CO_3-associated PO_4

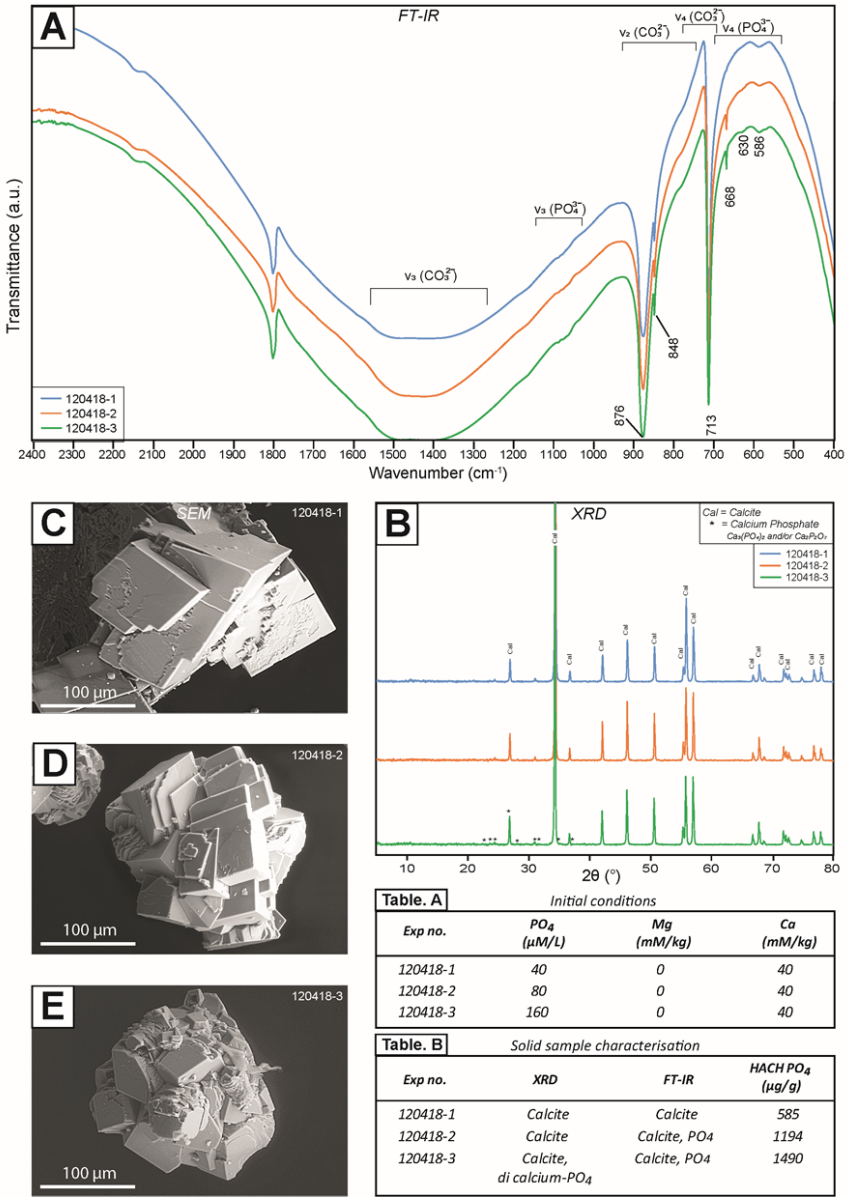

Table. A *Initial conditions*

Exp no.	PO_4 (µM/L)	Mg (mM/kg)	Ca (mM/kg)
120418-1	40	0	40
120418-2	80	0	40
120418-3	160	0	40

Table. B *Solid sample characterisation*

Exp no.	XRD	FT-IR	HACH PO_4 (µg/g)
120418-1	Calcite	Calcite	585
120418-2	Calcite	Calcite, PO4	1194
120418-3	Calcite, di calcium-PO_4	Calcite, PO4	1490

Figure S4 9. Characterized synthetic $CaCO_3$–PO_4 precipitated from PO_4–doped solutions. Resultant solids were analyzed to characterize the nature of PO_4. In addition to XANES spectroscopy (Figure S4 5), increasing PO_4 results in increased bulk PO_4 and different characteristics (Figure S4 8–10). A: FTIR

spectra of samples with colours corresponding to sample 120418-1, 120418-2 and 120418-3 (labelled) that contain increasing concentrations of PO_4. Vibrational frequencies of CO_3^{2-} and PO_4^{3-} are labelled. The spectra indicate that each sample is calcite, with additional vaterite in samples 120418-2 and 120418-3 (indicated by 744 and 876 cm^{-1} and monetite. In addition, PO_4^{3-} can be identified by the bands at 630 and 586 cm^{-1} possibly indicating lattice-bound PO_4 within the calcite crystals. B: XRD diagrams with colours corresponding with samples. PO_4 phases are indicated by asterisk (*). C-E: SEM images of samples 120418-1, 120418-2 and 120418-3 with increasing concentrations of PO_4 respectively. Pronounced morphological changes corresponding to increased PO_4 concentration are related to PO_4 inhibition of the growing calcite crystals. **A:** Table summarizing the initial chemical concentrations of PO_4^{3-} and Ca^{2+} (**B:** Summary of solid sample characterization of sample 120418-1, 120418-2 and 120418-3. The bulk PO_{4tot} concentrations were determined by spectrophotometry using the phosver3 ascorbic acid method 8048, Hach Lange) (Baird et al., 2017).

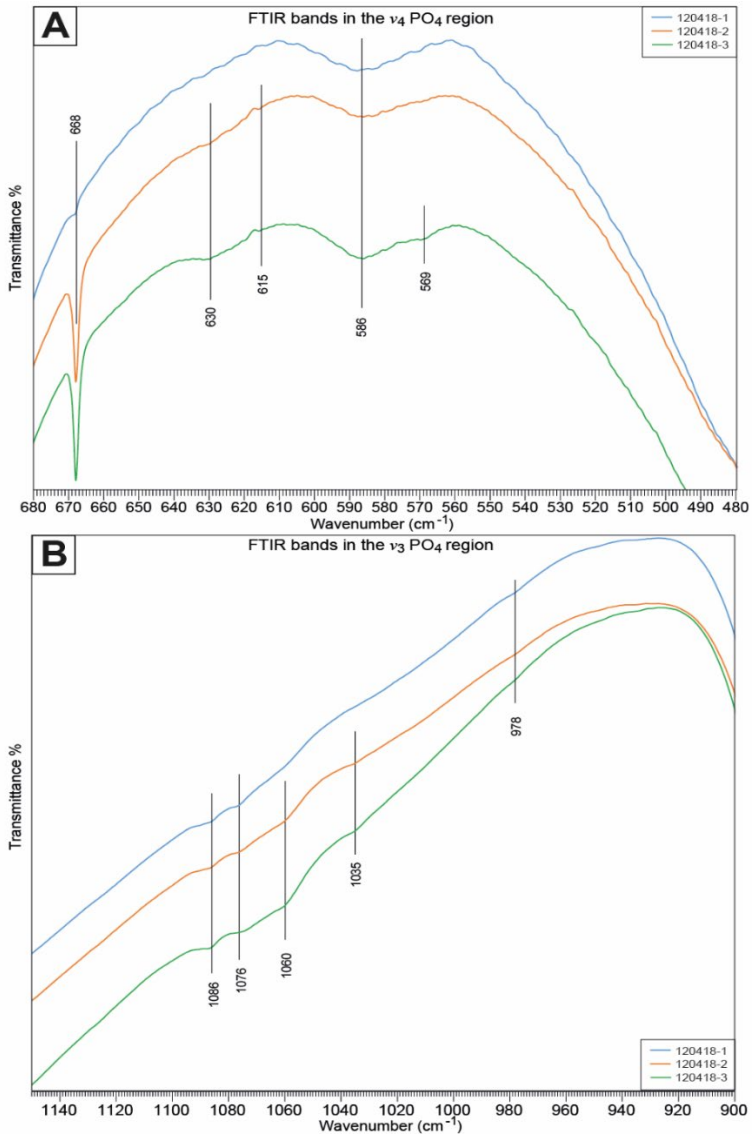

Figure S4 10. Zoomed in section of FTIR spectra (scale is exaggerated vertically to emphasize the band locations and each spectra is displaced vertically) of PO_4 doped synthetic calcite samples 120418-1, 120418-2 and 120418-3 (labelled) that contain increasing concentrations of PO_4. A: ν_4 PO_4 region indicating the 668 cm^{-1} sharp peak that develops with increasing PO_4 content and B:

v_3 PO_4 region contains defects in the spectra that indicate the presence of PO_4 within the samples. C: XANES spectroscopy for corresponding samples. Each spectra is the average of three spectra.

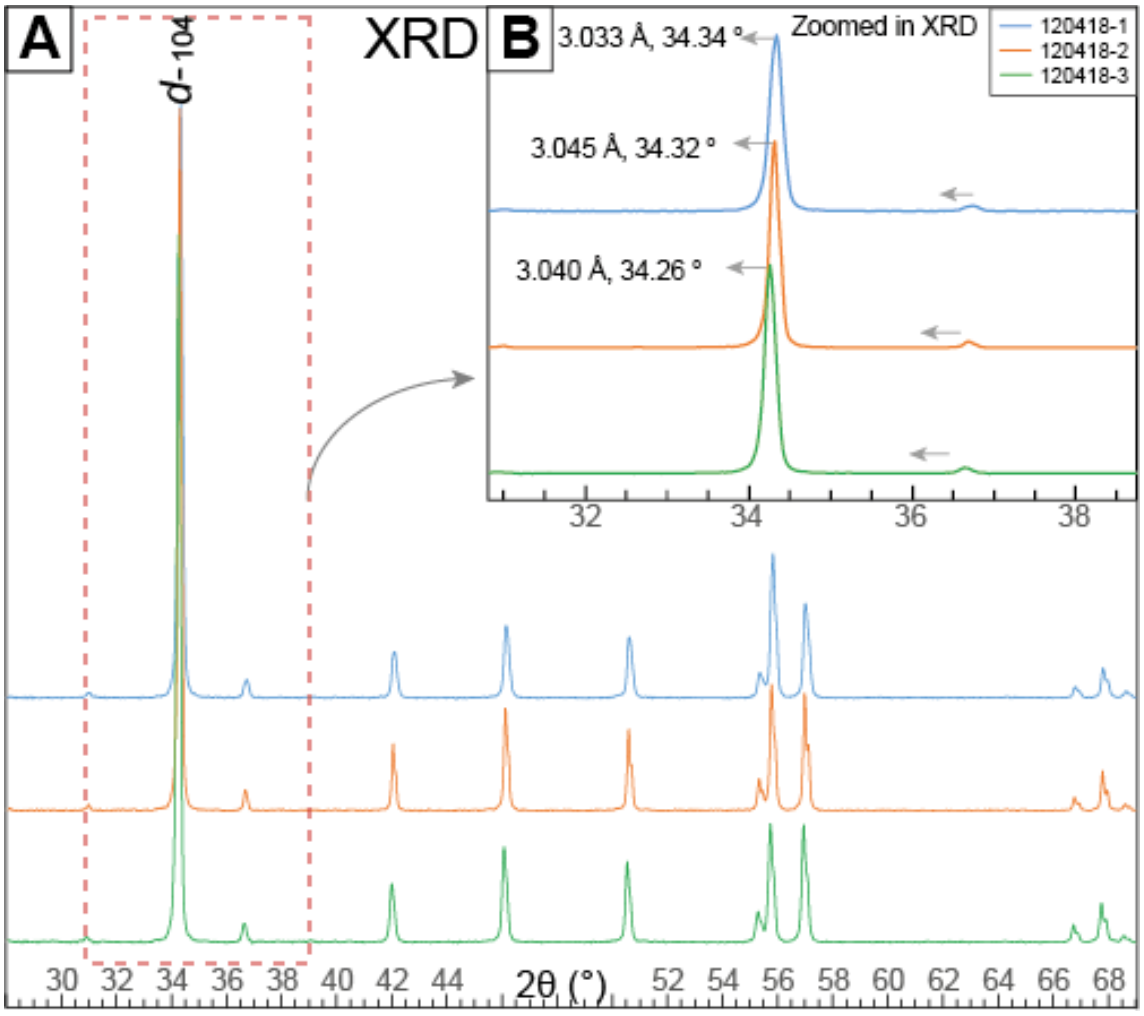

Figure S4 11. Synthetic $CaCO_3$–PO_4 XRD data are shifted vertically to expand the y-axis for clearer presentation. The three samples are calcite with increasing PO_4 from the top to the bottom of the plot (see figure 4.8 for measure PO_4 content) with defects that indicate incorporation of PO_4 ions in the calcite lattice. The samples display a minor but perhaps significant shift in 2θ (º) position to lower values with increasing measured [PO_4]. B: Inset shows a zoomed in section of the XRD diagram to clearly display the shift to lower 2θ (º) position with increasing PO_4 indicated by the arrows.

S4. 9 Notes on CO_3-associated phosphate (CAP)

The investigations characterizing P within geological carbonates conducted in this research have helped build a picture of P presence in Neoproterozoic carbonate sediments and provide

approximations of ancient marine P availability and the influence on biogeochemical systems during geologically important windows. Through these investigations, micro-analytical characterization of carbonate sediments has led to the identification of calcite associated orthophosphate or carbonate-associated phosphate (CAP) from Proterozoic carbonates based on techniques including ^{31}P NMR spectroscopy and XANES, (outlined in Chapter 4 and Phillips et al., 2016).

The incorporation of PO_4 into calcite or CAP has also been observed from synthetic laboratory precipitation experiments and in natural samples such as cave deposits (i.e., Mason et al., 2007; Phillips et al., 2016) providing evidence that dissolved PO_4 can be structurally incorporated into the calcite crystal lattice (Mason et al., 2007; Phillips et al., 2016). On the other hand, adsorption of calcium phosphate on calcite crystal surfaces can also result in incorporation in the resultant mineral (i.e., Watson, 2004) through subsequent growth. Either way, the incorporation can provide insight into the chemical environmental conditions of crystallization (i.e., Mason et al., 2007; Fairchild and Treble, 2009; Philips et al., 2016). In both synthetic samples, cave deposits (Phillips et al., 2016) and calcite in coral skeletons (Chen et al., 2019) the presence of P occurs mainly as inorganic PO_4 (Phillips et al., 2016). Based on solid-state NMR spectroscopy, incorporation of PO_4 in calcite was observed by changes in the ^{31}P NMR chemical shift of the PO_4 group (Phillips et al., 2016) and $^{31}P/^{13}C$ rotational echo double resonance (REDOR) experiments identified atomic-scale proximity of C-O-P of the PO_4 groups to C in the CO_3^{2-} ion of calcite providing evidence that the PO_4 is tightly enclosed within the calcite lattice (Phillips et al., 2016) and not precipitated on the calcite surface for example. The orthophosphate is identified by a broad peak with a chemical shift near ~3.5 ppm with narrow resonance at = 2.9 ppm (Mason et al., 2007; Philips et al., 2016).

Because dissolved PO_4 can be structurally incorporated into the calcite lattice, investigations carbonates and CAP in calcite when used together with kinetic constraints can provide a record of dissolved [PO_{4tot}] from the environment of precipitation. However, one

drawback is that CAP is relatively understudied component of carbonates and the mechanisms by which PO_4 is incorporated into calcite and the chemical environments conducive to the incorporation of PO_4 in calcite require better constraints. For example, what are the kinetics controlling CAP.

Furthermore, there is insufficient data and a poor understanding of the incorporation of PO_4 into Mg-Ca-carbonate minerals and the influence of these systems on PO_4 and CO_3 minerals. This is particularly important in the case of Mg-carbonates because Mg^{2+} stabilizes amorphous calcium phosphate phases and amorphous calcium carbonate phosphate phases and inhibits the transformation from octacalcium phosphate to hydroxyapatite (Jasielec et al., 2020). This inhibition results from Mg^{2+} ions inhibiting the formation and crystal growth of HAp and favours the formation of ACP and β-TCP (tricalcium phosphate) over HAp (Ding et al., 2014; Berg, 2017). This has geological significance because Mg-Ca-carbonate sedimentation dominates geological carbonate successions/ seawater precipitation through much of the Proterozoic (i.e., Grotzinger and James, 2000). In order to understand the formation of CAP and how this relates to P availability in synthetic environments and ancient marine environments, we must first understand fundamental chemical environmental conditions and specifically, the influence of $[PO_{4tot}]$, $[CO_3]$, [Ca] and [Mg] on the incorporation of P in $CaCO_3$ minerals. This provides an opportunity for future experimental and geological microanalytical investigations.